ISSN 2074-272X

науково-практичний
журнал 2022/4

Електротехніка і Електромеханіка

Electrical Engineering & Electromechanics

Електротехнічні комплекси та системи
Промислова електроніка
Електричні станції, мережі і системи
Безпека електрообладнання

Журнал включено до найвищої категорії «А»
Переліку фахових видань України

З 2021 р. журнал індексується у Scopus

З 2015 р. журнал індексується
у Web of Science Core Collection:
Emerging Sources Citation Index

Electrical Engineering & Electromechanics

Scientific Journal was founded in 2002
Founder – National Technical University «Kharkiv Polytechnic Institute» (Kharkiv, Ukraine)

EDITORIAL BOARD

Sokol Ye.I.	**Editor-in-Chief**, Professor, Corresponding member of NAS of Ukraine, Rector of National Technical University «Kharkiv Polytechnic Institute» (NTU «KhPI»), Ukraine
Korytchenko K.V.	**Deputy Editor,** Professor, NTU «KhPI», Ukraine
Rozov V.Yu.	**Deputy Editor,** Professor, Corresponding member of NAS of Ukraine, A. Pidhornyi Institute of Mechanical Engineering Problems of NAS of Ukraine, Kharkiv, Ukraine
Bolyukh V.F.	**Deputy Editor,** Professor, NTU «KhPI», Ukraine
Abu-Siada A.	Professor, Curtin University, Perth, Australia
Aman M.M.	Professor, NED University of Engineering & Technology, Karachi, Pakistan
Baltag O.	Professor, Grigore T. Popa University Medicine and Pharmacy, Romania
Baranov M.I.	Professor, Research and Design Institute «Molniya» of NTU «KhPI», Ukraine
Batygin Yu.V.	Professor, Kharkiv National Automobile and Highway University, Ukraine
Bíró O.	Professor, Institute for Fundamentals and Theory in Electrical Engineering, Graz, Austria
Bouktir T.	Professor, Ferhat Abbas University, Setif 1, Algeria
Buriakovskyi S.G.	Professor, NTU «KhPI», Ukraine
Butkevych O.F.	Professor, Institute of Electrodynamics of NAS of Ukraine (IED of NASU), Kyiv, Ukraine
Colak I.	Professor, Nisantasi University, Istanbul, Turkey
Cruz S.	Professor, University of Coimbra, Portugal
Doležel I.	Professor, University of West Bohemia, Pilsen, Czech Republic
Féliachi M.	Professor, Technological Institute of Saint-Nazaire, University of Nantes, France
Grinchenko V.S.	PhD, A. Pidhornyi Institute of Mechanical Engineering Problems of NAS of Ukraine, Kharkiv, Ukraine
Guerrero J.M.	Professor, Aalborg University, Denmark
Gurevich V.I.	PhD, Honorable Professor, Central Electrical Laboratory of Israel Electric Corporation, Haifa, Israel
Hajjar A.A.	Professor, Tishreen University, Latakia, Syrian Arab Republic
Ida N.	Professor, The University of Akron, Ohio, USA
Izykowski J.	Professor, Wroclaw University of Science and Technology, Poland
Kildishev A.V.	Associate Research Professor, Purdue University, USA
Klepikov V.B.	Professor, NTU «KhPI», Ukraine
Korzeniewska E.	Professor, Lodz University of Technology, Poland
Ktena A.	Professor, National and Kapodistrian University of Athens, Greece
Kuznetsov B.I.	Professor, A. Pidhornyi Institute of Mechanical Engineering Problems of NAS of Ukraine, Kharkiv, Ukraine
Kyrylenko O.V.	Professor, Academician of NAS of Ukraine, IED of NASU, Kyiv, Ukraine
Levin B.M.	Professor, Holon Institute of Technology, Tel Aviv-Yafo, Israel
Malik O.P.	Professor, University Of Calgary, Canada
Maslov V.I.	Professor, National Science Center «Kharkiv Institute of Physics and Technology», Ukraine
Mi Zou	PhD, Chongqing University of Posts and Telecommunications, China
Mikhaylov V.M.	Professor, NTU «KhPI», Ukraine
Miljavec D.	Professor, University of Ljubljana, Slovenia
Milykh V.I.	Professor, NTU «KhPI», Ukraine
Nacke B.	Professor, Gottfried Wilhelm Leibniz Universitat, Institute of Electrotechnology, Hannover, Germany
Petrushin V.S.	Professor, Odessa National Polytechnic University, Ukraine
Podoltsev A.D.	Professor, IED of NASU, Kyiv, Ukraine
Reutskiy S.Yu.	PhD, A. Pidhornyi Institute of Mechanical Engineering Problems of NAS of Ukraine, Kharkiv, Ukraine
Rezinkin O.L.	Professor, NTU «KhPI», Ukraine
Rezinkina M.M.	Professor, NTU «KhPI», Ukraine
Shcherbak Ya.V.	Professor, NTU «KhPI», Ukraine
Sikorski W.	Professor, Poznan University of Technology, Poland
Suemitsu W.	Professor, Universidade Federal Do Rio de Janeiro, Brazil
Trichet D.	Professor, Institut de Recherche en Energie Electrique de Nantes Atlantique, France
Vaskovskyi Yu.M.	Professor, National Technical University of Ukraine «Igor Sikorsky Kyiv Polytechnic Institute», Kyiv, Ukraine
Vazquez N.	Professor, Tecnológico Nacional de México en Celaya, Mexico
Vinnikov D.	Professor, Tallinn University of Technology, Estonia
Yagup V.G.	Professor, O.M. Beketov National University of Urban Economy in Kharkiv, Ukraine
Yatchev I.	Professor, Technical University of Sofia, Bulgaria
Zagirnyak M.V.	Professor, Member of NAES of Ukraine, Kremenchuk M.Ostrohradskyi National University, Ukraine
Zgraja J.	Professor, Lodz University of Technology, Poland
Grechko O.M.	**Executive Managing Editor,** PhD, NTU «KhPI», Ukraine

From no. 1 2021 Journal «Electrical Engineering & Electromechanics» is indexing in **Scopus** and from no. 1 2015 Journal is indexing in **Web of Science Core Collection: Emerging Sources Citation Index (ESCI)**.

Also included in DOAJ (Directory of Open Access Journals), in EBSCO's database, in ProQuest's databases – Advanced Technologies & Aerospace Database and Materials Science & Engineering Database, in Gale/Cengage Learning databases.

Editorial office address:
National Technical University «Kharkiv Polytechnic Institute», Kyrpychova Str., 2, Kharkiv, 61002, Ukraine
phones: +380 57 7076281, +380 67 3594696, **e-mail:** a.m.grechko@gmail.com (**Grechko O.M.)**
ISSN (print) 2074-272X
ISSN (online) 2309-3404

© National Technical University «Kharkiv Polytechnic Institute», 2022

Printed 20 July 2022. Format 60 × 90 ⅛. Paper – offset. Laser printing. Edition 200 copies.
Printed by Printing house «Madrid Ltd» (18, Gudanova Str., Kharkiv, 61024, Ukraine)

Electrical Engineering & Electromechanics

Scientific Journal

no. 4, 2022

Table of Contents

Electrotechnical Complexes and Systems

Industrial Electronics

Power Stations, Grids and Systems

Electrical Safety

UDC 621.3 https://doi.org/10.20998/2074-272X.2022.4.01

H. Chaabane, D.E. Khodja, S. Chakroune, D. Hadji

Model reference adaptive backstepping control of double star induction machine with extended Kalman sensorless control

Introduction. *Newly, the design of a controller for speed control of double star induction motor as a research focus. Consequently, backstepping technique is used to recursively construct a stable control law for speed and flux. Nevertheless, this control law coming from backstepping requires the knowledge of speed and flux values; in practice the measurement sensors are expensive and fragile.* ***The novelty*** *of this work consists to propose a control strategy which based on accurate Kalman filter observer that estimates speed, flux and torque. This extended Kalman filter is an optimal state estimator and is usually applied to a dynamic system that involves a random noise environment.* ***Purpose.*** *Apply a backstepping control of double star induction motor based on principle of rotor flux orientation. This approach consists in finding a Lyapunov function that allows deducing a control law and a modified adaptation rule is referred and sufficient conditions for the stability of the command-observer, in contrast to other techniques who use nonlinear principle.* ***Results.*** *The simulation results are shown to illustrate the performance of the proposed scheme under parametric uncertainties by simulation on MATLAB. The obtained results showed the robustness of the sensorless control in front of load and parameters variation of double stator induction motor. The research directions of the model were determined for the subsequent implementation of results with simulation samples.* References 17, tables 1, figures 18.

Key words: **double stator induction motor, model reference, backstepping control, extended Kalman filter.**

Вступ. *Новітня розробка контролера для регулювання швидкості асинхронного двигуна з подвійною зіркою є предметом дослідження. Отже, метод відступу використовується для рекурсивної побудови стабільного закону керування швидкістю та потоком. Тим не менш, цей закон керування, що випливає з відступу, вимагає знання значення швидкості та потоку; на практиці вимірювальні датчики коштовні та недовговічні.* ***Новизна*** *даної роботи полягає в тому, щоб запропонувати стратегію управління на основі точного спостерігача за фільтром Калмана, який оцінює швидкість, потік і крутний момент. Цей розширений фільтр Калмана є оптимальним засобом оцінки стану і зазвичай застосовується до динамічної системи, яка включає середовище випадкових шумів.* ***Мета***. *Застосування підходу відступу до керування асинхронним двигуном з подвійною зіркою на основі принципу орієнтації потоку ротора. Цей підхід полягає у знаходженні функції Ляпунова, яка дозволяє вивести закон керування та модифіковане правило адаптації, а також достатні умови для стабільності спостерігача команд, на відміну від інших методик, які використовують нелінійний принцип.* ***Результати***. *Результати моделювання наведені для ілюстрації роботи запропонованої схеми за параметричних невизначеностей шляхом моделювання на MATLAB. Отримані результати показали надійність безсенсорного керування перед зміною навантаження та параметрів асинхронного двигуна з подвійним статором. Визначені напрямки дослідження моделі для подальшої реалізації результатів на прикладах моделювання.* Бібл. 17, табл. 1, рис. 18.

Ключові слова: **асинхронний двигун з подвійним статором, еталонна модель, керування на основі відступу, розширений фільтр Калмана.**

Introduction. Recently, the double star induction motor (DSIM) has been widely used in various industrial applications due to its high reliability, relativity low cost, segment the power and easy maintenance requirements [1]. However, its nonlinear structure requires decoupled torque and flux control. Several methods of control are used to control the double star induction motor among which the field orientation control (FOC) that allows a decoupling between the flux and the torque in order to obtain an independent control of the flux and the torque like DC motors.

However, the control of dynamical systems in presence of uncertain and disturbances is a common problem, broadly speaking, process control refers to mechanisms for automatically maintaining the conditions of a mechanical, or electrical process at specified levels and to counteract random disturbances caused by external forces. Recently, several nonlinear control approaches have been introduced to control speed, flux and currents as backstepping control; and adaptive control which taking into account the effect of disturbances (varying parameters).

The process control is «adaptive» in the sense that it changes its output in response to a change in the error. A truly adaptive controller adapts not only its output, but its underlying control strategy as well. It can tune their own parameters or otherwise modify its own control law so as to accommodate fundamental changes in the behavior of the process. Hundreds of techniques for adaptive control have been developed for a wide variety of academic, military, and industrial applications, for example, MRAS (Model Reference Adaptive System), RST (Tracking Simplify Return) and M.I.T rule (Massachusetts Institute of Technology). Arguably the first rudimentary adaptive control scheme was implemented in the late 1950s using a custom-built analog computer (Kalman, 1958). Many «self-tuning» and «auto-tuning» techniques have been developed since then to automate the tuning procedures [2].

MRAS is an important adaptive controller. It may be regarded as an adaptive servo in which the desired performance is expressed in terms of a reference model, which gives the desired response to control signal; this is a convenient way to give specification for a servo problem. Indeed, most commercial controllers today namely model reference adaptive control system has proved very popular on account of a readymade, but heuristically based, rule for synthesizing the adaptive loops called «M.I.T. rule».

A theoretical analysis of loops so designed is generally very difficult, but at present, may be avoided if such systems are synthesized or redesigned on the basis of Lyapunov theory applied to the stability of the adaptive step response [3].

Because the dynamic structure of DSIM is strongly non-linear and coupled. The situation changes with the appearance of the theory of non-linear systems in control theory where the researchers are interested in new control as backstepping control method allow for approaching large systems with a systematic approach, which was introduced during the 1990s by several researchers, Kokotovic is quoted [4]. The application of the latter is found, for example, in the field of aeronautics in [4], and in the field of robotics in [5], and electrical machines [6], and also for power network power regulation in [7].

The majority of the control laws of induction machines such as vector and non-linear commands require the measurement not only of the stator currents (possibly stator voltages) but also of the mechanical speed. Moreover, the load torque is a measurable disturbance but the price of the sensor often makes this measurement unrealistic. The control without the mechanical sensor (speed, load torque) has become a major concern in the industry [8].

Among several approaches without mechanical sensor of the induction machine used neural networks [9], adaptive sliding mode [10], another approach widely used based on a model of behavior of the machine which is based on observation techniques from the extended Luenberger filters in [11, 12], which so with the presence of noise the error of estimations can't be equal to zero. This one decreases the performance of the observer. It is even possible to filter the output in order to eliminate the noise, but this filter can also eliminate its own information of the dynamic of the system, and generally complex to realize.

The goal of the paper is regulate the speed, flux, currents of double star induction motor by hybrid control «Model Reference Adaptive Backstepping Control» coupled by Kalman filter.

Basic calculation relationships and assumptions. The machine to be studied is of the induction type. It is formed of a stator consisting of two three-phase windings mounted in a star shifted by an electric angle α. The latter is equal to 30°. The rotor is formed either of a short-circuited three-phase winding or a squirrel cage. It is modeled by a short-circuited three-phase winding. The application of Park transformation to the model of the double star induction machine leads to equations expressed in a frame related to the rotating field (d, q) by [1, 13-15]. The mechanical equation is given by:

$$\frac{J}{p}\cdot\frac{\mathrm{d}\Omega}{\mathrm{d}t}=T_e-T_L-\frac{B_\omega}{p}\cdot\Omega \tag{1}$$

with the expression of electromagnetic torque T_e:

$$T_e=p\cdot\frac{L_m}{L_m+L_r}\cdot\left[\Phi_{dr}\cdot\left(i_{qs1}+i_{qs2}\right)-\Phi_{qr}\cdot\left(i_{ds1}+i_{ds2}\right)\right]; \tag{2}$$

$$\begin{cases}\Phi_{ds1}=L_{s1}i_{ds1}+L_m[i_{ds1}+i_{ds2}+i_{dr}];\\ \Phi_{qs1}=L_{s1}i_{qs1}+L_m[i_{qs1}+i_{qs2}+i_{qr}];\\ \Phi_{ds2}=L_{s2}i_{ds2}+L_m[i_{ds2}+i_{ds1}+i_{dr}];\\ \Phi_{qs2}=L_{s2}i_{qs2}+L_m[i_{qs1}+i_{qs2}+i_{qr}];\\ \Phi_{dr}=L_ri_{dr}+L_m[i_{ds1}+i_{ds2}+i_{dr}];\\ \Phi_{qr}=L_ri_{qr}+L_m[i_{qs1}+i_{qs2}+i_{qr}].\end{cases} \tag{3}$$

Equations of the stator and rotor voltages are:

$$\begin{cases}v_{ds1}=R_{s1}i_{ds1}+\dfrac{d\Phi_{ds1}}{dt}-\omega_s\Phi_{qs1};\\ v_{qs1}=R_{s1}i_{qs1}+\dfrac{d\Phi_{qs1}}{dt}+\omega_s\Phi_{ds1};\\ v_{ds2}=R_{s2}i_{ds2}+\dfrac{d\Phi_{ds2}}{dt}-\omega_s\Phi_{qs2};\\ v_{qs2}=R_{s2}i_{qs2}+\dfrac{d\Phi_{qs2}}{dt}+\omega_s\Phi_{qs1};\end{cases} \tag{4}$$

$$\begin{cases}v_{dr}=R_ri_{dr}+\dfrac{d\Phi_{qr}}{dt}-\left(\omega_s-\omega_r\right)\Phi_{qr}=0;\\ v_{qr}=R_ri_{qr}+\dfrac{d\Phi_{qr}}{dt}-\left(\omega_s-\omega_r\right)\Phi_{dr}=0.\end{cases} \tag{5}$$

where v_{ds}, v_{qs}, v_{qr}, v_{dr} are the stator and rotor voltages d-q axis components; i_{ds}, i_{qs}, i_{qr}, i_{dr} are the stator and rotor currents d-q axis components; Φ_r, Φ_s are the stator and rotor fluxes; Φ_d, Φ_q are the stator fluxes d-q axis components; ω_r, ω_s, ω^*_{sr} are the stator and rotor pulsation respectively and speed sleep reference; Φ^*_r is the rotor flux control reference; R_r, R_s are the rotor and stator resistances; T_L is the load torque; Ω is the mechanical speed; L_s, L_r, L_m are the stator and rotor inductance, and the mutual inductance respectively; J is the total inertia; B_ω is the friction coefficient; p is the number of pole pairs.

Indirect field oriented control of DSIM. The difficulty in controlling a dual stator induction machine lies in the fact that there is a strong coupling between the input and output variables and the internal variables of the machine such as flux, torque and speed. Conventional control methods such as torque control by frequency slip and flux ratio of voltage to frequency, can тще ensure significant dynamic performance. The development of electronics at the level in the use of static and semi-conductive converters has allowed the application of new control algorithms such as the vector control which is based on the decoupling of flux and torque.

The principle of the vector control called control by flux orientation, obtained by the adjustment of torque by a component of the current and the flux by the other component. Vector control leads to high industrial performance of induction drives. If we make the rotor flux coincide with the axis (d) of the frame linked to the rotating field. The rotor flux orientation by:

$$\Phi_{dr}=\Phi_d;\quad \Phi_{qr}=0\,, \tag{6}$$

where the electromagnetic torque in every moment given by:

$$T_e=p\cdot\frac{L_m}{L_m+L_r}\left(i_{qs1}+i_{qs2}\right)\Phi_r\,. \tag{7}$$

So the main objective in [1, 12] is to produce reference voltages for the static voltage converters supplying the DSIM. Note X^* for reference quantities, (torque, flux, voltages and currents). Applying the orientation of the rotor flux on the system of equations of the machine leads to [12-15] has been presented by ω^*_{sr} the slip angular frequency:

$$\begin{cases} \omega_s^* = \omega_{sr}^* + \omega_r; \quad T_r = \dfrac{L_r}{R_r}; \\ \Phi_r^* = L_m\left(i_{ds1} + i_{ds2}\right); \\ T_e = p \cdot \dfrac{L_m}{L_m + L_r}\Phi_r^*\left(i_{qs1} + i_{qs2}\right); \\ \omega_{sr}^* = \dfrac{R_r L_m}{\left(L_m + L_r\right)\Phi_r^*}\left(i_{qs1}^* + i_{qs2}^*\right) \end{cases} \tag{8}$$

$$\begin{cases} V_{ds1}^* = R_{s1} i_{ds1} + L_{s1}\dfrac{di_{ds1}}{dt} - \omega_s^*\left[L_{s1} i_{qs1} + T_r \Phi_r^* \omega_{sr}^*\right]; \\ V_{ds2}^* = R_{s2} i_{ds2} + L_{s2}\dfrac{di_{ds2}}{dt} - \omega_s^*\left[L_{s2} i_{qs2} + T_r \Phi_r^* \omega_{sr}^*\right]; \\ V_{qs1}^* = R_{s1} i_{qs1} + L_{s1}\dfrac{di_{qs1}}{dt} + \omega_s^*\left[L_{s1} i_{ds1} + \Phi_r^*\right]; \\ V_{qs2}^* = R_{s2} i_{qs2} + L_{s2}\dfrac{di_{qs2}}{dt} + \omega_s^*\left[L_{s2} i_{ds2} + \Phi_r^*\right] \end{cases} \tag{9}$$

Equations (9) constituted the reference equation voltage system.

Structure of the MRAS. The MRAS has proved to be one of the most popular methods in the growing field of adaptive control, particularly for practical application to devices such as autopilots, electrical engineering, where rapid adaption is required [3]. The system has an ordinary feedback loop composed of the process and the controller and another feedback loop that changes the controller parameters (identification algorithm).

The parameters are changed on the basis of feedback from the error, which the difference between the output of the system and the output of the reference model. The ordinary feedback loop is called the inner loop, and the parameters adjustment loop is called the outer loop (Fig. 1).

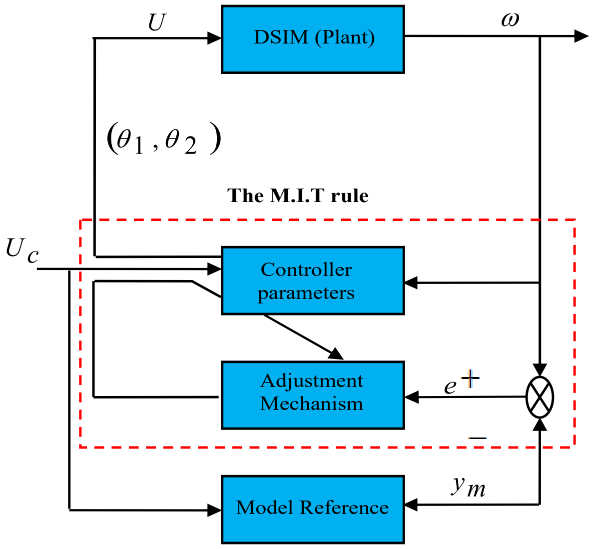

Fig. 1. Diagram of a MRAS based the M.I.T rule

The mechanism for adjustment the parameters in the MRAS can be obtained in two ways: by using a gradient method or by applying stability theory [2].

The M.I.T rule. There is the original approach to MRAS, the name is derived from the fact that was developed at the Instrumentation Laboratory at M.I.T «Massachusetts Institute of Technology» during 1960s [2].

In the MRAS the desired behavior of the system is specified by a model and the parameters of the controller are adjusted based on the error. Let's e be the error between the output y the closed loop system and the desired closed loop response specified by a model whose output is y_m.

One possibility is to adjust parameters θ in such a way that loss function $\Im(\theta) = 0.5e^2$ is minimized.

To make $\Im$ small, it is reasonable to change the parameters in the direction of the negative gradient of $\Im$, that is:

$$\frac{\mathrm{d}\theta}{\mathrm{d}t} = -\gamma\frac{\partial\Im}{\partial\theta} = -\gamma e\frac{\partial e}{\partial\theta}. \tag{10}$$

And the gradient method gives:

$$\frac{\mathrm{d}\theta}{\mathrm{d}t} = -\gamma\frac{\partial e}{\partial\theta}\operatorname{sign}e. \tag{11}$$

Generally the version of this algorithm is used in telecommunications, in which a simple implementation and a fast calculation are necessary [2], but in the application of machine controls the Lyapunov theory will be used.

Design of MRAS using Lyapunov theory for DSIM machine. We find a Lyapunov function and an adaptation mechanism such that the error will go to zero. When using the Lyapunov theory for adaptive systems, we find that dV/dt is usually only negative semi definite. The procedure is to determine the error equation and a Lyapunov function with a bounded second derivative [3].

The desired response is given by:

$$\frac{\mathrm{d}\omega_m}{\mathrm{d}t} = -a_m\omega_m + b_m\omega_r^*, \tag{12}$$

where a_m>0 and the reference speed ω^*_r is bounded.

The speed equation is described by (4) when $a = \dfrac{B_\omega}{J}$, $b = -\dfrac{1}{j}$, $U = T_e^* - \hat{T}_L$, Note $\hat{X}$ for estimated values $\left(\hat{\phi}_r, \hat{\omega}, \hat{T}_L\right)$ by Kalman filter:

$$\frac{\mathrm{d}\omega}{\mathrm{d}t} = -a\omega + bU. \tag{13}$$

The controller is:

$$U = \theta_1\omega_r^* - \theta_2\hat{\omega} \tag{14}$$

introduce the error: $e = \hat{\omega} - \omega_m$

Since we are trying to make the error small, it is natural to derive a deferential equation for the error. We get:

$$\frac{\mathrm{d}e}{\mathrm{d}t} = -a_m e - \left(b\theta_2 + a - a_m\right)\hat{\omega} + \left(b\theta_1 - b_m\right)\omega_r^*.$$

The error goes to zero if the parameters are equal to the value given by:

$$\theta_1^0 = \frac{b_m}{b}, \quad \theta_2^0 = \frac{a - a_m}{b}. \tag{15}$$

Practically these values (J, B_ω) are not real since, and they vary according to the cruel environmental conditions, therefore it can required to update to correct the online value, for this purpose, assume that γ>0 and introduce the following quadratic function [1]

$$V\left(e, \theta_1, \theta_2\right) = \frac{1}{2}\left[e^2 + \frac{1}{b\gamma}\left(b\theta_2 + a - a_m\right)^2 + \frac{1}{b\gamma}\left(b\theta_1 - b_m\right)^2\right]. \tag{16}$$

This function is zero when e is zero and the controller parameters are equal to the correct values.

For the function to qualify as a Lyapunov function the derivative $\mathrm{d}V/\mathrm{d}t$ must be negative. The derivative is:

$$\frac{\mathrm{d}V}{\mathrm{d}t}=e\frac{\mathrm{d}e}{\mathrm{d}t}+\frac{1}{\gamma}\left[\left(b\theta_2+a-a_m\right)\frac{\mathrm{d}\theta_2}{\mathrm{d}t}+\left(b\theta_1-b_m\right)\frac{\mathrm{d}\theta_1}{\mathrm{d}t}\right]=$$

$$=-a_m e^2+\frac{1}{\gamma}\left(b\theta_2+a-a_m\right)\left(\frac{\mathrm{d}\theta_2}{\mathrm{d}t}-\gamma\hat{\omega}e\right)+$$

$$+\frac{1}{\gamma}\left(b\theta_1-b_m\right)\left(\frac{\mathrm{d}\theta_1}{\mathrm{d}t}+\gamma\omega_r^*\hat{\omega}\right).$$

If the parameters are updated as:

$$\begin{cases}\dfrac{\mathrm{d}\theta_1}{\mathrm{d}t}=-\gamma\omega_r^* e;\\ \dfrac{\mathrm{d}\theta_2}{\mathrm{d}t}=\gamma\hat{\omega}e,\end{cases}\tag{17}$$

we get $\mathrm{d}V/\mathrm{d}t=-a_m e^2$.

The derivative of V with respect to time is thus negative semi-infinite this implies the error e will go to zero. A diagram of the system is shown in Fig. 2.

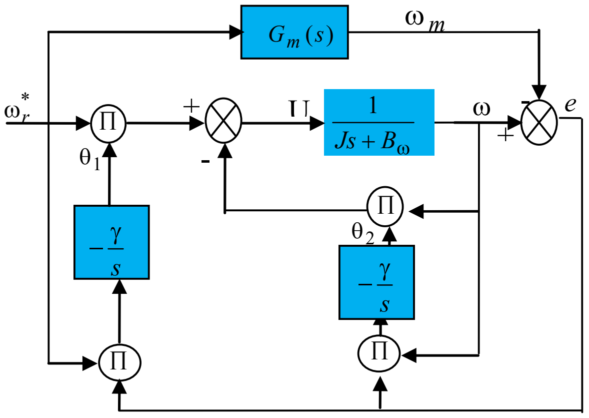

Fig. 2. Diagram of MRAS based on Lyapunov theory for DSIM

Backstepping control of the DSIM. The backstepping control technique provides a systematic method for designing a controller for nonlinear systems [6, 7]. The idea is to compute a control law in order to guarantee, for a certain positive definite (Lyapunov) function, an always negative derivative.

The method consists in breaking up the system into a set of decreasing nested subsystems [12, 16]. The calculation of the Lyapunov function is then performed recursively from inside of the loop. The objective of this technique is to calculate, at each stage of the process, a virtual control is thus generated to ensure the convergence of the system towards its equilibrium state [7, 12]. This can be achieved from the functions of Lyapunov which ensure step by step the stabilization of each synthesis step. Unlike most other methods, backstepping has no nonlinearity constraints.

The model of the double stator induction machine which has been presented is used later for the synthesis of the control law, where the factors μ_1, μ_2 given by:

$$\mu_1=\frac{L_m}{L_m+L_r},\quad \mu_2=\frac{R_r}{L_m+L_r};$$

$$\begin{cases}\dfrac{\mathrm{d}i_{ds1}}{\mathrm{d}t}=\dfrac{1}{L_{s1}}\left[V_{ds1}-R_{s1}i_{ds1}+\omega_s^*\left(L_{s1}i_{qs1}+T_r\Phi_r^*\omega_{sr}^*\right)\right];\\ \dfrac{\mathrm{d}i_{ds2}}{\mathrm{d}t}=\dfrac{1}{L_{s2}}\left[V_{ds2}-R_{s2}i_{ds2}+\omega_s^*\left(L_{s2}i_{qs2}+T_r\Phi_r^*\omega_{sr}^*\right)\right];\\ \dfrac{\mathrm{d}i_{qs1}}{\mathrm{d}t}=\dfrac{1}{L_{s1}}\left[V_{qs1}-R_{s1}i_{qs1}-\omega_s^*\left(L_{s1}i_{ds1}+\Phi_r^*\right)\right];\\ \dfrac{\mathrm{d}i_{qs2}}{\mathrm{d}t}=\dfrac{1}{L_{s2}}\left[V_{qs2}-R_{s2}i_{qs2}-\omega_s^*\left(L_{s2}i_{ds2}+\Phi_r^*\right)\right];\\ \dfrac{\mathrm{d}\Omega}{\mathrm{d}t}=\dfrac{1}{J}\left[P\mu_1\left(i_{qs1}+i_{qs2}\right)\Phi_r^*-B_\omega\Omega-T_L\right];\\ \dfrac{\mathrm{d}\phi_r}{\mathrm{d}t}=-\mu_2\Phi_r+R_r\mu_1\left(i_{ds1}+i_{ds2}\right).\end{cases}\tag{18}$$

First step «flux loop». To ensure the operation of the machine in the linear regime (out of saturation), a flux control is also carried out such that Φ_r follows an imposed trajectory Φ^*_r. To achieve this goal we pose:

$$e_1=\Phi_r^*-\Phi_r.\tag{19}$$

By derivation, we obtain $\dot{e}_1=\dot{\Phi}_r^*-\dot{\Phi}_r$. The first Lyapunov candidate function is defined by:

$$V_1=\frac{1}{2}e_1^2.\tag{20}$$

By derivation, we obtain:

$$\dot{V}_1=e_1\dot{e}_1;\qquad \dot{V}_1=e_1\left[\dot{\Phi}_r^*+\mu_2\Phi_r-R_r\mu_1\left(i_{ds1}+i_{ds2}\right)\right],$$

and according to Lyapunov stability, the origin $e_1 = 0$ of system (20) is asymptotically stable when $\dot{V}_1$ is defined as negative.

We then define (i_{ds1} + i_{ds2}) as the virtual control. Indeed, for an expert in the field of electrical machines, this choice of virtual control is normal, that is to say, one looks for the value that the virtual control must take origin as stable, so the stabilizing virtual function is determined by: $\dot{V}_1=-k_1e_1^2<0$ with $k_1 > 0$. We find:

$$i_{ds1}^*+i_{ds2}^*=\frac{1}{\mu_2 L_m}\left[\mu_2\hat{\phi}_r+\dot{\phi}_r^*+k_1e_1\right]\tag{21}$$

with $i_{ds1}^*=i_{ds2}^*$, represents the references of the components of the current.

Second step «currents loop». For this step, our goal is to eliminate the current regulators, by calculation of the control voltages. Other errors concerning the components of the stator current and their references are defined:

$$\begin{cases}e_2=i_{qs1}^*-i_{qs1};\\ e_3=i_{ds1}^*-i_{ds1};\\ e_4=i_{qs2}^*-i_{qs2};\\ e_5=i_{ds2}^*-i_{ds2}.\end{cases}\tag{22}$$

The dynamics of errors is given by:

$$\begin{cases} \dot{e}_2 = \dfrac{\mathrm{d}i_{qs1}^*}{\mathrm{d}t} - \dfrac{1}{L_{s1}}\left(V_{qs1} + \delta_1\right); \\ \dot{e}_3 = \dfrac{\mathrm{d}i_{ds1}^*}{\mathrm{d}t} - \dfrac{1}{L_{s1}}\left(V_{ds1} + \delta_2\right); \\ \dot{e}_4 = \dfrac{\mathrm{d}i_{qs2}^*}{\mathrm{d}t} - \dfrac{1}{L_{s2}}\left(V_{qs2} + \delta_3\right); \\ \dot{e}_5 = \dfrac{\mathrm{d}i_{ds2}^*}{\mathrm{d}t} - \dfrac{1}{L_{s2}}\left(V_{ds2} + \delta_4\right), \end{cases} \tag{23}$$

with:

$$\begin{cases} \delta_1 = -R_{s1}i_{qs1} - \omega_s^*\left(L_{s1}i_{ds1} + \Phi_r^*\right); \\ \delta_2 = -R_{s1}i_{ds1} + \omega_s^*\left(L_{s1}i_{ds1} + T_r\Phi_r^*\omega_{sr}^*\right); \\ \delta_3 = -R_{s2}i_{qs2} - \omega_s^*\left(L_{s2}i_{ds2} + \Phi_r^*\right); \\ \delta_4 = -R_{s2}i_{qs2} + \omega_s^*\left(L_{s2}i_{ds2} + \Phi_r^*\right). \end{cases} \tag{24}$$

The new function of Lyapunov is given by:

$$V_2 = \frac{1}{2}\left(V_1 + e_2^2 + e_3^2 + e_4^2 + e_5^2\right). \tag{25}$$

By derivation, we obtain:

$$\dot{V}_2 = \dot{V}_1 + e_3\dot{e}_3 + e_4\dot{e}_4 + e_5\dot{e}_5 + e_2\dot{e}_2 .$$

We look for the value that must be taken by the reference command [$V_{ds1}^*, V_{qs1}^*, V_{ds2}^*, V_{qs2}^*$] for the origin is stable. So the stabilizing virtual function is determined so that:

$$\dot{V}_2 = \dot{V}_1 - k_3e_3^2 - k_4e_4^2 - k_5e_5^2 - k_2e_2^2 < 0 .$$

The stability of the control is obtained if and only if a good choice of gains: k_1, k_2, k_3, k_4, k_5 is made. And k_2, k_3, k_4, k_5 positives gains. For this one poses:

$$\begin{cases} V_{qs1}^* = L_{s1}\left(k_2e_2 - \delta_1 + \dfrac{\mathrm{d}i_{qs1}^*}{\mathrm{d}t}\right); \\ V_{ds1}^* = L_{s1}\left(k_3e_3 - \delta_2 + \dfrac{\mathrm{d}i_{ds1}^*}{\mathrm{d}t}\right); \\ V_{qs2}^* = L_{s2}\left(k_4e_4 - \delta_3 + \dfrac{\mathrm{d}i_{qs2}^*}{\mathrm{d}t}\right); \\ V_{ds2}^* = L_{s2}\left(k_5e_5 - \delta_4 + \dfrac{\mathrm{d}i_{ds2}^*}{\mathrm{d}t}\right). \end{cases} \tag{26}$$

Proposed Kalman filter for speed, flux, and load torque sensorless control. The extended Kalman filter (EKF) is a mathematical tool capable of determining state values, immeasurable or parameters of the state system from measurable physical values. It allows estimating the state of a nonlinear system. This filter is based on a number of assumptions, including noise. Indeed, that supposes that the noises which affect the model are centered and white and that these are decor related from the estimated states. In addition, state noise must be decor related from measurement noise [8, 17].

The algorithm of the EKF is the same as that of the standard Kalman filter which has two steps:

- a prediction step which consists in evaluating the state variables from the system model;
- correction step which consists in correcting the prediction error on the variables using the existing differences between the observed and measured variables.

These two steps are preceded by an initialization of the state vector and of the covariance matrices [8]. This filter formulated by the following equations:

$$\begin{aligned} X(k+1) &= f\left(X(k), U(k)\right) + \psi(k) = \\ &= A_d X(k) + B_d U(k) + \psi(k); \end{aligned} \tag{27}$$

$$Y(k) = \hbar\left(X(k)\right) + \Gamma(k) = C_d X(k) + \Gamma(k) . \tag{28}$$

The discrete extended noises ($\psi(k)$ and $\Gamma(k)$) are white, Gaussian and of zero mean, and the covariance matrices ($Q(k)$, $R(k)$) are defined positive and symmetrical.

Equation of the Kalman observers. The extended Kalman observer is generally defined by the following equations [8, 17]:

- Estimate of the initial state: $\hat{X}(0)$;
- Variance the initial state $P(0)$ with:

$$P(k) = A_d P(k-1) A_d^T + Q ; \tag{29}$$

- Kalman gain:

$$G(k) = P(k) C_d^T \left[C_d P(k-1) C_d^T + R\right]^{-1} ; \tag{30}$$

- State estimates $\hat{X}(k)$ by (update):

$$\hat{X}(k+1) = \hat{X}(k) + G(k)\left[y(k) - C_d\hat{X}(k-1)\right]; \tag{31}$$

- Updating the covariance matrix P:

$$P(k+1) = (I - G) C_d P^{-1}(k) . \tag{32}$$

Application of the Kalman filter to DSIM. The application of the EKF is based on the reduced system model. The ideal case consists in choosing a reduced model of the DSIM established in the reference frame *d-q* linked to the rotor.

In this case, the EKF is applied to a system whose estimated state vector is extended to the mechanical speed of rotation $\hat{\omega}(k)$, the flux of the rotor $\hat{\phi}_r(k)$ and to the load torque $\hat{T}_L(k)$.

If it clears that the estimation the constant resistance torque T_L, we assume that it changes slowly, so we can use for the load torque the following model [15]:

$$\frac{\mathrm{d}T_L}{\mathrm{d}t} \cong 0 . \tag{33}$$

So, we choose the extended state model of the system is described by:

$$\begin{cases} \dot{X} = AX + BU; \\ y = CX, \end{cases} \tag{34}$$

with:

$$X = \begin{bmatrix} \vartheta & \omega & \phi_r & T_L \end{bmatrix}^T ;$$

$$U = \begin{bmatrix} i_{ds1} & i_{ds2} & i_{qs1} & i_{qs2} \end{bmatrix}^T ;$$

$$C = \begin{bmatrix} 1 & 0 & 0 & 0 \end{bmatrix};$$

$$A = \begin{bmatrix} 0 & 1 & 0 & 0 \\ 0 & -\dfrac{B_\omega}{J} & 0 & -\dfrac{1}{J} \\ 0 & 0 & -\mu_2 & 0 \\ 0 & 0 & 0 & 1 \end{bmatrix};$$

$$B=\begin{bmatrix} 0 & 0 & 0 & 0 \\ 0 & 0 & \dfrac{\mu_1\phi_r^*}{J} & \dfrac{\mu_1\phi_r^*}{J} \\ \mu_1 L_m & \mu_1 L_m & 0 & 0 \\ 0 & 0 & 0 & 0 \end{bmatrix}.$$

The discrete system which determines the behavior of the continuous filter at discrete times is necessary for the implementation of the Kalman filter in real time.

Considering the process noise and the measurement noise $\psi(k)$, and $\Gamma(k)$ assume the sampling time T_c. The discrete model for (34) is expressed by:

$$\begin{cases} X(k+1)=A_d X(k)+B_d U(k)+\psi(k); \\ y(k)=C_d X(k)+\Gamma(k); \end{cases} \tag{35}$$

with

$$A_d=\begin{bmatrix} 0 & T_c & 0 & 0 \\ 0 & 1-T_c\dfrac{B_\omega}{J} & 0 & -\dfrac{T_c}{J} \\ 0 & 0 & 1-\mu_2 T_c & 0 \\ 0 & 0 & 0 & 1 \end{bmatrix};$$

$$B_d=\begin{bmatrix} 0 & 0 & 0 & 0 \\ 0 & 0 & T_c\dfrac{\mu_1\phi_r^*}{J} & T_c\dfrac{\mu_1\phi_r^*}{J} \\ T_c\mu_1 L_m & T_c\mu_1 L_m & 0 & 0 \\ 0 & 0 & 0 & 0 \end{bmatrix};$$

$$C_d=\begin{bmatrix}1 & 0 & 0 & 0\end{bmatrix}.$$

Finally, the critical step in the EKF is the search for the best covariance matrices Q and R to be established based on the stochastic properties of the corresponding noise are chosen by simulation tests to achieve a desired evaluation performance.

Simulation results. In order to validate the control strategies as discussed, associate the parts of the article and achieve a numerical simulation using the system described in Fig. 3.

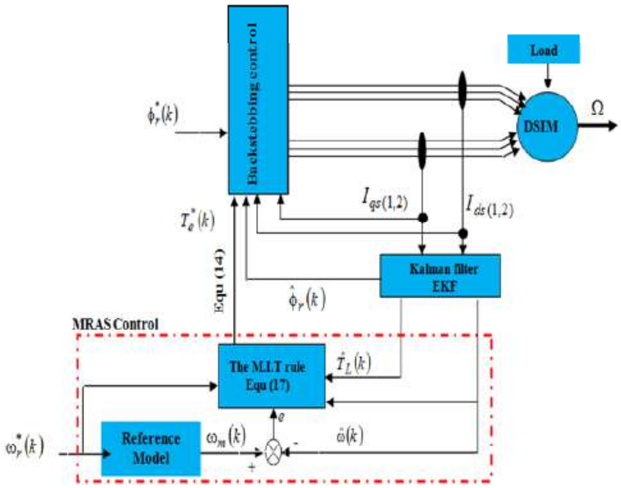

Fig. 3. Presentation of model reference adaptive backstepping control of DSIM motor combining with EKF

The verification and testing of the proposed command is synthesized for the induction double stator machine, and combined with the Kalman observer using simulation series by MATLAB. By the following points:

1. The machine parameters (DSIM) used in simulation is given in Table 1, the reference model chosen by: $a_m = b_m = 30$ (faster than the system).

Table 1

The used DSIM parameters [1, 12]

Parameter name	Symbol	Value	Unit
DSIM mechanical power	P_n	4.5	kW
Nominal voltage	V_n	220	V
Nominal current	I_n	5.6	A
Nominal speed	N	2970	rpm
Stator resistances	$R_{s1} = R_{s2} = R_s$	3.72	Ω
Rotor resistance	R_r	3.72	Ω
Stator self inductances	$L_{s1} = L_{s2} = L_s$	22	mH
Rotor self inductance	L_r	6	mH
Mutual inductance	L_m	0.3672	H
Moment of inertia	J	0.0662	kg·m^2
Viscous friction coefficient	B_ω	0.001	N·m/rad
Supply frequency	f	50	Hz
Pole pairs number	p	1	

2. The gains which guarantee backstepping stability are chosen by: K_1 = 300, K_2 = 500, K_3 = 500, K_4 = 500, K_5 = 500 and for the stability of Lyapunov $\gamma = 0.01$.

3. The Kalman filter parameters are set by: $P(0) = 0.2\cdot I_4$, $Q = 0.7\cdot I_4$, $R = 0.1$.

4. The estimated quantities ($\hat{\omega}_r$, $\hat{\phi}_r$, $\hat{T}_L$) can be used in the control law instead of real quantities (ω_r, ϕ_r, T_L) without posing a problem of stability. We place a white measurement noise (concerning the sensors) at the level of the quantities (ω_r, ϕ_r, T_L) or practically the noise is chosen according to the category of quantity measured, and note that in the worst cases the sensors are all assigned to the same time, in this case the EKF filters the maximum noise to maintain the nominal quantities of DSIM (avoid system malfunction).

5. Based on the error ($e = \omega_r - \omega_m$), and the estimated speed by adjusting the actual values of θ_1 and θ_2 online by (17) with their initial values θ_1^0, θ_2^0, which are given by (15). The law of M.I.T is used to calculate the command T_e^* by (14).

6. The objective of the speed control is to bring its value to 300 rad/s and maintain this value. In addition, the desired flux is fixed at 1 Wb. A positive resistance torque of 15 N·m is applied between 1.5 s and 2.5 s. The results presented as follows.

Figures 4–7 present the M.I.T regulator parameters (θ_1, θ_2), the rotor speed, rotor flux and the resistive torque.

The regulator parameters (θ_1, θ_2) have been improved (adapted) in order to check the condition that the error is equal to zero (Fig. 4).

We note that all the estimated quantities follow the evolution of these real values (speed, flux, load torque) of the DSIM well, so the estimation is done in a satisfactory manner (Fig. 5, 6). The speed follows its reference value (ω_m), and after the application of the load torque C_r = 15 N·m at t = 1.5 s, the electromagnetic torque takes the estimated load torque value (Fig. 7). The second consists in reversing the speed of rotation from 100 to –100 rad/s at time t = 1 s under load torque C_r = 15 N·m since t = 1.5 s.

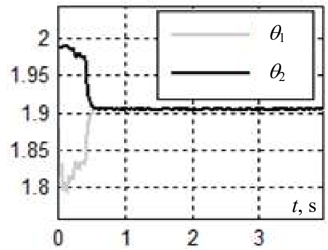

Fig. 4. The adjustment of parameters (θ_1, θ_2) of the controller

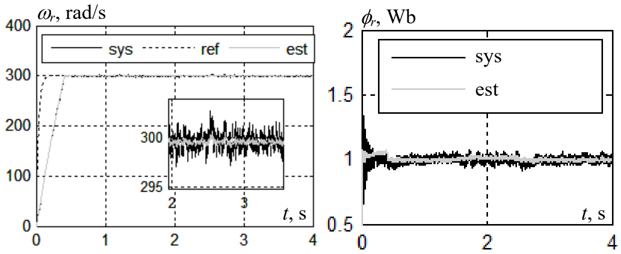

Fig. 5. Estimated and reference speed, rotor flux of the DSIM motor using Kalman filter

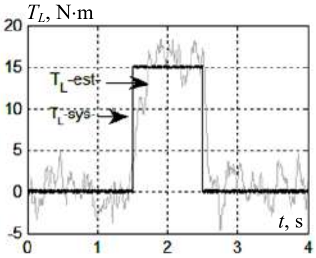

Fig. 6. Estimated and reference of the load torque by Kalman filter

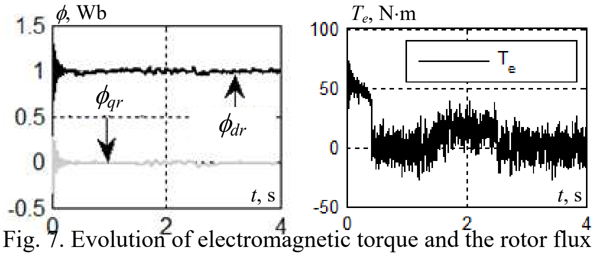

Fig. 7. Evolution of electromagnetic torque and the rotor flux components (ϕ_{dr}, ϕ_{qr}) of the DSIM

In Fig. 8 the regulator parameters (θ_1, θ_2) have been evolved (adapted) in a form which must check the condition of the error equal to zero and their stabilities are tied by speed stability ($\Im(0) = 0$).

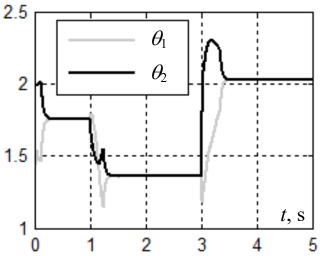

Fig. 8. The adjustment of parameters (θ_1, θ_2) of the controller during speed variation test under load

The speed follows its reference and reverses after (0.25 s) (Fig. 9) leads to a negative torque (-50 N·m) during the interval of the speed inversion, then it oscillates author zero when the speed reaches -100 rad/s (Fig. 10).

The estimated rotor flux follows its set point with a slight disturbance during the time of the speed reversal (Fig. 9). The speed reversal generates an increase in the stator current i_{as1}, but the latter retains its sinusoidal shape (Fig. 11).

The electromagnetic torque (Fig. 10) admits a significant peak at startup and also the components of the current i_{qs1} and finally the shape of the components of the rotor flux show that the decoupling is always maintained (Fig. 11).

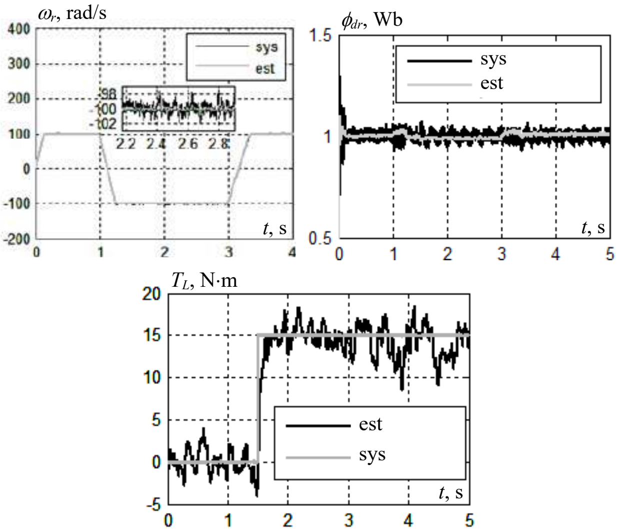

Fig. 9. Estimated and reference of speed, rotor flux, of the DSIM using Kalman filter during speed variation test under load

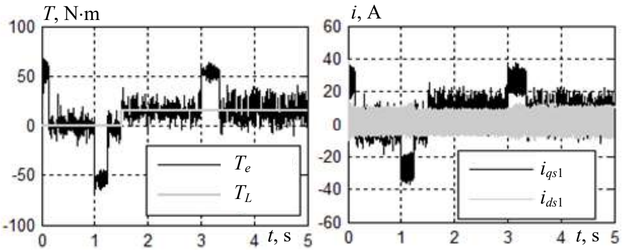

Fig. 10. Evolution of electromagnetic torque and currents i_{ds1}, i_{qs1} during speed variation test under load

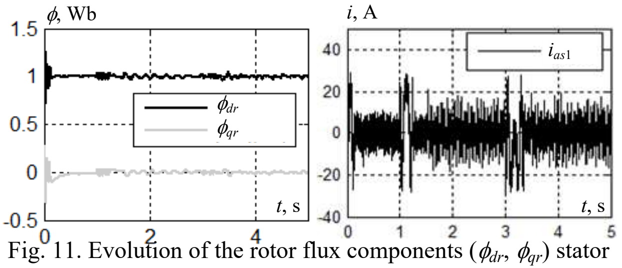

Fig. 11. Evolution of the rotor flux components (ϕ_{dr}, ϕ_{qr}) stator current i_{as1} during speed variation test under load

Robustness tests. Figures 12–14 show the performance of DSIM regulation with respect to the increase in the moment of inertia by 100 % of its nominal value. The regulator parameters (θ_1, θ_2) have been evolved (adapted) in a form which must verify the condition of the error equal to zero (Fig. 12), the estimated quantities follow the evolution of these real values well (Fig. 13), this increase does not affect the values of electromagnetic torque, and stator current (Fig. 13).

The second test contains the dynamic response of the controller during robustness tests to the increase in the rotor resistance by 100 % of its nominal value with varied load. In Fig. 15 the regulator parameters (θ_1, θ_2) have been changed (adapted) always in the sense that the estimation error is equal to zero.

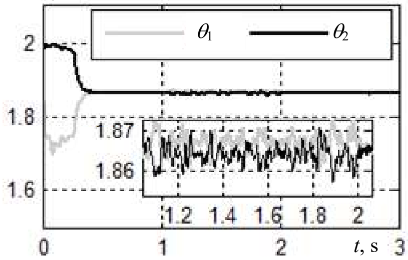

Fig. 12. Dynamic response of parameters (θ_1, θ_2) of the controller during robustness tests with respect to total inertia J

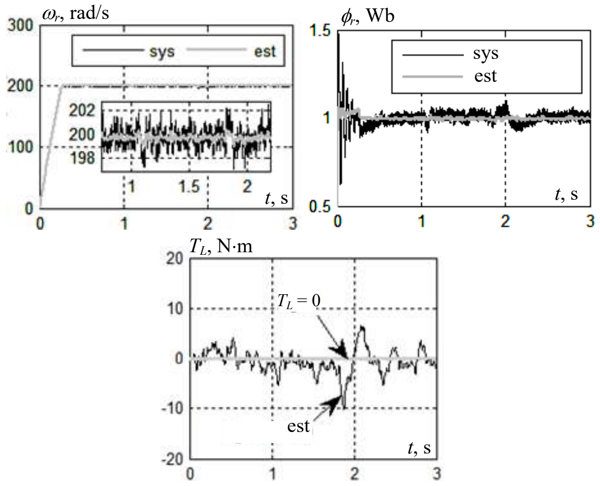

Fig. 13. Estimated speed, rotor flux and load torque

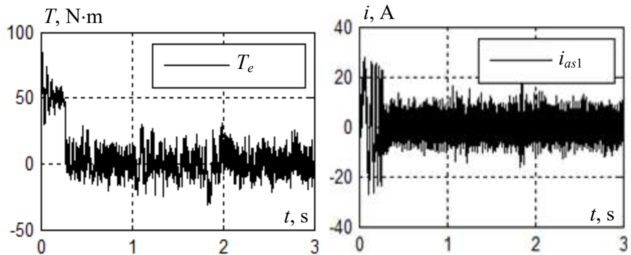

Fig. 14. Dynamic response of the DSIM using Kalman filter during robustness tests with respect to total inertia J

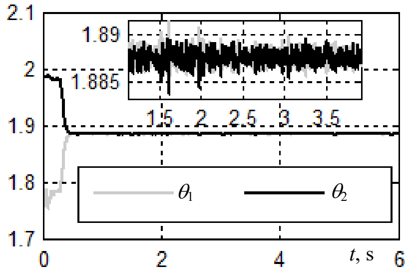

Fig. 15. Dynamic response of parameters (θ_1, θ_2) of the controller during robustness tests with $R_r = 2{\cdot}R_{rn}$ from $t = 1$; 2 s with varied load

From Fig. 16 we see that the quantities estimated by Kalman filter follow their real values obtained despite the variation of the rotor resistance. It is clearly noted that no influence appears during the variation of the rotor resistance in no-load operation [5; 6] s and operating under load $t > 1$ s. The electromagnetic torque compensates for the load torque even when applying a load greater than the nominal load torque $C_r = 21$ N·m (Fig. 17).

A large current draw i_{as1} appears during the application of the load where the rotor resistance $R_r = 2{\cdot}R_{rn}$. The components of the rotor flux follow their imposed values in Fig. 18.

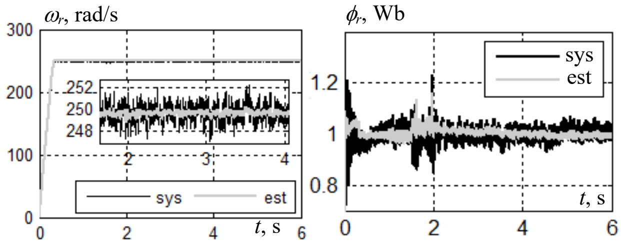

Fig. 16. Estimated speed and rotor flux

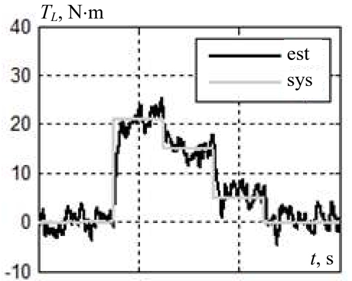

Fig. 17. Load torque

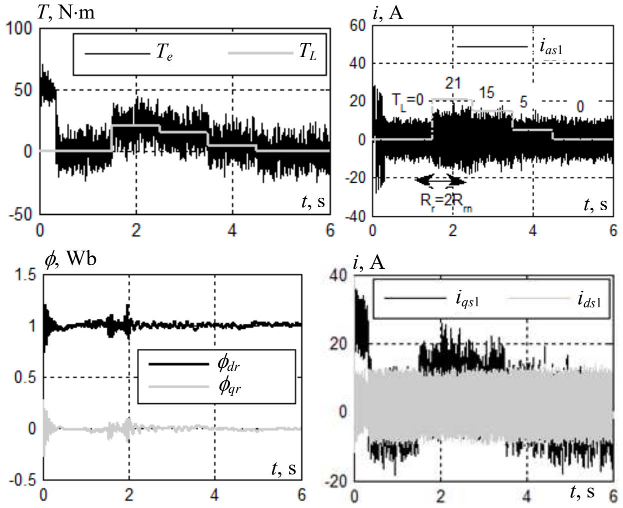

Fig. 18. Dynamic response of the DSIM using Kalman filter during robustness tests with $R_r = 2{\cdot}R_{rn}$ from $t = 1$; 2 s with varied load

Conclusions.

1. This study proposes a robust model reference adaptive backstepping control law for the speed regulation of double stator induction motor drive system demonstrating lumped uncertainty with Extended Kalman filter observer (speed, flux and load torque). First, the system mathematical model for the field oriented control is introduced. Then, based to the Lyapunov stability as a common point, the robust controller has hybrid by two loops.
2. The analyzed of the speed loop by the adaptive rule where the regulator parameters adjustment has been online and the current loops by backstepping control with load disturbance rejection into account.
3. It can clearly be seen that the development of the proposed robust control law has been applied. To avoid the problem of the persecutory effects of speed sensors and the resistant torque, a developed Kalman observer has been proposed.
4. The results obtained in simulation are very close to those obtained using a speed sensor. Finally, as a perspective, it would be interesting to add an estimator for the rotor resistance and the experimental implementation

of the proposed control scheme will be addressed in the future work.

Conflict of interest. The authors declare that they have no conflicts of interest.

REFERENCES

1. Hadiouche D., Razik H., Rezzoug A. Study and simulation of space vector PWM control of double-star induction motors. *7th IEEE International Power Electronics Congress. Technical Proceedings*. CIEP 2000 (Cat. No.00TH8529), 2000, pp. 42-47. doi: https://doi.org/10.1109/CIEP.2000.891389.

2. Astrom K.J., Wittenmark B. *Adaptive control (2nd Edition).* Prentice Hall Publ., 1994.

3. Parks P. Liapunov redesign of model reference adaptive control systems. *IEEE Transactions on Automatic Control*, 1966, vol. 11, no. 3, pp. 362-367. doi: https://doi.org/10.1109/TAC.1966.1098361.

4. Mian A.A., Daobo W. Modeling and Backstepping-based Nonlinear Control Strategy for a 6 DOF Quadrotor Helicopter. *Chinese Journal of Aeronautics*, 2008, vol. 21, no. 3, pp. 261-268. doi: https://doi.org/10.1016/S1000-9361(08)60034-5.

5. Bouadi H., Bouchoucha M., Tadjine M. Sliding mode control based on backstepping approach for an UAV type quadrotor. *International Journal of Mechanical and Mechatronics Engineering*, 2007, vol. 1, no 2, pp. 39-44. doi: https://doi.org/10.5281/zenodo.1077447.

6. Chaouch S., Nait Said M.S., Makoof A. Backstepping control design of sensorless speed induction motor based on MRAS technique. *International Review of Electrical Engineering*, 2007, vol. 2, no. 5, pp. 738-744. Available at: https://www.praiseworthyprize.org/latest_issues/IREE-latest/IREE_vol_2_n_5.html#Backstepping_Control_Design_of_Sensorless_Speed_Induction_Motor_Based_on_MRAS_Technique (accessed 10 May 2021).

7. Benakcha M., Benalia L. Tourqui D., Benakcha A. Backstepping control of dual stator induction generator used in wind energy conversion system. *International Journal of Renewable Energy Research*, 2018, vol. 8, no. 1, pp. 385-395. doi: https://doi.org/10.20508/ijrer.v8i1.7025.g7313.

8. Zerdali E., Barut M. Novel version of bi input-extended Kalman filter for speed-sensorless control of induction motors with estimations of rotor and stator resistances, load torque, and inertia. *Turkish Journal of Electrical Engineering & Computer Sciences*, 2016, vol. 24, pp. 4525-4544. doi: https://doi.org/10.3906/elk-1408-136.

9. Kuchar M., Brandstetter P., Kaduch M. Sensorless induction motor drive with neural network. *2004 IEEE 35th Annual Power Electronics Specialists Conference* (IEEE Cat. No.04CH37551), 2004, vol. 5, pp. 3301-3305. doi: https://doi.org/10.1109/PESC.2004.1355058.

10. Li J., Xu L., Zhang Z. An Adaptive Sliding-Mode Observer for Induction Motor Sensorless Speed Control. *IEEE Transactions on Industry Applications*, 2005, vol. 41, no. 4, pp. 1039-1046. doi: https://doi.org/10.1109/TIA.2005.851585.

11. You J., Wu W., Wang Y. An Adaptive Luenberger Observer for Speed-Sensorless Estimation of Induction Machines. *2018 Annual American Control Conference (ACC)*, 2018, pp. 307-312. doi: https://doi.org/10.23919/ACC.2018.8431006.

12. Chaabane H., Khodja D., Chakroune S. Sensorless backstepping control using an Luenberger observer for double star induction motor. *Archives of Electrical Engineering*, 2020, vol. 69, no. 1, pp. 101-116. doi: https://doi.org/10.24425/aee.2020.131761.

13. Chaabane H., Khodja D., Chakroune S. Indirect self tuning adaptive control of double stars induction machine by sliding mode. *Revue Roumaine Des Sciences Techniques Serie Electrotechnique et Energetique*, 2019, vol. 64, no. 4, pp. 409-415. Available at: http://revue.elth.pub.ro/viewpdf.php?id=878 (accessed 10 May 2021).

14. Bennassar A., Abbou A., Akherraz M., Barara M. Sensorless backstepping control using an adaptive Luenberger observer with three levels NPC inverter. *International Journal of Electrical and Computer Engineering*, 2013, vol. 7, no. 8, pp. 1171-1177. doi: https://doi.org/10.5281/zenodo.1088970.

15. Khouidmi H., Massoum A. Reduced-Order Sliding Mode Observer-based Speed Sensorless Vector Control of Double Stator Induction Motor. *Acta Polytechnica Hungarica*, 2014, vol. 11, no. 6, pp. 229-249. doi: https://doi.org/10.12700/APH.11.06.2014.06.14.

16. Ameid T., Menacer A., Talhaoui H., Ammar A., Azzoug Y. Sensorless speed estimation and backstepping control of induction motor drive using model reference adaptive system. *2017 5th International Conference on Electrical Engineering - Boumerdes (ICEE-B)*, 2017, pp. 1-6, doi: https://doi.org/10.1109/ICEE-B.2017.8191977.

17. Young-Real Kim, S.-K. Sul, Min-Ho Park. Speed sensorless vector control of induction motor using extended Kalman filter. *IEEE Transactions on Industry Applications*, 1994, vol. 30, no. 5, pp. 1225-1233. doi: https://doi.org/10.1109/28.315233.

Received 19.03.2022
Accepted 21.05.2022
Published 20.07.2022

Hadji Chaabane[1], *Doctor of Electrotechnical,*
Djalal Eddine Khodja[2], *Doctor of Electrotechnical, Professor,*
Salim Chakroune[1], *Doctor of Electrotechnical, Professor,*
Djamel Hadji[1], *M.S.,*
[1] Research Laboratory on the Electrical Engineering,
Faculty of Technology, University of M'Sila,
BP 166, Ichbilia 28000, Algeria,
e-mail: chaabane.hadji@univ-msila.dz,
salim.chakroune@univ-msila.dz (Corresponding author),
hadjiDjamel92@gmail.com
[2] Signals & Systems Lab,
Institute of Electrical and Electronic Engineering,
Boumerdes, 35000, Algeria.
e-mail: djalaleddine.khodja@univ-msila.dz

How to cite this article:
Chaabane H., Khodja D.E., Chakroune S., Hadji D. Model reference adaptive backstepping control of double star induction machine with extended Kalman sensorless control. *Electrical Engineering & Electromechanics*, 2022, no. 4, pp. 3-11. doi: https://doi.org/10.20998/2074-272X.2022.4.01

UDC 621.3.013 https://doi.org/10.20998/2074-272X.2022.4.02

B.I. Kuznetsov, T.B. Nikitina, I.V. Bovdui, O.V. Voloshko, V.V. Kolomiets, B.B. Kobylianskyi

The method of multi objective synthesis of nonlinear robust control by multimass electromechanical systems

Aim. *Development of the method of multi objective synthesis of nonlinear robust control by multimass electromechanical systems to satisfy various requirements for the operation of multi-mass systems in various modes.* ***Methodology.*** *The problem of multi objective synthesis of nonlinear robust control of multimass electromechanical systems is formulated and the possibility of satisfying various requirements for the operation of such systems in various modes based on the concept of functionally multiple membership of the state vector and the solution of the Hamilton-Jacobi-Isaacs equation is shown. A method for choosing weight matrices with the help the vector of purpose of nonlinear robust control is formed by solving a zero-sum vector antagonistic game has been substantiated and developed.* ***Results****. The results multi objective synthesis of nonlinear robust two-mass electromechanical servo systems in which differences requirements for the operation of such systems in various modes were satisfied are given. Based on the results of modeling and experimental studies it is established, that with the help of synthesized robust nonlinear controllers, it is possible to improve of quality indicators of two-mass electromechanical servo system in comparison with the system with standard regulators.* ***Originality.*** *For the first time the method of multi objective synthesis of nonlinear robust control by multimass electromechanical systems to satisfy various requirements for the operation of multimass systems in various modes is developed.* ***Practical value.*** *From the point of view of the practical implementation the possibility of solving the problem of multi objective synthesis of nonlinear robust control systems to satisfy various requirements for the operation of multimass electromechanical systems in various modes is shown.* References 32, figures 4.

Key words: **multimass electromechanical systems, nonlinear robust control, multi objective synthesis, Hamilton-Jacobi-Isaacs equation, computer simulation, experimental research.**

Мета*. Розробка методу багатокритеріального синтезу нелінійного робастного керування багатомасовими електромеханічними системами для задоволення різноманітних вимог до роботи багатомасових систем у різних режимах.* ***Методологія****. Сформульовано задачу багатокритеріального синтезу нелінійного робастного керування багатомасовими електромеханічними системами та показана можливість задоволення різноманітних вимог до роботи таких систем у різних режимах на основі концепції функціонально множинної належності вектора стану та рішення рівняння Гамільтона-Якобі-Айзекса. Обґрунтовано та розроблено метод вибору вагових матриць, за допомогою яких формується вектор мети нелінійного робастного керування, шляхом розв'язання векторної антагоністичної гри з нульовою сумою.* ***Результати****. Наведено результати багатокритеріального синтезу нелінійних робастних двомасових електромеханічних сервосистем керування, в яких були задоволені різноманітні вимоги до роботи таких систем у різних режимах. На основі результатів моделювання та експериментальних досліджень встановлено, що за допомогою синтезованих нелінійних робастних регуляторів можна підвищити якісні показники двомасової електромеханічної сервосистеми в порівнянні з системою зі стандартними регуляторами.* ***Оригінальність****. Вперше розроблено метод багатокритеріального синтезу нелінійного робастного керування багатомасовими електромеханічними системами для задоволення різноманітних вимог до роботи багатомасових систем у різних режимах.* ***Практичне значення****. З точки зору практичної реалізації показана можливість вирішення задачі багатокритеріального синтезу нелінійних робастних електромеханічних систем керування для задоволення різноманітних вимог до роботи таких систем у різних режимах.* Бібл. 32, рис. 4.

Ключові слова: **багатомасові електромеханічні системи, нелінійне робастне керування, багатокритеріальний синтез, рівняння Гамільтона-Якобі-Айзекса, комп'ютерне моделювання, експериментальні дослідження.**

Introduction. The central problem of modern theory and practice of automatic control is the creation of systems capable of providing high control accuracy under intense master and disturbing influences of a wide range of frequencies. Improving the accuracy of electromechanical control systems is often constrained by imperfect mechanical transmissions from the actuator to the working mechanism [1, 2]. This, first of all, manifests itself with an increase in the system bandwidth, when the frequencies of natural mechanical vibrations of the transmission, together with the actuator and the working mechanism, fall into the range of operating frequencies of the control systems. At the same time, it is necessary to take into account the presence of elastic elements between the shafts of the executive motor, the gearbox and the working mechanism, and instead of the single-mass model, the engine – the working mechanism, use two, three, and sometimes even a multi-mass model [3, 4]. The conditions of operation of electromechanical systems are also complicated by the presence of a nonlinear dependence of the moment (force) of friction on the speed of sliding of the working mechanism relative to the material being processed [5, 6]. This dependence often manifests itself in many modes of operation of electromechanical systems at low (creeping) speeds of movement of the working body. Moreover, for some mechanisms, this mode is working, and for others – emergency. The situation is even more aggravated when the presence of elastic elements is combined with the operation of the system on the falling section of the external friction characteristic, which can lead to the occurrence of sustained or even diverging mechanical vibrations [7, 8].

Various requirements are imposed on the designed multi-mass control systems during their operation in various modes. As a rule, certain restrictions are imposed on the quality of transient processes – the first coordination time, regulation time, overshoot, etc. are set. Usually, the maximum variance of the tracking error or stabilization during the development of random reference influences, or the compensation of random disturbing influences, is also specified, and in this case, naturally, the constraints on the state and control variables must be satisfied [9]. Another requirement for control systems is the limitation of mastering errors or compensation of disturbing influences in the form of harmonic signals. In this case, an input signal of one frequency, or several characteristic operating frequencies, can be set, and a range of operating frequencies can be set, in which certain conditions must be fulfilled. And, finally, for tracking systems of increased accuracy, the characteristic mode of operation is the development of low speeds or small displacements. For this mode, the roughness of movement is usually specified in the form of appropriate criteria. The reasons for the non-smooth movement of the working body at low speeds is the presence of nonlinearities such as dry friction in the executive motors and working bodies and elastic elements between the executive motor and the working body, which leads to stall vibrations of the moving parts of the executive motor and the working body, accompanied by stops and breakdowns of the moving parts relative to stop positions.

For such systems, in most practical cases, with the help of typical PID controllers, it is not possible to fulfill the technical requirements for the system, which necessitates the use of more complex controllers and modern methods of their synthesis [10–12]. One of the main requirements for multi-mass control systems is also the requirement for the robustness of the synthesized system, i.e. the ability of the system to maintain the technical requirements imposed on it when the parameters of the control object and external influences change within certain limits [13, 14].

The central problem of modern theory and practice of robust control is the creation of systems that can function effectively under conditions of uncertainty in the values of parameters, and possibly the structure of models of the control object, disturbing influences and measurement noises [15–17].

One of the rapidly developing approaches to the synthesis of robust control systems is the synthesis of controllers that minimize H_∞ the norm of the vector of the goal of control [18, 19]. However, when designing real control systems, there are no requirements for H_∞ the norm of the target vector, and the target vector of robust control itself is usually not specified.

In this case, the main difficulties in the practical application of modern control methods are associated not so much with the development of new control methods as with the informal choice of the vector of the goal of robust control or the criterion of the quality of optimal control.

The purpose of the work is to develop the method of multi objective synthesis of nonlinear robust control by multimass electromechanical systems to satisfy various requirements for the operation of multi-mass systems in various modes.

Problem statement. To solve the problem of multi objective synthesis of robust control, the concept of multi-functional membership on the elements of the state space has been developed. Let us consider the possibility of choosing such a quality criterion, under which it is possible to satisfy all the requirements for a system based on the concept of multi-functional membership.

Suppose that the original nonlinear system (1) can be described in the state space by a nonlinear differential equation of state in the following form:

$$\dot{x} = f(x,u,t),\ x(t_0) = x_0,\ t \ge t_0, \tag{1}$$

The classical optimal control problems solve the problem of control synthesis that minimizes the adopted performance criterion in form functional

$$J = \int_0^T f_0(\vec{x}(t), \vec{u}(t))dt. \tag{2}$$

The choice of the optimality criterion (2) characterizing the quality of control processes is a informal problem. As a rule, the criterion of optimality is conditional. When designing a system, it is necessary to select such an indicator of the quality of the system, which intuitively reflects the idea of what is good and what is bad for a given system. Therefore, the difficulties of designing an optimal system are actually reduced to the difficulties of forming such a criterion that would reflect the real requirements for the system. The semantic formulation of the optimization problem, as a rule, is a multi objective problem with constraints. Naturally, many methods for solving this problem are reduced to the formation of a one-criterion problem, when all the criteria and constraints with the help of the chosen compromise scheme are reduced into one indicator of the quality of the system. In conclusion, we note that the same value of the quality criterion in single-criterion optimization can correspond to transient processes that differ sharply in their form – oscillatory, aperiodic, and their quality indicators, such as regulation time, overshoot, differ by orders of magnitude. This is because in one criterion it is necessary to reflect both the quality of the dynamic characteristics of the systems and the energy consumption for control and constraints on the state variables of the system. Moreover, on the basis of the solution of the inverse problem of optimal control for any transient process, which is arbitrarily unsatisfactory in terms of the quality indicators, it is possible to choose such an indicator of the system quality, according to which it will be optimal. Therefore, it is the problem of choosing a quality criterion that is the main one, since the very solution of the optimization problem is not difficult.

The problem of choosing a quality criterion neither in optimal nor, even more so, in robust control remains unsolved to this day. The authors Letov and Kalman, as well as many researchers who tried to apply this theory to solving practical problems, also paid attention to the importance of the problem of choosing the quality functional in the problem of analytical design of regulators by integral quadratic quality criteria. However, to date, this problem has not been fully resolved.

In the concept of multi-functional membership on the elements of the state space it is assumed that all various requirements that are imposed for the operation of systems (1) in various modes for

$$u \in U(x,t), \tag{3}$$

where $U(x,\ t) \subset R^m$ – some given control vector set for each state vector x and $t \ge t_0$, to fulfill the following relation for the state vector:

$$x = x(t) \in Q(t),\ t \geq t_0, \tag{4}$$

$$Q(t) = \{x \in R^n : \psi(x,t) \leq 0\}, \tag{5}$$

where $\psi(x, t)$ – scalar function continuously differentiable in all its variables.

Usually, some of the requirements for the system can be formulated in the form of a minimum or maximum (2). For example, it is desirable to ensure the minimum variance of the system error, the minimum control time, the minimum error in the harmonic signal processing, etc. Then the control goal can be formulated as a vector

$$y = \varphi(x(t),t) \in Q(t),\ t \geq t_0, \tag{6}$$

where $\varphi(x, t)$ – some given continuously differentiable $(n\times1)$ – is a vector function, and the set

$$Q(t) = \{y \in R^n : \psi(y,t) \leq 0\}. \tag{7}$$

Note that specifying the set $Q(t)$ is a rather difficult task, and often can be formally unsolved problem. Probably the most versatile method of setting an area $Q(t)$ is to carry out simulation of a system with a specific control law. At the same time, the presence of a control law is necessary, since many quality indicators are presented not only to the executive motor, the plant, but also directly to the entire control system.

It is assumed that the goal of control, constraints on the state and control vector can be reduced to uniform constraints on the state vector of the system. To ensure the condition of membership of the state vector $x(t)$ the multitude $Q(t)$ in order to fulfill the constraints on the state vector and to ensure the condition that the control goal vector $y(t)$ the multitude $Q(t)$ and with minimization over the control vector in the synthesis of a robust control system for an object with uncertainties (parametric, structural, uncertainty of external influences, etc.) can be written in the form of the maximin inequality

$$\begin{gathered}\max_{x\in M(y,t)} \min_{u\in U(x,t)} \left(\nabla_y \psi, \nabla_x \varphi \cdot f(x,u,t)\right) + \cdots \\ \cdots + \left(\nabla_y \psi, \frac{\partial \varphi}{\partial t}\right) + \frac{\partial \psi}{\partial t} \leq 0,\end{gathered} \tag{8}$$

for each $y\in \mathrm{B}Q(t)$ and each $x\in M(y, t)$, $t \geq t_0$ where $\mathrm{B}Q(t) = \{x\in R^n : \psi(x, t) = 0\}$ is the boundary of the set $Q(t)$; $\nabla_y\psi$ is the gradient of the function $\psi(x, t)$; $\nabla_x\varphi$ – is the Jacobian of the function $\varphi(x, t)$; $(\nabla_x\psi, f(\cdot))$ – dot product of vectors $\nabla_x\psi$, $f(\cdot)\in R^n$; $M(y, t)$ – is a certain variety corresponding to $y\in \mathrm{B}Q(t)$ and determined according to the dependence

$$M(y,t) = \{x \in R^n : \varphi(x,t) = y\}, \tag{9}$$

$$Q(t) \subseteq \mathrm{B}_\varphi \text{ at } t \geq t_0. \tag{10}$$

These inequalities are valid for a robust control system for any structure of the control part of the system - software, with feedback, etc. We restrict ourselves to the law of control with feedback over the full state vector in the following form

The main difficulties of solving of the problem of multi objective synthesis of robust control based on functionally multiple membership are related to the difficulties of defining and calculating functions of the area of functional-set membership Q, defined by function $\psi(t)$. Note that obtaining analytical dependences of the functions $\psi(\vec{x},t)$ and $\varphi(\vec{x},t)$ can present significant difficulties, and often even impossible [20, 21]. However, to solve the problem, not the functions themselves are needed, but their gradient and Jacobian, which can be obtained by numerical methods.

Solution method. Consider the method of computation of this functions $\psi(\vec{x},t)$ and $\varphi(\vec{x},t)$ based on the modern theory of nonlinear robust control [22–24]. Consider the general case of a nonlinear system written in the following form

$$\dot{x} = F(x,\omega,u), \tag{11}$$

$$z = Z(x,u), \tag{12}$$

where ω is the vector of external uncontrolled disturbances.

Moreover, when synthesizing a robust control, this perturbation is considered to be independent and the worst-case condition is chosen for the control.

For this system, we write the Hamilton function in the following form

$$\begin{gathered}H(x,p,\omega,u) = p^T F(x,\omega,u) + \ldots \\ \ldots + \frac{1}{2}\|Z(x,u)\|^2 - \frac{1}{2}\|\omega\|^2.\end{gathered} \tag{13}$$

The Hamilton–Jacobi–Isaacs inequality for this nonlinear system takes the following form

$$\begin{gathered}H_*\left(x, V_x^T(x)\right) = V_x^T(x) F(x,\omega,u) + \ldots \\ \ldots + \frac{1}{2}\|Z(x,u)\|^2 - \frac{1}{2}\gamma^2\|\omega\|^2 \leq 0\end{gathered}. \tag{14}$$

Then the feedback in the form $u = \alpha_u(x, V_x^T(x))$, where $\alpha_u(x, p)$ is determined from the following system of Hamilton–Jacobi–Isaacs differential equations

$$\frac{\partial H}{\partial \omega}\left(x, p, \alpha_\omega(x,p), \alpha_u(x,p)\right) = 0, \tag{15}$$

$$\frac{\partial H}{\partial u}\left(x, p, \alpha_\omega(x,p), \alpha_u(x,p)\right) = 0, \tag{16}$$

$$\alpha_\omega(0,0) = 0, \quad \alpha_u(0,0) = 0. \tag{17}$$

These equalities are necessary conditions for the extremum of the Hamilton function, as in the control vector u, and by the vector of external disturbances ω. Moreover, it is necessary to find the minimum norm of the target vector by the control vector and the maximum of this norm by the vector of external disturbances, i.e. solve the maximin extreme problem. Note that these conditions are necessary conditions for optimizing a dynamic game in which the first player, the controller, minimizes the goal vector, and the second player, external disturbances, maximizes the same goal vector.

This approach can be interpreted as a zero-sum differential game of two players in which one player minimizes the accepted quality criterion for control u, and the other player maximizes this criterion with respect to the vector of external variables ω. In this case, the minimization strategy for control u

$$u^* = \alpha_u(x) = -g_u^T(x) V_x^T(x), \tag{18}$$

and the strategy of maximization along the vector of external influences ω

$$\omega(x) = \alpha_{\omega}(x) = \frac{1}{\gamma^2} g_{\omega}^T(x) V_x^T(x). \qquad (19)$$

In this case, external influences ω, found from the condition for the worst case, at which the energy of the target vector is maximized.

In contrast to optimal control under robust control, the role of the integrand $f_0(x, u)$ in (2) playing target vector norm $\|z(x, u)\|^2$ in (12), and, in addition, the norm of the vector of external influences is introduced into the Hamilton function $\|\omega\|^2$ is introduced into the Hamilton function (13) and this external influence during the synthesis of the system is considered independent and can be determined from the condition of maximum «harmfulness» (worst – case disturbance) – maximum deviation of the target vector norm.

Naturally, the dynamics of the synthesized robust system is largely determined by the goal function $z(x, u)$, and all system requirements must be satisfied by the appropriate selection of this function of the goal. Setting the functional-multiple membership of the state vector in the form of a set Q in the form of inequality $\psi(x, t) \leq 0$ in (7) together with setting the vector of the control goal $y(t) = \varphi(x, t)$ in (6) is equivalent to specifying the integrand f_0 in the integral criterion (2) for optimal control or goal function $Z(x, \omega, t)$ in robust control (12). Moreover, by choosing these functions, in fact, it is necessary to satisfy all the requirements for the system.

Thus based on the concept of functional – multiple membership of the state vector and the solution of the Hamilton-Jacobi-Isaacs equation it shown that it is possible to satisfy all the requirements for the system by choosing the target vector of nonlinear robust control, when multi objective synthesis of nonlinear robust control by multimass electromechanical systems is calculated.

The method of computation of the goal vector of nonlinear robust control. Let us now consider a method for calculating the goal vector $z(x, u)$ of a robust control (12) in a multi objective synthesis of a nonlinear robust control. Let us introduce the vector J of quality indicators that apply to the operation of the system in various operating modes. The components of this vector, in particular, can be: the transient times are usually specified when certain input signals are applied: the accuracy of working off the specified minimum speed value the uneven movement of the working body at the minimum speed: minimum value of the stabilization dispersion of a given random change in the reference action is usually required under the action of random disturbing influences caused, for example, by a random change in the road profile.

In addition, we introduce a vector G of limitations, the components of which can be the limiting values of voltages, currents, rates of change of currents, moments, elastic moments, rates of change of moments (jerks), speeds of various elements of a multi-mass electromechanical system, their positions, etc.

We also introduce the vector S of uncertainties in the parameters of the initial system and external influences. The components of this wind, in particular, can be changes in the moments of inertia of the working body.

The dynamic characteristics of the synthesized nonlinear robust system are determined by the mole of the control object, external master and disturbing influences, and, of course, the parameters of the synthesized nonlinear robust controllers. The control system designer can only change the robust control target vector. Let us perform a parameterization of the function, with the help of which the goal vector of the nonlinear robust control is set and introduce the vector Z of these desired parameters.

Then, using the given value of the Z vector of these desired parameters, the vector J of the values of quality indicators that are imposed on the system operation, and the vector G of the restrictions when the system is operating in various operating modes and for various setting and disturbing and for various values of the vector S of the uncertainty of the initial system parameters and external influences.

Then the problem of multi objective synthesis of non-linear robust control can be formulated as the zero-sum vector antagonistic game [25, 26].

In this game, the first player is the vector Z parameterization of the function, with the help of which the goal vector of the nonlinear robust control is set, and it strategy is to minimize the game payoff vector. The second player is the vector S of uncertainties in the parameters of the initial system and external influences, and it strategy is to maximize the same game payoff vector J. This approach is the standard approach in the robust control synthesis for the «worst» case.

To correctly calculation of solution of this vector antagonistic game from the set of Pareto-optimal solutions, binary preference relations of local performance criteria B are used.

In conclusion, we note that the computation of the pay game vector J, the constraint vector G, and the vector B of binary preference relations is algorithmic in nature and requires large computational resources. First, to calculate the nonlinear robust control it is need to solve the Hamilton-Jacobi-Isaacs equation.

Then, in order to calculate the values of payoff game vector J, the constraint vector G, and the vector B of binary preference relations it is necessary to simulate the initial non-linear system closed by synthesized nonlinear robust controllers for given system operation modes and for given driving and perturbing influences at given values of the nonlinear vector certainty of the parameters of the original system.

The calculation of the solution of this vector antagonistic game from set of Pareto-optimal solutions based on stochastic multiagent optimization [27, 28]. To date, a large number of particle swarm optimization algorithms have been developed – PSO algorithms based on the idea of collective particle swarm intelligence, such as gbest PSO and lbest PSO algorithms. The use of stochastic multi-agent optimization methods to solve vector antagonistic game today causes some difficulties and this area continues to develop intensively. To solve the initial vector antagonistic game with constraints, we construct an algorithm for stochastic multiagent optimization based on a set of swarms of particles, the number of which is equal to the number of components of the payoff vector game, In a standard particle swarm optimization algorithm, the change in particle velocities is performed according to linear laws. To increase the speed of finding a global solution, special nonlinear algorithms for stochastic multi-agent optimization have recently become widespread [29–32].

Simulation results. As an example, consider the results of modeling an electromechanical servo system synthesized in the course of multi objective synthesis. There are elastic elements between the motor shaft and the working body in the system under consideration, therefore the mathematical model is adopted in the form of a two-mass electromechanical system.

There are also nonlinear elements in the control system. This, first of all, concerns the presence of dry friction both in the executive engine and in the control object drive in the horizontal guidance channel and in the control object drive in the vertical guidance channel. In addition, the system has nonlinear characteristics of the elastic elements between the actuating motors and drive mechanisms due to backlash-selecting springs. Let us consider the influence of these elements on the dynamic characteristics of the system.

In this case, we will consider the dynamic characteristics of the system for three values of the moments of inertia of the working mechanism – the nominal value and those that differ from the nominal value by a factor of two up and down.

One of the intense criteria imposed on the synthesized system is the requirement for the quality of transient processes in the mode of working out small angles.

As an example, in Figure 1 are shown the transients of state variables: *a*) the angle of the plant; *b*) the speed of the plant; *c*) moment of elasticity; and *d*) the speed of the motor in this mode of operation.

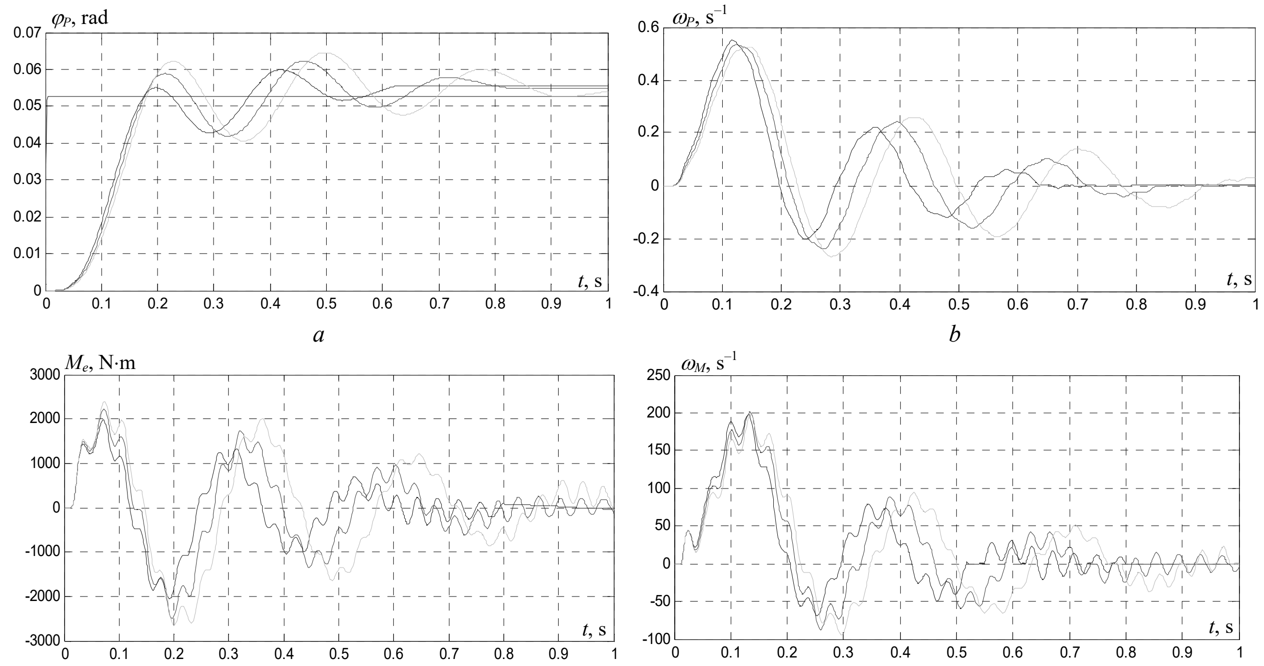

a *b*

c *d*

Fig. 1. Transient processes of state variables of the electromechanical servo system in the mode of working out small angles

The time of the first coordination in the synthesized robust control system is significantly less compared to the time of the first coordination in the existing system, which is usually about one second, and, therefore, with the help of synthesized robust controllers for improved mathematical models, it is possible to reduce the time of transients by 1.5–2 times compared to a system with typical regulators.

One of the intense criteria imposed on the synthesized system is the requirement for the accuracy of compensation for random disturbances acting on the control object during its operation. As an example, in Figure 2 are shown the implementation of random processes of state variables of an electromechanical servo system under random external influences

In the Fig. 2 are shown the implementation of random processes of state variables *a*) changes in the angle of plant; *b*) the derivative of the plant; *c*) the moment of stabilization of the plant; and *d*) the derivative of the moment of stabilization of the plant under random external influences.

With the help of synthesized robust nonlinear controllers for improved mathematical models, it is possible to reduce the variance of the error in compensating for random disturbance acting on the control object by 1.7–2.3 times compared to a system with typical controllers. Note that this requirement largely determines the potential accuracy of the synthesized electromechanical tracking system.

Experimental research. A stand of a two-mass electromechanical servo system was developed for experimental research. The mechanical part of the stand is made on the basis of two identical micro-motors of a direct current like DPT-25-H2. The motor shafts are connected by an elastic transmission. With the help of the second motor, a load is created on the first motor. Sensors are located on the motor shafts, which are used to measure the angles of rotation and angular velocities of the first and second motor.

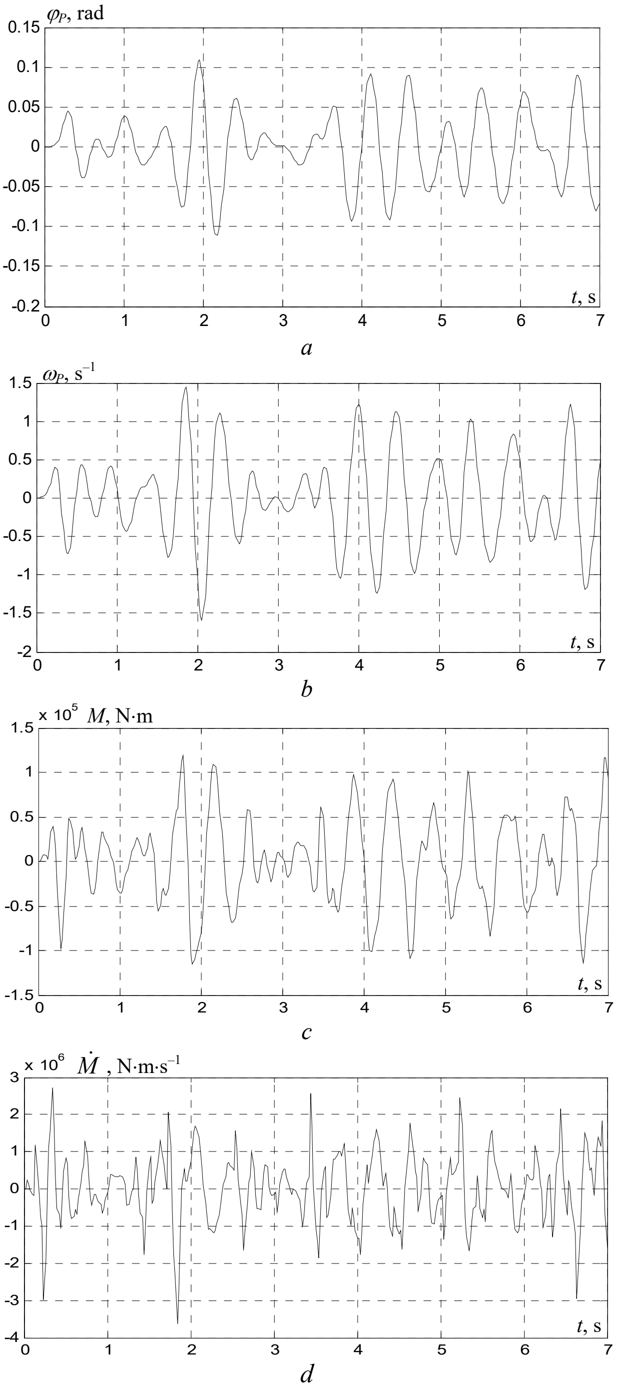

Fig. 2. Implementation of random processes of state variables of an electromechanical servo system under random external influences

Let us now consider the results of experimental studies of the stand with robust controllers. As an example in Fig. 3 are shown the experimental transient processes of state variables: the angles of rotation of the first φ_1 (*a*) and the second φ_2 (*b*) motor; rotation speeds of the first ω_1 (*c*) and the second ω_2 (*d*) motor and moment of elasticity M_e (*e*), when the system is working out a given angle of rotation $\varphi_{in} = 1$ rad.

Experimental studies have shown that the use of robust control of a stand of two mass electromechanical systems synthesized during multi objective synthesis reduces the time of the first negotiation of the transition process at the shaft angle of the second engine by more than 1.7 times compared to the system with standard regulators.

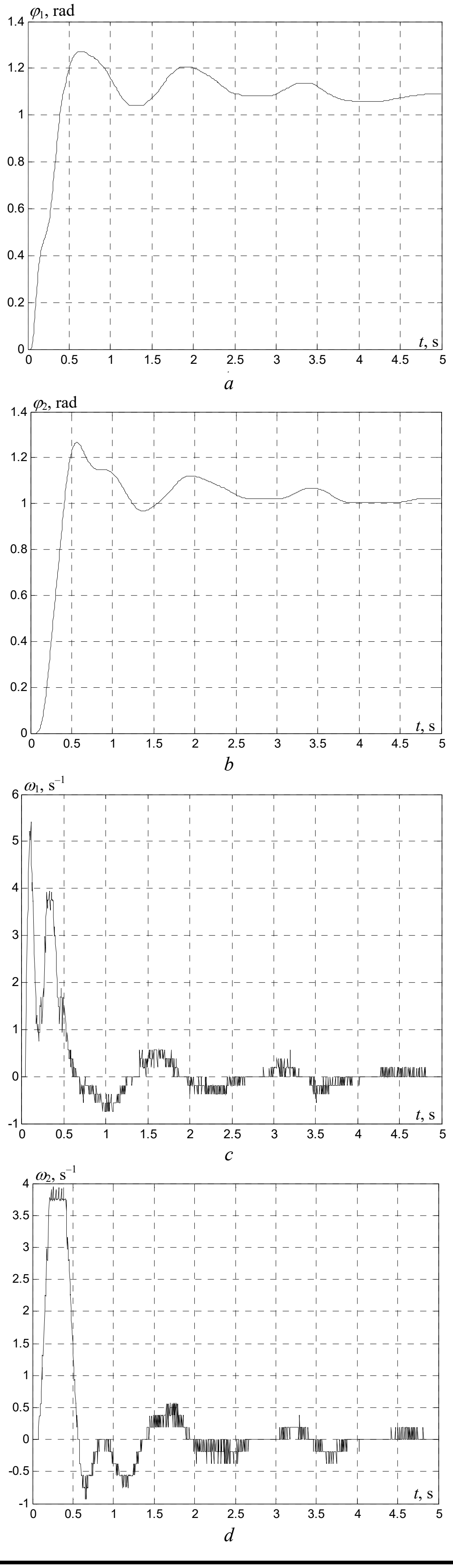

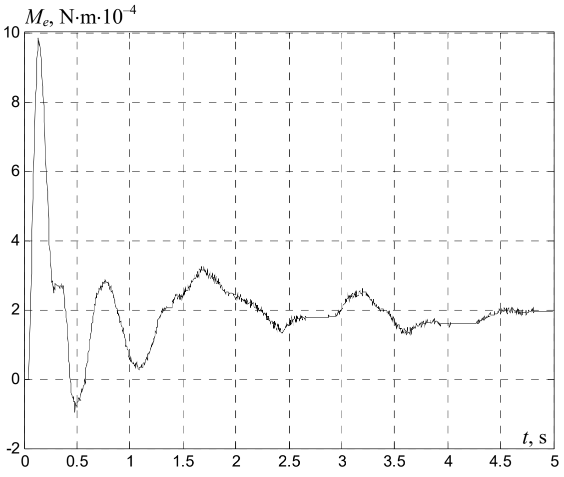

e

Fig. 3. Experimental transient processes of the of state variables when the system is working out a given angle of rotation φ_{in} = 1 rad

In the experimental transient process of the stand rotation angle, there are nonlinear sections due to the presence of friction moments in the stand. The experimental transients of state variables of motor rotor speeds and voltages on motor armature circuits obtained on the stand contain high-frequency components, while model transients of the same state variables change more smoothly.

Note that the quality of transients is significantly influenced by the characteristics of nonlinearities of actuators and it is they who determine the potential accuracy of the system with synthesized optimal regulators.

As an example, in Figure 4 are shown the implementation of random processes of the stand of a two-mass electromechanical system in the mode of stabilization of the rotation speed of the shaft of the second motor under the action of random changes in the moment of resistance created by the second motor.

In Fig. 4 are shown the following state variables: rotational speeds of the first *a*) and second *b*) motors and currents of anchor circuits of the first *c*) and second *d*) motors.

Experimental studies have shown that the use of robust control of a stand of two mass electromechanical systems synthesized during multi objective synthesis reduces the error of adjusting the speed of rotation of the shaft of the second motor by more than 1.2 times, as well as reduces the control error the angle of rotation of the shaft of the second motor more than 2 times in comparison with the system with standard regulators at random change of the moment of resistance formed by means of the second motor.

Notice, that improving the control accuracy of the system with robust controllers is accompanied by more intense work of the actuator motor. In particular, the armature current of the first motor in a system with a robust regulator has significantly higher-frequency components and a larger amplitude c of rotation of the shaft of the second motor more than 2 times in comparison with the system with standard regulators.

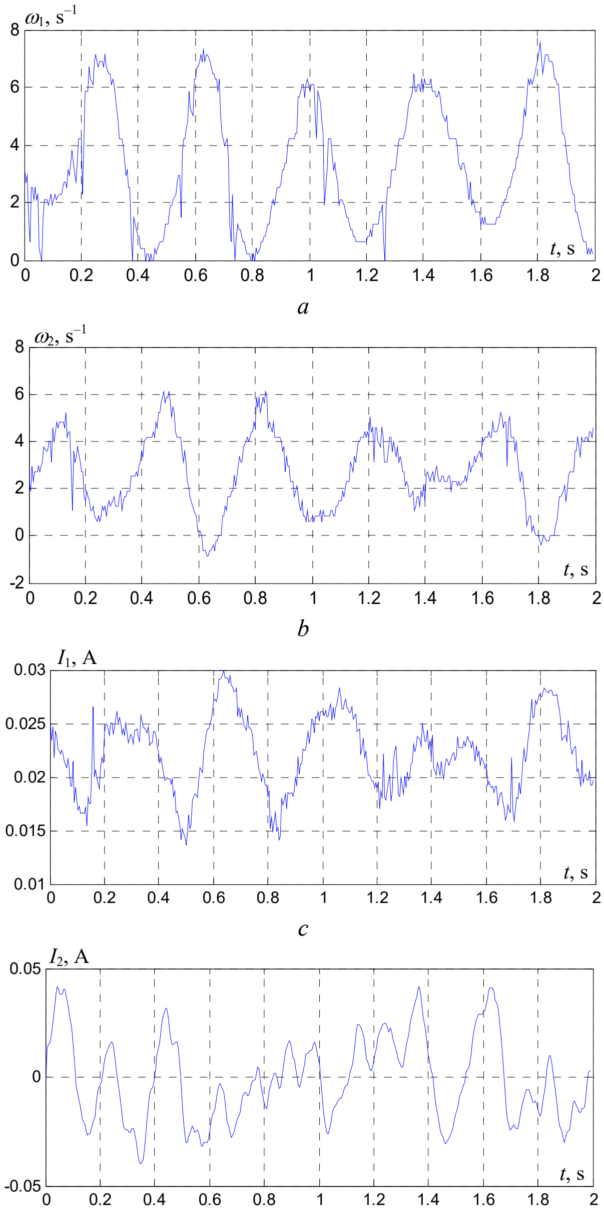

a

b

c

d

Fig. 4. Implementations of random processes of variables of the state of the stand of a two-mass electromechanical system with a random change in the moment of resistance

Conclusions.

1. For the first time the method of multi objective synthesis of nonlinear robust control by multimass electromechanical systems to satisfy various requirements for the operation of multi-mass systems in various modes is developed.
2. Based on the concept of functional – multiple membership of the state vector and the solution of the Hamilton-Jacobi-Isaacs equation it is shown that it is possible to satisfy all the requirements for the system by choosing the target vector of nonlinear robust control. The problem of multi objective synthesis of nonlinear robust control of multimass electromechanical systems is formulated by solving a zero-sum vector antagonistic game.
3. The computation of the game payoff vector, the constraint vector, and the vector of binary preference relations is algorithmic in nature and requires large computational resources. To calculate the non-linear

robust control it is need to solve the Hamilton-Jacobi-Isaacs equation. Then as a result of modeling a closed system, the vector of the values of the quality indicators that are imposed on the system operation, and the vector of the restrictions, when the system is operating in various operating modes and for various setting and disturbing and for various values of the vector of the initial uncertainty of the system parameters and external influences are calculated.

4. The results of multi objective synthesis of nonlinear robust control by servo two-mass electromechanical systems in which differences requirements for the operation of such systems in various modes were satisfied are given. The results of modeling and experimental studies of transients of two-mass servo electromechanical tracking system and realizations of state variables of this system under random external influences are presented.

5. Based on the results of modeling and experimental studies it is established, that with the help of synthesized robust nonlinear controllers, it is possible to reduce the error of adjusting the speed of rotation of the shaft of the second motor by more than 1.2 times, as well as reduces the control error the angle of rotation of the shaft of the second motor more than 2 times and to reduce the variance of the error in compensating for random disturbance acting on the plant by 1.7–2.3 times in comparison with the system with standard regulators.

Conflict of interest. The authors declare that they have no conflicts of interest.

REFERENCES

1. Volosyuk V., Zhyla S., Pavlikov V., Ruzhentsev N., Tserne E., Popov A., Shmatko O., Dergachov K., Havrylenko O., Ostroumov I., Kuzmenko N., Sushchenko O., Averyanova Yu., Zaliskyi M., Solomentsev O., Kuznetsov B., Nikitina T. Optimal Method for Polarization Selection of Stationary Objects Against the Background of the Earth’s Surface. *International Journal of Electronics and Telecommunications*, 2022, vol. 68, no. 1, pp. 83-89. doi: https://doi.org/10.24425/ijet.2022.139852.

2. Shmatko O., Volosyuk V., Zhyla S., Pavlikov V., Ruzhentsev N., Tserne E., Popov A., Ostroumov I., Kuzmenko N., Dergachov K., Sushchenko O., Averyanova Y., Zaliskyi M., Solomentsev O., Havrylenko O., Kuznetsov B., Nikitina T. Synthesis of the optimal algorithm and structure of contactless optical device for estimating the parameters of statistically uneven surfaces. *Radioelectronic and Computer Systems*, 2021, no. 4, pp. 199-213. doi: https://doi.org/10.32620/reks.2021.4.16.

3. Ostroverkhov M., Chumack V., Monakhov E., Ponomarev A. Hybrid Excited Synchronous Generator for Microhydropower Unit. *2019 IEEE 6th International Conference on Energy Smart Systems (ESS)*, Kyiv, Ukraine, 2019, pp. 219-222. doi: https://doi.org/10.1109/ess.2019.8764202.

4. Ostroverkhov M., Chumack V., Monakhov E. Ouput Voltage Stabilization Process Simulation in Generator with Hybrid Excitation at Variable Drive Speed. *2019 IEEE 2nd Ukraine Conference on Electrical and Computer Engineering (UKRCON)*, Lviv, Ukraine, 2019, pp. 310-313. doi: https://doi.org/10.1109/ukrcon.2019.8879781.

5. Krot P.V., Korennoy V.V. Nonlinear Effects in Rolling Mills Dynamics. *Proceedings of the 5th International Conference on Nonlinear Dynamics ND-KhPI2016*, September 27-30, 2016, Kharkov, Ukraine. Available at: https://www.researchgate.net/publication/308901445_Nonlinear_Effects_in_Rolling_Mills_Dynamics (accessed 06 October 2021).

6. Kugi A., Schlacher K., Novak R. Nonlinear control in rolling mills: a new perspective. *IEEE Transactions on Industry Applications*, 2001, vol. 37, no. 5, pp. 1394-1402. doi: https://doi.org/10.1109/28.952515.

7. Martynenko G. Practical application of the analytical method of electromagnetic circuit analysis for determining magnetic forces in active magnetic bearings. *2020 IEEE Problems of Automated Electrodrive. Theory and Practice (PAEP)*, 2020, pp. 1-4, doi: https://doi.org/10.1109/paep49887.2020.9240774.

8. Martynenko G., Martynenko V. Modeling of the dynamics of rotors of an energy gas turbine installation using an analytical method for analyzing active magnetic bearing circuits. *2020 IEEE KhPI Week on Advanced Technology (KhPIWeek)*, 2020, pp. 92-97 .doi: https://doi.org/10.1109/KhPIWeek51551.2020.9250156.

9. Buriakovskyi S.G., Maslii A.S., Pasko O.V., Smirnov V.V. Mathematical modelling of transients in the electric drive of the switch – the main executive element of railway automation. *Electrical Engineering & Electromechanics*, 2020, no. 4, pp. 17-23. doi: https://doi.org/10.20998/2074-272X.2020.4.03.

10. Tytiuk V., Chornyi O., Baranovskaya M., Serhiienko S., Zachepa I., Tsvirkun L., Kuznetsov V., Tryputen N. Synthesis of a fractional-order $PI^{\lambda}D^{\mu}$-controller for a closed system of switched reluctance motor control. *Eastern-European Journal of Enterprise Technologies*, 2019, no. 2 (98), pp. 35-42. doi: https://doi.org/10.15587/1729-4061.2019.160946.

11. Zagirnyak M., Chornyi O., Zachepa I. The autonomous sources of energy supply for the liquidation of technogenic accidents. *Przeglad Elektrotechniczny*, 2019, no. 5, pp. 47-50. doi: https://doi.org/10.15199/48.2019.05.12.

12. Chornyi O., Serhiienko S. A virtual complex with the parametric adjustment to electromechanical system parameters. *Technical Electrodynamics*, 2019, pp. 38-41. doi: https://doi.org/10.15407/techned2019.01.038.

13. Shchur I., Kasha L., Bukavyn M. Efficiency Evaluation of Single and Modular Cascade Machines Operation in Electric Vehicle. *2020 IEEE 15th International Conference on Advanced Trends in Radioelectronics, Telecommunications and Computer Engineering (TCSET)*, Lviv-Slavske, Ukraine, 2020, pp. 156-161. doi: https://doi.org/10.1109/tcset49122.2020.235413.

14. Shchur I., Turkovskyi V. Comparative Study of Brushless DC Motor Drives with Different Configurations of Modular Multilevel Cascaded Converters. *2020 IEEE 15th International Conference on Advanced Trends in Radioelectronics, Telecommunications and Computer Engineering (TCSET)*, Lviv-Slavske, Ukraine, 2020, pp. 447-451. doi: https://doi.org/10.1109/tcset49122.2020.235473.

15. Ostroumov I., Kuzmenko N., Sushchenko O., Pavlikov V., Zhyla S., Solomentsev O., Zaliskyi M., Averyanova Y., Tserne E., Popov A., Volosyuk V., Ruzhentsev N., Dergachov K., Havrylenko O., Kuznetsov B., Nikitina T., Shmatko O. Modelling and simulation of DME navigation global service volume. *Advances in Space Research*, 2021, vol. 68, no. 8, pp. 3495-3507. doi: https://doi.org/10.1016/j.asr.2021.06.027.

16. Averyanova Y., Sushchenko O., Ostroumov I., Kuzmenko N., Zaliskyi M., Solomentsev O., Kuznetsov B., Nikitina T., Havrylenko O., Popov A., Volosyuk V., Shmatko O., Ruzhentsev N., Zhyla S., Pavlikov V., Dergachov K., Tserne E. UAS cyber security hazards analysis and approach to qualitative assessment. In: Shukla S., Unal A., Varghese Kureethara J., Mishra D.K., Han D.S. (eds) *Data Science and Security. Lecture Notes in Networks and Systems*, 2021, vol. 290, pp. 258-265. Springer, Singapore. doi: https://doi.org/10.1007/978-981-16-4486-3_28.

17. Zaliskyi M., Solomentsev O., Shcherbyna O., Ostroumov I., Sushchenko O., Averyanova Y., Kuzmenko N., Shmatko O., Ruzhentsev N., Popov A., Zhyla S., Volosyuk V., Havrylenko O., Pavlikov V., Dergachov K., Tserne E., Nikitina T., Kuznetsov B. Heteroskedasticity analysis during operational data processing of radio electronic systems. In: Shukla S., Unal A., Varghese Kureethara J., Mishra D.K., Han D.S. (eds) *Data Science and Security. Lecture Notes in Networks and Systems*, 2021, vol. 290, pp. 168-175. Springer, Singapore. doi: https://doi.org/10.1007/978-981-16-4486-3_18.

18. Sushchenko O.A. Robust control of angular motion of platform with payload based on H_∞-synthesis. *Journal of Automation and Information Sciences*, 2016, vol. 48, no. 12, pp. 13-26. doi: https://doi.org/10.1615/jautomatinfscien.v48.i12.20.

19. Chikovani V., Sushchenko O. Self-compensation for disturbances in differential vibratory gyroscope for space navigation. *International Journal of Aerospace Engineering*, 2019, vol. 2019, Article ID 5234061, 9 p. doi: https://doi.org/10.1155/2019/5234061.

20. Gal'chenko V.Y., Vorob'ev M.A. Structural synthesis of attachable eddy-current probes with a given distribution of the probing field in the test zone. *Russian Journal of Nondestructive Testing*, Jan. 2005, vol. 41, no. 1, pp. 29-33. doi: https://doi.org/10.1007/s11181-005-0124-7.

21. Halchenko V.Y., Ostapushchenko D.L., Vorobyov M.A. Mathematical simulation of magnetization processes of arbitrarily shaped ferromagnetic test objects in fields of given spatial configurations. *Russian Journal of Nondestructive Testing*, Sep. 2008, vol. 44, no. 9, pp. 589-600. doi: https://doi.org/10.1134/S1061830908090015.

22. Ostroumov I., Kuzmenko N., Sushchenko O., Zaliskyi M., Solomentsev O., Averyanova Y., Zhyla S., Pavlikov V., Tserne E., Volosyuk V., Dergachov K., Havrylenko O., Shmatko O., Popov A., Ruzhentsev N., Kuznetsov B., Nikitina T. A probability estimation of aircraft departures and arrivals delays. In: Gervasi O. et al. (eds) *Computational Science and Its Applications – ICCSA 2021. ICCSA 2021. Lecture Notes in Computer Science*, vol. 12950, pp. 363-377. Springer, Cham. doi: https://doi.org/10.1007/978-3-030-86960-1_26.

23. Chystiakov P., Chornyi O., Zhautikov B., Sivyakova G. Remote control of electromechanical systems based on computer simulators. *2017 International Conference on Modern Electrical and Energy Systems (MEES)*, Kremenchuk, Ukraine, 2017, pp. 364-367. doi: https://doi.org/10.1109/mees.2017.8248934.

24. Zagirnyak M., Bisikalo O., Chorna O., Chornyi O. A Model of the Assessment of an Induction Motor Condition and Operation Life, Based on the Measurement of the External Magnetic Field. *2018 IEEE 3rd International Conference on Intelligent Energy and Power Systems (IEPS)*, Kharkiv, 2018, pp. 316-321. doi: https://doi.org/10.1109/ieps.2018.8559564.

25. Ummels M. *Stochastic Multiplayer Games Theory and Algorithms*. Amsterdam University Press, 2010. 174 p.

26. Shoham Y., Leyton-Brown K. *Multiagent Systems: Algorithmic, Game-Theoretic, and Logical Foundations.* Cambridge University Press, 2009. 504 p.

27. Xin-She Yang, Zhihua Cui, Renbin Xiao, Amir Hossein Gandomi, Mehmet Karamanoglu. *Swarm Intelligence and Bio-Inspired Computation: Theory and Applications*, Elsevier Inc., 2013. 450 p.

28. Zilzter Eckart. *Evolutionary algorithms for multiobjective optimizations: methods and applications*. PhD Thesis Swiss Federal Institute of Technology, Zurich, 1999. 114 p.

29. Xiaohui Hu, Eberhart R.C., Yuhui Shi. Particle swarm with extended memory for multiobjective optimization. *Proceedings of the 2003 IEEE Swarm Intelligence Symposium*. SIS'03 (Cat. No.03EX706), Indianapolis, IN, USA, 2003, pp. 193-197. doi: https://doi.org/10.1109/sis.2003.1202267.

30. Pulido G.T., Coello C.A.C. A constraint-handling mechanism for particle swarm optimization. *Proceedings of the 2004 Congress on Evolutionary Computation* (IEEE Cat. No.04TH8753), Portland, OR, USA, 2004, vol. 2, pp. 1396-1403. doi: https://doi.org/10.1109/cec.2004.1331060.

31. Michalewicz Z., Schoenauer M. Evolutionary Algorithms for Constrained Parameter Optimization Problems. *Evolutionary Computation*, 1996, vol. 4, no. 1, pp. 1-32. doi: https://doi.org/10.1162/evco.1996.4.1.1.

32. Parsopoulos K.E., Vrahatis M.N. Particle swarm optimization method for constrained optimization problems. *Proceedings of the Euro-International Symposium on Computational Intelligence*, 2002, pp. 174-181.

Received 10.04.2022
Accepted 21.05.2022
Published 20.07.2022

B.I. Kuznetsov[1], *Doctor of Technical Science, Professor,*
T.B. Nikitina[2], *Doctor of Technical Science, Professor,*
I.V. Bovdui[1], *PhD, Senior Research Scientist,*
O.V. Voloshko[1], *PhD, Junior Research Scientist,*
V.V. Kolomiets[2], *PhD, Associate Professor,*
B.B. Kobylianskyi[2], *PhD, Associate Professor,*
[1] A. Pidhornyi Institute of Mechanical Engineering Problems of the National Academy of Sciences of Ukraine,
2/10, Pozharskogo Str., Kharkiv, 61046, Ukraine,
e-mail: kuznetsov.boris.i@gmail.com (Corresponding author)
[2] Educational scientific professional pedagogical Institute of Ukrainian Engineering Pedagogical Academy,
9a, Nosakov Str., Bakhmut, Donetsk Region, 84511, Ukraine,
e-mail: tatjana55555@gmail.com; nnppiuipa@ukr.net

How to cite this article:
Kuznetsov B.I., Nikitina T.B., Bovdui I.V., Voloshko O.V., Kolomiets V.V., Kobylianskyi B.B. The method of multi objective synthesis of nonlinear robust control by multimass electromechanical systems. *Electrical Engineering & Electromechanics*, 2022, no. 4, pp. 12-20. doi: https://doi.org/10.20998/2074-272X.2022.4.02

UDC 621.314 https://doi.org/10.20998/2074-272X.2022.4.03

D.S. Krylov, O.I. Khold

Determination of the input filter parameters of the active rectifier with a fixed modulation frequency

Goal. *Development of a methodology for calculating the parameters of the active rectifier-voltage source input filter operating with a fixed modulation frequency to ensure electromagnetic compatibility with the supply network acceptable by standards at minimum values of the input inductance and checking its main characteristics on a mathematical model.* ***Methodology***. *The authors have developed a methodology for calculating the parameters of the input filter of an active rectifier-voltage source. The calculation results are verified on the constructed mathematical model of a frequency converter, the scheme of which is an active rectifier and an autonomous voltage inverter. A series of experiments was carried out on a mathematical model to study the dependence of the total harmonic distortion of current and mains voltage on the value of the input inductance for various parameters of the input filter.* ***Results***. *The structure and calculation procedure the input filter of an active rectifier operating with a fixed modulation frequency are proposed. The simulation results showed that the inclusion of a filter at the input of the active rectifier significantly improves its electromagnetic compatibility with the supply network in the entire range of variation of the input inductance of the circuit and makes it possible to achieve the values of the total harmonic distortion permissible by the norms.* ***Originality***. *A structure and a calculation procedure the input filter of an active rectifier-voltage source operating with a fixed modulation frequency are proposed.* ***Practical significance***. *The dependencies obtained in the article allow us to evaluate the relationship between the parameters of the filter elements and its characteristics among themselves and come to a compromise between them when designing a scheme for specific technical conditions.* References 12, tables 1, figures 13.

Key words: **input filter, active rectifier, autonomous voltage inverter, output filter, Q factor, pulse-width modulation, total harmonic distortion.**

В статті запропоновано структуру та методику розрахунку вхідного фільтру активного випрямляча-джерела напруги, який працює з фіксованою частотою модуляції. Отримані залежності дозволяють оцінити взаємозв'язок параметрів елементів фільтра та його характеристик між собою та дійти компромісу між ними під час проектування схеми для конкретних технічних умов. Результати моделювання показали, що включення додаткового ланцюга RC фільтра на вході активного випрямляча істотно покращує його електромагнітну сумісність з мережею живлення у всьому діапазоні зміни вхідної індуктивності схеми та дозволяє досягати допустимих нормами значень сумарного коефіцієнту гармонічних спотворень. Бібл. 12, табл. 1, рис. 13.

Ключові слова: **вхідний фільтр, активний випрямляч, автономний інвертор напруги, вихідний фільтр, добротність, широтно-імпульсна модуляція, сумарний коефіцієнт гармонійних спотворень.**

Introduction. Active controlled rectifiers – voltage sources (ARVS) are increasingly being used as input converters of industrial drives of medium power based on autonomous voltage inverters (AVI). They have significant advantages over uncontrolled diode rectifiers: they provide a two-way energy exchange between the motor and the mains; an almost sinusoidal current shape on the side of the supply network with zero or any given shift relative to the phase voltage [1, 2]. The completeness and quality of the implementation of these advantages depends on the selected scheme key management algorithm and the structure of its control system [3, 4]. Here, it is possible to use various concepts that have their own advantages and disadvantages. According to the key control algorithm used, ARVS schemes are with a fixed and variable modulation frequency. This imposes its own peculiarities on the choice of parameters of the elements of the power circuit and the structure of the control system used. In [5, 6], the authors analyzed the operation of the main structures of control systems (CS) of ARVS with a fixed modulation frequency and proposed a new structure of the CS based on the theory of representing instantaneous currents and voltages of a three-phase network in the form of generalized vectors [7, 8]. The analysis showed that a serious problem is high-frequency distortion of the mains current and voltage of the circuit, the value of which depends both on the modulation frequency and on the value of the input inductance of the circuit. To reduce them, it is desirable to use an additional *RC* circuit in the input filter by analogy with the structure of the AVI output filter, the definition of parameters and efficiency criteria of which is proposed in [9]. In the literature reviewed by the authors, such a study in relation to the ARVS input filter was not revealed.

The goal of the work is to develop a methodology for calculating the parameters of the ARVS input filter operating with a fixed modulation frequency to ensure electromagnetic compatibility with the supply network acceptable by the standards [10] for given values of the input inductance and to check its main indicators on a mathematical model.

Structural diagram of the converter. The structural diagram of the medium power frequency drive under consideration based on an autonomous voltage inverter using a three-phase ARVS in the input circuit is shown in Fig. 1.

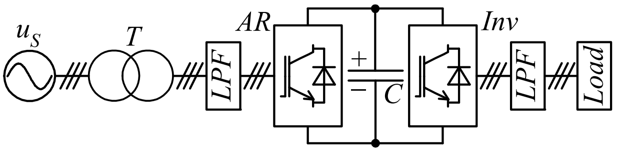

Fig. 1. Structural diagram of the frequency converter with ARVS

It consists of: a three-phase alternating voltage source u_S; a converter transformer *T*; ARVS input reactors combined with an *LPF* filter that suppresses high frequencies; an active rectifier *AR* made according to the bridge circuit on the keys of alternating current; a capacitor *C* in the intermediate DC circuit; a three-phase bridge independent voltage inverter *Inv* also made according to the bridge circuit on alternating current switches; an output filter *LPF* suppressing high frequencies; a three-phase symmetrical active-inductive load *Load*.

Having considered the structure of the converter in Fig. 1, it is easy to verify that it is circuit symmetrical with respect to the DC link, namely: a three-phase alternating voltage acts at the input and output of the circuit, and the energy flow can be carried out both from the source to the load and vice versa; ARVS and AVI circuits are made according to the same three-phase bridge circuit on alternating current switches and operate with the same fixed frequency of pulse-width modulation (PWM) for the same installed power of these links. The PWM frequency in this case is determined by the allowable losses in the keys with the cooling system used. Thus, it can be assumed that the influence of both converters on their AC links will be of the same nature and the methods of dealing with its negative factors may be similar.

Output filter of an autonomous voltage inverter. The output voltage of the AVI operating in the PWM mode consists of segments of the DC link voltage connected to the load with a modulation frequency. High-frequency voltage pulses can have different duty cycles depending on the shape of the control voltage generated by the CS. Therefore, the output voltage of AVI with PWM can be represented as the sum of the fundamental harmonic, which changes with the control voltage frequency ω_0, and higher harmonics, the highest of which will change with the modulation frequency ω_M. All harmonics other than the fundamental are unwanted and must be filtered out.

Figure 2 shows the circuit of the connected between the inverter and the load, which was proposed and discussed in detail in [9].

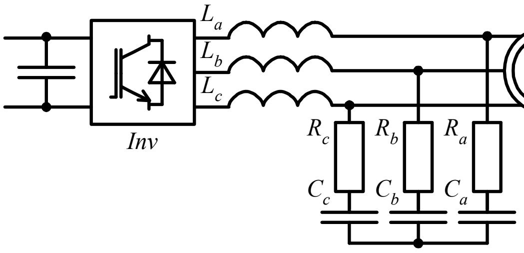

Fig. 2. AVI output filter

It consists of a throttle connected in series with the load, which creates a sufficiently large resistance for the higher harmonics of the phase current, reducing their value at the filter output. However, the load also has an inductance, on which a part of the higher harmonics of the AVI output voltage will be allocated, proportional to the ratio of the load inductance to the total phase inductance. To increase the efficiency of the filter, it is necessary to create a parallel path with low resistance for the current of higher harmonics at its output, which will reduce the voltage drop from their flow at the load terminals. To do this, capacitors are connected in parallel with the load. To reduce the risk of self-oscillations, damping resistors are connected in series with the capacitors. The quality factor of the resonant circuit of the filter is determined by the expression

$$Q = \frac{\sqrt{L/C}}{R}, \tag{1}$$

and can be taken in the range of 0.5–1 [9] for efficient damping of self-oscillations.

The presence of a resistor reduces the efficiency of the circuit due to energy losses in it. Therefore, the calculation of the filter parameters is aimed at reducing these losses with a sufficient filtering coefficient, which shows how many times the filter attenuates the higher harmonic with the modulation frequency.

It is known from [9] that for the filter in Fig. 2, configured to suppress the higher harmonics of the output voltage of AVI with PWM, there is an optimal filtering coefficient K_{fO}, which ensures the minimum value of total losses in the filter. It can be defined by the expression

$$K_{fO} = Q\sqrt{\omega_M^* \cdot U_\omega^*}, \tag{2}$$

where Q is the filter quality factor; $\omega_M^* = \omega_M / \omega_0$ is the relative modulation frequency; $U_\omega^* = U_\omega / U_0$ is the relative voltage of higher harmonics at the filter input; U_ω and U_0 are the effective values of voltages with PWM frequency and with the main frequency at the filter input, respectively.

Thus, *the achievement of the maximum value of the optimal filtration coefficient K_{fO} when setting the filter parameters will be an indicator of its effectiveness.*

When the filter operates with the optimal filtration coefficient K_{fO}, the relative value of the power losses in it is found as

$$P^* = \frac{P}{S_{base}} = U_\omega^* \sqrt{\frac{2}{K_{fO} \cdot \omega_M^* \cdot K_X}}, \tag{3}$$

where $S_{base} = U_L \cdot I_L$ is the load phase base full power; U_L and I_L are the rated effective values of voltage and current of the load phase, respectively; K_X is the coefficient that determines the ratio between the reactive power of the throttle and the active power of losses in the filter. It follows from [9] that the value K_X can be taken in the range of 10–20.

Given the value K_X, it is possible to determine the relative value of the inductive resistance of the throttle X_L^* in the form

$$X_L^* = \frac{\omega_0 \cdot L}{Z_{base}} = K_X \cdot P^*, \tag{4}$$

where $Z_{base} = U_L / I_L$ is the load phase base impedance; L is the filter throttle inductance.

The relative resistance of the filter resistor is then determined by the formula

$$R^* = \frac{R}{Z_{base}} = \frac{X_L^* \cdot \omega_M^*}{K_{fO}}, \tag{5}$$

and the relative conductivity of the capacitance – as

$$b_C^* = \omega_0 \cdot C \cdot Z_{base} = \frac{X_L^*}{(Q \cdot R^*)^2}, \tag{6}$$

where C and R are the capacitance of the capacitor and the active resistance of the filter resistor, respectively.

Thus, given the values Q, U_{ω}^{*} and K_X, from (2)–(6) it is possible to calculate the values of inductance, capacitance, active resistance and power losses in the filter. Here, acceptable power losses in the filter are provided at a relatively high value $\omega_M^{*} \geq 40$, which can be easily implemented on the modern element base of medium power converters [11].

Input filter of an active controlled rectifier. The main difference between the ARVS input circuit and the AVI output circuit is that there may not be a filter at the inverter output (its function, to some extent, will be performed by the inductance of the stator winding of the AC machine), and at the ARVS input, the throttle must be present by operating conditions of the scheme. The voltage drop across it, formed as the difference between the voltage of the power source and the voltage at the input of the circuit in the switching interval, forms the required shape and phase of the envelope of the network current of the circuit at the frequency of the supply network. In this case, as in the AVI, the input voltage of the active rectifier consists of segments of the DC link voltage connected to the input of the circuit with a modulation frequency.

It is known [12] that when the ARVS operates with a fixed modulation frequency, the value of its input inductance can lie within wide limits, ensuring the correct operation of the converter. From the point of view of weight, size and cost characteristics of the converter, it is desirable to reduce the value of the input inductance. However, here the qualitative indicators of the operation of the circuit suffer – the frequency distortion of the mains current and supply voltage increases. As well as at the output of the AVI, the input inductance of the ARVS also serves as a filter of higher harmonics generated by the converter into the mains. Its ability to suppress higher harmonics in the mains current and voltage will depend on the ratio of the inductance of the supply network at the point of connection to the total inductance of the phase, taking into account the value of the ARVS input throttle. Since in practice it is often difficult to determine the inductance of the supply network at the connection point of the converter, it is desirable, by analogy with the AVI output filter, to provide a parallel path with low resistance at the converter input for the flow of higher harmonic currents. Thus, the ARVS input filter circuit shown in Fig. 3, in composition and principle of operation, will be completely similar to the output filter circuit and, when ARVS operates with a fixed modulation frequency, the relationships for its calculation will be the same.

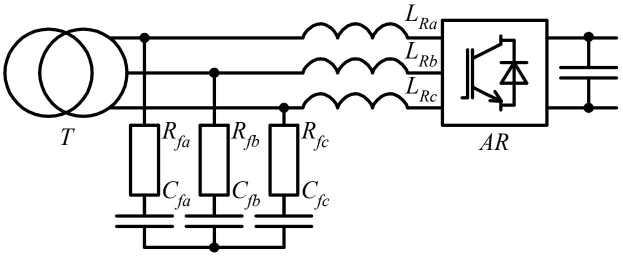

Fig. 3. ARVS input filter

The fundamental difference between the method of calculating the input filter and the one given above is that the value of its inductance is set when calculating the ARVS circuit. We modify the algorithm for calculating the filter of higher harmonics of the active rectifier of Fig. 3 for a known value of its input inductance:

- knowing from the calculation of the ARVS circuit the values of the nominal effective values of the voltage and current of the network phase U_S and I_S, the circular frequency of the source voltage ω_S, as well as the inductance of the input reactor of the circuit L_R, by (4) we determine the relative value of the inductive resistance of the throttle $X_{L_R}^{*}$ as

$$X_{L_R}^{*} = \frac{\omega_S \cdot L_R}{Z_{Sbase}}, \qquad (7)$$

where $Z_{Sbase} = U_S / I_S$ is the basic phase impedance;

- given the value K_X from (4) we obtain an expression for the power losses in the filter

$$P_f = \frac{S_{Sbase} \cdot X_{L_R}^{*}}{K_X}, \qquad (8)$$

where $S_{Sbase} = U_S \cdot I_S$ is the phase base full power;

- jointly solving (2) and (3) we obtain a formula for determining the relative voltage of higher harmonics at the filter input

$$U_{S\omega}^{*} = \frac{U_{S\omega}}{U_S} = \sqrt[3]{\frac{P_f \cdot Q^2 \cdot K_X^2 \cdot \omega_{SM}^{*3}}{4 \cdot S_{Sbase}}}, \qquad (9)$$

where $\omega_{SM}^{*} = \omega_{SM} / \omega_S$ is the relative modulation frequency of ARVS; $U_{S\omega}$ is the effective phase voltage values with PWM frequency at the filter input; ω_{SM} is the circular frequency modulation of ARVS.

Here, the quality factor of the input filter circuit Q is usually taken in the same range of 0.5–1 [9] as that of the output filter.

- using (2), we determine the optimal filtration coefficient K_{fSO} corresponding to the minimum value of total losses in the filter

$$K_{fSO} = Q\sqrt{\omega_{SM}^{*} \cdot U_{S\omega}^{*}}; \qquad (10)$$

- the resistance of the filter resistor is determined from (5)

$$R_f = \frac{Z_{Sbase} \cdot X_{L_R}^{*} \cdot \omega_{SM}^{*}}{K_{fSO}}, \qquad (11)$$

and its capacity – from (6)

$$C_f = \frac{Z_{Sbase} \cdot X_{L_R}^{*}}{\omega_S \cdot (Q \cdot R_f)^2}. \qquad (12)$$

Having previously calculated the basic values S_{Sbase} and Z_{Sbase}, using (8), (11) and (12) it is possible to obtain the value of the power losses in the filter P_f, as well as the values of the active resistance R_f and capacitance C_f of the ARVS input filter in absolute units. Their value will depend on the accepted inductance of the filter input reactor L_R at given values of Q and K_X. Let us obtain these dependencies on the example of a specific converter.

The structure of its power circuit corresponds to Fig. 1, and the parameters are taken the same as in previous studies conducted by the authors on this topic [5, 6, 12]:

- a three-phase alternating voltage source with a short circuit power 150 MVA and a line voltage level of 6 kV;
- a transformer 6 kV/0.4 kV, power 1 MVA;
- a DC link capacity 28 mF;
- ARVS and AVI bridge circuits operate in the sinusoidal PWM mode with a modulation frequency of 4 kHz;
- ARVS operates with a vector control system, and the AVI control system supports the allocation of active power at the level of 315 kW in an equivalent *RL* load for any circuit operation mode.

In [12], the required value of the input inductance for such a converter structure was calculated and it was concluded that for the effective operation of the ARVS circuit, its value can be taken in the range of 100–600 μH.

Since the main criterion for calculating the filter is *to achieve the maximum value of the optimal filtration coefficient* K_{fSO}, which ensures the minimum value of the total losses in the filter elements, from (8) we construct the dependence of the power losses on the value of the input inductance and coefficient K_X. In this case, as for the input filter [9], we take the value K_X in the range of 10–20. The dependence is shown in Fig. 4.

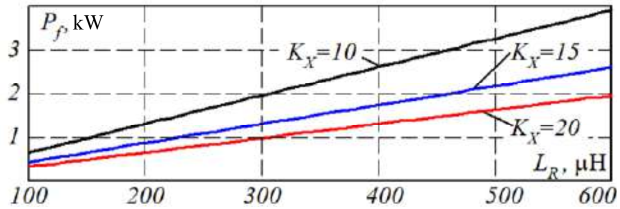

Fig. 4. Dependence of the power losses in the filter on the value of the input inductance

From Fig. 4 it can be seen that with increasing K_X, the power losses in the filter decrease. Therefore, we construct dependencies for capacitance and active resistance on the value of the input inductance of the filter and the quality factor of its circuit at the maximum accepted value $K_X = 20$. They are shown in Fig. 5, 6.

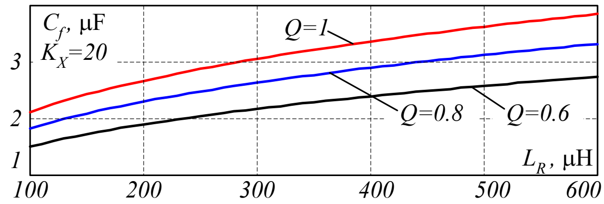

Fig. 5. Dependence of the filter capacitance on the value of the input inductance at $K_X = 20$

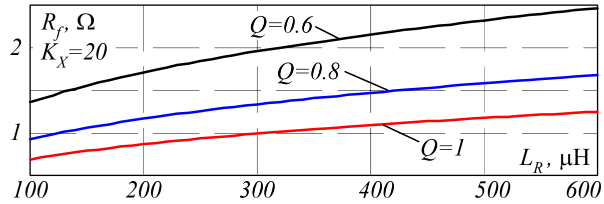

Fig. 6. Dependence of the filter resistance on the value of the input inductance at $K_X = 20$

Also, according to (10), we obtain the dependence of the optimal filtering coefficient K_{fSO} on the inductance and quality factor of the resonant circuit of the filter, shown in Fig. 7.

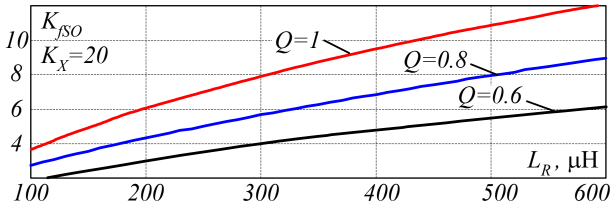

Fig. 7. Dependence of the optimal filtering coefficient on the value of the input inductance at $K_X = 20$

From Fig. 5–7 it can be seen that an increase in the quality factor of the resonant circuit of the filter leads to an increase in its optimal filtering coefficient K_{fSO}, as well as to an increase in capacitance and a decrease in the active resistance of the filter with an increase in the input inductance of the ARVS. Within the framework of the calculation algorithm under consideration, according to (8), the power losses in the filter do not directly depend on its quality factor. Based on the above, we can conclude that it is desirable to increase the quality factor of the resonant circuit of the filter. However, this increases the risk of self-oscillations. For completeness of the analysis, we construct the same dependencies for a fixed quality factor $Q = 0.8$ and various values of K_X. They are shown in Fig. 8–10.

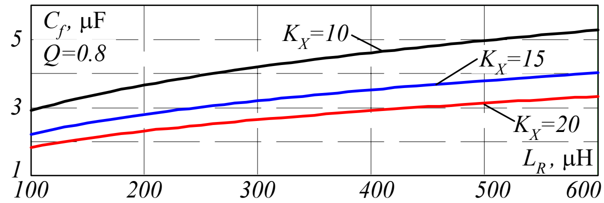

Fig. 8. Dependence of the filter capacitance on the value of the input inductance at $Q = 0.8$

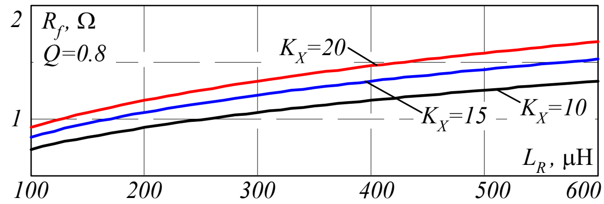

Fig. 9. Dependence of the filter resistance on the value of the input inductance at $Q = 0.8$

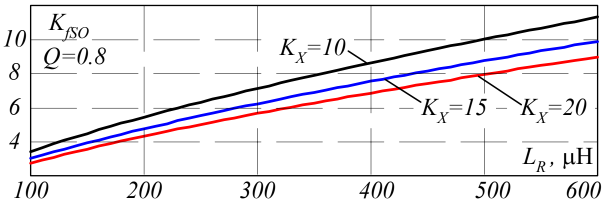

Fig. 10. Dependence of the optimal filtering coefficient on the value of the input inductance at $Q = 0.8$

Comparing Fig. 7 and Fig. 10 it can be seen that a change in the quality factor of the resonant circuit Q has a greater effect on the value of the optimal filtering coefficient K_{fSO} of the filter than a change in the coefficient K_X. Here, an increase in K_X leads not only to a decrease in the power losses in the filter, but also to a decrease in its capacitance with the same input inductance. Therefore, when designing the ARVS input filter, it can be recommended to take the maximum values of K_X and Q to increase its efficiency. Let s check it on the mathematical model of the converter.

Modelling the operation of the circuit. The modelling of the studied converter system was performed in the MATLAB/Simulink software package. The external view of the power circuit of the model is shown in Fig. 11. It fully corresponds to the structure shown in Fig. 1 and has the set parameters of the source, load, converters and control systems described above, when obtaining theoretical dependencies.

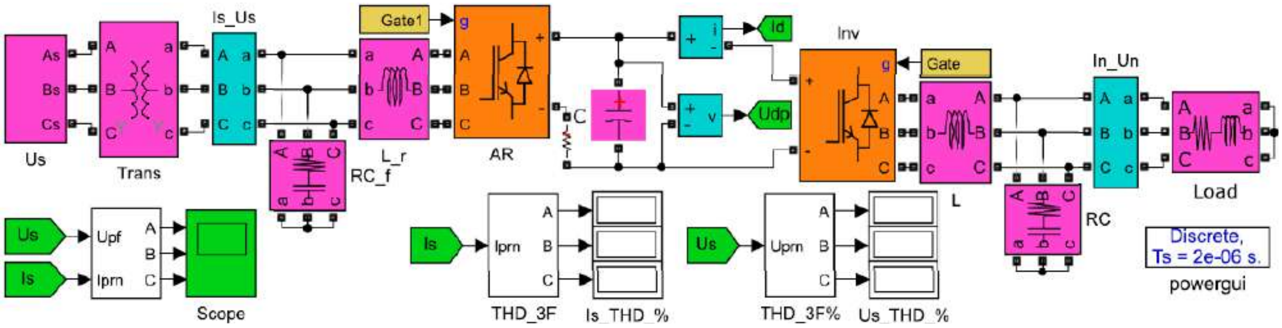

Fig. 11. MATLAB model of the ARVS power circuit

It is known [5] that the voltage at the terminals of the ARVS network phase u_V is determined by the difference between the phase voltage of the power source u and the voltage drop at the input throttle from the phase current i_S flowing through it. That is, at any time

$$u_V = u_S - u_{L_R} = u_S - L_R \cdot \frac{\mathrm{d}i_S}{\mathrm{d}t}. \qquad (13)$$

Figure 12 shows the machinodiagrams obtained in the model by (13) for the operation of the ARVS without an additional RC circuit of the low-pass filter. It can be seen from them that the instantaneous voltage u_V at the terminals of the phase of ARVS operating with a fixed modulation frequency, is formed similarly to the voltage at the output of the AVI with PWM. Here, the relative position of the mains current, as well as of the first harmonics of the ARVS input voltage $u_{V(1)}$ and the throttle voltage $u_{L(1)}$ relative to the sinusoid of the mains voltage u_S, indicate the correct operation of the circuit in the full reactive power compensation mode.

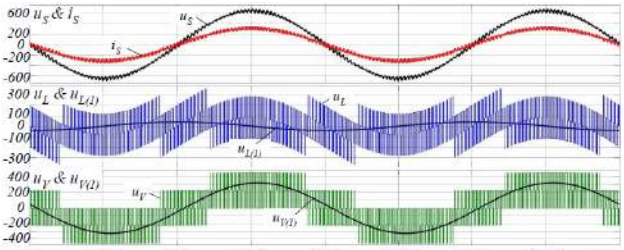

Fig. 12. Machinograms of the circuit operation

With the help of the model in Fig. 11, the dependencies of the total harmonic distortion factor of current (THD_I) and voltage (THD_U) of the phase at the input of the converter on the inductance of the ARVS input reactor were obtained. The studies were carried out for the case of the absence of an additional RC low-pass filter circuit in the ARVS input circuit, as well as for the use of a full-fledged input filter according to the structure of Fig. 3, tuned according to the proposed method for the coefficient $K_X = 20$ at two values of the quality factor of the resonant circuit: $Q = 0.6$ and $Q = 1$. The results are given in Table 1.

According to Table 1 the graphic dependencies of THD_I and THD_U at the converter connection point on the value of the input inductance are plotted, which are shown in Fig. 13. Also in Fig. 13 the dotted line shows the values of THD_I and THD_U allowed by the norms [10], which are 5 % and 8 %, respectively.

Table 1

Experimental data of the study

THD, %	Filter reactor inductance, μH					
	100	200	300	400	500	600
Without *RC* filter						
THD_I	7.43	4.14	2.91	2.25	1.85	1.60
THD_U	18.07	10.26	7.14	5.45	4.39	3.65
$Q = 0.6$, $K_x = 20$						
THD_I	7.27	3.99	2.74	2.12	1.73	1.49
THD_U	14.2	7.75	5.43	4.21	3.44	2.91
$Q = 1.0$, $K_x = 20$						
THD_I	6.63	3.49	2.41	1.87	1.55	1.35
THD_U	11.74	6.35	4.46	3.47	2.86	2.44

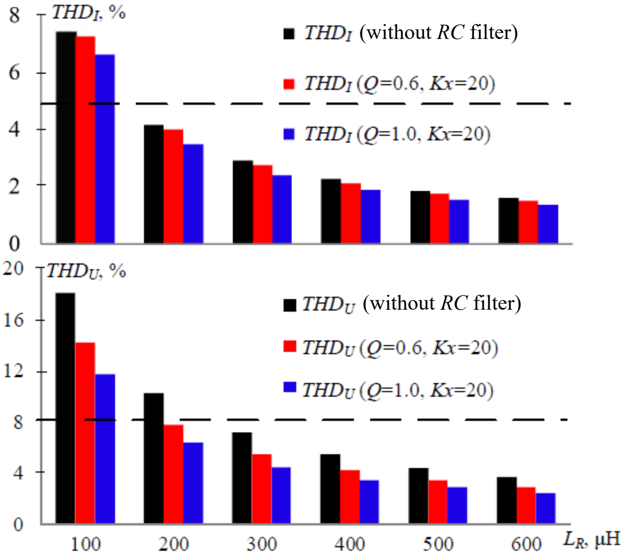

Fig. 13. Graphical dependencies of THD_I and THD_U

Conclusions.

1. A new technique is proposed for calculating the parameters of the input filter of an active rectifier – a voltage source operating with a fixed modulation frequency. It is based on the identity of the effect of ARVS and AVI, which are part of the overall structure of the frequency electric drive, on their AC links.

2. In the paper, the authors obtained calculation relationships for determining the values of the active resistance and capacitance of the input filter, as well as the value of the power losses in it in absolute units, depending on the given value of the input inductance of the ARVS. Relationships are constructed that allow estimating the interrelation between the parameters of the filter elements and its characteristics and reaching a compromise between them when designing a circuit for specific technical conditions.

3. Mathematical modelling in an object-oriented software environment has shown that the inclusion of an additional *RC* circuit of the input low-pass filter significantly improves the electromagnetic compatibility of the ARVS with the supply network in the entire studied range of the input inductance of the circuit, allowing already in the first third of it to reach the allowable values of the total harmonic distortion factor of current and voltage of the source.

Conflict of interest. The authors declare no conflict of interest.

REFERENCES

1. Bie Y., Li Y., He G., Zhang X. PWM rectifier impedance modelling and analysis. *IOP Conference Series: Earth and Environmental Science*, 2021, vol. 675, no. 1, p. 012064. doi: https://doi.org/10.1088/1755-1315/675/1/012064.

2. Pandurangan R., Kaliannan P., Shanmugam P. Effects of Current Distortion on DC Link Inductor and Capacitor Lifetime in Variable Frequency Drive Connected to Grid With Active Harmonic Filter. *IEEE Transactions on Industry Applications*, 2021, vol. 57, no. 1, pp. 492-505. doi: https://doi.org/10.1109/TIA.2020.3028555.

3. Xiao X., Zhang Y., Wang J., Du H. An Improved Model Predictive Control Scheme for the PWM Rectifier-Inverter System Based on Power-Balancing Mechanism. *IEEE Transactions on Industrial Electronics*, 2016, vol. 63, no. 8, pp. 5197-5208. doi: https://doi.org/10.1109/TIE.2016.2558138.

4. Shklyarskiy J.E., Bardanov A.I. Novel Approach to Active Rectifier Control During Voltage Dips. *2018 International Multi-Conference on Industrial Engineering and Modern Technologies (FarEastCon)*, 2018, pp. 1-5. doi: https://doi.org/10.1109/FarEastCon.2018.8602678.

5. Krylov D., Kholod O., Radohuz S. Active rectifier with different control system types. *2020 IEEE 4th International Conference on Intelligent Energy and Power Systems (IEPS), 2020*, pp. 273-278. doi: https://doi.org/10.1109/IEPS51250.2020.9263226.

6. Krylov D.S., Kholod O.I. The efficiency of the active controlled rectifier operation in the mains voltage distortion mode. *Electrical Engineering & Electromechanics*, 2021, no. 2, pp. 30-35. doi: https://doi.org/10.20998/2074-272X.2021.2.05.

7. Wai R.-J., Yang Y. Design of Backstepping Direct Power Control for Three-Phase PWM Rectifier. *IEEE Transactions on Industry Applications*, 2019, vol. 55, no. 3, pp. 3160-3173. doi: https://doi.org/10.1109/TIA.2019.2893832.

8. He H., Si T., Sun L., Liu B., Li Z. Linear Active Disturbance Rejection Control for Three-Phase Voltage-Source PWM Rectifier. *IEEE Access*, 2020, vol. 8, pp. 45050-45060. doi: https://doi.org/10.1109/ACCESS.2020.2978579.

9. Goncharov Y.P., Panasenko M.V. *Statychni peretvoriuvachi tiahovoho rukhomoho skladu* [Static converters of traction rolling stock]. Kharkiv, NTU «KhPI» Publ., 2007. 192 p. (Ukr).

10. *IEEE Std 519-2014. IEEE Recommended Practice and Requirements for Harmonic Control in Electric Power Systems*. 2014, 29 p. doi: https://doi.org/10.1109/IEEESTD.2014.6826459.

11. Bose B.K. Power semiconductor devices. In *Power Electronics and Motor Drives*, 2021, pp. 59-109. Elsevier. doi: https://doi.org/10.1016/B978-0-12-821360-5.00002-6.

12. Krylov D., Kholod O. The influence of the input inductance on the qualitative indicators of active controlled rectifier. *Bulletin of the National Technical University «KhPI» Series: New Solutions in Modern Technologies*, 2021, no. 1(7), pp. 18-23. doi: https://doi.org/10.20998/2413-4295.2021.01.03.

Received 01.01.2022
Accepted 04.04.2022
Published 20.07.2022

D.S. Krylov[1]*, PhD, Associate Professor,*
O.I. Kholod [1]*, PhD, Senior Lecturer,*
[1] National Technical University «Kharkiv Polytechnic Institute»,
2, Kyrpychova Str., Kharkiv, 61002, Ukraine,
e-mail: Denis.Krylov@khpi.edu.ua (Corresponding author),
Olha.Kholod@khpi.edu.ua

How to cite this article:
Krylov D.S., Kholod O.I. Determination of the input filter parameters of the active rectifier with a fixed modulation frequency. *Electrical Engineering & Electromechanics*, 2022, no. 4, pp. 21-26. doi: https://doi.org/10.20998/2074-272X.2022.4.03

UDC 621.314 https://doi.org/10.20998/2074-272X.2022.4.04

S. Louarem, F.Z. Kebbab, H. Salhi, H. Nouri

A comparative study of maximum power point tracking techniques for a photovoltaic grid-connected system

Purpose. *In recent years, the photovoltaic systems (PV) become popular due to several advantages among the renewable energy. Tracking maximum power point in PV systems is an important task and represents a challenging issue to increase their efficiency. Many different maximum power point tracking (MPPT) control methods have been proposed to adjust the peak power output and improve the generating efficiency of the PV system connected to the grid.* ***Methods.*** *This paper presents a Beta technique based MPPT controller to effectively track maximum power under all weather conditions. The effectiveness of this algorithm based MPPT is supplemented by a comparative study with incremental conductance (INC), particle swarm optimization (PSO), and fuzzy logic control (FLC).* ***Results*** *Faster MPPT, lower computational burden, and higher efficiency are the key contributions of the Beta based MPPT technique than the other three techniques.* References 51, table 3, figures 10.

Key words: **maximum power point tracking, incremental conductance, particle swarm optimization, fuzzy logic controller, Beta algorithm.**

Мета*. В останні роки фотоелектричні системи набули популярності завдяки низці переваг серед відновлюваних джерел енергії. Відстеження точки максимальної потужності у фотоелектричних системах є важливим завданням і складною проблемою для підвищення їх ефективності. Було запропоновано безліч різних методів керування відстеженням точки максимальної потужності (ВТМП) для регулювання пікової вихідної потужності та підвищення ефективності генерації фотоелектричної системи, підключеної до мережі.* ***Методи****. У цій статті представлений контролер ВТМП, заснований на бета-методі, для ефективного відстеження максимальної потужності за будь-яких погодних умов. Ефективність ВТМП на основі цього алгоритму доповнюється порівняльним дослідженням з інкрементною провідністю, оптимізацією рою частинок та нечітким логічним управлінням.* ***Результати.*** *Швидше ВТМП, менші витрати на обчислення та більша ефективність є ключовими перевагами методу ВТМП на основі бета-методу порівняно з трьома іншими методами.* Бібл. 51, табл. 3, рис. 10.

Ключові слова: **відстеження точки максимальної потужності, інкрементна провідність, оптимізація рою частинок, нечіткий логічний контролер, бета-алгоритм.**

Introduction. Due to the advancement of industry and population growth the demand for energy is increasing, the exhaustion nature of fossil fuels and to reduce greenhouse emissions have drawn big interest to renewable energy which are sustainable, illimitable, and pollution-free [1, 2]. During the last decades, one of the solutions is solar photovoltaic (PV) energy drawing massive attention owing to its various advantages [3, 4]. PV cell transmutes photon energy into electrical energy whereas the PV cells are connected in series to construct PV module, moreover, PV module's series and parallel connection makes PV array [5].

One of the main hindrance of PV systems relates to the operation with the highest power under all environmental conditions such as changing irradiation and temperature, shading condition and ageing of module that require an effective algorithm named Maximum Power Point Tracking (MPPT) [6, 7] to increase efficiency and decrease the cost of PV system [8].

Several research papers suggest different techniques for achieving MPPT.

Perturb and observe (P&O), incremental conductance (INC) and hill-climbing (HC) are amongst the conventional MPPT algorithms have been widely adopted to track the MPP, once they are easy to implement and moderate cost [9, 10].

In addition, their tendency propensity gives rise to oscillations around MPP. These techniques suffer from the low tracking speed and high oscillations around MPP [11, 12].

In order, to settle this issue, various studies have been attempted by introducing optimization techniques such artificial intelligence methods, including fuzzy logic controller (FLC) [13, 14]. Fuzzy logic can deal with the nonlinearities because it does not require a mathematical model as well as a technical knowledge for the exact mode [15]. Artificial neural networks (ANN) methods are well adopted for handling nonlinearity in many applications [16, 17]. And machine learning (ML) [18] is used in exploring the most effective solution for MPPT. Their efficiency is highly dependent upon extensive training, which usually takes a long time and consumes much computation power for training the model [19, 20].

For more perfection and faster speed, recent studies have exhibited special interest on the bio-inspired MPPT algorithms, particularly swarm intelligence-based algorithms that have given better results than evolutionary algorithms MPPT controllers using particle swarm optimization (PSO) algorithms have been presented in [21, 22]. The difficult of this technique is the random initialization of the PSO particles that may cause premature convergence [23].

However, many hybrid methods, which include of more than two methods, have been proposed recent, the neural network has been trained by data that are optimized by genetic algorithms [6], neuro-fuzzy IC variable step size [24] and new hybrid fuzzy-neural is presented in [25], etc.

The goal of the paper. The current research work presents a design methodology of MPPT based on a Beta technique. The main advantage of Beta is fast tracking speed in the transient stage, small oscillations in the steady state and easy to implement. A comprehensive study has been presented for checking the effectiveness and robustness Beta technique with INC, FLC and PSO under rapid varying irradiance.

The proposed technique are validated a 100 kW on-grid PV array is modeled on MATLAB.

PV modeling. A PV module is generally is comprised of multiple cells in parallel and series to achieve the required output current and voltage whose purpose the connection series allows goes up the voltage, it is the same for the parallel connection increases the current [7, 26] which are further connected to make PV array of desired output. The equivalent circuit of the PV cell is shown in Fig. 1 [27, 28].

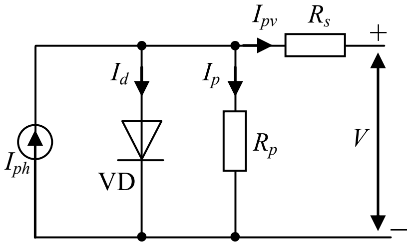

Fig. 1. The single-diode equivalent circuit of a solar cell

The output current generated here is presented in (1) – (3) [29, 30]:

$$I_{PV} = I_{ph} - I_d - I_p ; \tag{1}$$

$$I_{PV} = I_{ph} - I_0 \left[\exp.\left(\frac{\left(V + R_s I_{PV}\right)}{a} - 1 \right) \right] - \left(\frac{V + R_s I_{PV}}{R_p} \right), \tag{2}$$

$$a = \frac{N_s n k_B T}{q}, \tag{3}$$

where I_{ph} is the photo generated current; I_0 is the dark saturation current at standard test conditions (STC); R_s and R_p are the series and shunt resistance of the module respectively; a is the ideality factor; N_s is the series-connected PV cell(s); n is the diode ideality constant; k_B is the Boltzmann constant; T is the cell temperature (K); q is the electron charge.

MPPT techniques. Incremental conductance (INC) algorithm. The incremental conductance algorithm is based on the slope of the power-voltage (dP/dV) relation at the MPP is zero [31]. INC method is very precise in controlling the voltage even in rapidly changing atmospheric conditions [32, 33].

The equations implicated in the INC method are shown below:

$$P = \left(P_{PV} \times I_{PV}\right). \tag{4}$$

For MPP:

$$\frac{dP_{PV}}{dV_{PV}} = \frac{d\left(V_{PV} . I_{PV}\right)}{dV_{PV}} = I_{PV} . \frac{dV_{PV}}{dV_{PV}} + V_{PV} . \frac{dI_{PV}}{dV_{PV}} ; \tag{5}$$

$$\frac{dP_{PV}}{dV_{PV}} = I_{PV} + V_{PV} . \frac{dI_{PV}}{dV_{PV}} . \tag{6}$$

If:

$$I_{PV} + V_{PV} . \frac{dI_{PV}}{dI_{PV}} = 0 \rightarrow \frac{dI_{pv}}{dV_{pv}} = -\frac{I_{PV}}{V_{PV}} \text{ for MPP.} \tag{7}$$

If:

$$I_{PV} + V_{PV} \cdot \frac{\mathrm{d}I_{PV}}{\mathrm{d}I_{PV}} > 0 \rightarrow \frac{\mathrm{d}I_{PV}}{\mathrm{d}V_{PV}} > -\frac{I_{PV}}{V_{PV}} \text{ for } P<MPP. \tag{8}$$

If:

$$I_{PV} + V_{PV} \cdot \frac{\mathrm{d}I_{PV}}{\mathrm{d}I_{PV}} < 0 \rightarrow \frac{\mathrm{d}I_{PV}}{\mathrm{d}V_{PV}} < -\frac{I_{PV}}{V_{PV}} \text{ for } P>MPP. \tag{9}$$

In this method the MPP can be tracked by comparing the instantaneous conductance (I/V) to the INC (ΔI/ΔV) [34].

PSO algorithm. PSO technique is one of a swarm intelligence developed by Eberhart and Kennedy in 1995 [35, 36]. PSO is a global optimization algorithm for dealing with problems on a point or surface in an n-dimensional space which are linked with the best solution that has achieved by that particle [37]. Whereas the current state of the particle is, specify by the position x_i and the speed of movement v_i [38].

The particle has a random velocity vector. At each after iteration of the algorithm, the position is changed on the basis of new velocity, last best position and velocity, and distance from p_{best} and g_{best} [39].

The PSO algorithm is described by the following system of equations [40]:

$$v_i^{k+1} = w v_i^k + c_1 r_1 \left(p_{best_i} - x_i^k\right) + c_2 r_2 \left(g_{best} - x_i^k\right) ; \tag{10}$$

$$x_i\left(k+1\right) = x_i\left(k\right) + v_i\left(k+1\right), i \in \left\{1,...,N\right\} ; \tag{11}$$

where x_i is the i particle position; v_i is the i particle speed; k is the number of repetitions; r_1, r_2 are the uniformly distributed random variables; w is the weighted inertia coefficient; c_1, c_2 are the cognitive and social coefficients, respectively; $p_{best\ i}$ is the best position used for the i particle; g_{best} is the best position of all particles.

The corresponding PV current and voltage to each sample of duty cycle are observed. The PV power which represents the fitness function of particle i is resolved. Afterwards, the new calculated power of particle i is compared with the power corresponding to $p_{best\ i}$ stored in the history. The new calculated power is choose the best fitness value of particle i. The velocity and position of each particle in the swarm must be modified by the above equations [41, 42]:

$$D_i^{k+1} = D_i^k + v_i^k ; \tag{12}$$

$$v_i^{k+1} = v_i^k w^k + c_1 r_1 \left(D_{best_i}^k - D_i^k\right) + c_2 r_2 \left(g_{best_i}^k - D_i^k\right). \tag{13}$$

When the maximum number of iterations is achieved, the algorithm will stop and give the optimum value of the duty cycle D_{best}.

The objective function is defined as:

$$P\left(D_i^k\right) > P\left(D_i^{k+1}\right), \tag{14}$$

where P is the output power; D is the duty cycle; k is the number of iterations; i is the number of current particles.

Fuzzy logic controller. FLC is the most famous control technique with a remarkable ability the nonlinearity applications. The advantages of this method are its simplicity and robustness and no need the precise mathematical model of a system [5, 27].

In FLC, the change of error (dE) and error (E) are the input variables at sampling time t. These are expressed by (15) and (16) [43, 44]:

$$E\left(t\right) = \frac{P_{PV}\left(t\right) - P_{PV}\left(t-1\right)}{V_{PV}\left(t\right) - V_{PV}\left(t-1\right)} = \frac{\Delta P}{\Delta V} ; \tag{15}$$

$$dE = E\left(t\right) - E\left(t-1\right) = \Delta E , \tag{16}$$

where $P_{PV}(t)$ and $V_{PV}(t)$ are the output power and voltage of PV module, respectively.

The output variable of the controller is also to change in the duty cycle value (dD) [27]:

$$dD = D\left(t\right) - D\left(t-1\right). \tag{17}$$

The rule table of MPPT is shown in Table 1, and the membership functions are shown in Fig. 2.

Table 1

Rule base used in the fuzzy logic controller

E / d*E*	NB	ZE	PB
NB	PB	NB	ZE
ZE	NB	ZE	NB
PB	ZE	NB	PB

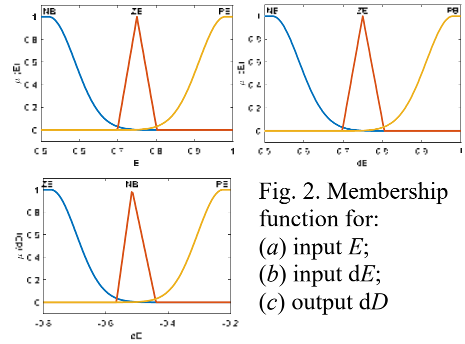

Fig. 2. Membership function for:
(*a*) input *E*;
(*b*) input d*E*;
(*c*) output d*D*

The fuzzy inference is carried out by using Mamdani’s method, and the defuzzification uses the centre of gravity to compute the output of this FLC which is the duty cycle.

Beta method. The beta parameter based MPPT algorithm was presented in [45], where the coefficient beta (β) is expressed by (18) to find an intermediary value amongst the voltage and current [46]:

$$\beta = \ln\left(\frac{I_{PV}}{V_{PV}}\right) - C \times V_{PV} , \tag{18}$$

where V_{PV} and I_{PV} are the PV module output voltage and output current, respectively; C is the diode constant, obtained from (19) [47]:

$$C = q / N_s A k_B T , \tag{19}$$

where q is an electronic charge; k_B is Boltzmann constant; A is diode quality factor; T is the ambient temperature (K); N_s is the cell number of the module.

Firstly, the voltage and current are measured, so the value of β can be continuously calculated. The value of β remains within a narrow band as the array operating point approaches the MPP.

The β is defined once based on PV characteristics at STC, using the MPP voltage and current, as expressed by (20):

$$\beta^{*} = \ln\left(\frac{I_{PV_{mpp}}}{V_{PV_{mpp}}}\right) - C \cdot V_{PV_{mpp}} , \tag{20}$$

where I_{PVmpp}, V_{PVmpp} are the respective MPP current and voltage of the PV array at STC.

Simulation results and discussion. In this section, we will present the obtained results of the global system for the control of the grid-connected PV system. The simulations are performed using MATLAB. The suggested MPPT methods for this comparative study are: INC, FLC, PSO and Beta controllers. Figure 3 depicts the PV arrays of 100 kW connected to 25 kV grid using MATLAB software. A filter is used to reduce the harmonics before connecting the inverter a 260 V / 25 kV transformer [48]. The parameters of the SPR-305-WHT PV module used in the simulation are listed in Table 2.

The PV farm consists of 66 parallel strings each string consists of 5 series PV modules with each module rated at 305.2 W. The total power of the array is 100.7 kW at STC [49]. PV module characteristics; current-voltage characteristics, power-voltage characteristics are shown in Fig. 4.

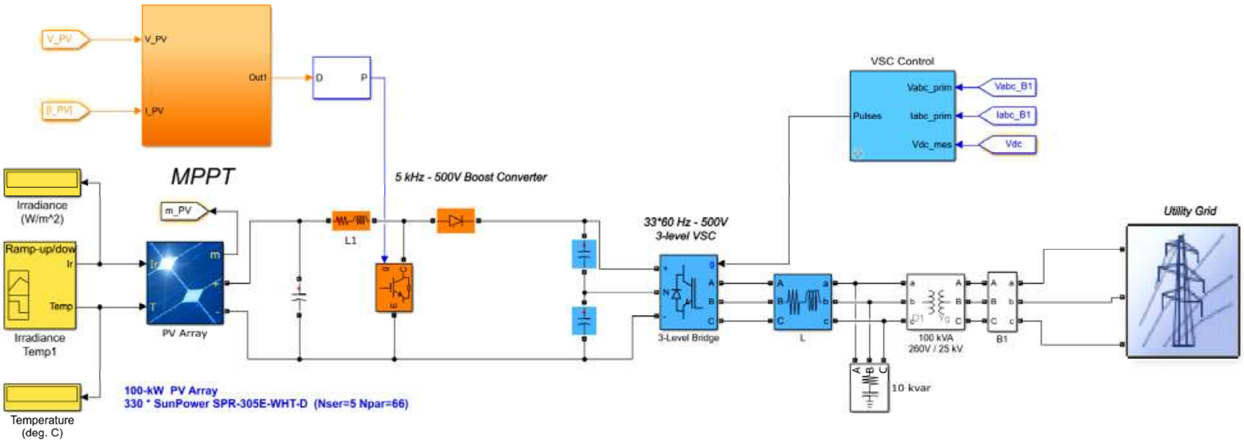

Fig. 3. Simulink model of the 100 kW grid-connected PV system

Table 2

PV module specifications [50]

Parameters	Value	Parameters	Value
Maximum power	305.02 W	$V_{\max}$ (voltage at the maximum power)	54.7 V
Peak efficiency	18.7 %	Short circuit current	5.96 A
Number of cells	96	Open circuit voltage	62.4 V
$I_{\max}$ (current at maximum power)	5.58 A	NOCT (Nominal operating cell temperature)	45°C

The proposed system is also validated by varying the irradiance level of the PV system with a constant temperature for calculating the performance evaluation. To investigate the solar irradiation change resulted from weather conditions variation, two consecutive step changes in solar irradiation are applied, which decrease from 1 kW/m^2 to 0.5 kW/m^2 at t = 0.5 s and increase to 1 kW/m^2 at t = 1.5 s, respectively (Fig. 5). While the temperature is assumed to be constant at 25 °C.

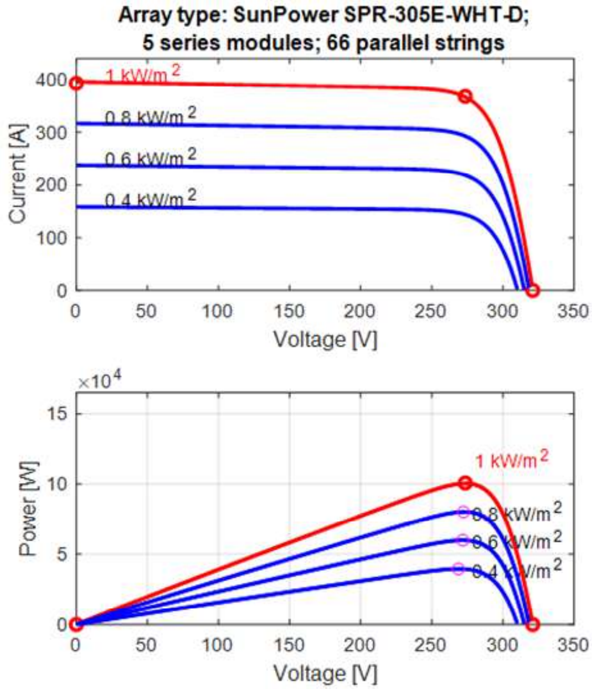

Fig. 4. *I-V* and *P-V* characteristics of the PV module at various irradiances and constant temperature

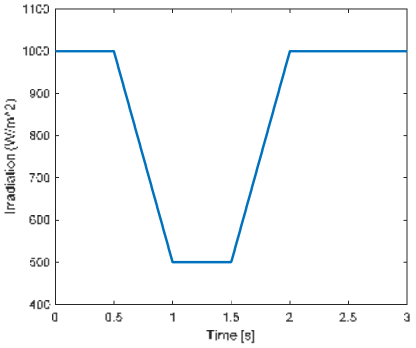

Fig. 5. The solar irradiance pattern applied to PV arrays

Figure 6 shows the output voltage variation of the PV system. The Beta technique has a good transition response 0.02802 s and a very fast system reaction against the set point change compared to another controller.

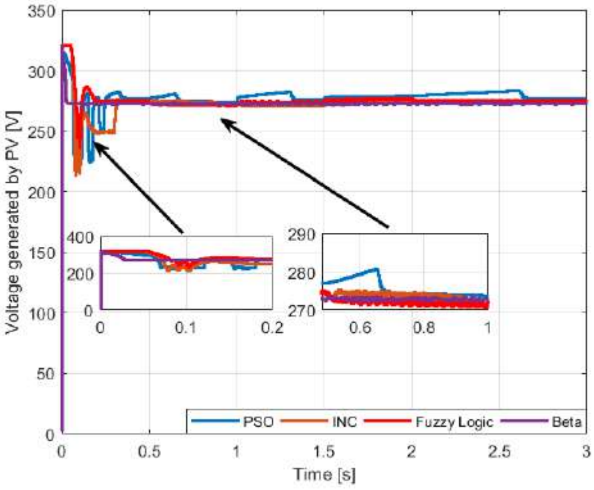

Fig. 6. PV voltage V_{PV}

Figure 7 illustrates the time evolution of photovoltaic current for different techniques. The system with INC controller suffers from failure in tracking of current. So we can see that Beta algorithm is better than other algorithm.

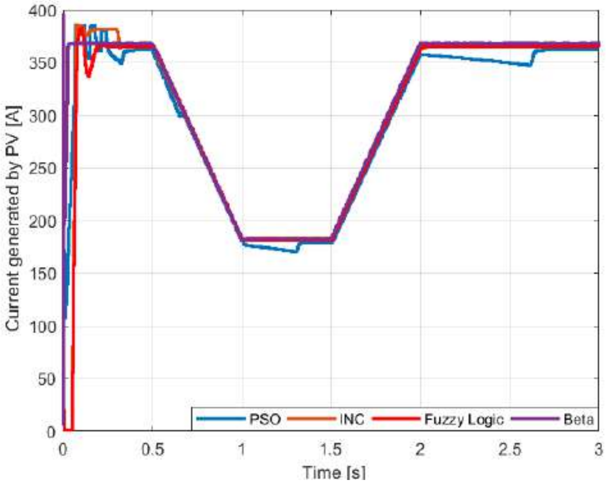

Fig. 7. PV current I_{PV}

Figures 8,*a* and 8,*b* indicate the PV system's power output: at STC condition and sudden change of irradiance.

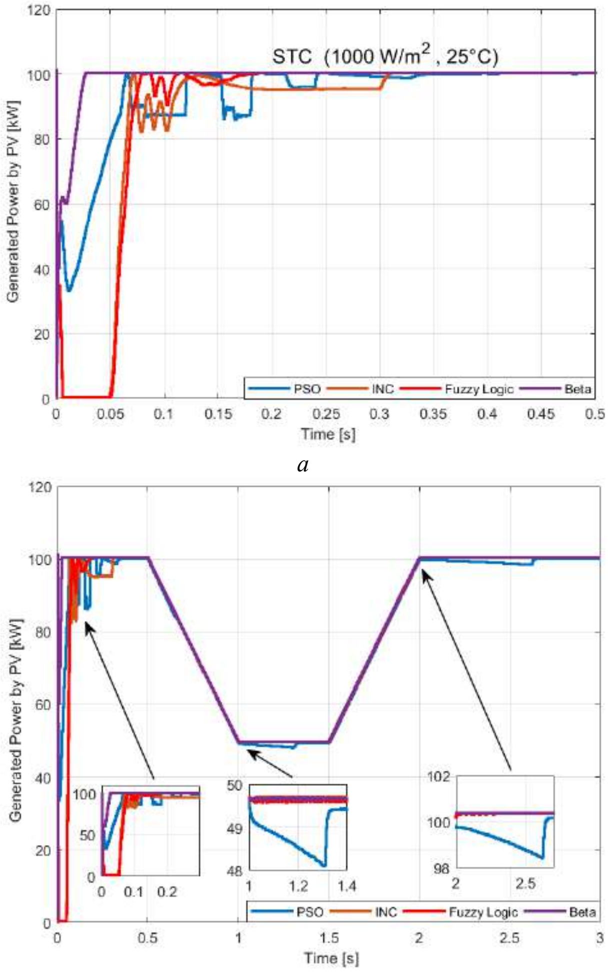

a

b

Fig. 8. PV system's power output:
(*a*) at STC condition; (*b*) sudden change of irradiance

The first step. The proposed MPPT methods is first compared under constant conditions 1 kW/m^2 and 25 °C as shown in Fig. 8,*a*.

From the simulation results, the fuzzy logic based MPPT produce the output power of 100.37 kW, INC

100.37 kW, and PSO 100.18 kW whereas the Beta based MPPT method generates 100.4 kW output power during the 0–0.5 s this strategy demonstrated performance superiority. Efficiency can be determined as the total output power of the system to the total input power of the system. Formula can be written below it is [51]:

$$\eta = \frac{P_0}{P_{\max}} \cdot 100\% , \tag{21}$$

where P_0 is the energy obtained from the PV module; $P_{\max}$ is the value of the maximum real power.

The output power of PV system at STC condition for different MPPT methods is compared in Fig. 8,*a*.

It is clear that the efficiency of tracking using PSO MPPT method is 99.48 % which is smaller than that obtained using other methods. In this situation, the Beta MPPT method tracks the maximum power successfully with efficiency of tracking 99.7 %.

Time to capture MPP for the Beta MPPT method is 0.0256 s, for PSO is 0.3349 s, for INC the time is 0.307 s and for the fuzzy logic method is 0.1614 s. This result shows that the speed of Beta MPPT method to capture MPP is best. It has the shortest MPP tracking period, the least transient fluctuations, zero oscillation around MPP and high tracking accuracy, this means the lowest power loss.

The second step. From Fig. 8,*b* in zoomed part [1 s – 1.4 s] where the irradiance level is changed from 1 to 0.5 kW/m^2. The Beta and fuzzy logic controller succeeds in instantaneously tracking the maximum power point, the oscillations are lesser at MPP in steady state in comparison the PSO and INC suffer from oscillations at MPP and tracking speed is less.

The third step. Another test is implemented to further validate the performance of the proposed controller. The application of irradiance from 0.5 to 1 kW/m^2 at t = [2 s – 3 s] (Fig. 8,*b*).

The results show that fuzzy and Beta are capable of tracking MPP under a sudden change in irradiance. Besides, the power loss in steady state due to MPP is quite low and power oscillations around MPP are minor with a higher convergence rate than others. INC and PSO method require a high response time and it has large power oscillations at MPP.

The equation representing power loss is given in (22). It can be represented in %:

$$\Delta P_{Loss} = \frac{P_{\max} - P_0}{P_{\max}} \cdot 100\% , \tag{21}$$

From Table 3 it can also be observed that the dynamic response with high efficacy of Beta technique under variation irradiance of 0.5 kW/m^2 to 1 kW/m^2 at [2 s – 3 s] compared with the methods studied.

Table 3

Results comparison for the four MPPT

Algorithm	Power generated by PV, kW	Stelling time, s	ΔP_{loss}, %
PSO	100.18	0.69	0.51
INC	100.36	0.03	0.33
Fuzzy logic	100.37	0.023	0.32
Beta	100.40	0.02	0.29

The proposed method is efficient and extracts the maximum power with minimum error, it converges fast and precisely compared to other methods, it treats in a flexible and clear way and is very effective for this type of problem.

But this method needs only the knowledge of the I-V characteristics and which is much related to the specific conditions of PV system. The use of this method requires an in-depth understanding of physical behavior, mathematical modeling, and computer science.

It is very apparent, in dynamic climatic change conditions at time periods (1, 1.5 and 2 s) the INC, FLC and PSO controller suffer to track rapid or fast changing conditions, with an error and low tracking efficiency.

It can be said that despite the sudden changes in irradiance, the proposed method performs better in terms of stability and power extraction.

Figure 9 shows the reference signal for the voltage controller and the resulting DC link voltage. The voltage is constant throughout the time (500 V) and no boost converter output voltage values up and down when the radiation values increases and decrease respectively. So, the Beta technique has the fastest converge speed among all the other suggested MPPT techniques.

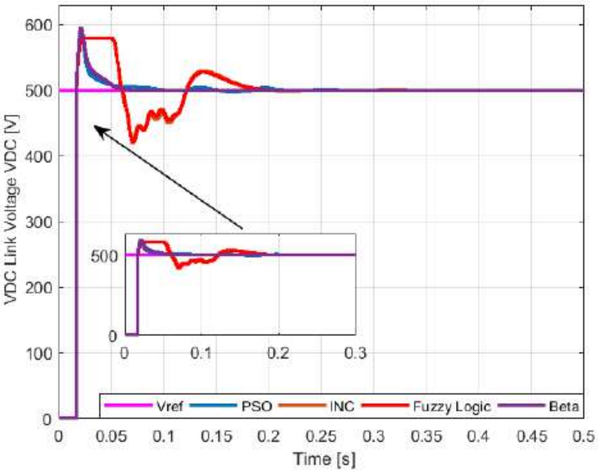

Fig. 9. Reference voltage and actual DC link voltage

Figure 10 shows the time evolution of the active power which flows between the analyzed system and the main grid. The power achieved by Fuzzy logic is 98.70 kW; Beta is 98.75 kW; PSO is 98.55 kW and INC is 98.65 kW. This confirms that Beta presented negligible power oscillations in steady state and the lowest convergence times.

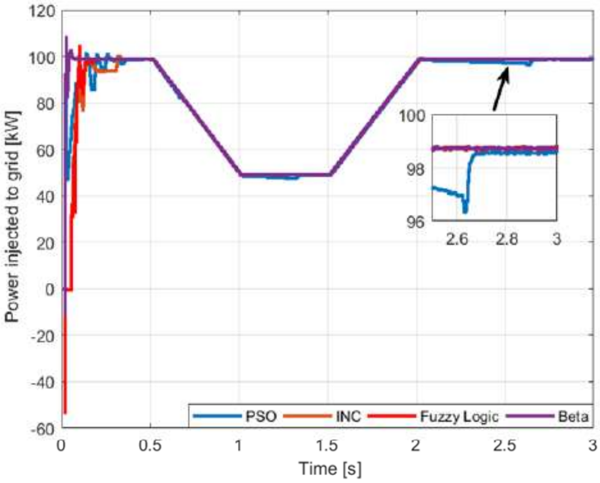

Fig. 10. Power injected to grid

From the simulation results, the Beta based MPPT algorithms is realized with a 100 kW PV array connected to a 25 kV grid whither in the literature application in PV systems with the load resistance. From the data, it has been demonstrated that the Beta controller has a better time response process. Since the computations show that the Beta achieves a high efficiency for all the irradiance ranges whereas the other methods fail in achieving high efficiency. It also, avoid power loss around the MPP. However, this technique depends on the PV characteristics.

Conclusions.

The use of photovoltaic systems to generate electricity is developing around the world. The photovoltaic system efficiency is a crucial index to estimate the performance of grid-connected photovoltaic systems where the maximum power point tracking performance is a key word to improve and increase the efficiency of this structure.

This paper presents the control of a grid-connected photovoltaic system using: incremental conductance, particle swarm optimization algorithm, fuzzy logic control and Beta for the achievement of photovoltaic maximum power point tracking.

The comparative study confirmed that the Beta controller was presented as an excellent solution regarding the low oscillations, the highest speed, and efficiently tracking the maximum power point even during an abrupt change in the solar irradiance.

Conflict of interest. The authors declare no conflict of interest.

REFERENCES

1. Belhaouas N., Mehareb F., Assem H., Kouadri-Boudjelthia E., Bensalem S., Hadjrioua F., Aissaoui A., Bakria K. A new approach of PV system structure to enhance performance of PV generator under partial shading effect. *Journal of Cleaner Production*, 2021, vol. 317, p. 128349. doi: https://doi.org/10.1016/j.jclepro.2021.128349.

2. Li C., Yang Y., Zhang K., Zhu C., Wei H. A fast MPPT-based anomaly detection and accurate fault diagnosis technique for PV arrays. *Energy Conversion and Management*, 2021, vol. 234, p. 113950. doi: https://doi.org/10.1016/j.enconman.2021.113950.

3. Fu L., Fu X., Yang P. Maximum Power Point Tracking in Solar Cells with Power Quality Preservation Based on Impedance Matching Concept for Satellite Electrical Energy Supply. *Journal of New Materials for Electrochemical Systems*, 2021, vol. 24, no. 2, pp. 111-119. doi: https://doi.org/10.14447/jnmes.v24i2.a08.

4. Slama F., Radjeai H., Mouassa S., Chouder A. New algorithm for energy dispatch scheduling of grid-connected solar photovoltaic system with battery storage system. *Electrical Engineering & Electromechanics*, 2021, no. 1, pp. 27-34. doi: https://doi.org/10.20998/2074-272X.2021.1.05.

5. Verma P., Garg R., Mahajan P. Asymmetrical interval type-2 fuzzy logic control based MPPT tuning for PV system under partial shading condition. *ISA Transactions*, 2020, vol. 100, pp. 251-263. doi: https://doi.org/10.1016/j.isatra.2020.01.009.

6. Tao H., Ghahremani M., Ahmed F.W., Jing W., Nazir M.S., Ohshima K. A novel MPPT controller in PV systems with hybrid whale optimization-PS algorithm based ANFIS under different conditions. *Control Engineering Practice*, 2021, vol. 112, p. 104809. doi: https://doi.org/10.1016/j.conengprac.2021.104809.

7. Ge X., Ahmed F.W., Rezvani A., Aljojo N., Samad S., Foong L.K. Implementation of a novel hybrid BAT-Fuzzy controller based MPPT for grid-connected PV-battery system. *Control Engineering Practice*, 2020, vol. 98, p. 104380. doi: https://doi.org/10.1016/j.conengprac.2020.104380.

8. Yilmaz U., Kircay A., Borekci S. PV system fuzzy logic MPPT method and PI control as a charge controller. *Renewable and Sustainable Energy Reviews*, 2018, vol. 81, pp. 994-1001. doi: https://doi.org/10.1016/j.rser.2017.08.048.

9. Vimalarani C., Kamaraj N., Chitti Babu B. Improved method of maximum power point tracking of photovoltaic (PV) array using hybrid intelligent controller. *Optik*, 2018, vol. 168, pp. 403-415. doi: https://doi.org/10.1016/j.ijleo.2018.04.114.

10. Eltawil M.A., Zhao Z. MPPT techniques for photovoltaic applications. *Renewable and Sustainable Energy Reviews*, 2013, vol. 25, pp. 793-813. doi: https://doi.org/10.1016/j.rser.2013.05.022.

11. Hamza Zafar M., Mujeeb Khan N., Feroz Mirza A., Mansoor M., Akhtar N., Usman Qadir M., Ali Khan N., Raza Moosavi S.K. A novel meta-heuristic optimization algorithm based MPPT control technique for PV systems under complex partial shading condition. *Sustainable Energy Technologies and Assessments*, 2021, vol. 47, pp. 101367. doi: https://doi.org/10.1016/j.seta.2021.101367.

12. Ali A.I.M., Mohamed H.R.A. Improved P&O MPPT algorithm with efficient open-circuit voltage estimation for two-stage grid-integrated PV system under realistic solar radiation. *International Journal of Electrical Power & Energy Systems*, 2022, vol. 137, p. 107805. doi: https://doi.org/10.1016/j.ijepes.2021.107805.

13. Priyadarshi N., Padmanaban S., Holm-Nielsen J.B., Blaabjerg F., Bhaskar M.S. An Experimental Estimation of Hybrid ANFIS–PSO-Based MPPT for PV Grid Integration Under Fluctuating Sun Irradiance. *IEEE Systems Journal*, 2020, vol. 14, no. 1, pp. 1218-1229. doi: https://doi.org/10.1109/JSYST.2019.2949083.

14. Dehghani M., Taghipour M., Gharehpetian B.G., Abedi M. Optimized Fuzzy Controller for MPPT of Grid-connected PV Systems in Rapidly Changing Atmospheric Conditions. *Journal of Modern Power Systems and Clean Energy*, 2021, vol. 9, no. 2, pp. 376-383. doi: https://doi.org/10.35833/MPCE.2019.000086.

15. Charaabi A., Zaidi A., Barambones O., Zanzouri N. Implementation of adjustable variable step based backstepping control for the PV power plant. *International Journal of Electrical Power & Energy Systems*, 2022, vol. 136, p. 107682. doi: https://doi.org/10.1016/j.ijepes.2021.107682.

16. Liu L., Meng X., Liu C. A review of maximum power point tracking methods of PV power system at uniform and partial shading. *Renewable and Sustainable Energy Reviews*, 2016, vol. 53, pp. 1500-1507. doi: https://doi.org/10.1016/j.rser.2015.09.065.

17. Fathi M., Parian J.A. Intelligent MPPT for photovoltaic panels using a novel fuzzy logic and artificial neural networks based on evolutionary algorithms. *Energy Reports*, 2021, vol. 7, pp. 1338-1348. doi: https://doi.org/10.1016/j.egyr.2021.02.051.

18. Chen Z., Yu H., Luo L., Wu L., Zheng Q., Wu Z., Cheng S., Lin P. Rapid and accurate modeling of PV modules based on extreme learning machine and large datasets of I-V curves. *Applied Energy*, 2021, vol. 292, p. 116929. doi: https://doi.org/10.1016/j.apenergy.2021.116929.

19. Oshaba A.S., Ali E.S., Abd Elazim S.M. MPPT control design of PV system supplied SRM using BAT search algorithm. *Sustainable Energy, Grids and Networks*, 2015, vol. 2, pp. 51-60. doi: https://doi.org/10.1016/j.segan.2015.04.002.

20. Mirza A.F., Mansoor M., Ling Q., Yin B., Javed M.Y.A Salp-Swarm Optimization based MPPT technique for harvesting maximum energy from PV systems under partial shading conditions. *Energy Conversion and Management*, 2020, vol. 209, p. 112625. doi: https://doi.org/10.1016/j.enconman.2020.112625.

21. Eltamaly A.M., Al-Saud M.S., Abokhalil A.G., Farh H.M. H. Simulation and experimental validation of fast adaptive particle swarm optimization strategy for photovoltaic global peak tracker under dynamic partial shading. *Renewable and Sustainable Energy Reviews*, 2020, vol. 124, p. 109719. doi: https://doi.org/10.1016/j.rser.2020.109719.

22. Shi J., Zhang W., Zhang Y., Xue F., Yang T. MPPT for PV systems based on a dormant PSO algorithm. *Electric Power Systems Research*, 2015, vol. 123, pp. 100-107. doi: https://doi.org/10.1016/j.epsr.2015.02.001.

23. Guichi A., Mekhilef S., Berkouk E.M., Talha A. Optimal control of grid-connected microgrid PV-based source under partially shaded conditions. *Energy*, 2021, vol. 230, p. 120649. doi: https://doi.org/10.1016/j.energy.2021.120649.

24. Harrag A., Bahri H. Novel neural network IC-based variable step size fuel cell MPPT controller. *International Journal of Hydrogen Energy*, 2017, vol. 42, no. 5, pp. 3549-3563. doi: https://doi.org/10.1016/j.ijhydene.2016.12.079.

25. Vincheh M.R., Kargar A., Markadeh G.A. A Hybrid Control Method for Maximum Power Point Tracking (MPPT) in Photovoltaic Systems. *Arabian Journal for Science and*

Engineering, 2014, vol. 39, no. 6, pp. 4715-4725. doi: https://doi.org/10.1007/s13369-014-1056-0.

26. Doubabi H., Salhi I., Chennani M., Essounbouli N. High Performance MPPT based on TS Fuzzy–integral backstepping control for PV system under rapid varying irradiance – Experimental validation. *ISA Transactions*, 2021, vol. 118, pp. 247-259. doi: https://doi.org/10.1016/j.isatra.2021.02.004.

27. Zhao L., Jiang M., Dadfar S., Ibrahim A., Aboelsaud R., Jamali F. Grid-Tied PV-BES system based on modified bat algorithm-FLC MPPT technique under uniform conditions. *Neural Computing and Applications*, 2021, vol. 33, no. 21, pp. 14929-14943. doi: https://doi.org/10.1007/s00521-021-06128-x.

28. Behera M.K., Saikia L.C. An intelligent hybrid GMPPT integrating with accurate PSC detection scheme for PV system using ESSA optimized AWFOPI controller. *Sustainable Energy Technologies and Assessments*, 2021, vol. 46, p. 101233. doi: https://doi.org/10.1016/j.seta.2021.101233.

29. Celikel R., Yilmaz M., Gundogdu A. A voltage scanning-based MPPT method for PV power systems under complex partial shading conditions. *Renewable Energy*, 2022, vol. 184, pp. 361-373. doi: https://doi.org/10.1016/j.renene.2021.11.098.

30. Sahraoui H., Mellah H., Drid S., Chrifi-Alaoui L. Adaptive maximum power point tracking using neural networks for a photovoltaic systems according grid. *Electrical Engineering & Electromechanics*, 2021, no. 5, pp. 57-66. doi: https://doi.org/10.20998/2074-272X.2021.5.08.

31. Ali M.N., Mahmoud K., Lehtonen M., Darwish M.M.F. An Efficient Fuzzy-Logic Based Variable-Step Incremental Conductance MPPT Method for Grid-Connected PV Systems. *IEEE Access*, 2021, vol. 9, pp. 26420-26430. doi: https://doi.org/10.1109/ACCESS.2021.3058052.

32. Lorenzini G., Kamarposhti M.A., Solyman A.A.A. Maximum Power Point Tracking in the Photovoltaic Module Using Incremental Conductance Algorithm with Variable Step Length. *Journal Européen Des Systèmes Automatisés*, 2021, vol. 54, no. 3, pp. 395-402. doi: https://doi.org/10.18280/jesa.540302.

33. Gupta A.K., Chauhan Y.K., Maity T. Experimental investigations and comparison of various MPPT techniques for photovoltaic system. *Sādhanā*, 2018, vol. 43, no. 8, p. 132. doi: https://doi.org/10.1007/s12046-018-0815-0.

34. Hlaili M., Mechergui H. Comparison of Different MPPT Algorithms with a Proposed One Using a Power Estimator for Grid Connected PV Systems. *International Journal of Photoenergy*, 2016, vol. 2016, pp. 1-10. doi: https://doi.org/10.1155/2016/1728398.

35. Kennedy J., Eberhart R. Particle swarm optimization. *Proceedings of ICNN'95 – International Conference on Neural Networks*, 1995, vol. 4, pp. 1942-1948. doi: https://doi.org/10.1109/ICNN.1995.488968.

36. Eberhart R., Kennedy J. A new optimizer using particle swarm theory. *MHS'95. Proceedings of the Sixth International Symposium on Micro Machine and Human Science*, 1995, pp. 39-43. doi: https://doi.org/10.1109/MHS.1995.494215.

37. Maleki A., Ameri M., Keynia F. Scrutiny of multifarious particle swarm optimization for finding the optimal size of a PV/wind/battery hybrid system. *Renewable Energy*, 2015, vol. 80, pp. 552-563. doi: https://doi.org/10.1016/j.renene.2015.02.045.

38. Chaieb H., Sakly A. A novel MPPT method for photovoltaic application under partial shaded conditions. *Solar Energy*, 2018, vol. 159, pp. 291-299. doi: https://doi.org/10.1016/j.solener.2017.11.001.

39. Koad R.B.A., Zobaa A.F., El-Shahat A. A Novel MPPT Algorithm Based on Particle Swarm Optimization for Photovoltaic Systems. *IEEE Transactions on Sustainable Energy*, 2017, vol. 8, no. 2, pp. 468-476. doi: https://doi.org/10.1109/TSTE.2016.2606421.

40. Benamrane K., Abdelkrim T., Benlahbib B., Bouarroudj N., Borni A., Lakhdari A., Bahri A. New Optimized Control of Cascaded Multilevel Converters for Grid Tied Photovoltaic Power Generation. *Journal Européen Des Systèmes Automatisés*, 2021, vol. 54, no. 5, pp. 769-776. doi: https://doi.org/10.18280/jesa.540512.

41. Ibrahim A., Aboelsaud R., Obukhov S. Improved particle swarm optimization for global maximum power point tracking of partially shaded PV array. *Electrical Engineering*, 2019, vol. 101, no. 2, pp. 443-455. doi: https://doi.org/10.1007/s00202-019-00794-w.

42. Sudhakar Babu T., Rajasekar N., Sangeetha K. Modified Particle Swarm Optimization technique based Maximum Power Point Tracking for uniform and under partial shading condition. *Applied Soft Computing*, 2015, vol. 34, pp. 613-624. doi: https://doi.org/10.1016/j.asoc.2015.05.029.

43. Laagoubi T., Bouzi M., Benchagra M. MPPT and Power Factor Control for Grid Connected PV Systems with Fuzzy Logic Controllers. *International Journal of Power Electronics and Drive Systems (IJPEDS)*, 2018, vol. 9, no. 1, pp. 105-113. doi: https://doi.org/10.11591/ijpeds.v9.i1.pp105-113.

44. Rezk H., Eltamaly A.M. A comprehensive comparison of different MPPT techniques for photovoltaic systems. *Solar Energy*, 2015, vol. 112, pp. 1-11. doi: https://doi.org/10.1016/j.solener.2014.11.010.

45. Jain S., Agarwal V. A New Algorithm for Rapid Tracking of Approximate Maximum Power Point in Photovoltaic Systems. *IEEE Power Electronics Letters*, 2004, vol. 2, no. 1, pp. 16-19. doi: https://doi.org/10.1109/LPEL.2004.828444.

46. Li X., Wen H., Hu Y., Jiang L. A novel beta parameter based fuzzy-logic controller for photovoltaic MPPT application. *Renewable Energy*, 2019, vol. 130, pp. 416-427. doi: https://doi.org/10.1016/j.renene.2018.06.071.

47. Poltronieri Sampaio L., Vichoski da Rocha M., Oliveira da Silva S.A., Hideo Takami de Freitas M. Comparative analysis of MPPT algorithms bio-inspired by grey wolves employing a feed-forward control loop in a three-phase grid-connected photovoltaic system. *IET Renewable Power Generation*, 2019, vol. 13, no. 8, pp. 1379-1390. doi: https://doi.org/10.1049/iet-rpg.2018.5941.

48. Mokhtar M., Marei M.I., Attia M.A. Hybrid SCA and adaptive controller to enhance the performance of grid-connected PV system. *Ain Shams Engineering Journal*, 2021, vol. 12, no. 4, pp. 3775-3781. doi: https://doi.org/10.1016/j.asej.2021.03.019.

49. Nicola M., Nicola C.-I. Fractional-Order Control of Grid-Connected Photovoltaic System Based on Synergetic and Sliding Mode Controllers. *Energies*, 2021, vol. 14, no. 2, p. 510. doi: https://doi.org/10.3390/en14020510.

50. Saad N.H., El-Sattar A.A., Mansour A.E.-A.M. Improved particle swarm optimization for photovoltaic system connected to the grid with low voltage ride through capability. *Renewable Energy*, 2016, vol. 85, pp. 181-194. doi: https://doi.org/10.1016/j.renene.2015.06.029.

51. Bhavani M., Vijaybhaskar Reddy K., Mahesh K., Saravanan S. Impact of variation of solar irradiance and temperature on the inverter output for grid connected photo voltaic (PV) system at different climate conditions. *Materials Today: Proceedings*. 2021. doi: https://doi.org/10.1016/j.matpr.2021.06.120.

Received 02.01.2022
Accepted 08.04.2022
Published 20.07.2022

Sabah Louarem [1], *Doctor of Technical Science,*
Fatima Zohra Kebbab [2], *Doctor of Technical Science,*
Houria Salhi [1], *PhD,*
Hamou Nouri [1], *Professor of Electrical Engineering,*
[1] Automatic Laboratory of Setif (LAS),
Ferhat Abbas University Setif 1, 19000, Algeria,
e-mail: slouarem@univ-setif.dz (Corresponding author),
houria.salhi@univ-setif.dz; hnouri19@univ-setif.dz
[2] Department of Electrical Engineering,
DAC HR Laboratory,
Ferhat Abbas University Setif 1, Algeria,
e-mail: fatimazohra.kebbab@univ-setif.dz

How to cite this article:
Louarem S., Kebbab F.Z., Salhi H., Nouri H. A comparative study of maximum power point tracking techniques for a photovoltaic grid-connected system. *Electrical Engineering & Electromechanics*, 2022, no. 4, pp. 27-33. doi: https://doi.org/10.20998/2074-272X.2022.4.04

UDC 621.3.013 https://doi.org/10.20998/2074-272X.2022.4.05

G. Merlin Suba, M. Kumaresan

Design of LLC resonant converter with silicon carbide MOSFET switches and nonlinear adaptive sliding controller for brushless DC motor system

Introduction. *The high voltage gain DC-DC converters are increasingly used in many power electronics application systems, due to their benefits of increased voltage output, reduced noise contents, uninterrupted power supply, and ensured system reliability. Most of the existing works are highly concentrated on developing the high voltage DC-DC converter and controller topologies for goal improving the steady state response of brushless DC motor driving system and also obtain the regulated voltage with increased power density and reduced harmonics, the LLC resonant DC-DC converter is implemented with the silicon carbide MOSFET switching devices* ***Problem****. Yet, it facing the major problems of increased switching loss, conduction loss, error outputs, time consumption, and reduced efficiency. Also the existing works are mainly concentrating on improving the voltage gain, regulation, and operating performance of the power system with reduced loss of factors by using the different types of converters and controlling techniques. The* ***goal*** *of this work is to obtain the improved voltage gain output with reduced loss factors and harmonic distortions.* ***Method****. Because, this type of converter has the ability to generate the high gain DC output voltage fed to the brushless DC motor with reduced harmonics and loss factors. Also, the nonlinear adaptive sliding controller is implemented to generate the controlling pulses for triggering the switching components properly. For this operation, the best gain parameters are selected based on the duty cycle, feedback DC voltage and current, and gain of silicon carbide MOSFET. By using this, the controlling signals are generated and given to the converter, which helps to control the brushless DC motor with steady state error.* ***Practical value****. The simulation results of the proposed LLC silicon carbide MOSFET incorporated with nonlinear adaptive sliding controller controlling scheme are validated and compared by using various evaluation indicators.* References 40, tables 3, figures 22.

Key words: **power conversion, brushless DC motor, silicon carbide MOSFET switches, LLC resonant converter, nonlinear adaptive sliding controller, voltage regulation harmonics suppression.**

Вступ*. Високовольтні перетворювачі постійного струму з високим коефіцієнтом посилення напруги все частіше використовуються в багатьох прикладних системах силової електроніки через їх переваги, пов'язані з підвищеною вихідною напругою, зниженим рівнем шуму, безперебійним живленням і гарантованою надійністю системи. Більшість існуючих робіт значною мірою зосереджені на розробці топологій високовольтного перетворювача постійного струму і контролера з метою поліпшення усталеного відгуку системи приводу безщіткового двигуна постійного струму, а також отримання регульованої напруги з підвищеною щільністю потужності і зменшеними гармоніками; резонансний LLC-перетворювач постійного струму, реалізований на перемикаючих пристроях на основі польових МОП-транзисторах з карбіду кремнію.* ***Проблема****. Тим не менш, це стикається з основними проблемами, пов'язаними зі збільшенням втрат при перемиканні, втратами провідності, помилками на виході, витратами часу та зниженням ефективності. Крім того, існуючі роботи в основному зосереджені на покращенні коефіцієнта посилення напруги, регулювання та робочих характеристик енергосистеми із зменшенням факторів втрат за рахунок використання різних типів перетворювачів та методів управління.* ***Метою*** *роботи є отримання покращеного коефіцієнта посилення напруги зі зниженими коефіцієнтами втрат і гармонійних спотворень.* ***Метод****. Таким чином, цей тип перетворювача здатний генерувати вихідну постійну напругу з високим коефіцієнтом посилення, що подається на безщітковий двигун постійного струму, зі зменшеними коефіцієнтами гармонік та втрат. Крім того, реалізований нелінійний адаптивний ковзний регулятор для генерування керуючих імпульсів для належного спрацьовування перемикаючих компонентів. Для цієї операції вибираються найкращі параметри посилення на основі робочого циклу, постійної напруги та струму зворотного зв'язку, а також коефіцієнта посилення польового МОП-транзистора з карбіду кремнію. При цьому керуючі сигнали генеруються і передаються на перетворювач, який допомагає керувати безщітковим двигуном постійного струму з помилкою, що встановилася.* ***Практична цінність****. Результати моделювання запропонованого LLC-перетворювача на основі польових МОП-транзисторів з карбіду кремнію зі схемою управління нелінійним адаптивним ковзним регулятором перевіряються та порівнюються з використанням різних показників оцінки.* Бібл. 40, табл. 3, рис. 22.

Ключові слова: **перетворення потужності, безщітковий двигун постійного струму, перемикачі на основі польових МОП-транзисторів, резонансний *LLC*-перетворювач, нелінійний адаптивний ковзний регулятор, придушення гармонік регулювання напруги.**

1. Introduction. In the recent days, the power electronics DC-DC converters [1-3] has gained a significant attention in many power application systems, due to their benefits of increased conversion efficiency, regulated voltage, reliability, uninterrupted power supply, and optimal cost consumption. When compared to the other DC-DC converters, the LLC resonant converter [4, 5] is more popular and increasingly used in the power electronics system like renewable energy sources, battery charging systems, plug-in electric vehicles and other low power applications. Because, the LLC converter [6, 7] could regulate the voltage gain based on the frequency of modulation. If the switching frequency of converter is matched with the resonance frequency [8, 9] it is determined as the circuit operations are efficient. Since, the LLC converter has the ability to efficiently reduce the switching as well as conduction losses. The modern power supply systems, DC micro-grids and high voltage DC power transmission systems [10, 11] widely utilized the LLC resonant converter due to its soft switching characteristics and increased density of power. Nevertheless, the conventional Si based converters [12, 13] facing difficulties related to the factors of high conduction loss, reduced switching frequency, and reduced voltage gain, which affects the efficiency and performance of entire power system.

Hence, the SiC-MOSFET [14-16] is one of the most suitable options for designing the LLC resonant converters, because it provides increased power outputs with reduced switching stress. Therefore, the proposed work intends to utilize the SiC-MOSFET [17] based inverter topology for efficiently controlling the brushless

DC (BLDC) motor system [18-20] with minimized harmonics distortions. Generally, the SiC-MOSFET circuitry has the major benefits of increased switching frequency, high speed in nature, ensured dynamic response, and minimized ripples. Hence, this work intends to utilize the SiC-MOSFET topology for controlling the BLDC motor [21, 22] system with the help of resonant DC-DC converter. For this purpose, a novel nonlinear adaptive sliding controller (NASC) mechanism is developed in this work, which is used to generate the controlling signals for actuating the SiC-MOSFET switching devices. This main objective of using this controlling mechanism is to control the speed and torque of BLDC motor based on the feedback signals. Also, the LLC resonant DC-DC converter is employed for regulating the random power obtained from the power source. The main intention of using this DC-DC converter is to efficiently boost the output power for charging batteries, and improving the performance of BLDC motor. The novel contributions of this works are two fold:

- to obtain the regulated voltage with increased power density and reduced harmonics, the LLC resonant DC-DC converter is implemented with the SiC-MOSFET switching devices;
- to improve the efficiency and controlling performance of BLDC motor, a novel NASC mechanism is developed;
- to attain the increased switching frequency, reduced error rate and optimal performance results, the mode of converter operations are properly performed according to the generated controlling signals;
- to assess the performance of proposed LLC-SiC MOSFET and NASC scheme, various evaluation indicators have been utilized.

2. Related works. This sector reviews some of the existing works related to the different types of converter and controller designs used in the power system applications based on its operating modes, key characteristics and functionalities. Also, it examines the benefits and limitations of the conventional converter and controlling techniques based on the factors of voltage gain, power conversion efficiency, controlling complexity, error rate, and harmonics.

In [23] was suggested a modulation based voltage control mechanism for controlling the speed of BLDC motor with the help of load resonant converter. Here, the main reason of using the LLC resonance converter circuit was to obtain the zero voltage switching with respect to varying switching conditions. It also objects to reduce the effect of electromagnetic interference noises with increased power density by using the LLC converter design. In [24] was designed a series resonant DC-DC converter topology for obtaining the improved voltage gain and power outputs based on the quality factor estimation. The key factor of this work was to reduce the switching losses by reduced loop inductance value. In [25] was suggested the LLC resonant converters with MOSFET switching devices for satisfying the requirements of high voltage applications. Here, the loss model of the converter design has been discussed, which includes both the conduction and switching loss factors. In addition to that, the key characteristics of Si-MOSFET and SiC-MOSFET switches were illustrated with its driving voltage speed. Based on this analysis, it was observed that the SiC-MOSFET switches provided the better performance outcomes in terms of increased voltage and speed, when compared to the Si-MOSFET switches. Also, the LLC converters could effectively reduce the loss factors by properly operating the mode of switching operations. In [26] was designed a power loss models with the LLC converter for optimally improving the level of system accuracy. Here, the time domain modelling could be adopted with this controlling strategy for obtaining increased power conversion efficiency. In [27] was provided the detailed overview about the design of LLC converters based on the synchronous rectification and power loss breakdown analysis. The key contribution of this work was to minimize the effect of duty loss by using the noise filtering circuit and the inclusion of phase compensation unit. In addition to that, the adaptive turnoff algorithm could be used to maximize the conduction time and to improve the performance of high speed digital controller. The different types of loss factors discussed in this work were copper loss, switching loss, core loss, diode and MOSFET conduction loss.

In [28] was developed a rotating coordinate system using the LLC resonant converter topology for obtaining the improved output dynamics. This paper discussed about the key benefits of using the LLC converter design, which includes high power density, better power conversion efficacy, minimal switching loss and increased switching frequency. Moreover, the state space analysis model was utilized for improving the design of LLC converter. In [29] was utilized the first harmonic approximation model with the H-bridge LLC converter for enhancing the stability and reliability of power conversion under varying load conditions. For this converter design, the MOSFET switching device was utilized to reduce both the voltage ripples and switching harmonics. The major benefit of this work was better system efficiency, stabilized output voltage, and minimal loss. In [30] was utilized a resonant LLC converter for obtaining an increased voltage gain. The main purpose of this work was to increase the gain of output voltage according to the quality factor, primary inductance, and secondary inductance value. Moreover, this circuit design was highly depends on the minimum and maximum voltage range. However, it limits with the major problems of increased error output, high harmonic contents, and complex design.

In [31] was developed a two stage LLC converter with SiC-MOSFET switching components for obtaining an increased voltage gain. Also, it objects to optimize the entire performance of converter with ensured peak efficiency and reduced harmonics. In [32] was implemented a voltage quadrupler rectifier incorporated with LLC converter for efficiently regulating the output voltage and improving the switching frequency. This work stated that the LLC converter could efficiently reduce the conduction and switching losses with normalized frequency outputs. In [33] was employed a power loss estimation model with LLC-MOSFET converter topology for efficiently minimizing the body diode, switching, and conduction losses. However, it limits with the issues of high controlling complexity, increased average error rate, and reduced power efficiency. In [34] was introduced a GaN based LCCL-LC controlling topology for improving the ability of fault ride through, improving the voltage regulation, and power density. Also, a multi-objective optimization methodology was utilized in this paper for designing the power transformer with reduced core and volume losses. In [35] was employed a multi-mode controlling strategy for enhancing the power conversion efficiency and density factors. The different types of factors mainly concentrated on this work were conduction loss, switching loss, driving loss, magnetic loss, and breakdown loss. It also intends to enhance the operating performance of controller under varying load conditions.

In [36] was introduced a medium voltage series resonant converter with SiC-MOSFET switching devices for solving the voltage imbalance issues. The key factor of this work was to design a new converter with reduced switching and conductance loss factors. In addition to that, it highly concentrated on protecting the circuit from over voltage, over current and over temperature issues. The main advantages of this work were regulated output voltage, reduced switching loss, and error output. Yet, it has the problems of high complexity in circuit design, inefficient output gain, and reduced power factor. In [37] was deployed a voltage sharing control scheme with the closed loop DC-DC converter for improving the voltage conversion efficiency of power systems. Here, the importance of using SiC-MOSFET switches have been discussed with respect to the parameters of voltage and current. Though, the major limitation of this work was reduced level of efficiency, which degrades the performance of entire system.

From this review, it is analyzed that the existing works are mainly concentrating on improving the voltage gain, regulation, and operating performance of the power system with reduced loss of factors by using the different types of converters and controlling techniques. But it facing the major problems of increased error outputs, high controlling complexity, harmonics distortions, and reduced switching frequencies. Hence, the proposed work intends to implement an LLC DC-DC converter with SiC-MOSFET switching devices and intelligent controlling technique for optimally improving the overall performance of system with reduced complexity.

3. Proposed methodology. This sector presents the clear description about the proposed converter and controlling scheme used for regulating the output voltage of the DC source with its equivalent circuit representations and algorithms.

The **goal** of this work is to obtain the improved voltage gain output with reduced loss factors and harmonic distortions. For this purpose, an advanced DC-DC converter and controlling techniques are developed, and the novel contribution of the proposed work is to design an intelligent NASC with the LLC resonant – SiC MOSFET DC-DC converter for controlling the speed of BLDC motor with improved voltage gain outputs.

The overall flow of the proposed model is depicted in Fig. 1, and its equivalent circuit representation is shown in Fig. 2.

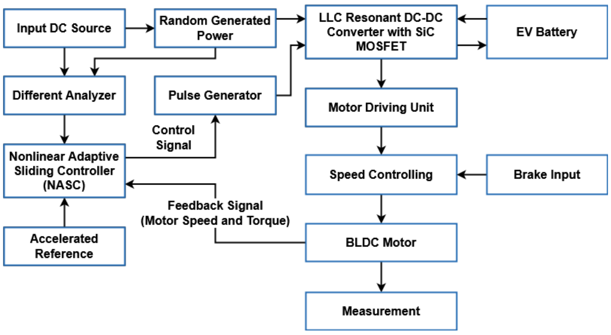

Fig. 1. Flow of the proposed LLC resonant with SiC-MOSFET and NASC controlling model

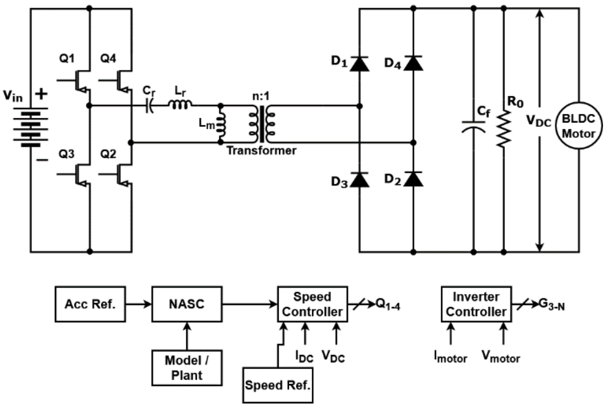

Fig. 2. Overall schematic representation

Typically, the power generated from the input DC source is an unregulated form, which must be regulated before giving it into the output load. Hence, the LLC resonant DC-DC converter incorporated with silicon carbide SiC-MOSFET switching devices are utilized in this model, which properly actuating the operating modes of switching components for boosting the voltage fed to the BLDC motor driving system. For efficiently generating the controlling signals to operate the switches of converter, the novel NASC controller scheme is developed in this work. It obtains the inputs of feedback signals from BLDC motor, accelerated reference, and output of different analyzer for generating the controlling signals with the help of pulse generator. Based on the generated controlling pulses, the LLC resonant converter can be operated for providing the maximum gain outputs to the motor driving system. The key benefits of this work are as follows: minimized controlling complexity, increased and regulated voltage gain output, minimal switching loss, conduction loss and harmonic contents.

A) LLC resonant – SiC MOSFET DC-DC converter. Conventionally, there are different types of resonant DC-DC converters are utilized for improving the voltage gain outputs, which includes the types of series resonant, parallel resonant and series-parallel resonant. In which, the LLC resonant DC-DC converter is widely used in different power application systems, due to its enormous benefits like simple designing, minimal losses, high operating efficiency, and increased voltage support. When compared to the Si-MOSFET switches, the SiC-MOSFET switches are the most option for designing the

LLC resonant converter, because it has the ability to operate under high switching frequencies with high efficiency. Also, the SiC-MOSFET switches are small in size, and it does not require any cooling necessities. Due to these facts, the proposed work intends to utilize the LLC resonant converter incorporated with the SiC-MOSFET switching devices for improving the efficiency and performance of BLDC motor system, and its equivalent circuit models are depicted in Fig 3,*a*,*b*.

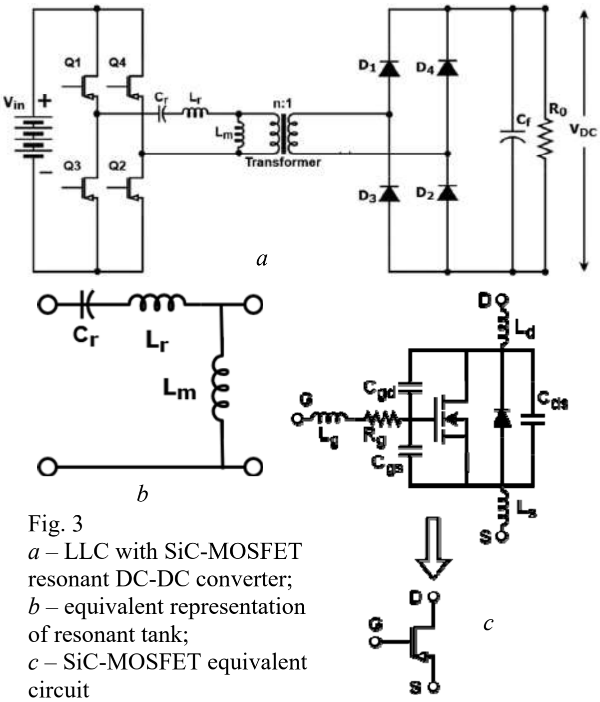

Fig. 3
a – LLC with SiC-MOSFET resonant DC-DC converter;
b – equivalent representation of resonant tank;
c – SiC-MOSFET equivalent circuit

As shown in Fig. 3,*c* the transfer function of SiC-MOSFET is determined as follows:

$$G(s)=\frac{\dfrac{1}{L_g\cdot C_{gg}}}{s^2+\dfrac{s\cdot R_g}{L_g}+\dfrac{1}{L_g\cdot C_{gg}}}, \qquad (1)$$

where s is the step signal; C_{gg} is the gate parallel capacitance; L_g is the line parasitic inductance; C_{gs} is the gate source capacitance; C_{gd} is the drain capacitance; R_g is the drive resistance.

The power for unit step $U_g(s)$ can be derived as:

$$U_g(s)=U_g/s\,. \qquad (2)$$

Consequently, the damping ratio is computed as follows:

$$\xi=\frac{R_g}{2}\cdot\sqrt{\frac{C_{gg}}{L_g}}\,. \qquad (3)$$

In this work the full-bridge LLC-SiC MOSFET DC-DC converter is mainly used to increase the voltage gain output with reduced harmonics fed to BLDC motor system. Typically, the LLC is a kind of the resonant converter that comprises the elements of inductors (L_r and L_m), capacitor (C_r), diodes (D_1 to D_4), and SiC-MOSFET switches (Q1 to Q4), and its equivalent circuit topology is shown in Fig. 3,*a*. In this model, there are 2 resonant frequencies have been gained with the combination of inductor L_r and capacitor C_r, and inductors (L_r, L_m) and capacitor (C_r), which are in the form of series arrangement. Then the frequencies of full bridge LLC resonant converter are estimated as follows:

$$f_{r1}=\frac{1}{2\pi\sqrt{L_r\cdot C_r}}\,; \qquad (4)$$

$$f_{r2}=\frac{1}{2\pi\sqrt{(L_r+L_m)\cdot C_r}}\,. \qquad (5)$$

The LLC resonant DC-DC converter's equivalent circuit mode of operations as 0 and 1 are illustrated in Fig. 4,*a*,*b*.

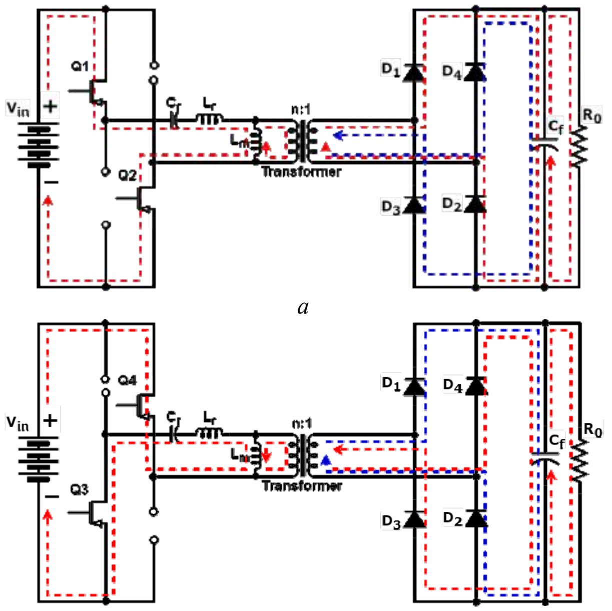

Fig. 4. *a* – operation mode 1 (Q1 & Q2 ON and Q3 & Q4 OFF);
b – operation mode 2 (Q1 & Q2 OFF and Q3 & Q4 ON)

Since, the LLC converter is working based on the functionality of inverter circuit at the input side of transformer. The switches Q1 and Q2 are turned ON and Q3 and A4 are turned off as shown in Fig. 4,*a*. This makes the capacitor C_r and the inductors L_r and L_m to charge up to the rated voltage, where the flow of current passes through the transformer. Then, the converter along with capacitor C_f to bypass the AC ripples, which provides the desired DC voltage at the load side.

In mode 2, the switches Q1 and Q2 are in OFF state and Q3 and Q4 are in ON state. At this time, the reverse current passes through the capacitor C_r and inductors L_r and L_m. This reverse flow of current also passes through the transformer and rectifier circuit. Since, this is a full bridge rectifier, hence it provides the constant DC voltage at the load side with C_f capacitor.

As shown in Fig. 5, the resonance induction ratio of RI_r and quality factor QF_L of the LLC resonant converter are calculated as follows:

$$RI_r=L_r/L_m\,; \qquad (6)$$

$$QF_L=R_i\cdot\sqrt{\frac{C_r}{L_r+L_m}}\,. \qquad (7)$$

According to the Kirchhoff's laws the output voltage and current are estimated as follows:

$$V_{ab}=i\cdot\left(A_{C_r}+A_{L_r}+A_{L_m}\right)-i_R\cdot X_{L_m}\,; \qquad (8)$$

$$i_R = \frac{i \cdot A_{L_m}}{\left(R_i + X_{L_m}\right)};\qquad(9)$$

$$i_R = \frac{n \cdot V_o}{R_i},\qquad(10)$$

where V_{ab} is the AC voltage generated from the inverter circuit of resonant converter; V_o is the output voltage; A is the temporary variable.

Based on (5), (6), the output value is obtained as follows:

$$i = \frac{n \cdot V_o \cdot \left(R_i + X_{L_m}\right)}{R_i \cdot X_{L_m}}.\qquad(11)$$

Finally, the voltage gain of LLC resonant converter is expressed with respect to the ratio of output voltage and input voltage as illustrated in below:

$$\left|\frac{V_o}{V_i}\right| = $$

$$= \frac{1}{2n\sqrt{(1+RI_r)^2 \cdot \left(1-\left(\frac{\delta_L}{\delta}\right)^2\right)^2 + \left(\frac{1}{\delta_L}\right)^2 \cdot \left(\left(\frac{\delta}{\delta_L}\right)\cdot\left(\frac{RI_r}{1+RI_r}\right)-\left(\frac{\delta_L}{\delta}\right)\right)^2}},\qquad(12)$$

where V_i is the input voltage; RI_r is the resonance inductance ratio; δ, δ_L are the second resonant frequencies.

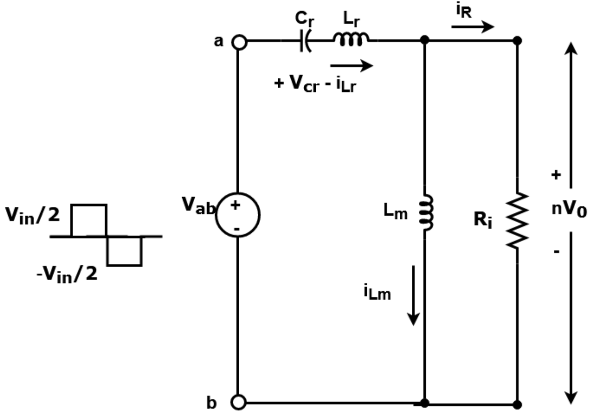

Fig. 5. Design properties of converter

B) Nonlinear adaptive sliding controller. The NASC algorithm is used to generate the controlling signals for operating the switching components of LLC resonant converter. This technique considers the inputs of converter parameters like duty cycle, feedback DC voltage, DC current, and gain parameters of SiC-MOSFET, and it produced output as the best selection of gain parameters. At first, the gain parameters are initialized with the maximum limits as indicated by K_p(max) and K_i(max), and the pitch ratio and harmonic limits are also initialized with the time instant. Then, the loop has been executed until reaching the maximum of iterations and number of decision parameter, where the random values are initialized as $r_1 = 1$ and $r_2 = 1$. If the harmonic rate (HR) is greater than the random value r_1, the gain parameters of K_p and K_i are updated as shown in below:

$$k_s = \left\lfloor k_p', k_i' \right\rfloor.\qquad(13)$$

Similar to that, of the pitch ratio (PR) is greater than the random value r_2, the new gain parameter is updated as represented below:

$$k_s' = \left\lfloor \left(k_p' + \text{rand}\right), \left(k_i' + \text{rand}\right) \right\rfloor.\qquad(14)$$

Otherwise, the new value is selected for updating the gain parameter, which is estimated as follows:

$$k_s' = \text{rand} \times \left[\left(k_s(\text{upper}) - k_s(\text{lower})\right) + k_s(\text{lower})\right].\qquad(15)$$

Then, the convergence function is validated and the gain parameters are updated based on its maximum value, which is represented as follows:

$$k_s' = k_s(i+1);\qquad(16)$$

$$k_s' = k_s(i).\qquad(17)$$

Finally, the best selection of gain parameters are derived as indicated below:

$$K_p' = k_s(t)[0].\qquad(18)$$

$$K_i' = k_s(t)[1].\qquad(19)$$

Based on this value, the controlling pulses p' are generated and given to the converter for operating the switches to obtain the increased voltage output:

Algorithm: NASC controlling algorithm

```
Input: converter parameters (duty cycle, feedback DC voltage and current, gain parameter of SiC MOSFET)
Output: best selection of $K_p$, and $K_i$
Initialize gain parameters $K$ and $K_{max}$ and the maximum limit of $K_p$(max) and $K_i$(max) as $Z(k)$,
where $k_n \in K_n$, $\forall n = \{1, 2, ..., t\}$,
«t» – time instant / sample time.
initialize pitch ratio (PR), and harmonic rate (HR).
while ($i \le$ Max_iter), Do // Loop running for maximum number of iteration.
    while ($j \le N$), Do // Loop running for number of decision parameter ($N$).
        $r_1$ = rand(1); $r_2$ = rand(1) // Initialize random value for gain parameter.
        If ($r_1 \le$ HR), then
            Update the gain parameter of $k_p$ and $k_i$ by using (13);
            If ($r_2 \le$ PR), then
                Update the new gain parameter using (14);
            End if
        Else
            Select new value of gain parameters by using (15);
        End if
    End «j» loop
    Check for convergence function $F(t)^i$
    If $F(t)^{i+1} < F(t)^i$, then
        Compute $k'_s$ by using (16);
    Else
        Compute $k'_s$ by using (17);
    End if
End «i» loop
Select $K_p$, and $K_i$ as shown in (18) and (19) respectively;
Generate the pulse $p'$ according to the gain parameters.
```

Finally, the generated high voltage DC output is fed to the BLDC motor driving system for improving its performance in terms of high torque and speed. The BLDC motor is a kind of synchronous motor system, which is widely used in many real time application systems like electric vehicles, automation industries, and medical sector. The major advantages of using the BLDC motor are fast dynamic response, increased speed and torque, improved operating efficiency, and minimal friction losses. Due to these facts, the proposed work intends to use the BLDC motor as the load unit for providing the increased voltage gain output.

Figure 6 shows the controlling structure of BLDC motor system used in the proposed model, where the magnetic field of both rotor and stator could be maintained at same frequency. For this motor, the DC output voltage is fed by the LLC resonant converter incorporated with SiC-MOSFET, where the DC output is transformed into three phase AC through the inverter circuit.

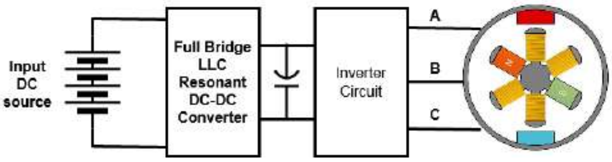

Fig. 6. BLDC driver

4. Results and discussion. This unit discusses about the performance analysis of the proposed controlling scheme by using various evaluation measures. Here, the simulation is performed with the help of MATLAB/Simulink tool, and scope results are illustrated according to the converter and controller circuits. Also, the obtained results are compared with some other recent state-of-the-art models for proving the efficiency and superiority of the proposed model.

A) Simulation analysis. Table 1 presents the performance analysis of the proposed LLC resonant DC-DC converter incorporated with SiC-MOSFET switches with respect to the measures of input voltage, output voltage, efficiency and gain. Based on this evaluation, it is assessed that the output voltage is efficiently increased with enhanced gain and efficiency measures. Because, the proposed NASC scheme could efficiently generating the controlling signals for properly actuating the switching modes of operations, which helps to increase the output voltage with high gain and efficiency values.

Table 1

Performance analysis of LLC resonant DC-DC converter

S. No	Input voltage, V	Output voltage, V	Gain	Efficiency, %
1	100	20.23	–11.68	50.2
2	200	38.66	–11.53	52.6
3	300	58.36	–11.25	53.5

Figure 7 shows the DC voltage obtained the DC input source with respect to varying time samples. This analysis shows that the minimum amount of voltage has been obtained from the DC source, which is in the form of unregulated voltage. So, it is efficiently regulated by using the LLC resonant converter in order to meet the requirements of BLDC motor. Consequently, the output DC voltage gain obtained from the converter is shown in Fig. 8 with respect to different time samples. This analysis proved that the obtained input voltage has been efficiently improved by using the DC-DC converter. Then, it can be fed to the BLDC motor driver system for controlling the speed with increased efficiency.

Figures 9, 10 show the output current of capacitor (C_f and C_r) with respect to corresponding varying time samples. Similarly, the current at inductor (I_r) is depicted under varying time sequences as depicted in Fig. 11, and final DC output current is shown in Fig. 12. The obtained results depict that the capacitor current could be effectively controlled by properly operating the switching components.

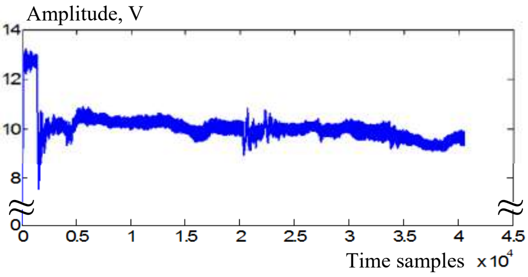

Fig. 7. DC voltage from input source

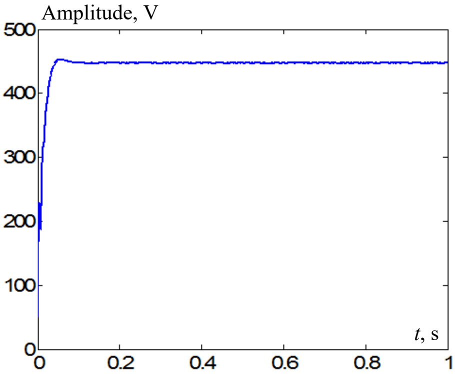

Fig. 8. Output DC voltage obtained from converter

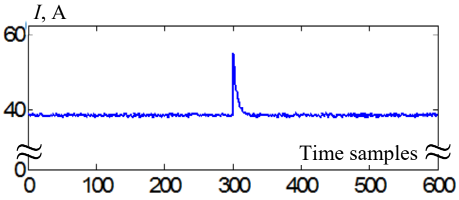

Fig. 9. Current at capacitor (C_f)

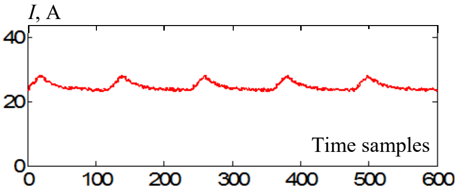

Fig. 10. Current at capacitor (C_r)

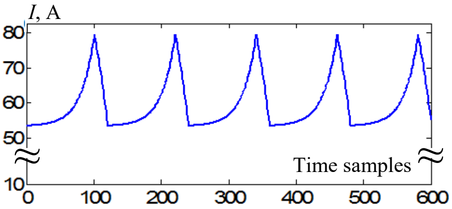

Fig. 11. Current at inductor (L_r)

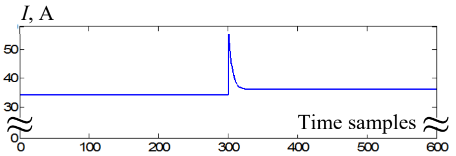

Fig. 12. DC current

Figure 13 illustrates the stator current of BLDC motor, and the results stated that the current is efficiently maintained under varying time instances. Also, the obtained results prove the improved performance and efficiency of the proposed converter and controlling scheme. Then, the generated gate pulses given to the converter by controlling unit is shown in Fig. 14, where the amplitude in volts is efficiently maintained according to the proper switching operations.

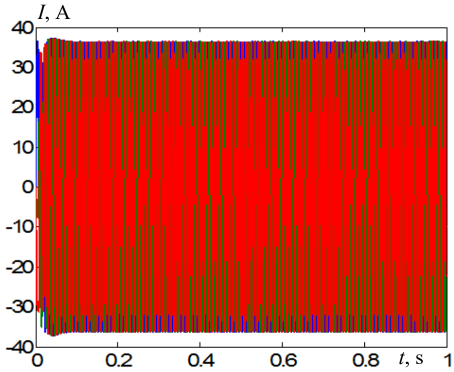

Fig. 13. Motor current

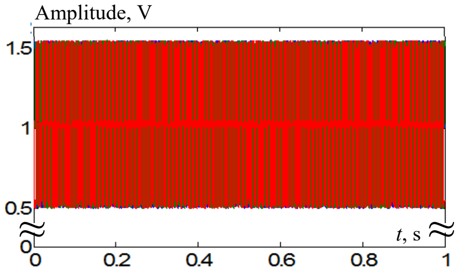

Fig. 14. Gate pulse

Figure 15 represents the step response of converter with respect to the amplitude (V) and time (s), and the generated waveform indicates that the time behavior characteristic of the proposed model is efficiently balanced with 0.5 V to 1 V.

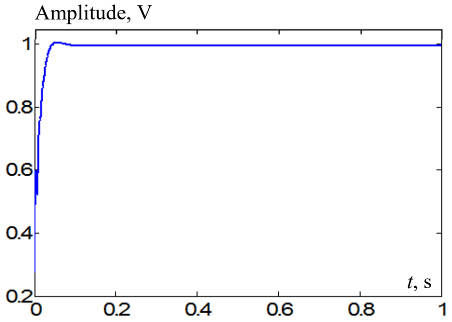

Fig. 15. Step response

Figure 16,*a*,*b* shows the motor speed and torque of the proposed LLC resonant integrated with NASC controlling mechanism with respect to varying time measures in terms of seconds correspondingly. Generally, the speed of motor drive system is highly depends on the generated switching pulses of controller. Also, controlling the speed of BLDC motor is more essential for driving the system at the required speed. The increased speed of motor is mainly correlated with the high gain voltage output generated by the converter. From this analysis, it is visibly perceived that the speed of BLDC motor is improved around 1500 rpm with increased voltage gain.

Figure 17 shows the overall efficiency analysis of the proposed LLC resonant with NASC scheme with respect to different time samples. Here, the efficiency of BLDC motor controlling is highly improved with the help of LLC resonant SiC MOSFET converter and NASC controlling technique. Since, it generates the regulated output voltage with high gain and reduced losses, which ensures the increased efficiency and optimal performance of the proposed system. Moreover, the THD analysis of the proposed scheme is validated according to the fundamental frequency. Due to the increased efficiency, high voltage gain output, and reduced losses, the THD level of the proposed converter and controlling scheme is competently reduced as shown in Fig. 18.

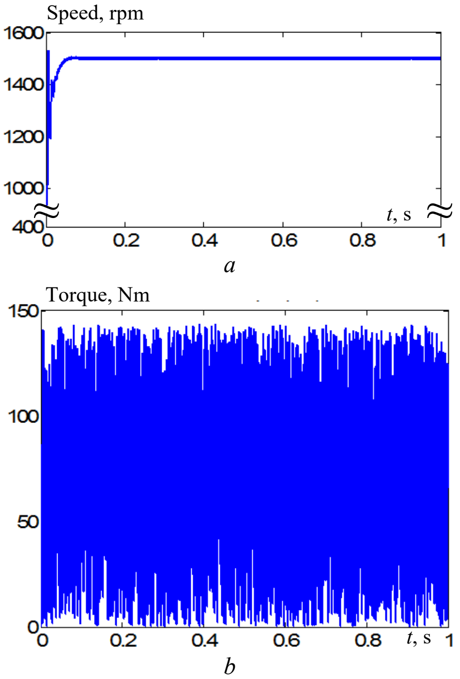

a

b

Fig. 16. *a* – motor speed; *b* – motor torque

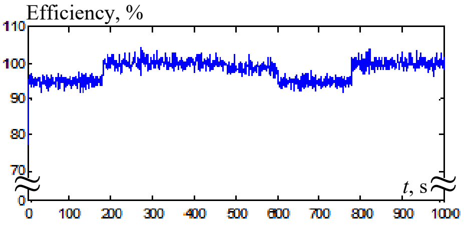

Fig. 17. Efficiency analysis

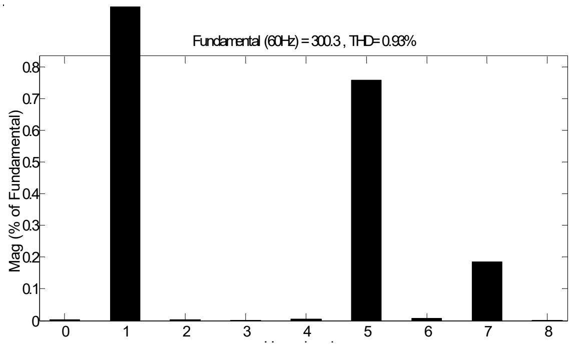

Fig. 18. THD analysis

C) Comparative analysis. Figure 19 compares the DC voltage gain of both conventional [38] and proposed converters under different duty cycles, which includes the topologies of step up DC-DC, multi-input DC-DC, boost DC-DC, and interleaved resonant PWM high step-up (IRPHS) DC-DC. In addition to that, the efficiency of converter is highly depends on the voltage gain output. Based on this evaluation, it is perceived that the voltage gain characteristics of the proposed LLC resonant – SiC MOSFET DC-DC converter is highly improved, when compared to the other converters. Moreover, the increased voltage gain of converter ensures the reduced conduction and switching losses of circuitry.

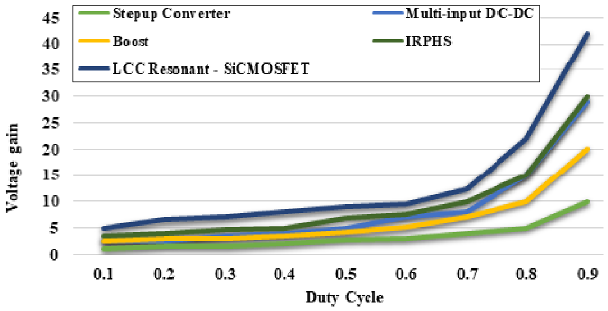

Fig. 19. Comparative analysis between various DC-DC converters based on the voltage gain

Consequently, the efficiency of existing IRPHS DC-DC and proposed LLC resonant – SiC MOSFET DC-DC converters are compared with respect to the output power as shown in Fig. 20. Due to the proper controlling of switching devices used in the converter, the efficiency of proposed converter has been highly improved under all output power values. The obtained results indicated that the proposed model achieved increased power conversion efficiency over the other technique.

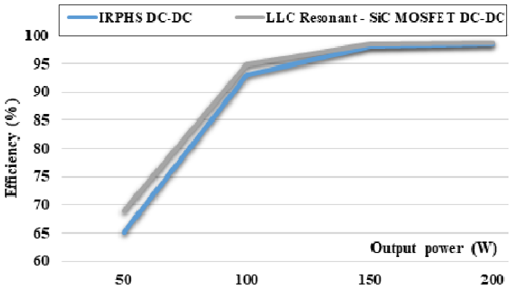

Fig. 20. Efficiency of existing and proposed converters

Figure 21 evaluates the voltage peak, settling time, and output voltage of the conventional [39] and proposed controlling techniques, in which the peak overshoot is estimated by analyzing that how much the level of peak value is increased compared to the steady state. Similarly, the settling time is defined as the amount of time of taken by the system for converging into the steady state. Based on this evaluation, it is analyzed that the voltage peak and settling time of the proposed model is efficiently reduced, and the output voltage is highly increased, when compared to the other controlling techniques. These results prove the improved performance and efficacy of the proposed technique over the other existing techniques.

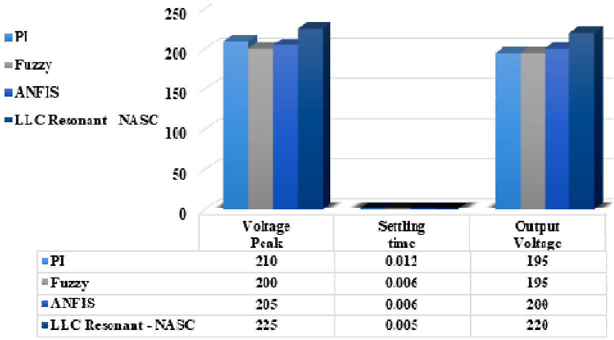

	Voltage Peak	Settling time	Output Voltage
PI	210	0.012	195
Fuzzy	200	0.006	195
ANFIS	205	0.006	200
LLC Resonant - NASC	225	0.005	220

Fig. 21. Voltage peak, settling time and output voltage of existing and proposed controlling techniques

The rise time, peak time and peak value of the conventional controllers in [40] was proposed NASC controller are compared as shown in Table 2. When compared to these controlling mechanisms, the rise time, peak time and peak value of the proposed scheme is efficiently reduced based on the best selection of parameters for generating the controlling pulses. Moreover, the reduced time consumption ensures the improved performance of entire power conversion system.

Table 2

Comparative analysis based on time response

Controllers	Rise time, s	Peak time, s	Peak value, rpm
Anti-windup PID	0.4391	0.9987	1519.8
FLC	0.4024	0.9989	1517.1
Neuro-Fuzzy 1	0.4069	0.9981	1502.7
Neuro-Fuzzy 2	0.4121	1.0024	1500.6
BAT	0.4120	1.0009	1501
FPA	0.3785	1.0007	1500.7
Sugeno Fuzzy PID	0.3351	0.9971	1500
Proposed NASC	0.3245	0.9899	1500

Table 3 and Fig. 22 compare the time efficiency of conventional and proposed controlling techniques based on the parameters of peak overshoot, settling time, and steady state error. The obtained results proved that the proposed controlling technique provides the minimized peak overshoot, settling time, and steady state error, when compared to the other controlling schemes. Because, the power conversion efficiency of the proposed system is highly enhanced with reduced losses by selecting the optimal parameters for controlling the operating modes of switches. It helps to improve the system performance under varying load conditions with reduced error outputs.

Table 3

Comparative analysis of existing and proposed controlling schemes based on peak overshoot, settling time, and steady state error

Controllers	Peak overshoot, %	Settling time, s	Steady state error, %
Anti-windup PID	0.4963	0.6958	0.6391
FLC	0.1654	0.6549	0.6887
Neuro-Fuzzy 1	0.2334	0.6690	0.1749
Neuro-Fuzzy 2	0.2201	0.6664	0.3259
BAT	0.2200	0.6671	0.0647
FPA	0.0792	0.6243	0.0100
Sugeno Fuzzy PID	0.0216	0.5695	0.0061
Proposed NASC	0.0211	0.5280	0.0058

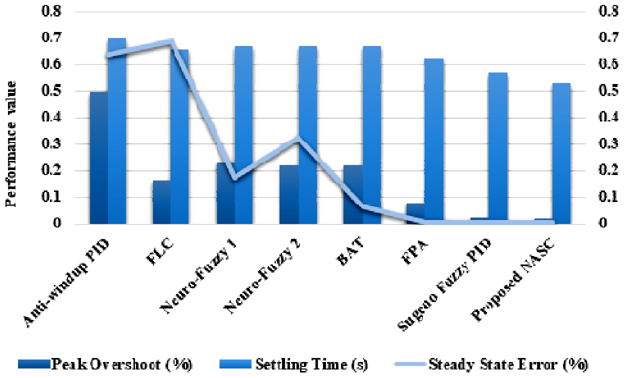

Fig. 22. Analysis of peak overshoot, settling time and steady state error

5. Future scope. As the future progresses, nonlinear adaptive sliding controllers will be replaced by genetic algorithms, neurofuzzy algorithms, or artificial intelligence systems. Additionally, SiC MOSFETs can be investigated in terms of their thermal resistance using the ON state voltage drop as a temperature-sensitive electrical parameter.

Conclusions. This paper developed an enhanced converter and controlling methodology for controlling the speed and improving the performance of brushless DC motor. For this purpose, the LLC resonant DC-DC converter incorporated with silicon carbide MOSFET switching device has been used for improving the voltage gain outputs with reduced harmonic distortions. Here, the main reason of using the silicon carbide MOSFET switching components are increased power outputs, reduced switching stress, fast dynamic response, and minimized ripples. Here, the novel nonlinear adaptive sliding controller mechanism is implemented to improve the efficiency and controlling performance of brushless DC motor with reduced conduction and switching losses. Also, it helps to obtain the increased switching frequency, reduced error rate and optimal performance results by properly generating the controlling signals in order to perform the mode of converter operations. For this operation, it acquires the input feedback signal, accelerated reference, and output of different analyzer for generating the controlling signals with the help of pulse generator. Then, it produced the best gain parameters as the output, which is used to generate the controlling signals. Finally, the obtained high gain voltage output is fed to the brushless DC motor system with reduced harmonics and losses. During simulation, the performance of conventional and proposed controlling topologies are validated and compared by using various evaluation measures. Based on the obtained results, it is evident that the proposed LLC resonant silicon carbide MOSFET incorporated with nonlinear adaptive sliding controller controlling scheme provided the better performance results over the other state-of-the-art models, which includes reduced error rate, peak overshoot, settling time, rise time and increased power conversion efficiency.

Conflict of interest. The authors of the paper state that there is no conflict of interest.

REFERENCES

1. Mukherjee S., Kumar A., Chakraborty S. Comparison of DAB and LLC DC–DC Converters in High-Step-Down Fixed-Conversion-Ratio (DCX) Applications. *IEEE Transactions on Power Electronics*, 2021, vol. 36, no. 4, pp. 4383-4398. doi: https://doi.org/10.1109/TPEL.2020.3019796.

2. Kumar G.K., Elangovan D. Review on fault-diagnosis and fault-tolerance for DC–DC converters. *IET Power Electronics*, 2020, vol. 13, no. 1, pp. 1-13. doi: https://doi.org/10.1049/iet-pel.2019.0672.

3. Jassim B.M., Jassim H. Modelling of a solar array simulator-based on multiple DC-DC converters. *International Journal of Renewable Energy Research*, 2018, vol. 8, no. 2, pp. 1038-1044. doi: https://doi.org/10.20508/ijrer.v8i2.6916.g7412.

4. Guan Y., Cecati C., Alonso J.M., Zhang Z. Review of High-Frequency High-Voltage-Conversion-Ratio DC–DC Converters. *IEEE Journal of Emerging and Selected Topics in Industrial Electronics*, 2021, vol. 2, no. 4, pp. 374-389. doi: https://doi.org/10.1109/JESTIE.2021.3051554.

5. Nie H., Bai Y., Cheng Q., Scott M.J. Evaluation of Conducted EMI in GaN and Si based Isolated DC/DC Converters. *2019 IEEE 7th Workshop on Wide Bandgap Power Devices and Applications (WiPDA)*, 2019, pp. 251-254. doi: https://doi.org/10.1109/WiPDA46397.2019.8998788.

6. Zhou X., Sheng B., Liu W., Chen Y., Wang L., Liu Y.-F., Sen P.C. A High-Efficiency High-Power-Density On-Board Low-Voltage DC–DC Converter for Electric Vehicles Application. *IEEE Transactions on Power Electronics*, 2021, vol. 36, no. 11, pp. 12781–12794. doi: https://doi.org/10.1109/TPEL.2021.3076773.

7. Salem M., Ramachandaramurthy V.K., Jusoh A., Padmanaban S., Kamarol M., Teh J., Ishak D. Three-Phase Series Resonant DC-DC Boost Converter With Double LLC Resonant Tanks and Variable Frequency Control. *IEEE Access*, 2020, vol. 8, pp. 22386-22399. doi: https://doi.org/10.1109/ACCESS.2020.2969546.

8. Rouzbehi K., Miranian A., Escaño J.M., Rakhshani E., Shariati N., Pouresmaeil E. A Data-Driven Based Voltage Control Strategy for DC-DC Converters: Application to DC Microgrid. *Electronics*, 2019, vol. 8, no. 5, p. 493. doi: https://doi.org/10.3390/electronics8050493.

9. Dhanalakshmi R., Usha Rani P. A Review on Two-Stage Back End DC-DC Converters in On-Board Battery Charger for Electric Vehicle. *International Journal of Renewable Energy Research*, 2020, vol. 10, no. 4. pp. 1685-1695. doi: https://doi.org/10.20508/ijrer.v10i4.11181.g8054.

10. Yang X., Cheng Zhang Y., Wen P., Liu Y., Zheng T.Q., Takaku T., Igarashi S. Improved Phase Shift Control for SiC-MOSFET Based Resonant Switched-Capacitor Converter With Parasitics Consideration. *IEEE Transactions on Industry Applications*, 2020, vol. 56, no. 4, pp. 3995-4006. doi: https://doi.org/10.1109/TIA.2020.2989389.

11. Manikandan R., Raja Singh R., Edison G., Gnanaraj S.D. Hardware-in-Loop-Based Reliability Improvement of Power Converter for Critical Electrical Drive Applications. In: Priyadarshi N., Bhoi A.K., Bansal R.C., Kalam A. (eds) *DC-DC Converters for Future Renewable Energy Systems. Energy Systems in Electrical Engineering*, 2022, Springer, Singapore. doi: https://doi.org/10.1007/978-981-16-4388-0_14.

12. Kawa A., Stala R. SiC-Based Bidirectional Multilevel High-Voltage Gain Switched-Capacitor Resonant Converter with Improved Efficiency. *Energies*, 2020, vol. 13, no. 10, p. 2445. doi: https://doi.org/10.3390/en13102445.

13. Monopoli V.G., Sidella P., Cupertino F. A Si-IGBT-Based Solution to Drive High-Speed Electrical Machines. *IEEE Transactions on Industry Applications*, 2019, vol. 55, no. 5, pp. 4900-4909. doi: https://doi.org/10.1109/TIA.2019.2919821.

14. Nakahara M., Kawaguchi Y., Furukawa K., Kadota M., Mabuchi Y., Kanoda A. Development of a Control Method for LLC Converter Utilized for Input-Parallel-Output-Series Inverter System with Solid-State Transformers. *IEEJ Journal of Industry Applications*, 2019, vol. 8, no. 4, pp. 652-659. doi: https://doi.org/10.1541/ieejjia.8.652.

15. Frivaldský I.M., Drgoňa P., Špánik P. Experimental analysis and optimization of key parameters of ZVS mode and its application in the proposed LLC converter designed for distributed power system application. *International Journal of Electrical Power & Energy Systems*, 2013, vol. 47, pp. 448-456. doi: https://doi.org/10.1016/j.ijepes.2012.11.016.

16. Chakraborty S., Vu H.-N., Hasan M.M., Tran D.-D., Baghdadi M.El, Hegazy O. DC-DC Converter Topologies for Electric Vehicles, Plug-in Hybrid Electric Vehicles and Fast Charging Stations: State of the Art and Future Trends. *Energies*, 2019, vol. 12, no. 8, p. 1569. doi: https://doi.org/10.3390/en12081569.

17. Li Y., Liang M., Chen J., Zheng T.Q., Guo H. A Low Gate Turn-OFF Impedance Driver for Suppressing Crosstalk of SiC MOSFET Based on Different Discrete Packages. *IEEE Journal of Emerging and Selected Topics in Power Electronics*, 2019, vol. 7, no. 1, pp. 353-365. doi: https://doi.org/10.1109/JESTPE.2018.2877968.

18. Rahul Charles C.M., Savier J.S. Bidirectional DC-DC Converter Fed BLDC Motor in Electric Vehicle. *2021 International Conference on Advances in Electrical, Computing, Communication and Sustainable Technologies (ICAECT)*, 2021, pp. 1-6. doi: https://doi.org/10.1109/ICAECT49130.2021.9392394.

19. Darcy Gnana Jegha A., Subathra M.S.P., Manoj Kumar N., Subramaniam U., Padmanaban S. A High Gain DC-DC Converter with Grey Wolf Optimizer Based MPPT Algorithm for PV Fed BLDC Motor Drive. *Applied Sciences*, 2020, vol. 10, no. 8, p. 2797. doi: https://doi.org/10.3390/app10082797.

20. Nikhila M., Saritha E. Solar PV fed Common Grounded Z-Source DC-DC Converter based BLDC Motor Drive. *In proceedings of the International Conference on Systems, Energy & Environment (ICSEE) 2019*, GCE Kannur, Kerala, July 2019, doi: https://doi.org/10.2139/ssrn.3447745.

21. Dineshkumar S., Sachinamreiss G. Control and optimal design of DC – DC converter of electric vehicle fed by BLDC motor drive. *International Journal of Recent Technology and Engineering*, 2019, vol. 8, no. 1, pp. 1557-1560. Available at: https://www.ijrte.org/wp-content/uploads/papers/v8i1/A1115058119.pdf (accessed 11 May 2021).

22. Karthikeyan B., Kalyanasundaram V., Vidyasagar S., Sundararaju K., Palanisamy R. FFNN based MPPT controller for PEMFC powered non-isolated high gain DC-DC converter with SPWM inverter fed BLDC motor. *IOP Conference Series: Materials Science and Engineering*, 2021, vol. 1055, no. 1, p. 012147. doi: https://doi.org/10.1088/1757-899X/1055/1/012147.

23. Riczeena Jose, Santhi B. Simulation of Pulse Amplitude Modulation based Voltage Control Technique for the Speed Control of BLDC Motor using Class-E Load Resonant Converter. *International Journal of Engineering Research & Technology*, 2015, vol. 4, no. 9, pp. 516-518. doi: https://doi.org/10.17577/IJERTV4IS090593.

24. Shen Y., Wang H., Al-Durra A., Qin Z., Blaabjerg F. A Structure-Reconfigurable Series Resonant DC–DC Converter With Wide-Input and Configurable-Output Voltages. *IEEE Transactions on Industry Applications*, 2019, vol. 55, no. 2, pp. 1752-1764. doi: https://doi.org/10.1109/TIA.2018.2883263.

25. Chen G., Li H., Sun X., Zhou J., Bai L. Analysis and design of LLC converter based on SiC MOSFET. *2018 13th IEEE Conference on Industrial Electronics and Applications (ICIEA)*, 2018, pp. 1443-1448. doi: https://doi.org/10.1109/ICIEA.2018.8397936.

26. Wei Y., Mantooth A. Experimental Validations of the SiC MOSFET based LLC Converter Circuit and Power Loss Models. *2021 IEEE 8th Workshop on Wide Bandgap Power Devices and Applications (WiPDA)*, 2021, pp. 322-327. doi: https://doi.org/10.1109/WiPDA49284.2021.9645112.

27. Wei Y., Luo Q., Mantooth H.A. Synchronous Rectification for LLC Resonant Converter: An Overview. *IEEE Transactions on Power Electronics*, 2021, vol. 36, no. 6, pp. 7264-7280. doi: https://doi.org/10.1109/TPEL.2020.3040603.

28. Cao S., Zhang Y., Zheng C. High Efficiency LLC Converter Design Using a novel Modelling Method based on SiC MOSFET. *2019 22nd International Conference on Electrical Machines and Systems (ICEMS)*, 2019, pp. 1-5. doi: https://doi.org/10.1109/ICEMS.2019.8921615.

29. Han P., He X., Ren H., Zhao Z., Peng X. Research on High Efficiency LLC DC-DC Converter Based on SiC MosFet. *2018 International Power Electronics Conference (IPEC-Niigata 2018 - ECCE Asia)*, 2018, pp. 2714-2717. doi: https://doi.org/10.23919/IPEC.2018.8507508.

30. Dimitrov B., Sharkh S., Cruden A., Balabozov I. Implementation of a DC current sensing transformer with H-bridge MOSFET rectifier in a resonant LLC converter. *2018 20th International Symposium on Electrical Apparatus and Technologies (SIELA)*, 2018, pp. 1-4. doi: https://doi.org/10.1109/SIELA.2018.8447120.

31. Wang F., Wang X., Ruan X. An Optimal Design Scheme of Intermediate Bus Voltage for two-stage LLC Resonant Converter Based on SiC MOSFET. *2021 IEEE Workshop on Wide Bandgap Power Devices and Applications in Asia (WiPDA Asia)*, 2021, pp. 488-492. doi: https://doi.org/10.1109/WiPDAAsia51810.2021.9655998.

32. Shang M., Wang H. A Voltage Quadrupler Rectifier Based Pulsewidth Modulated LLC Converter With Wide Output Range. *IEEE Transactions on Industry Applications*, 2018, vol. 54, no. 6, pp. 6159-6168. doi: https://doi.org/10.1109/TIA.2018.2850033.

33. Glitz E.S., Ordonez M. MOSFET Power Loss Estimation in LLC Resonant Converters: Time Interval Analysis. *IEEE Transactions on Power Electronics*, 2019, vol. 34, no. 12, pp. 11964-11980. doi: https://doi.org/10.1109/TPEL.2019.2909903.

34. Hu J., Wang J., Burgos R., Wen B., Boroyevich D. High-Density Current-Transformer-Based Gate-Drive Power Supply With Reinforced Isolation for 10-kV SiC MOSFET Modules. *IEEE Journal of Emerging and Selected Topics in Power Electronics*, 2020, vol. 8, no. 3, pp. 2217-2226. doi: https://doi.org/10.1109/JESTPE.2019.2943742.

35. Sha D., Zhang J., Sun T. Multimode Control Strategy for SiC mosfets Based Semi-Dual Active Bridge DC–DC Converter. *IEEE Transactions on Power Electronics*, 2019, vol. 34, no. 6, pp. 5476-5486. doi: https://doi.org/10.1109/TPEL.2018.2866700.

36. Lu Z., Li C., Zhu A., Luo H., Li C., Li W., He X. Medium Voltage Soft-Switching DC/DC Converter With Series-Connected SiC MOSFETs. *IEEE Transactions on Power Electronics*, 2021, vol. 36, no. 2, pp. 1451-1462. doi: https://doi.org/10.1109/TPEL.2020.3007225.

37. Qu L., Zhang D. Input voltage sharing control scheme for input series and output series DC/DC converters using paralleled MOSFETs. *IET Power Electronics*, 2018, vol. 11, no. 2, pp. 382-390. doi: https://doi.org/10.1049/iet-pel.2017.0519.

38. Karthikeyan B., Sundararaju K., Palanisamy R. ANN-Based MPPT Controller for PEM Fuel Cell Energized Interleaved Resonant PWM High Step Up DC-DC Converter with SVPWM Inverter Fed Induction Motor Drive. *Iranian Journal of Science and Technology, Transactions of Electrical Engineering*, 2021, vol. 45, no. 3, pp. 861-877. doi: https://doi.org/10.1007/s40998-021-00413-0.

39. Rajani B., Bapayya Naidu K. Renewable Source DCMicrogrid Connected BLDC Water Pumping System with Adaptive Control Techniques. *2020 4th International Conference on Electronics, Communication and Aerospace Technology (ICECA)*, 2020, pp. 216-222. doi: https://doi.org/10.1109/ICECA49313.2020.9297486.

40. Karuppannan A., Muthusamy M. Wavelet neural learning-based type-2 fuzzy PID controller for speed regulation in BLDC motor. *Neural Computing and Applications*, 2021, vol. 33, no. 20, pp. 13481-13503. doi: https://doi.org/10.1007/s00521-021-05971-2.

Received 06.03.2022
Accepted 26.05.2022
Published 20.07.2022

G. Merlin Suba[1], *Research Scholar,*
M. Kumaresan[1], *Professor,*
[1] Department of Electrical and Electronics Engineering,
Dr. M.G.R Educational and Research Institute,
Maduravoyal, Chennai 600095, Tamil Nadu, India,
e-mail: merlinsubagphd@gmail.com (Corresponding author);
dr.kumaresn09@gmail.com

How to cite this article:

Merlin Suba G., Kumaresan M. Design of LLC resonant converter with silicon carbide MOSFET switches and nonlinear adaptive sliding controller for brushless DC motor system. *Electrical Engineering & Electromechanics*, 2022, no. 4, pp. 34-43. doi: https://doi.org/10.20998/2074-272X.2022.4.05

UDC 621.3 https://doi.org/10.20998/2074-272X.2022.4.06

P. Balakishan, I.A. Chidambaram, M. Manikandan

Improvement of power quality in grid-connected hybrid system with power monitoring and control based on internet of things approach

Purpose. *This article proposes a new control monitoring grid connected hybrid system. The proposed system, improvement of power quality is achieved with internet of things power monitoring approach in solar photovoltaic grid system network.* ***The novelty*** *of the proposed work consists in presenting solar power monitoring and power control based internet of things algorithm, to generate DC voltage and maintain the constant voltage for grid connected hybrid system.* ***Methods.*** *The proposed algorithm which provides sophisticated and cost-effective solution for measuring the fault and as maximum power point tracking assures controlled output and supports the extraction of complete power from the photovoltaic panel.* ***The objective*** *of the work is to monitor and control the grid statistics for reliable and efficient delivery of power to a hybrid power generation system. Internet of things is regarded as a network comprising of electronic embedded devices, physical objects, network connections, and sensors enabling the sensing, analysis, and exchange of data. The proposed control technique strategy is validated using MATLAB/Simulink software and real time implementation to analysis the working performances.* ***Results.*** *The results obtained show that the power quality issue, the proposed system to overcome through monitoring of fault solar panel and improving of power quality. The obtained output from the hybrid system is fed to the grid through a 3ϕ voltage source inverter is more reliable and maintained power quality. The power obtained from the entire hybrid setup is measured by the sensor present in the internet of things-based module. In addition to that, the photovoltaic voltage is improved by a boost converter and optimum reliability is obtained with the adoption of the perturb & observe approach. The challenges in the integration of internet of things – smart grid must be overcome for the network to function efficiently.* ***Originality.*** *Compensation of power quality issues, grid stability and harmonic reduction in distribution network by using photovoltaic based internet of things approach is utilized along with sensor controller.* ***Practical value****. The work concerns a network comprising of electronic embedded devices, physical objects, network connections, and sensors enabling the sensing, analysis, and exchange of data. In this paper, internet of things sensors are installed in various stages of the smart grid in a hybrid photovoltaic – wind system. It tracks and manages network statistics for safe and efficient power delivery. The study is validated by the simulation results based on MATLAB/Simulink software and real time implementation.* References 28, tables 1, figures 22.

Key words: **renewable energy source, photovoltaic system, power quality, internet of things, hybrid grid connected system.**

Мета*. У статті пропонується нова гібридна система управління моніторингом, підключена до мережі. У запропонованій системі покращення якості електроенергії досягається за допомогою підходу Інтернету речей до моніторингу потужності у мережі сонячної фотоелектричної мережі.* ***Новизна*** *запропонованої роботи полягає у поданні алгоритму моніторингу сонячної енергії та управління потужністю, заснованого на Інтернеті речей, для генерації напруги постійного струму та підтримки постійної напруги для гібридної системи, підключеної до мережі.* ***Методи****. Пропонований алгоритм, який забезпечує складне та економічне рішення для вимірювання несправності та відстеження точки максимальної потужності, забезпечує контрольований вихід та підтримує вилучення повної потужності з фотоелектричної панелі.* ***Метою*** *роботи є моніторинг та управління статистикою мережі для надійної та ефективної подачі електроенергії до гібридної системи виробництва електроенергії. Інтернет речей розглядається як мережа, що складається з електронних вбудованих пристроїв, фізичних об'єктів, мережевих підключень та датчиків, що дозволяють сприймати, аналізувати та обмінюватися даними. Запропонована стратегія методу управління перевіряється з використанням програмного забезпечення MATLAB/Simulink та реалізації у режимі реального часу для аналізу робочих характеристик.* ***Результати*** *показують, що запропонована система вирішує проблему якості електроенергії за рахунок моніторингу несправності сонячної панелі та покращення якості електроенергії. Отриманий вихід гібридної системи подається в мережу через інвертор джерела напруги 3ϕ, що є більш надійним і підтримує якість електроенергії. Потужність, отримана від усієї гібридної установки, вимірюється датчиком, що є присутнім у модулі на основі Інтернету речей. На додаток до цього фотогальванічна напруга покращується за допомогою перетворювача, що підвищує, а оптимальна надійність досягається за рахунок застосування підходу «збурюй і спостерігай». Щоб мережа функціонувала ефективно, необхідно вирішити проблеми інтеграції Інтернету речей – смарт-мереж.* ***Оригінальність****. Поряд із сенсорним контролером використовується компенсація проблем з якістю електроенергії, стабільністю мережі та зменшенням гармонік у розподільній мережі з використанням підходу до Інтернету речей на основі фотоелектричних систем.* ***Практична цінність****. Робота стосується мережі, що складається з електронних вбудованих пристроїв, фізичних об'єктів, мережевих підключень та датчиків, що дозволяють сприймати, аналізувати та обмінюватися даними. У цій статті датчики Інтернету речей встановлюються на різних етапах інтелектуальної мережі у гібридній фотоелектричній та вітровій системі. Він відстежує та керує мережевою статистикою для безпечної та ефективної подачі енергії. Дослідження підтверджено результатами моделювання, що базуються на програмному забезпеченні MATLAB/Simulink та реалізації в реальному часі.* Бібл. 28, табл. 1, рис. 22.

Ключові слова: **відновлюване джерело енергії, фотоелектрична система, якість електроенергії, Інтернет речей, підключена до мережі гібридна система.**

Introduction. The concept of renewable energy source (RES) faces increasing concentration by general public and experts in the last years. These sources address the issues caused by global warming and depletion of fossil fuels. Depending on fossil fuels results in environmental pollution, green house problems and carbon dioxide emissions. This paved the way for an increase in clean environment awareness. Due to the environmental friendly nature, RES is crucially significant and is regarded as clean energy sources. RES possess the ability of providing energy services generating almost zero or zero air pollutant emissions. These emissions also have the ability to fulfill the requirements of domestic energy. RES provide pollution free environment, environmental protection, economic benefits and energy security. Therefore, it is important for the future and present generation to rely on RES for meeting energy needs [1].

Considering the renewable energy sources, the solar energy is more fascinating due to its advancements [2-4]. The photovoltaic (PV) systems utilize cells comprising of semi-conductor material for extracting the solar energy and its conversion to electricity. The PV systems are utilized as standalone systems or may be connected to grid [5]. Operating conditions like geometric location of the sun, irradiance level and the ambient temperature of the sun highly influence the performance of the PV system [6]. This uncertain nature of solar energy results in technical problems corresponding to the control of power system [7, 8].

Due to partial shading, loss of considerable amount of energy occurs in PV systems forcing the voltage to zero. This demands a maximum power point tracking (MPPT) approach to capture the maximized power from the PV system and differentiate the global peak from the local peak [9-13]. The MPPT algorithms regulate the pulse width modulation (PWM) generator's duty cycle with the help of the current and voltage obtained from the PV system. The generated pulses are fed to the converter switches for the regulation of its current and voltage [14]. A simple boost DC-DC converter [15] can be used for the boosting of input voltage obtained from PV system. When compared to the improvement of converter efficiency and conversion ratio of PV cells, the improvement of the MPPT efficiency is easier. This paves the way for the adoption of MPPT algorithms and Hill Climbing (HC) [16] approach is the most common among them. It uses the PV characteristics for finding the MPP but gets influenced by varying atmospheric conditions [17]. Incremental Conductance (INC) [18] is regarded as a version of HC and tracks the MPP even in times of rapid variations in solar radiation. Anyway, INC requires extra voltage and current sensors which in turn increases the system complexity. Henceforth, this work adopts Perturb & Observe (P&O) algorithm for the tracking of maximized power by oscillating around the peak point on attaining steady state condition.

Subsequently, the wind energy source exhibits a remarkable progress everywhere as a clean and inexhaustible energy source due to the growing power demand [19-22]. An unsteady pattern occurs in the production of wind power due to its intermittent nature. Added to this, fast ramps occur in the patterns of wind output power. Serious challenges exist in the grid stability when such intermittent sources are integrated with grid [23].

Considering the above mentioned issues of renewable energy sources, the monitoring of power obtained from these sources becomes mandatory. This introduces the concept of smart grids. Smart grids improve the performance quality, reliability, efficiency, sustainability and balance the power production with the integration of renewable energy sources [24, 25]. It also enables the consumers in employing alternate energy sources for efficient power source utilization and cost reduction [26]. By using Internet of Things (IOT), the components of SG are enhanced with the connection of internet [27]. The smart grids based on IOT comprises of smart sensors, actuators and objects for providing reliable energy transmission [28]. Hence, smart grid based on IoT is opted by the renewable energy sources for the efficient monitoring of power.

On the whole, this paper concentrates on an IoT-based smart grid system utilizing hybrid PV-wind energy renewable source. A boost converter is deployed for enhancing the resultant voltage of the PV system. The obtained power from the hybrid renewable energy source is continuously monitored by the IoT device and is applied to the grid via a three phase voltage source inverter (3ϕ VSI).

Proposed control system. Generally, the smart grid is termed as an electric grid of next generation that combines control system along with information and communication technologies with the power grid. The system has to be in dynamic and must be mandatorily in bidirectional communication as depicted in Fig. 1. The major purpose of the system is to quickly find the solutions to the problems with continuous monitoring and automation. Thus it reduces the man power targeting the reliability, safety and quality in electric power to all the consumers.

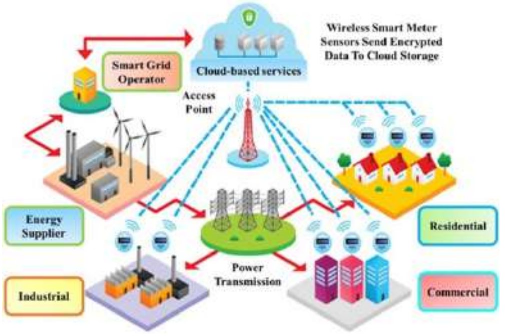

Fig. 1. Smart grid layout depicting the bidirectional communication

In order to establish a smart grid, following technologies must be grouped together as shown in Fig. 2:

- smart appliances;
- smart algorithms in power generation;
- smart power meters;
- super conducting cables;
- smart substations;
- integrated communications.

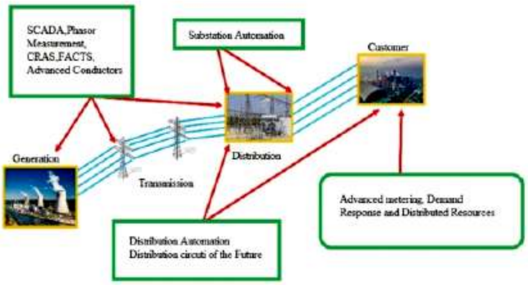

Fig. 2.Vital components of smart grid

By implementing all the advanced technologies one can achieve the smart grid technology with the integration of advanced software and can be managed easily from a remote location. When compared to the conventional grid structure the smart grid structure is easy to maintain and robust in performance making it more reliable and feasible to add more and more technologies and integrating any compatible hardware making it atomized as an ever ending evolution process (Fig. 3).

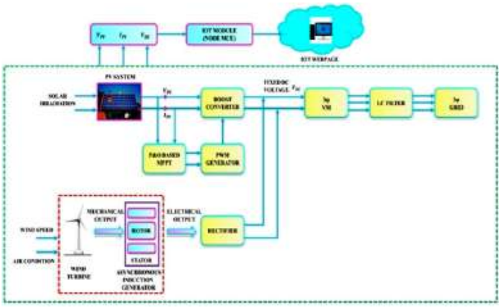

Fig. 3. Proposed generation system

PV system. The basic PV cell circuit is given in Fig. 4. It comprises of a series resistance R_s, parallel resistance R_{sh} and diode VD.

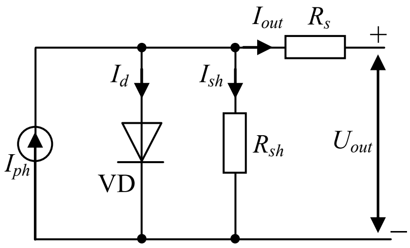

Fig. 4. PV system

The equations relating the PV cell and the output current are given by

$$I_{out} = I_{ph} - I_d ; \tag{1}$$

$$I_d = I_0 \cdot \left[\exp\left(\frac{q \cdot (U + I \cdot R_s)}{n \cdot K \cdot T} \right) - 1 \right]; \tag{2}$$

$$I_{out} = I_{ph} - I_0 \cdot \left[\exp\left(\frac{q \cdot (U + I \cdot R_s)}{n \cdot K \cdot T} \right) - 1 \right], \tag{3}$$

where I_{out} is the output current; I_{ph} is the photovoltaic current; I_d is the diode current; I_0 is the reverse saturation current; K is the Boltzmann constant; q is the charge of an electron; U is the work voltage of a PV cell; n is the p-n junction curve constant; T is the temperature.

The obtained power from the PV system is enhanced by a DC-DC boost converter modelled as follows.

DC-DC boost converter. It is a step-up converter which boosts the input low level voltage to an output high level voltage. The basic circuit of boost converter is indicated in Fig. 5.

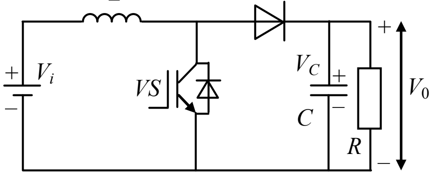

Fig. 5. Boost converter

The energy is stored in inductor L due to the current flow during the ON condition of the switch VS. During the OFF condition of the switch, a voltage is induced across the inductor due to the energy stored. The voltage across the inductor and the input voltage charge the capacitor C to an improved voltage. The duty cycle is:

$$D = 1 - V_0 / V_i \, . \tag{4}$$

The inductance value is:

$$L = \frac{V_0 \cdot (V_i - V_0)}{\Delta I_L \cdot f_s \cdot V_0}, \tag{5}$$

where f_s is the switching frequency; ΔI_L is the determined ripple current of the inductor.

The capacitance value is:

$$C = \frac{D}{R_0 \cdot f_s \cdot \left(\frac{\Delta V_0}{V_0} \right)}, \tag{6}$$

where ΔV_0 is the desired ripple of output voltage.

The estimated inductor ripple current at maximum input voltage determines the value of the inductor. Subsequently, the variation in the output ripple or voltage estimates the capacitor value. The pulses for the converter switch are obtained from the PWM generator. The MPPT algorithm in turn supplies the maximum power point voltage to the PWM generator and the corresponding operation is explained below.

P&O based MPPT. The MPPT algorithm is utilized for improving the efficiency of the solar panel. The main aim is to maintain the system operating point nearer to MPP. Here, P&O is adopted due to its simple structure, less parameters, ease of implementation and low cost. Fig. 6 represents the P&O flowchart.

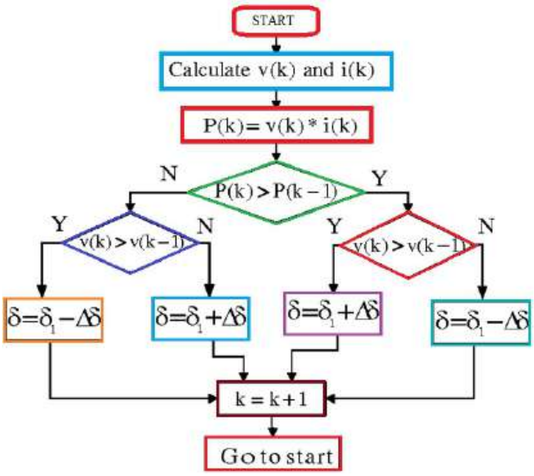

Fig. 6. P&O flowchart

At first, the current along with voltage from the PV system are estimated. The actual power is obtained from the product of voltage and current and the condition $\Delta P = 0$ is checked. The operating point occurs at MPP if this condition is satisfied else the condition $\Delta P > 0$ is checked. Another condition $\Delta V > 0$ is checked if the former gets satisfied and the operating point lies in the left portion of MPP. The operating point lies in the right portion of MPP if $\Delta V > 0$ is not satisfied. Till the reach of MPP, the process gets repeated. The obtained V_{MPP} is fed to the PWM generator which in turn generates the pulses for the boost converter.

A wind energy conversion system (WECS). The basic principle of the wind turbine is to perform the conversion of the linear wind motion to rotational energy. This drives the electrical generator which further converts the wind kinetic energy to electric power. The captured wind power is:

$$P_V = \frac{1}{2}\cdot \rho_a \cdot A_v \cdot u^3, \tag{7}$$

where ρ_a is the density of wind; u is the speed of the wind; A_v is the area swept by the turbine.

The mechanical power P_m obtained from is given by:

$$P_m = C_p(\lambda, \beta)\cdot P_V, \tag{8}$$

where C_p denotes the pitch angle β function and tip speed ratio λ.

Due to the wind speed, the rotational wind turbine speed varies. The obtained variable AC output is applied to the rectifier for the generation of DC voltage and is transferred to the DC link.

Grid connected 3ϕ VSI. A grid connected 3ϕ VSI is given in Fig. 7. The constant DC link voltage V_{DC} is applied as the input to the inverter and the conversion to AC output is carried out by *dq* theory

$$u_d = v_d^* - \omega \cdot i_q \cdot L_f + v_d; \tag{9}$$

$$u_q = v_q^* - \omega \cdot i_d \cdot L_f + v_q; \tag{10}$$

where $\omega = 2\cdot\pi\cdot f$ and

$$v_d^* = \left(k_p + \frac{k_i}{s}\right) + \left(i_{dref} - i_d\right); \tag{11}$$

$$v_q^* = \left(k_p + \frac{k_i}{s}\right) + \left(i_{qref} - i_q\right), \tag{12}$$

where i_{dref}, i_{qref} represent the d-axis and q-axis currents respectively.

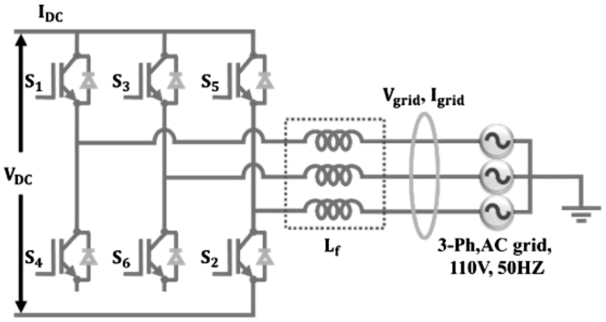

Fig. 7. Grid connected 3ϕ VSI

The AC parameters are obtained from:

$$\begin{bmatrix} u_a \\ u_b \\ u_c \end{bmatrix} = \begin{bmatrix} \sin\omega t & \cos\omega t & 1 \\ \sin(\omega t - 120) & \cos(\omega t - 120) & 1 \\ \sin(\omega t + 120) & \cos(\omega t + 120) & 1 \end{bmatrix} \begin{bmatrix} u_d \\ u_q \\ u_0 \end{bmatrix}, \tag{13}$$

where u_a, u_b, u_c are the controlling input signals which are sinusoidal in nature.

Comparison of these signals is carried out with the carrier signal in the sinusoidal pulse width modulation (SPWM) block. The gate pulses are generated from this block and these pulses are responsible for the inverter operation. The entire grid connected PV wind system is monitored by the IoT and the controller used is demonstrated as follows.

IoT based power monitoring. In this work, the power obtained from the hybrid PV wind system is monitored by the IoT based Node MCU controller. The overall system for power monitoring using IoT is shown in Fig. 8. The IoT module used is Node MCU ESP8266 and the sensor used is INA219 sensor.

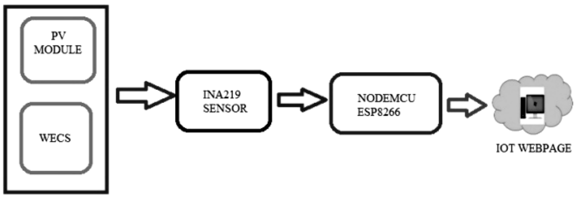

Fig. 8. Power monitoring system using IoT

The sensor is attached to the Node MCU ESP8266 module for the tracking of voltage and current form the hybrid system. The power is determined with the obtained value of current and voltage. Node MCU controller collects the data from the sensor and processes it. The processed data is further send to the web page. The corresponding flowchart is given Fig. 9.

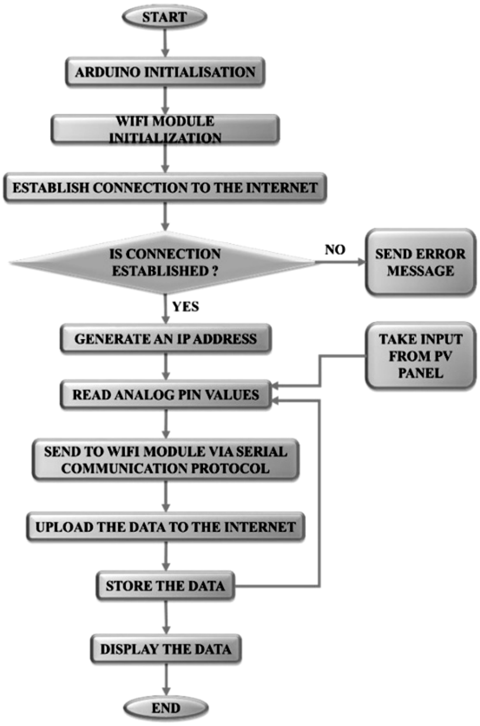

Fig. 9. Flowchart

INA219 sensor. It has the ability to measure the current and voltage from the hybrid system. The input supply ranges from 3 V to 5.5 V. The 5 V output pin of the Node MCU supplies the 5 V to the sensor. The pins D_1 and D_2 of the controller are connected to the INA219 sensor. The current and voltage of the hybrid system are estimated by V_{in+} and V_{in-} which indicate the measuring pins.

Node MCU ESP8266 module. The pin diagram of the Node MCU ESP8266 module is given in Fig. 10. The controller communicates with the INA219 sensor, drives the LCD display and connects to the internet through a Wi-Fi module. It comprises of a built-in capability to access the internet and also supports numerous peripheral communication protocols. The Node MCU is connected to the internet and sends the measured data to the web page for future analysis. Thus the described IoT based monitoring system performs the efficient monitoring of power in grid connected hybrid PV-wind system.

Results and discussion. The monitoring of power in a grid connected hybrid PV wind system with the adoption of IoT based module is demonstrated in this

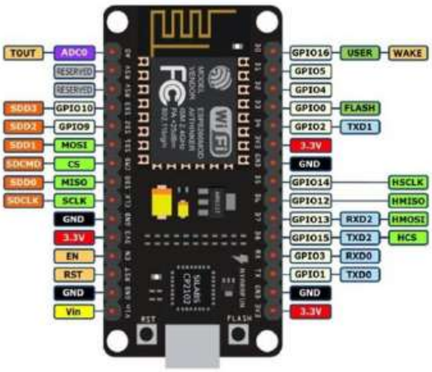

Fig. 10. Node MCU ESP8266 pin diagram

paper. The simulation diagram of the solar PV model and wind turbine model are illustrated in Fig. 11, 12 respectively. The proposed generation model is shown in Fig. 13. In this the solar PV module take the solar radiation, temperature are measured by IoT web portal. In addition to that, wind speed and active power, reactive power, voltage and current are measured.

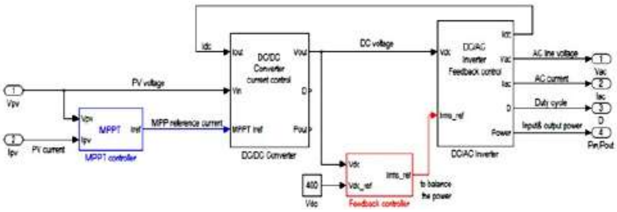

Fig. 11. Solar PV model

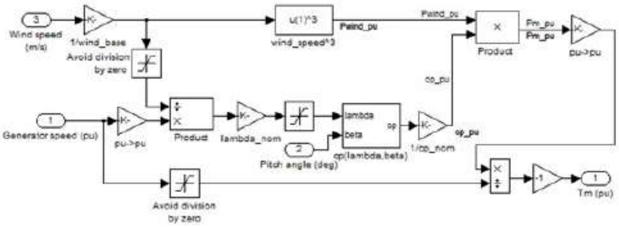

Fig. 12. Wind turbine model

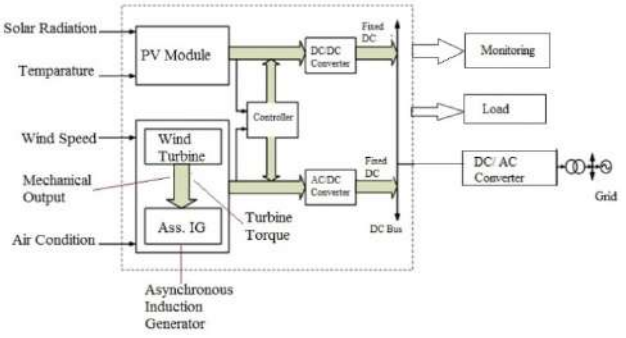

Fig. 13. Proposed generation model

The hybrid smart grid load are connected to an IoT based system, its performance are evaluated. It is shown the loads real time results. Initially, load data is connected through the IoT based Wi-Fi module and communicated to load data. The system allows for various loads monitoring in terms of active power, reactive power, voltage and current respectively.

At any instant of load, the user can see the local details of active power, reactive power, voltage, current and total harmonic distortion (THD) of voltage and currents are shown in Fig. 14–19 respectively.

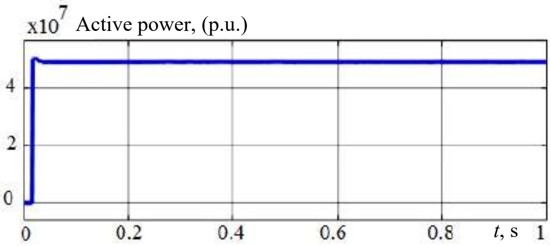

Fig. 14. Active power

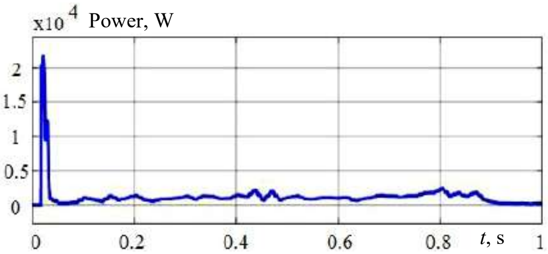

Fig. 15. Reactive power

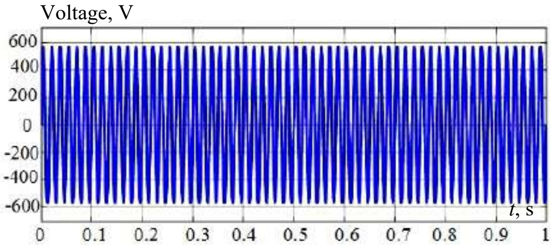

Fig. 16. Output voltage

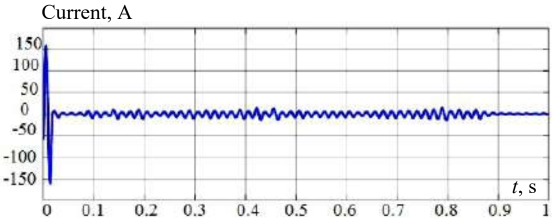

Fig. 17. Output current

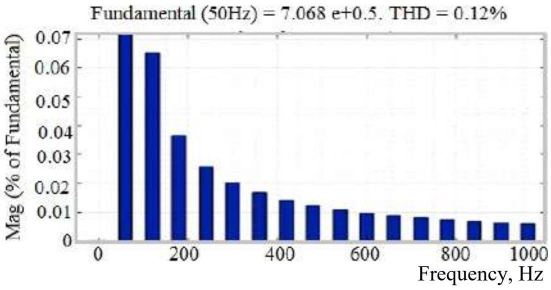

Fig. 18. Voltage harmonic

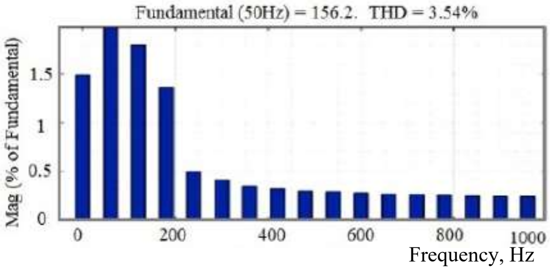

Fig. 19. Current harmonic

The IoT based PV power under shading effect is depicted in Fig. 20. And also the irradiance of the PV system is shown in Fig. 21.

The hybrid smart grid based IoT system, voltage harmonic on the grid side is shown in Fig. 20. In this the fundamental frequency takes in to 50 Hz. The system reduced the THD of 0.12 %. The current harmonics are depicted in Fig. 21. It shows the fundamental frequency of 156.2 Hz and THD reduced 3.54 %.

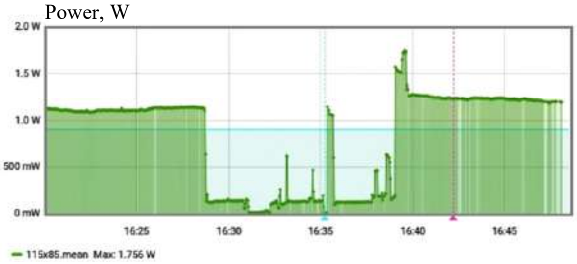

Fig. 20. Monitored PV power under shading effect

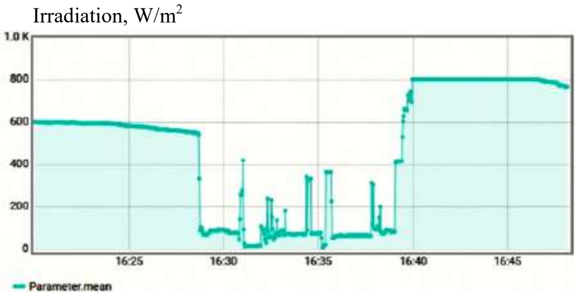

Fig. 21. Monitored irradiance in shading effect

The hybrid power generation for smart grid integration facilitates and enhances communication between grid and consumer. The power consumption and power quality is the main aim of smart grid integration. In this method effective monitoring and maintain power quality achieved by proposed IoT based hybrid smart grid.

The comparison of the PV solar panel power quality is depicted in Table 1. It shows the THD values of current and voltage harmonic with and without IOT approach.

Table 1

Comparison THD – PV module with and without IoT

Conditions	THD, %
Without IoT monitoring and control approach current harmonic THD	20.25
With IoT Monitoring and control approach current harmonic THD	3.54
Without IoT monitoring and control approach voltage harmonic THD	4.59
With IoT monitoring and control approach voltage harmonic THD	0.12

The obtained IoT results are mentioned in Fig. 22. The display indicates the measured values of current and voltage of the hybrid PV-wind system. The ESP8266 communication is performed with the utilization of serial monitoring of the Node MCU.

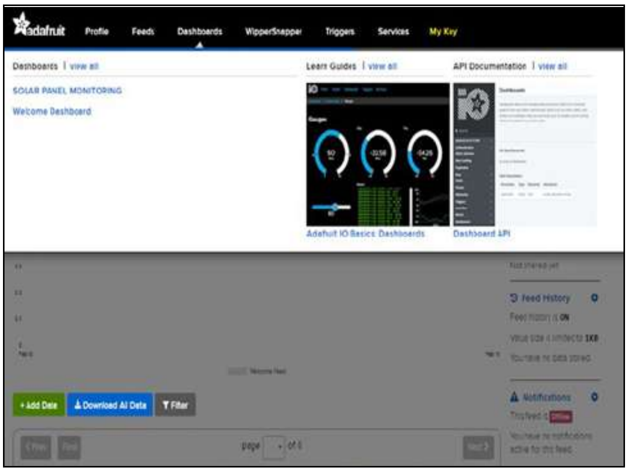

Fig. 22. IoT system results

Conclusions. In this work, an efficient power monitoring approach is introduced for a hybrid photovoltaic wind system. This approach adopts internet of things based module with node microcontroller unit which processes the measured data obtained from sensor. The tracking of maximum power from the photovoltaic system is carried out by perturb & observe algorithm which in turn generates the maximum voltage for the operation of the boost converter. Subsequently, the obtained voltage from the photovoltaic system and wind energy conversion system is maintained constant at the direct current link. This fixed direct current voltage is converted to AC form by a 3ϕ voltage source inverter and further supplied to grid. The power of the entire setup is monitored by the internet of things based module which facilitates the smart consumption of power.

Conflict of interest. The authors declare that they have no conflicts of interest.

Appendix.

```
/*Sg= Smart Grid
/*Ed= Energy Demand
/*Eg = Generation Energy
/*Pq =Power Quality
Void Power Quality Analysier ( )
{
For(PQ<=10%)
Write the system is normal and record the data
}
Terminate the terminal
Void Main ( )
If (Sg=Ed)
{
Void Power Quality Analysier ( )
}
Else if (Sg> Ed)
{
The system Id on surplus and non peak time tariff
Void Power Quality Analysier ( )
}
Else if (Sg< Ed)
{
Set Peak time and tariff change on Peak
Void Power Quality Analysier ( )
}
Else (Ed<Eg)
{
Cause voltage rise and terminate production terminal
Production exceeds threshold
Void Power Quality Analysier ( )
}
```

REFERENCES

1. Qazi A., Hussain F., Rahim N.A., Hardaker G., Alghazzawi D., Shaban K., Haruna K. Towards Sustainable Energy: A Systematic Review of Renewable Energy Sources, Technologies, and Public Opinions. *IEEE Access*, 2019, vol. 7, pp. 63837-63851. doi: https://doi.org/10.1109/ACCESS.2019.2906402.

2. Humada A.M., Darweesh S.Y., Mohammed K.G., Kamil M., Mohammed S.F., Kasim N.K., Tahseen T.A., Awad O.I., Mekhilef S. Modeling of PV system and parameter extraction based on experimental data: Review and investigation. *Solar Energy*, 2020, vol. 199, pp. 742-760. doi: https://doi.org/10.1016/j.solener.2020.02.068.

3. Fadhel S., Delpha C., Diallo D., Bahri I., Migan A., Trabelsi M., Mimouni M.F. PV shading fault detection and classification based on I-V curve using principal component analysis: Application to isolated PV system. *Solar Energy*, 2019, vol. 179, pp. 1-10. doi: https://doi.org/10.1016/j.solener.2018.12.048.

4. Kumar N., Hussain I., Singh B., Panigrahi B.K. MPPT in Dynamic Condition of Partially Shaded PV System by Using WODE Technique. *IEEE Transactions on Sustainable Energy*, 2017, vol. 8, no. 3, pp. 1204-1214. doi: https://doi.org/10.1109/TSTE.2017.2669525.

5. Bataineh K. Improved hybrid algorithms-based MPPT algorithm for PV system operating under severe weather conditions. *IET Power Electronics*, 2019, vol. 12, no. 4, pp. 703-711. doi: https://doi.org/10.1049/iet-pel.2018.5651.

6. Mosaad M.I., abed el-Raouf M.O., Al-Ahmar M.A., Banakher F.A. Maximum Power Point Tracking of PV system Based Cuckoo Search Algorithm; review and comparison. *Energy Procedia*, 2019, vol. 162, pp. 117-126. doi: https://doi.org/10.1016/j.egypro.2019.04.013.

7. Rahmann C., Vittal V., Ascui J., Haas, J. Mitigation Control Against Partial Shading Effects in Large-Scale PV Power Plants. *IEEE Transactions on Sustainable Energy*, 2016, vol. 7, no. 1, pp. 173-180. doi: https://doi.org/10.1109/TSTE.2015.2484261.

8. Batzelis E.I., Papathanassiou S.A., Pal B.C. PV System Control to Provide Active Power Reserves Under Partial Shading Conditions. *IEEE Transactions on Power Electronics*, 2018, vol. 33, no. 11, pp. 9163-9175. doi: https://doi.org/10.1109/TPEL.2018.2823426.

9. Babu V., Ahmed K.S., Shuaib Y.M., Manikandan M. Power Quality Enhancement Using Dynamic Voltage Restorer (DVR)-Based Predictive Space Vector Transformation (PSVT) With Proportional Resonant (PR)-Controller. *IEEE Access*, 2021, vol. 9, pp. 155380–155392. doi: https://doi.org/10.1109/ACCESS.2021.3129096.

10. Babu V., Ahmed K.S., Shuaib Y.M., Mani M. A novel intrinsic space vector transformation based solar fed dynamic voltage restorer for power quality improvement in distribution system. *Journal of Ambient Intelligence and Humanized Computing*, 2021, vol. 7, no. 1, pp. 173-180. doi: https://doi.org/10.1007/s12652-020-02831-0.

11. Ahmed J., Salam Z. An Accurate Method for MPPT to Detect the Partial Shading Occurrence in a PV System. *IEEE Transactions on Industrial Informatics*, 2017, vol. 13, no. 5, pp. 2151-2161. doi: https://doi.org/10.1109/TII.2017.2703079.

12. Abdulrazzaq A.A., Hussein Ali A. Efficiency Performances of Two MPPT Algorithms for PV System With Different Solar Panels Irradiancess. *International Journal of Power Electronics and Drive Systems (IJPEDS)*, 2018, vol. 9, no. 4, pp. 1755-1764. doi: https://doi.org/10.11591/ijpeds.v9.i4.pp1755-1764.

13. Wang F., Zhu T., Zhuo F., Yi H. An Improved Submodule Differential Power Processing-Based PV System With Flexible Multi-MPPT Control. *IEEE Journal of Emerging and Selected Topics in Power Electronics*, 2018, vol. 6, no. 1, pp. 94–102. doi: https://doi.org/10.1109/JESTPE.2017.2719919.

14. Yilmaz U., Kircay A., Borekci S. PV system fuzzy logic MPPT method and PI control as a charge controller. *Renewable and Sustainable Energy Reviews*, 2018, vol. 81, pp. 994-1001. doi: https://doi.org/10.1016/j.rser.2017.08.048.

15. Pradhan A., Panda B. A Simplified Design and Modeling of Boost Converter for Photovoltaic System. *International Journal of Electrical and Computer Engineering (IJECE)*, 2018, vol. 8, no. 1, pp. 141-149. doi: https://doi.org/10.11591/ijece.v8i1.pp141-149.

16. Nzoundja Fapi C.B., Wira P., Kamta M., Badji A., Tchakounte H. Real-Time Experimental Assessment of Hill Climbing MPPT Algorithm Enhanced by Estimating a Duty Cycle for PV System. *International Journal of Renewable Energy Research*, 2019, vol. 9, no. 3, pp. 1180-1189. doi: https://doi.org/10.20508/ijrer.v9i3.9432.g7705.

17. Gouda E.A., Kotb M.F., Elalfy D.A. Modelling and Performance Analysis for a PV System Based MPPT Using Advanced Techniques. *European Journal of Electrical Engineering and Computer Science*, 2019, vol. 3, no. 1, pp. 1-7. doi: https://doi.org/10.24018/ejece.2019.3.1.47.

18. Ali M.N., Mahmoud K., Lehtonen M., Darwish M.M.F. An Efficient Fuzzy-Logic Based Variable-Step Incremental Conductance MPPT Method for Grid-Connected PV Systems. *IEEE Access*, 2021, vol. 9, pp. 26420-26430. doi: https://doi.org/10.1109/ACCESS.2021.3058052.

19. Li S., Li J. Output Predictor-Based Active Disturbance Rejection Control for a Wind Energy Conversion System With PMSG. *IEEE Access*, 2017, vol. 5, pp. 5205-5214. doi: https://doi.org/10.1109/ACCESS.2017.2681697.

20. Kushwaha A., Gopal M., Singh B. Q-Learning based Maximum Power Extraction for Wind Energy Conversion System With Variable Wind Speed. *IEEE Transactions on Energy Conversion*, 2020, vol. 35, no. 3, pp. 1160-1170. doi: https://doi.org/10.1109/TEC.2020.2990937.

21. Afghoul H., Krim F., Babes B., Beddar A., Kihel A. Design and real time implementation of sliding mode supervised fractional controller for wind energy conversion system under sever working conditions. *Energy Conversion and Management*, 2018, vol. 167, pp. 91-101. doi: https://doi.org/10.1016/j.enconman.2018.04.097.

22. Reddy D., Ramasamy S. Design of RBFN Controller Based Boost Type Vienna Rectifier for Grid-Tied Wind Energy Conversion System. *IEEE Access*, 2018, vol. 6, pp. 3167-3175. doi: https://doi.org/10.1109/ACCESS.2017.2787567.

23. Sattar A., Al-Durra A., Caruana C., Muyeen S.M. Testing the Performance of Battery Energy Storage in a Wind Energy Conversion System. *2018 IEEE Industry Applications Society Annual Meeting (IAS)*, 2018, pp. 1-8. doi: https://doi.org/10.1109/IAS.2018.8544521.

24. Cheddadi Y., Cheddadi H., Cheddadi F., Errahimi F., Es-sbai N. Design and implementation of an intelligent low-cost IoT solution for energy monitoring of photovoltaic stations. SN *Applied Sciences*, 2020, vol. 2, no. 7, pp. 1165. doi: https://doi.org/10.1007/s42452-020-2997-4.

25. Li Y., Cheng X., Cao Y., Wang D., Yang L. Smart Choice for the Smart Grid: Narrowband Internet of Things (NB-IoT). *IEEE Internet of Things Journal*, 2018, vol. 5, no. 3, pp. 1505-1515. doi: https://doi.org/10.1109/JIOT.2017.2781251.

26. Pawar P., Vittal K.P. Design and development of advanced smart energy management system integrated with IoT framework in smart grid environment. *Journal of Energy Storage*, 2019, vol. 25, pp. 100846. doi: https://doi.org/10.1016/j.est.2019.100846.

27. Hussain M., Beg M.M. Fog Computing for Internet of Things (IoT)-Aided Smart Grid Architectures. *Big Data and Cognitive Computing*, 2019, vol. 3, no. 1, pp. 8. doi: https://doi.org/10.3390/bdcc3010008.

28. Bera B., Saha S., Das A.K., Vasilakos A.V. Designing Blockchain-Based Access Control Protocol in IoT-Enabled Smart-Grid System. *IEEE Internet of Things Journal*, 2021, vol. 8, no. 7, pp. 5744-5761. doi: https://doi.org/10.1109/JIOT.2020.3030308.

Received 01.04.2022
Accepted 19.05.2022
Published 20.07.2022

Padakanti Balakishan[1]*, Research Scholar,*
Ilanji Akilandam Chidambaram[1]*, Professor,*
Mani Manikandan[2]*, Professor,*
[1] Annamalai University,
Chidambaram, Tamil Nadu, 608002, India,
e-mail: balakishan1975@gmail.com (Corresponding author),
driacdm@gmail.com
[2] Jyothishmathi Institute of Technology and Science,
Karimnagar, Telangana, 505481, India,
e-mail: cm.manikandan@gmail.com

How to cite this article:

Balakishan P., Chidambaram I.A., Manikandan M. Improvement of power quality in grid-connected hybrid system with power monitoring and control based on internet of things approach. *Electrical Engineering & Electromechanics*, 2022, no. 4, pp. 44-50. doi: https://doi.org/10.20998/2074-272X.2022.4.06

UDC 621.3 https://doi.org/10.20998/2074-272X.2022.4.07

A. Chemidi, M.C. Benhabib, M.A. Bourouis

Performance improvement of shunt active power filter based on indirect control with a new robust phase-locked loop

Introduction. *Since the development of the first active power filter (APF) in 1976, many efforts have been focused on improving the performances of the APF control as the number of different nonlinear loads has continued to increase. These nonlinear loads have led to the generation of different types of current harmonics, which requires more advanced controls, including robustness, to get an admissible total harmonic distortion (THD) in the power system.* ***Purpose.*** *The purpose of this paper is to develop a robust phase-locked loop (PLL) based on particle swarm optimization-reference signal tracking (PSO-RST) controller for a three phase three wires shunt active power filter control.* ***Methodology.*** *A robust PLL based on PSO-RST controller insert into the indirect d-q control of a shunt active power filter* ***was*** *developed.* ***Results.*** *Simulation results performed under the MATLAB/SimPowerSystem environment show a higher filtering quality and a better robustness compared to the classical d-q controls.* ***Originality.*** *Conventional PLLs have difficulty determining the phase angle of the utility voltage sources when grid voltage is distorted. If this phase angle is incorrectly determined, this leads to a malfunction of the complete control of the active power filters. This implies a bad compensation of the current harmonics generated by the nonlinear loads. To solve this problem we propose a robust and simple PLL based on PSO-RST controller to eliminate the influence of the voltage harmonics.* ***Practical value.*** *The proposed solution can be used to improve the functioning of the shunt active power filter and to reduce the amount of memory implementation.* References 23, tables 3, figures 19.

Key words: **active power filter, robust phase-locked loop, harmonics, particle swarm optimization-reference signal tracking controller.**

Вступ*. З моменту розробки першого фільтра активної потужності (ФАП) у 1976 р. багато зусиль було спрямовано на покращення характеристик управління ФАП, оскільки кількість різних нелінійних навантажень продовжувала зростати. Ці нелінійні навантаження призвели до генерації різних типів гармонік струму, що потребує більш досконалих засобів управління, у тому числі стійких, для отримання допустимого повного гармонічного спотворення (THD) в енергосистемі.* ***Мета****. Метою даної статті є розробка надійного контуру фазового автопідстроювання частоти (ФАПЧ) на основі контролера відстеження еталонного сигналу оптимізації рою частинок (ВЕС ОРЧ) для трифазного трипровідного шунтуючого фільтра активної потужності.* ***Методологія****. Розроблено надійну систему ФАПЧ на основі контролера ВЕС ОРЧ, вбудованого в непрямий d-q контроль шунтуючого фільтра активної потужності.* ***Результати****. Результати моделювання, виконаного в середовищі MATLAB/SimPowerSystem, демонструють високу якість фільтрації та більшу надійність у порівнянні з класичним d-q керуванням.* ***Оригінальність****. Звичайні ФАПЧ мають труднощі з визначенням фазового кута джерел напруги, коли напруга мережі спотворена. Неправильне визначення цього фазового кута призводить до порушення повного керування фільтрами активної потужності. Це означає погану компенсацію гармонік струму, створюваних нелінійними навантаженнями. Для вирішення цієї проблеми ми пропонуємо стійкий та простий ФАПЧ на основі контролера ВЕС ОРЧ для усунення впливу гармонік напруги.* ***Практична цінність****. Запропоноване рішення може бути використане для поліпшення роботи шунтуючого фільтра активної потужності і зменшення обсягу потрібної пам'яті.* Бібл. 23, табл. 3, рис. 19.

Ключові слова: **фільтр активної потужності, надійний контур фазового автопідстроювання частоти, гармоніки, контролер відстеження еталонного сигналу оптимізації рою частинок.**

Introduction. In the last three decades a significant development and study of shunt active power filter (SAPF) control has been made. The main one is the direct control method based on instantaneous power introduced by Akagi [1]. Many other direct or indirect control strategies to achieve good filtering results for three-wire power systems have also been proposed [2-4]. Concerning the indirect control it has been developed by [5, 6]. Unlike the direct strategy, the alternating components of the instantaneous power will be removed to leave only the continuous component. This method allows compensating the current harmonics indirectly.

Since the appearance of SAPF many algorithms have been developed. Those algorithms can accomplish good performances (harmonics elimination) when the grid voltage is balanced and undistorted. Contrariwise, if the grid voltage is distributed, the performance of the SAPF will widely decrease [8]. To handle this issue some researchers propose the use of a self-tuning filter [8]. However, this method increases the number of filters and transformations. In this paper we propose to keep the basic indirect control without additional filters or transformations and the use of a new simple and robust phase-locked loop (PLL) to deal with the grid voltage perturbations.

In the first part of this paper we will present the classical active power filter (APF) control which is; the d-q theory for indirect control. The harmonics and total harmonic distortion (THD) of the lines current are the quality criteria chosen all over the paper. Then, an improvement will be made for this control in order to minimize the influence of grid voltage harmonics by introducing a new robust PLL based on a particle swarm optimization-reference signal tracking (PSO-RST) controller, where unlike the PLL proposed in [7]; this new PLL is simple and his implementation doesn't need a large amount of memory. This new approach is then applied to the control of a three-phase three-leg SAPF and its effectiveness is validated by simulations.

All the simulations are carried out with MATLAB/Simulink. They are conducted under the same conditions, with the same parameters for the system and the control in order to compare the results obtained between the classical and the proposed control.

Basic indirect control theory for SAPF. The active power filter that we will be using in our study is a three-leg active power filter connected in parallel to a three-wire electrical network. The control strategy used for this SAPF is an indirect d-q control. The active power filter and its control are shown in Fig. 1. The control strategy is based on the theory introduced in 1983 by Akagi et al [1] which uses the Concordia transform. It is stated as follows.

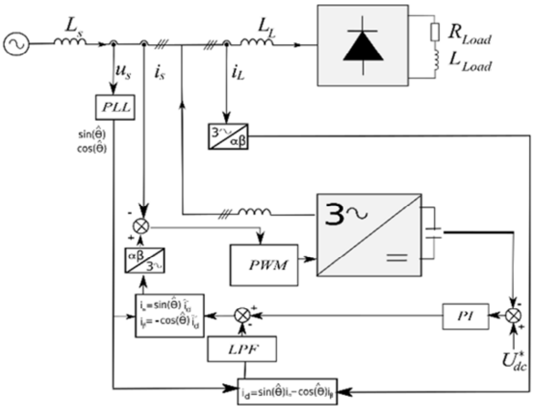

Fig. 1. Indirect control of SAPF system

Let be respectively the simple voltages and the line currents of a three-phase system without homopolar $v_{sa}(t)$, $v_{sb}(t)$, $v_{sc}(t)$ and $i_{La}(t)$, $i_{Lb}(t)$, $i_{Lc}(t)$.

The Concordia transformation of the line current allows us to obtain:

$$\begin{pmatrix} i_\alpha \\ i_\beta \end{pmatrix} = \sqrt{\frac{2}{3}} \cdot \begin{pmatrix} 1 & -\frac{1}{2} & -\frac{1}{2} \\ 0 & \frac{\sqrt{3}}{2} & -\frac{\sqrt{3}}{2} \end{pmatrix} \cdot \begin{pmatrix} i_{La} \\ i_{Lb} \\ i_{Lc} \end{pmatrix}. \tag{1}$$

A PLL is used to extract $(\hat{\theta})$ in order to generate two signals $\sin(\hat{\theta})$ and $\cos(\hat{\theta})$ which are in phase with the simple voltage of the electrical network. We then multiply these two signals by i_α and i_β to obtain only the current in the d-axis, as shown by the following expression:

$$i_d = i_\alpha \cdot \sin(\hat{\theta}) - i_\beta \cdot \cos(\hat{\theta}). \tag{2}$$

The resulting current can be expressed as the sum of a continuous component and an alternating component:

$$i_d = \bar{i}_d + \tilde{i}_d, \tag{3}$$

where $\bar{i}_d$ is the continuous component of i_d; $\tilde{i}_d$ is the alternating component of i_d.

In order to extract only the continuous component, which will be injected by the APF, the alternating component should be eliminated by a low pass filter (LPF). Thus, the currents in α–β coordinates will become:

$$\begin{cases} i_\alpha^{ref} = \sin(\hat{\theta}) \cdot i_d; \\ i_\beta^{ref} = -\cos(\hat{\theta}) \cdot i_d. \end{cases} \tag{4}$$

The reference currents are given as before by the inverse Concordia transformation:

$$\begin{pmatrix} i_{La}^{ref} \\ i_{Lb}^{ref} \\ i_{Lc}^{ref} \end{pmatrix} = \sqrt{\frac{2}{3}} \cdot \begin{pmatrix} 1 & 0 \\ -\frac{1}{2} & \frac{\sqrt{3}}{2} \\ -\frac{1}{2} & -\frac{\sqrt{3}}{2} \end{pmatrix} \cdot \begin{pmatrix} i_\alpha^{ref} \\ i_\beta^{ref} \end{pmatrix}. \tag{5}$$

New robust PLL. There are several types of PLL that have been developed to synchronize the signal outputs to the single-phase or to the three-phase fundamental voltage component. For the three-phase, for example, we find the following PLLs:

Three-phase synchronous reference frame phase locked loop (*SRF PLL*) (*dqPLL*) [9, 10, 12], where the instantaneous phase angle is determined by synchronizing when the PI controller sets the direct or quadrature axis reference voltage v_d or v_q to zero, resulting in the reference being latched to the phase angle of the utility's voltage vector.

Instantaneous power three-phase PLL (*pPLL*) [11, 12]. Its structure is the same as that of the classical SRF-PLLs, but the theory behind this PLL is the use of the instantaneous power theory.

Dual second-order generalized integrator based PLL (*DSOGI-PLL*) [15, 16]. This PLL builds the orthogonal signals generator (OSG) using two first-order integrators based on a second-order integrator, which is easy to be implemented digitally, and the nonlinearity is lower than that of Park-PLL.

However, in single phase applications, we find the following PLLs:

Single-phase enhanced PLL (EPLL) [14] and single-phase adaptive linear combiner PLL (PLL-ALC) [13, 14]. This PLL method is designed on the basis of the adaptive filter theory by estimating its phase and frequency through the steepest descent algorithm.

Over time the PLLs have been improved to make them more robust against distortion and unbalance insensitivity. Among these PLLs we have the one proposed by [7] which add a multi-variable filter to eliminate the influence of voltages disturbance. This method has the disadvantage of making its implementation more complex due to the increase of a multivariate filter in the PLL.

The goal of this work is to develop a new robust and simple phase-locked loop to deal with the harmonic voltages, where the PI controller on the SRF-PLL structure is replaced by RST controller. This controller has a simple structure and good performances in large range of operating conditions. Moreover, we propose a new approach to adjust the RST parameters where unlike the conventional methods proposed in [17, 18], the parameters of the regulator are set by utilizing the particle swarm optimization (PSO) algorithm.

RST controller. The structure of the RST controller is based on the determination of a three polynomials $R(p)$, $S(p)$ and $T(p)$ in order to obtain a good performances in term of reference tracking and disturbance rejection. It's based on pole placement theory by determining an arbitrary stability polynomial $D(p)$ and computing $S(p)$ and $R(p)$ according to Bezout's equation [19]

$$D(p) = A(p) \cdot S(p) + B(p) \cdot R(p). \tag{6}$$

The design structure of a system with RST controller is represented in Fig. 2.

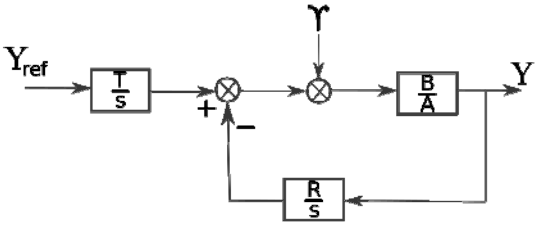

Fig. 2. Block diagram of the RST controller

The closed loop transfer function of the system is:

$$Y=\frac{B(p)T(p)}{A(p)S(p)+B(p)R(p)}Y_{ref}+\frac{B(p)S(p)}{A(p)S(p)+B(p)R(p)}\gamma \;.(7)$$

The key to have good results depends on the choice of polynomials orders. A strictly proper regulator is chosen which mean if deg(A) is n than:

$$\begin{cases}\deg(D)=2n+1\\ \deg(S)=\deg(A)+1\\ \deg(R)=\deg(A)\end{cases} \qquad (8)$$

However, the polynomial forms are described as follows:

$$\begin{cases}A(p)=a_1p+a_0\\ B(p)=b_0\\ D(p)=d_3p^3+d_2p^2+d_1p+d_0\;.\\ R(p)=r_1p+r_0\\ S(p)=s_2p^2+s_1p\end{cases} \qquad (9)$$

The transfer function of the PLL is [7] $\frac{\sqrt{3}\cdot V_m}{p}$, which mean that: $A(p)=p$; $B(p)=\sqrt{3}$, where V_m is the peak value of the source voltage.

To find the coefficients of each polynomial a robust pole placement strategy is used [20]. By assuming that $C(p)$ is the control pole and $F(p)$ is the filter pole, we obtain the following expression:

$$D(p)=C(p)\cdot F(p)=\left(p+\frac{1}{T_c}\right)\cdot\left(p+\frac{1}{T_f}\right)^2, \qquad (10)$$

where $P_c=-1/T_c$ is the pole of $C(p)$; $P_f=-1/T_f$ is the double pole of $F(p)$.

Usually P_c is chosen 2-5 times greater than P_A, where P_A is the pole of A; and P_f is chosen 3–5 times greater than P_c. The identification between Bezout equation and equation (9) gives a system of four equations with four unknown terms, as is shown in the following equation:

$$\begin{cases}a_1s_2=1\\ a_1s_1+a_0s_2=\frac{2}{T_f}+\frac{1}{T_c}\\ a_0s_1+b_0r_1=\frac{1}{T^2_f}+\frac{2}{T_cT_f}\;.\\ b_0r=\frac{1}{T_cT^2_f}\end{cases} \qquad (11)$$

For the determination of polynomial T we consider $S(0)=0$ and in the steady state $Y_{ref}=Y$. Then we get the following equation:

$$\lim_{p\to 0}\frac{B(p)T(p)}{A(p)S(p)+B(p)R(p)}=1 \qquad .(12)$$

After finding the coefficients of the filter pole $F(p)$ with the pole placement, we obtain the following equation:

$$T(p)=h\cdot F(p)=h\cdot\left(p+\frac{1}{T_f}\right)^2, \qquad (13)$$

where $h=R(0)/F(0)$.

PSO algorithm. The PSO algorithm is an evolutionary technique which uses a population of candidate solutions to find an optimal solution to a problem. The degree of optimality is evaluated by an objective function. The algorithm used in this work is inspired by the collective comportment and the synchronous formation flight of birds. This technique is considered as a progressive algorithm with a populace of agents called particles «i» which are dispersed in the problem space [21].

In the beginning swarms are randomly allocated in the search space, each particle also having a random speed as shown in Fig. 3.

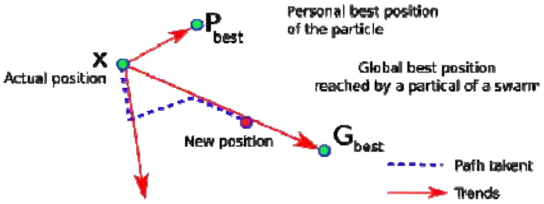

Fig. 3. A particle movement

A particle is capable to evaluate her position quality and remember her best performance. By asking her congeners she can also obtain their best performances. According to this information, each particle changes its speed and moves. A particle «i» of the swarm is represented in the D-dimensional search space by its position vector (X) and by its speed vector (V) formulated as follows:

$$X_i=(x_{i1},x_{i2},\dots,x_{in})\;; \qquad (14)$$

$$V_i=(v_{i1},v_{i2},\dots,v_{in})\;. \qquad (15)$$

The evaluation of his position quality is stopped by the objective function at this point. It is important that this particle can memorize the best position through which it has already passed, formulated as follows:

$$P_i=(p_{i1},p_{i2},\dots,p_{in})\;. \qquad (16)$$

The equation of a particle movement for each iteration (i_{ter}) is:

$$V_i^{iter+1}=X(w.v_i^{iter}+c_1.r_1^{iter}(p_i^{iter}-X_i^{iter})+c_2.r_2^{iter}(p_g^{iter}-X_i^{iter})) \;,(17)$$

where ω is the coefficient of inertia; c_1, c_2 are the acceleration coefficients which control respectively the attraction at its best and the attraction at the best overall; $r_1, r_2 \in [0, 1]$ are the uniform random variables.

The update of the position of the particle is done through the following equation:

$$X_i^{iter+1}=X_i^{iter}+V_i^{iter+1}\;. \qquad (18)$$

RST controller parameters optimization with PSO algorithm. We will now integrate the PSO described in the previous paragraph in order to optimize the RST parameters in such a way to have a better rejection of the perturbations and a better tracking of the reference. In other words s_1, s_2, r_1, r_0 and t in (11) and (13) are optimized so that the error is minimized.

An algorithm was developed for which the «min-max» function is adopted to perform the preprocessing data. The population size was set at 200 particles. This parameter has an influence on the behavior of the algorithm (a small population does not create enough interactions to guarantee the proper functioning of the algorithm). If the acceleration coefficient is too small, the algorithm will explore very slowly, which degrades its performance. Experience has shown that with a value of 2.05 often achieves the best results [22]. According to [23] the coefficient of inertia is chosen between 0.5 and 1. In our study we have chosen a value of 0.5 that we consider suitable.

The PSO begins to search for a solution in a research space. These values are then injected into Simulink (Fig. 4). The difference between the measure and the reference is evaluated by the objective function. The values of s_1, s_2, r_1, r_0 and t are then modified until the objective function (19) is minimized, as shown in the following equation:

$$f_{\min} = \int_0^{\infty} (U_{ref} - U_{mes})^2 (t) dt = \int_0^{\infty} (e)^2 (t) dt . \qquad (19)$$

The process is repeated until the difference between the measured values and the reference values is minimal or a maximum number of iterations are achieved.

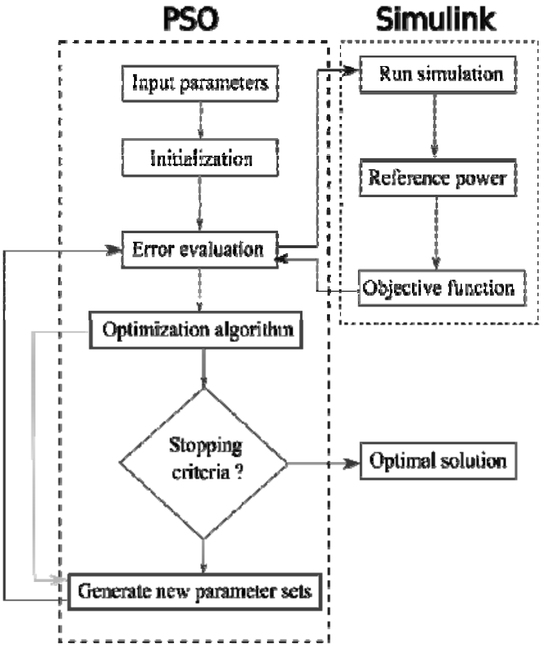

Fig. 4 .Schematic steps of proposed RST controllers with PSO algorithm

Simulation and results. The performances of the proposed system (Fig. 5) are evaluated and simulated in MATLAB/Simulink environment where the robustness of the PLL is tested under distorted voltage source.

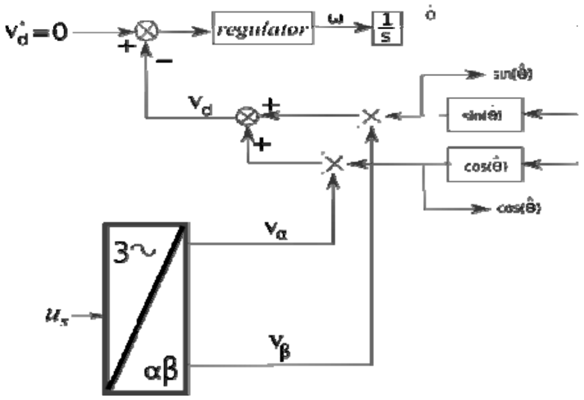

Fig. 5. Block diagram of PLL

Figures 6-14 give respectively the simulation results of the proposed controller (RST-PSO) that are compared to classical PLL with PI controller and the PLL with conventional RST controller.

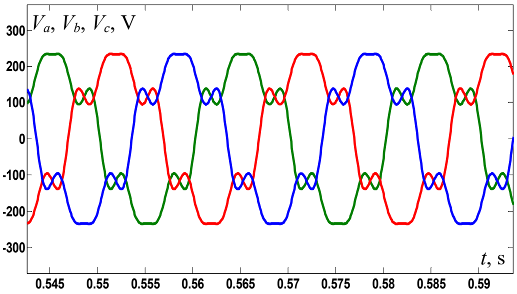

Fig. 6. Utility voltages source under harmonics

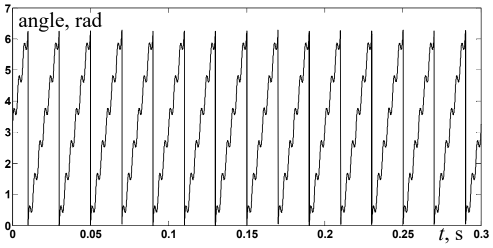

Fig. 7. Angular position estimated by the PLL based on PI controller

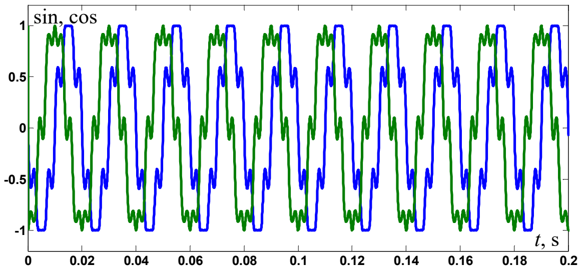

Fig. 8. Sin and cos generated by the PLL based on PI controller

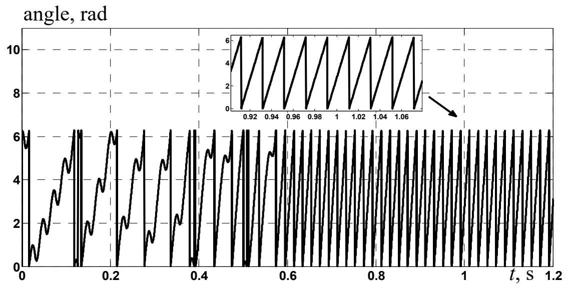

Fig. 9. Angular position estimated by the PLL based on RST controller

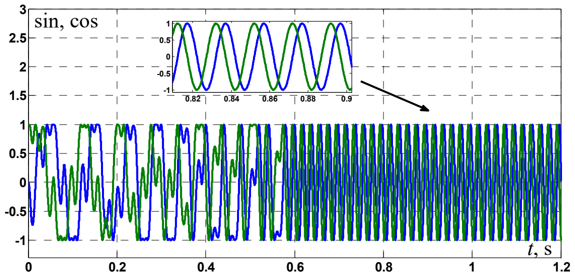

Fig. 10. Sine and cosine generated by the PLL based on RST controller

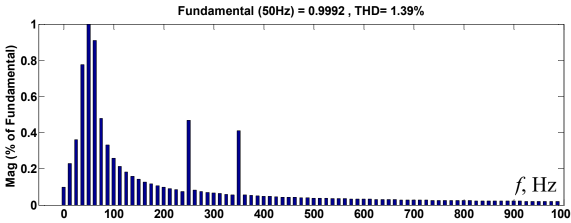

Fig. 11. Spectrum of the cosine generated by the PLL based on RST controller

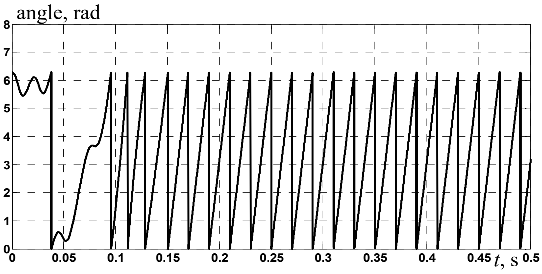

Fig. 12. Angular position estimated by the PLL based on PSO-RST

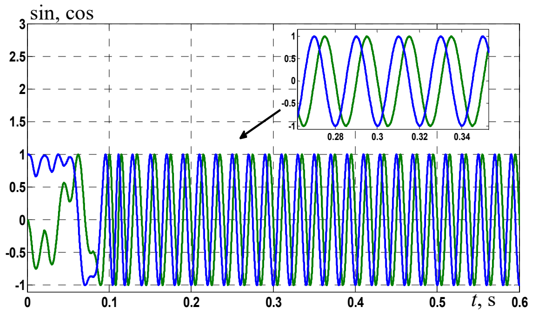

Fig. 13. Sin and cos generated by the PLL based on PSO-RST controller

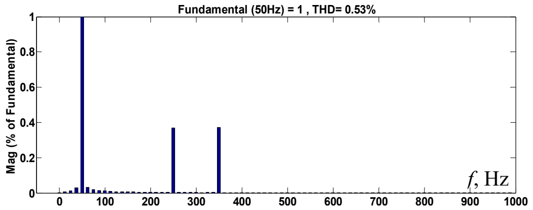

Fig. 14. Spectrum of the cosine generated by the PLL based on PSO-RST controller

We notice from these simulations that the PLL using the PSO-RST gives very good results compared to the use of the classical PLL which uses a PI regulator or the conventional RST when the source voltage contains harmonics. Where from Fig. 7, 8 we can see that the classical PLL doesn’t reject the harmonics; Fig. 9, 10, 12, 13 show that the PLL based on the RST controller and the PSO-RST controller respectively can reject the harmonics with faster response for the PSO-RST (0.1 s). From Fig. 11, 14 it can be seen that the proposed PLL has better rejection for the harmonics where the THD obtained in the steady state is 0.53 %.

To show the efficiency of our PLL using a PSO-RST controller we will show in addition the results of simulations of the APF. Thus the Fig. 15-19 show the utility voltage source containing harmonics, the current load before filtering, the current injected by the APF, the current source after filtering and the DC voltage. We notice from these simulations that the APF correctly compensates the current harmonics despite a voltage source containing harmonics and the step change in load current at 0.5 s (Table 1).

The controller’s parameters and studied system parameters are represented in Table 2, 3 respectively.

Table 1

Source current THD’s

	Before filtering	After filtering
Before 0.5 s	24.3 %	1.92 %
After 0.5 s	28.51 %	3.66 %

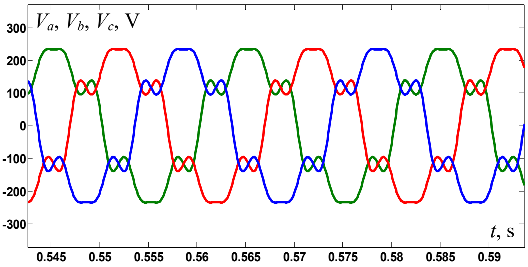

Fig. 15. Utility voltages source under harmonics for SAPF system

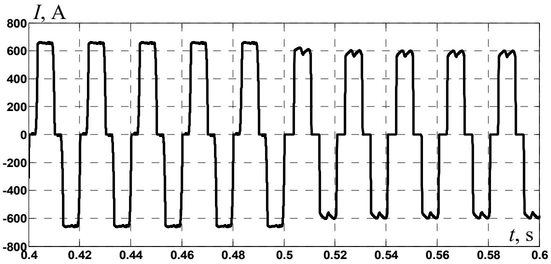

Fig. 16. Current before filtering

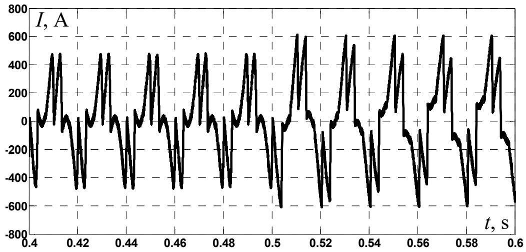

Fig. 17. Current injected by the active power filter

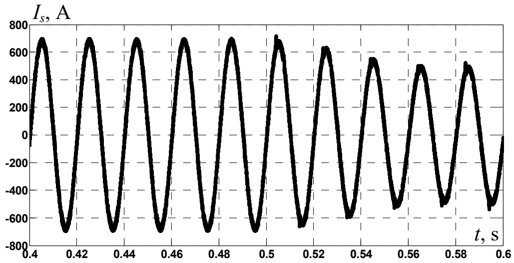

Fig. 18. Current source after filtering

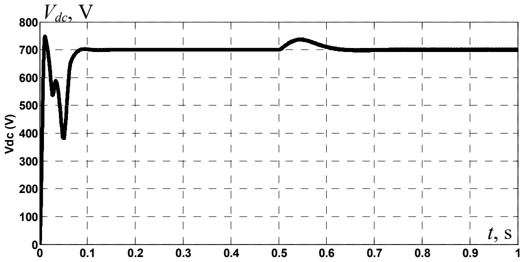

Fig. 19. DC voltage

Table 2

Controller’s parameters

	RST	PSO-RST
s_2	1	2
s_1	439	1452.048
r_1	316.557	603
r_0	900	71348.6
t	900	71348.6

Table 3

Studied system parameters

V, V	240	L_{Load}, mH	2.6
R_s, mΩ	1.59	R_f, mΩ	5
L_s, µH	45.56	L_f, µH	100
R_{Load}, Ω	0.788	V_{dc}, V	700

Conclusions. In this paper, a new robust phase-locked loop based on PSO-RST controller is proposed and applied to an indirect control of a shunt active power filter. The performances of the proposed phase-locked loop has been evaluated and compared to the classical phase-locked loop based on PI and conventional RST controller. The obtained results show that the proposed phase-locked loop reject disturbances in the utility voltage source with fast response which allow having good performances in the control of SAPF even if the source grid is distorted.

Conflict of interest. The authors declare that they have no conflicts of interest.

REFERENCES

1. Akagi H., Kanazawa Y., Fujita K., Nabae A. Generalized theory of instantaneous reactive power and its application. *Electrical Engineering in Japan*, 1983, vol. 103, no. 4, pp. 58-66. doi: https://doi.org/10.1002/eej.4391030409.

2. Jalil M., Amiri A. An Effective Structure of Three-Phase Parallel Hybrid Active Power Filter to Accurate Harmonic Elimination. *2020 15th International Conference on Protection and Automation of Power Systems (IPAPS)*, 2020, pp. 123-129. doi: https://doi.org/10.1109/IPAPS52181.2020.9375544.

3. Bekakra Y., Zellouma L., Malik O. Improved predictive direct power control of shunt active power filter using GWO and ALO – Simulation and experimental study. *Ain Shams Engineering Journal*, 2021, vol. 12, no. 4, pp. 3859-3877. doi: https://doi.org/10.1016/j.asej.2021.04.028.

4. Chelli Z., Lakehal A., Khoualdia T., Djeghader Y. Study on Shunt Active Power Filter Control Strategies of Three-phase Grid-connected Photovoltaic Systems. *Periodica Polytechnica Electrical Engineering and Computer Science*, 2019, vol. 63, no. 3, pp. 213-226. doi: https://doi.org/10.3311/PPee.14025.

5. Mahanty R. Indirect current controlled shunt active power filter for power quality improvement. *International Journal of Electrical Power & Energy Systems*, 2014, vol. 62, pp. 441-449. doi: https://doi.org/10.1016/j.ijepes.2014.05.002.

6. Singh B.N. Sliding mode control technique for indirect current controlled active filter. *Annual Technical Conference IEEE Region 5*, 2003, pp. 51-58. doi: https://doi.org/10.1109/REG5.2003.1199710.

7. Choukri Benhabib M., Saadate S. A New Robust Experimentally Validated Phase Locked Loop for Power Electronic Control. *EPE Journal*, 2005, vol. 15, no. 3, pp. 36-48. doi: https://doi.org/10.1080/09398368.2005.11463595.

8. Biricik S., Ozerdem O.C., Redif S., Kmail M.I.O. Performance Improvement of Active Power Filter under Distorted and Unbalanced Grid Voltage Conditions. *Elektronika Ir Elektrotechnika*, 2013, vol. 19, no. 1, pp. 35-39. doi: https://doi.org/10.5755/j01.eee.19.1.3247.

9. Kaura V., Blasko V. Operation of a phase locked loop system under distorted utility conditions. *IEEE Transactions on Industry Applications*, 1997, vol. 33, no. 1, pp. 58-63. doi: https://doi.org/10.1109/28.567077.

10. Ali S., Setiawan I., Handoko S. Design and Performance Test of Three Phased Synchronous Reference Frame-Phase Locked Loop (SRF-PLL) using DSPIC30F4011. *2018 5th International Conference on Information Technology, Computer, and Electrical Engineering (ICITACEE)*, 2018, pp. 51-56. doi: https://doi.org/10.1109/ICITACEE.2018.8576978.

11. Aredes M., Monteiro L.F.C., Miguel J.M. Control strategies for series and shunt active filters. *2003 IEEE Bologna Power Tech Conference Proceedings*, 2003, vol. 2, pp. 955-960. doi: https://doi.org/10.1109/PTC.2003.1304675.

12. Verma A.K., Jarial R.K., Rao U.M. An Improved Pre-Filtered Three-Phase SRF-PLL for Rapid Detection of Grid Voltage Attributes. *2019 National Power Electronics Conference (NPEC)*, 2019, pp. 1-4. doi: https://doi.org/10.1109/NPEC47332.2019.9034706.

13. Han B., Bae B. Novel Phase-Locked Loop Using Adaptive Linear Combiner. *IEEE Transactions on Power Delivery*, 2006, vol. 21, no. 1, pp. 513-514. doi: https://doi.org/10.1109/TPWRD.2005.860436.

14. Sepahvand H., Saniei M., Mortazavi S.S., Golestan S. Performance improvement of single-phase PLLs under adverse grid conditions: An FIR filtering-based approach. *Electric Power Systems Research*, 2021, vol. 190, p. 106829. doi: https://doi.org/10.1016/j.epsr.2020.106829.

15. Xu J., Qian H., Hu Y., Bian S., Xie S. Overview of SOGI-Based Single-Phase Phase-Locked Loops for Grid Synchronization Under Complex Grid Conditions. *IEEE Access*, 2021, vol. 9, pp. 39275-39291. doi: https://doi.org/10.1109/ACCESS.2021.3063774.

16. Nazib A.A., Holmes D.G., McGrath B.P. Decoupled DSOGI-PLL for Improved Three Phase Grid Synchronisation. *2018 International Power Electronics Conference (IPEC-Niigata 2018-ECCE Asia)*, 2018, pp. 3670-3677. doi: https://doi.org/10.23919/IPEC.2018.8507364.

17. Elmansouri A., El mhamdi J., Boualouch A. Wind energy conversion system using DFIG controlled by back-stepping and RST controller. *2016 International Conference on Electrical and Information Technologies (ICEIT)*, 2016, pp. 312-318. doi: https://doi.org/10.1109/EITech.2016.7519612.

18. Vongkoon P., Liutanakul P. Frequency Estimation Improvement for Single-Phase Phase-Locked Loop Using Digital RST controller. *2019 IEEE PES GTD Grand International Conference and Exposition Asia (GTD Asia)*, 2019, pp. 490-494. doi: https://doi.org/10.1109/GTDAsia.2019.8715963.

19. Robert D., Sename O., Simon D. Sampling period dependent RST controller used in control/scheduling co-design. *IFAC Proceedings Volumes*, 2005, vol. 38, no. 1, pp. 225-230. doi: https://doi.org/10.3182/20050703-6-CZ-1902.01077.

20. Poitiers F., Machmoum M., Le Doeuff R., Zaim M.E. Control of a doubly-fed induction generator for wind energy conversion systems. *International Journal of Renewable Energy Engineering*, 2001, vol. 3, no. 3, pp. 373-378.

21. Eberhart R., Kennedy J. A new optimizer using particle swarm theory. *MHS'95. Proceedings of the Sixth International Symposium on Micro Machine and Human Science*, 1995, pp. 39-43. doi: https://doi.org/10.1109/MHS.1995.494215.

22. Bourouis M. el A., Zadjaoui A., Djedid A. Contribution of two artificial intelligence techniques in predicting the secondary compression index of fine-grained soils. *Innovative Infrastructure Solutions*, 2020, vol. 5, no. 3, p. 96. doi: https://doi.org/10.1007/s41062-020-00348-1.

23. Eberhart R., Yuhui Shi. Particle swarm optimization: developments, applications and resources. *Proceedings of the 2001 Congress on Evolutionary Computation (IEEE Cat. No.01TH8546)*, 2001, vol. 1, pp. 81-86. doi: https://doi.org/10.1109/CEC.2001.934374.

Received 15.02.2022
Accepted 04.04.2022
Published 20.07.2022

Abdelkarim Chemidi[1,2]*, Doctor of Electrical Engineering, Associate Professor,*
Mohamed Choukri Benhabib[2,3]*, Doctor of Electrical Engineering, Professor,*
Mohammed el amin Bourouis[3]*, PhD,*
[1] School of Applied Sciences Tlemcen,
BP 165 RP Bel horizon, 13000 Tlemcen, Algeria,
e-mail: chemidi.abdelkarim@gmail.com (Corresponding author),
[2] Manufacturing Engineering Laboratory of Tlemcen,
13000 Tlemcen, Algeria,
e-mail: benhabibc@gmail.com
[3] University of Tlemcen,
22, Rue Abi Ayed Abdelkrim Fg Pasteur B.P 119 13000,
Tlemcen, Algeria,
e-mail: medamin_bourouis@yahoo.fr

How to cite this article:
Chemidi A., Benhabib M.C., Bourouis M.A. Performance improvement of shunt active power filter based on indirect control with a new robust phase-locked loop. *Electrical Engineering & Electromechanics*, 2022, no. 4, pp. 51-56. doi: https://doi.org/10.20998/2074-272X.2022.4.07

UDC 621.3 https://doi.org/10.20998/2074-272X.2022.4.08

N. Mezhoud, B. Ayachi, M. Amarouayache

Multi-objective optimal power flow based gray wolf optimization method

Introduction. *One of predominant problems in energy systems is the economic operation of electric energy generating systems. In this paper, one a new evolutionary optimization approach, based on the behavior of meta-heuristic called grey wolf optimization is applied to solve the single and multi-objective optimal power flow and emission index problems.* ***Problem.*** *The optimal power flow are non-linear and non-convex very constrained optimization problems.* ***Goal*** *is to minimize an objective function necessary for a best balance between the energy production and its consumption, which is presented as a nonlinear function, taking into account of the equality and inequality constraints.* ***Methodology.*** *The grey wolf optimization algorithm is a nature inspired comprehensive optimization method, used to determine the optimal values of the continuous and discrete control variables.* ***Practical value.*** *The effectiveness and robustness of the proposed method have been examined and tested on the standard IEEE 30-bus test system with multi-objective optimization problem. The* ***results*** *of proposed method have been compared and validated with hose known references published recently.* ***Originality.*** *The results are promising and show the effectiveness and robustness of proposed approach.* References 35, tables 3, figures 6.

Keywords: **optimization, power networks, optimal power flow, emission index, grey wolf optimization.**

Вступ*. Однією з головних проблем енергетичних системах є економічна експлуатація систем виробництва електроенергії. У цій статті один новий підхід до еволюційної оптимізації, заснований на поведінці метаевристики, яка називається оптимізацією сірого вовка, застосовується для вирішення одно- та багатокритеріальних завдань оптимального потоку потужності та індексу викидів.* ***Проблема****. Оптимальний потік потужності - це нелінійні та неопуклі задачі оптимізації з дуже обмеженнями.* ***Метою*** *є мінімізація цільової функції, необхідної для найкращого балансу між виробництвом та споживанням енергії, яка представлена у вигляді нелінійної функції з урахуванням обмежень рівності та нерівності.* ***Методологія****. Алгоритм оптимізації сірого вовка - це натхненний природою комплексний метод оптимізації, що використовується для визначення оптимальних значень безперервних і дискретних змінних, що управляють.* ***Практична цінність****. Ефективність та надійність запропонованого методу були перевірені та протестовані на стандартній 30-шинній тестовій системі IEEE із завданням багатокритеріальної оптимізації.* ***Результати*** *запропонованого методу були зіставлені та підтверджені нещодавно опублікованими відомими посиланнями.* ***Оригінальність****. Результати є багатообіцяючими та показують ефективність та надійність запропонованого підходу.* Бібл. 35, табл. 3, рис. 6.

Ключові слова: **оптимізація, енергетичні мережі, оптимальний потік потужності, індекс викидів, оптимізація методом сірого вовка.**

Introduction. The optimal power flow (OPF) problem has a long history of development of more than 60 years. Since the OPF problem was first discussed by Carpenter in 1962, then formulated by Dommel and Tinney in 1968 [1].

Power plants coal-fired contribute a large quantity of polluting gases to the atmosphere, as they produce large amounts of carbon oxides CO_2 and some toxic and dangerous gases such as emissions of sulfur oxides SO_x, and nitrogen oxides NO_x [1, 2].

Over the past few years, various methods have been implemented to solve the OPF and emission index (EI) problems such as: quadratic programming method (QP) [3], Newton and quasi-Newton methods [4, 5], linear and non-linear programming methods [6, 7], and nonlinear internal point methods (IPM) [8].

Several methods of optimization are formulated in the last two decades such as: artificial bee colony (ABC) [9], bacterial foraging algorithms (BFA) [10], artificial neutral networks (ANN) [11], harmony search (HS) [12], Cuckoo search algorithm (CSA) [13], evolution programming (EP) [14], differential evaluation (DE) [15], tabu search (TS) [16], simulated annealing (SA) [17], gravitational search algorithms (GSA) [18], genetic algorithms (GA) [19], particle swarm optimization (PSO) [20], ant colony optimization (ACO) [21], firefly algorithm (FFA) [22], sine-cosine algorithm (SCA) [23], modified imperialist competitive algorithm (MICA) [24], moth swarm algorithm (MSA) [25], electromagnetism-like mechanism method (ELM) [26], wind driven optimization (WDO) method [27], machine learning [28], teaching-learning-studying-based optimization algorithm [29], and more recently grey wolf optimizer (GWO) [30, 31]. Variants of these algorithms were proposed to handle multi-objective functions in electric power systems.

The proposed GWO approach is tested and illustrated by numerical examples based on IEEE 30-bus test system.

Problem formulation. The OPF and EI are nonlinear optimization problems, represented by a predefined objective function *f*, subject to a set of equality and inequality constraints [27, 32]. Generally, these problems can be expressed as follows:

$$\min f(x, u), \tag{1}$$

subject to

$$h(x, u) = 0; \tag{2}$$

$$g(x, u) \le 0; \tag{3}$$

$$x_{\min} \le x \le x_{\max} \text{ and } u_{\min} \le u \le u_{\max}, \tag{4}$$

where $f(x, u)$ is a scalar objective function to be optimized; and $g(x, u)$ are, respectively, the set of nonlinear equality constraints represented by the load flow equations and inequality constraints consists of state variable limits and functional operating constraints; x and u are the state and control variables vectors respectively; $x_{\min}$, $x_{\max}$, $u_{\min}$, $u_{\max}$ are the acceptable limits of the variables.

Hence, x and u can be expressed as given

$$x^t = \left\{P_{G_1}, \left|V_{L_1}\right|, \ldots \left|V_{L_{nL}}\right|, Q_{G_1}, \ldots Q_{G_{ng}}, S_1, \ldots, S_{n_{br}}\right\}, \tag{5}$$

where P_G, Q_G, V_L, and S_k are the generating active power at slack bus, reactive power generated by all generators, magnitude voltage of all load buses and apparent power flow in all branches, respectively; n_g, n_L, and n_{br} are, respectively, the total number of generators, the total number of load buses and the total number of branches.

The set control parameters are represented in terms of the decision vector as follows:

$$u^t = \left\{P_{G_2},...,P_{G_{ng}},\left|V_{G_1}\right|,...\left|V_{G_{ng}}\right|,Q_{1_{com}},...Q_{n_{com}},T_1,...,T_{n_T}\right\}, \quad (6)$$

where P_G is the active power generation excluding the slack generator; V_G is the generators magnitude voltage; T is tap settings transformers; Q_{com} is the reactive power compensation by shunt compensator; n_T and n_{com} are the total number of transformers and the total number of compensators units, respectively.

Cost without valve-point optimization. The objective function of cost optimization f_1 of quadratic cost equation for all generators as given below:

$$f_1 = \min\sum_{k=1}^{n_g} C(P_{gk}) = \min\sum_{k=1}^{n_g} a_k + b_k P_{gk} + c_k P_{gk}^2 \ , \quad (7)$$

where f_1 is the total generation cost in (\$/h); P_{gk} and n_g are the active power output generated by the i^{th} generator and the total number of generators; a_k, b_k, c_k are the cost coefficients of the generator k.

Cost with valve-point optimization. Generally, when every steam valves begins to open, the valve-point shows rippling. However, the characteristics of input-output of generation units make nonlinear and non-smooth of the fuel costs function. To consider the valve-point effect, the sinusoidal function is incorporated into the quadratic function. Typically, this function is represented as follows

$$\begin{aligned} f_2 = \min\sum_{k=1}^{n_g}\left[a_k + b_k P_{gk} + c_k P_{gk}^2\right] + \\ + \left|d_k \sin\left(e_k\left(P_{gk}^{\min} - P_{gk}\right)\right)\right|, \end{aligned} \quad (8)$$

where d_k and e_k are the cost coefficients of unit with valve-point effect.

Active power loss optimization. The active power loss function f_3 in MW to be minimized can be expressed as follows:

$$f_3 = \sum_{k=1}^{n_b} G_{kj}\left[V_k^2 + V_j^2 - 2V_k V_j \cos\theta_{kj}\right], \quad (9)$$

where V_k and V_j are the magnitude voltage at buses k and j, respectively; G_{kj} is the conductance of line kj; θ_{kj} is the voltage angle between buses k and j; n_b is total number of buses.

Emission optimization. The emission function is the sum of exponential and quadratic functions of real power generating. Using a quadratic equation, emission of harmful gases is calculated in (ton/h) as given below

$$\begin{aligned} f_4 = \min\sum_{k=1}^{n_g} 10^{-2}\left(\alpha_k + \beta_k P_{gk} + \gamma_k P_{gk}^2\right) + \\ + \zeta_k \exp\left(\lambda_k P_{gk}\right), \end{aligned} \quad (10)$$

where f_4 is the emission function in (ton/h); α_k, β_k, γ_k, ζ_k, λ_k are the emission coefficients of the generator k.

All multi-objective functions using aggregation weighting function. The function used in the case of weighted aggregation is given as

$$\min F = \sum_{i=1}^{n_f} \omega_i f_i \ \text{with} \ \omega_i \geq 0 \ \text{and} \ \sum_{i=1}^{n_f} \omega_i = 1, \quad (11)$$

where $\sum_{i=1}^{n_f} \omega_i = 1$ and $i = 1 : n_f$, ω_i is the weighting factor; n_f is the number of objective function considered.

Equality constraints. These equality constraints are the sets of nonlinear load flow equations that govern the power system, i.e.:

$$\begin{cases} P_{gk} = P_k + P_{dk}; \\ Q_{gk} - Q_{Comk} = Q_k + Q_{dk}, \end{cases} \quad (12)$$

where P_{gk} and Q_{gk} are, respectively, the scheduled active and reactive power generations at bus k; P_k, Q_k are the active and reactive power injections at bus k; P_{dk}, Q_{dk}, Q_{Comk} are the active and reactive power loads at bus k and the reactive power compensation at bus k.

Inequalitie constraints. The inequality constraints $g(x, u)$ are represented by the system operational and security limits, listed below:

- Active and reactive power generations limits:

$$P_{gk}^{\min} \leq P_{gk} \leq P_{gk}^{\max} \ \text{where} \ k = 1,...,n_g \ ; \quad (13)$$

$$Q_{gk}^{\min} \leq Q_{gk} \leq Q_{gk}^{\max} \ \text{where} \ k = 1,...,n_g \ ; \quad (14)$$

- Voltage magnitudes and angles limits:

$$V_k^{\min} \leq V_k \leq V_k^{\max} \ \text{where} \ k = 1,...,n_b; \quad (15)$$

$$\theta_k^{\min} \leq \theta_k \leq \theta_k^{\max} \ \text{where} \ k = 1,...,n_b; \quad (16)$$

- Tap settings transformers limits:

$$T_k^{\min} \leq T_k \leq T_k^{\max} \ \text{where} \ k = 1,...,n_T \ ; \quad (17)$$

- Reactive power compensation limits:

$$Q_{Comk}^{\min} \leq Q_{Comk} \leq Q_{comk}^{\max} \ \text{where} \ k = 1,.....,n_{Com} \ ; \quad (18)$$

- Security constraint limits:

$$S_{kj} \leq S_{kj}^{\max} \ \text{where} \ k = j = 1,.....,n_b \ , \quad (19)$$

where n_T, n_{Com}, T and Q_{Com} are the total number of transformers, the total number of compensator, the transformers tap settings, the reactive power compensation; $S_{kj}^{\max}$ is the maximum apparent power between buses k and j.

Grey wolf optimization (GWO) is a typical swarm-intelligence based meta-heuristic algorithm proposed by Mirjalili et al. in 2014 [33] which is inspired from the leadership hierarchy and hunting mechanism of Grey Wolves in nature. In nature, Gray Wolf (Canis lupus) belongs to Canidae family. It is considered as a top level of predators and residing at the top in the food chain.

The population hierarchies of grey wolves are separated by 4 layers which are named as, alpha (α) is the fittest solution. Beta (β) is the second optimum solution and delta (δ) is the third one. Omega (ω) is the candidate solutions that are left over [30]. Generally, the populations of grey wolves have average crowd size of 5-12 and the cluster organizes compactly through the hierarchy [30].

The position of the wolves is considered as the variables to be optimized and the distance between prey and grey wolves determine the fitness value of the objective function. The movement of each individual is influenced by 4 processes, namely [30]:

1. Searching for prey (exploration);
2. Encircling prey;
3. Hunting;
4. Attacking prey (exploitation).

The following sub-section explained these operators.

A. Social hierarchy. The grey wolves diverge from each other position for searching a victim. Make use of $\vec{A}_M$ with random values to compel the search agent to diverge from the victim. The component $\vec{C}_M$ provides random weights for searching prey in the search space.

B. Encircling prey. As mentioned above, grey wolves encircle prey during the hunt. α, β and δ estimate the position of the 3 best wolves and other wolves updates their positions using the positions of these 3 best wolves. Encircling behavior can be represented by $\vec{D}_M$. When the wolves do hunting, they tend to encircle their prey. The following equations depicted the encircling behavior [33, 34].

$$\vec{D}_M = \left| \vec{C}_M \, \vec{X}_P(t) - \vec{X}(t) \right| ; \tag{20}$$

$$\vec{X}(t+1) = \vec{X}_P(t) - \vec{A}_M . \vec{D}_M \, , \tag{21}$$

where t is the current iteration; $\vec{X}$ is the position vector of gray wolf; $\vec{X}_P$ is the position of the prey; $\vec{A}_M$ and $\vec{C}_M$ are the coefficient vectors calculated using the following expressions [30, 33]:

$$\vec{A}_M = 2\,\vec{a}\,.\,\vec{r}_1 - \vec{a} \quad \text{and} \quad \vec{C}_M = 2\vec{r}_2 \, , \tag{22}$$

where $\vec{r}_1$ and $\vec{r}_2$ are random vectors between 0 and 1 and $\vec{a}$ is set to decreased from 2 to 0 over the course of iterations. The 3 best solutions so far are saved and then the other search agents (omega wolves) update their positions according to the current best position [31, 34].

C. Hunting. Conservation of regional habitat connectivity has the potential to facilitate recovery of the grey wolf. After encircling, α wolf guides for hunting. Later, β and δ wolves join in hunting [33]. It is tough to predict about the optimum location of prey. These situations are expressed in the following expressions [33]:

$$\vec{D}_{M\alpha} = \left| \vec{C}_{M\alpha} \cdot \vec{X}_\alpha(t) - \vec{X}(t) \right| ; \tag{23}$$

$$\vec{D}_{M\beta} = \left| \vec{C}_{M\beta} \cdot \vec{X}_\beta(t) - \vec{X}(t) \right| ; \tag{24}$$

$$\vec{D}_{M\delta} = \left| \vec{C}_{M\delta} \cdot \vec{X}_\delta(t) - \vec{X}(t) \right| ; \tag{25}$$

$$\begin{aligned} \vec{X}_{1\alpha} &= \vec{X}_\alpha - \vec{A}_{M1} \, \vec{D}_{M\alpha} ; \\ \vec{X}_{1\beta} &= \vec{X}_\beta - \vec{A}_{M2} \, \vec{D}_{M\beta} ; \\ \vec{X}_{1\delta} &= \vec{X}_\delta - \vec{A}_{M3} \, \vec{D}_{M\delta} . \end{aligned} \tag{26}$$

The best position of grey wolf is calculated taking average sum of positions and given as

$$\vec{X}(t+1) = \frac{\vec{X}_{1\alpha} + \vec{X}_{1\beta} + \vec{X}_{1\delta}}{3} . \tag{27}$$

D. Attacking prey. The grey wolves stop the hunting by attacking the prey when it stops moving. It depends on the value of a. $\vec{A}_M$ is a random value in the interval [–2a, 2a]. In GWO, search agents update their positions based on the location of α, β and δ and attack towards the prey [32, 33]. However, GWO algorithm is prone to stagnation in local solutions with these operators. It is true that the encircling mechanism proposed shows exploration to some extent, but GWO needs more operators to emphasize exploration [33, 34].

Simulation and results. The 5 generators system, IEEE 30-bus system is used throughout this work to test the proposed algorithm. This system consist 30 buses, 6 generators units and 41 branches, 37 of them are the transmissions lines and 4 are the tap changing transformers. One of these buses is chosen like as a reference bus (slack bus), the buses containing generators are taken the PV buses, the remaining buses are the PQ buses or loads buses. It is assumed that 9 capacitors compensation is available at buses 10, 12, 15, 17, 20, 21, 23, 24 and 29. The network data, the cost and emission coefficients of the five generators are referred in [35]. The one-line diagram IEEE 30-bus system is shown in Fig. 1.

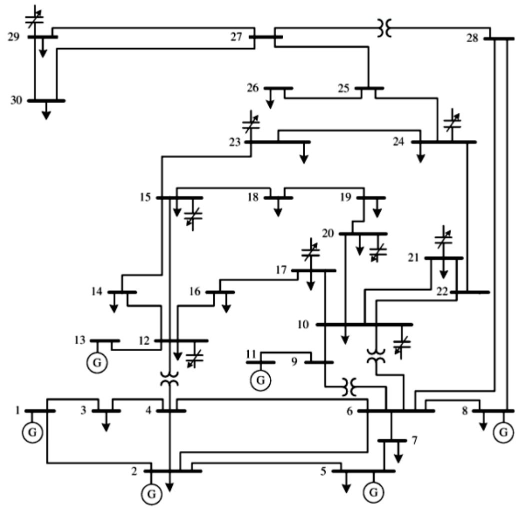

Fig. 1. One-line diagram of IEEE 30-bus system

The total loads of active and reactive powers are 283.4 MW and 126.2 MVAr, respectively, with 24 control variables. The basis apparent power used in this paper is 100 MVA. The simulation results of load flow problem of test system are summarized in Table 1.

A. Case 1: Cost optimization without valve-point effect. The cost function f_1 given in (7) is optimized. Therefore, in this case, the cost has resulted in 801.65 $/h, which is considered 8.301 % lower than the initial case (load flow). Figure 2 shows the convergence of cost using GWO algorithm. Table 1 summarizes the optimal control variables of this case.

B. Case 2: Cost optimization with valve-point effect. The cost function f_2 is optimized. Therefore, in this case, the cost has resulted in 836.73 $/h, which is considered 4.288 % lower than the initial case. The convergence characteristic of cost for this case is introduced in Fig. 2. The optimal control variables of this case are presented in Table 1.

C. Case 3: Active power loss optimization. The optimal control variables of this case are introduced in Table 1. Figure 3 shows the trend for convergence characteristics of active power losses using GWO algorithm. The active power loss minimization has dramatically decreased to 5.072 MW.

Table 1

Results of case 1, 2 and 3 for test system

Control variables	Optimal values			
	Base	Case 1	Case 2	Case 3
P_{G2}, MW	40	46.53	36.57	66.930
P_{G5}, MW	0	21.71	17.06	50
P_{G8}, MW	0	18.36	18.44	13.533
P_{G11}, MW	0	15.03	12.64	22.466
P_{G13}, MW	0	15.26	12.45	29.854
V_1, pu	1.060	1.085	1.087	1.071
V_2, pu	1.045	1.066	1.064	1.061
V_5, pu	1.050	1.035	1.032	1.040
V_8, pu	1.070	1.038	1.036	1.040
V_{11}, pu	1.090	1.088	1.047	1.068
V_{13}, pu	1.090	1.022	1.027	1.064
Q_{com10}, MVAr	0	2.372	1.185	2.083
Q_{com12}, MVAr	0	0.330	4.804	2.198
Q_{com15}, MVAr	0	3.462	3.158	0.934
Q_{com17}, MVAr	0	1.139	4.612	1.319
Q_{com20}, MVAr	0	1.667	3.320	0.864
Q_{com21}, MVAr	0	2.321	2.095	1.756
Q_{com23}, MVAr	0	1.962	2.136	1.516
Q_{com24}, MVAr	0	4.765	3.672	1.586
Q_{com29}, MVAr	0	3.180	2.985	3.012
$T_{6\text{-}9}$	0.978	1.046	1.000	0.985
$T_{6\text{-}10}$	0.969	0.971	0.995	0.975
$T_{4\text{-}12}$	0.966	0.974	0.996	0.991
$T_{27\text{-}28}$	0.932	0.993	0.999	0.973
Cost, $/h	**874.22**	**801.65**	**836.73**	–
Losses, MW	**17.56**	–	–	**5.072**
Emission, ton/h	**4.100**	–	–	–
Slack, MW	260.96	175.43	196.4	105.687
CPU time, s	19.820	79.710	83.77	91.791

D. Case 4: Emission optimization. In this case, the emission reduction yielded 0.215 ton/h. The optimal control variables settings for this case are detailed in Table 1. The convergence characteristics of emission is shown in Fig. 4.

E. Case 5: Cost and active loss optimization. The control variables of this case are tabulated in detail in Table 2. The cost and the power losses has resulted in 814.45 $/h and 7.4 MW, respectively. The convergence result of this case is presented in Fig. 5.

F. Case 6: Cost and emission optimization. The control variables of this case are tabulated in detail in Table 2. The cost and emission has resulted, respectively, in 801.88 $/h and 0.267 ton/h. Figure 6 shows the convergence algorithm obtained in case 5.

G. Case 7: Cost, active power loss and emission. The control variables of this case are presented in detail in Table 2. The cost optimization obtained in this case is presented in Fig. 2.

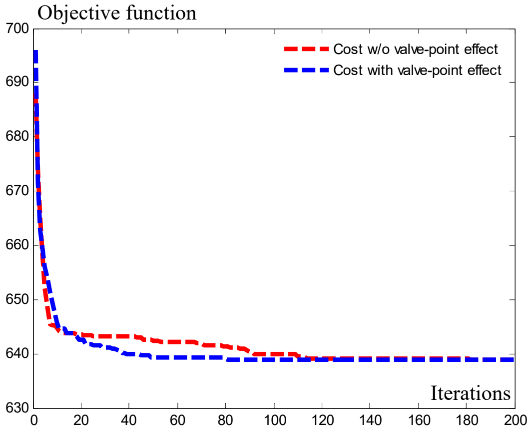

Fig. 2. Convergence algorithm for cases 1 and 2

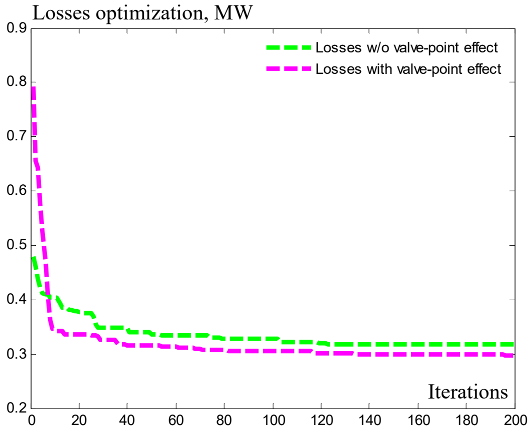

Fig. 3. Convergence algorithm for case 3

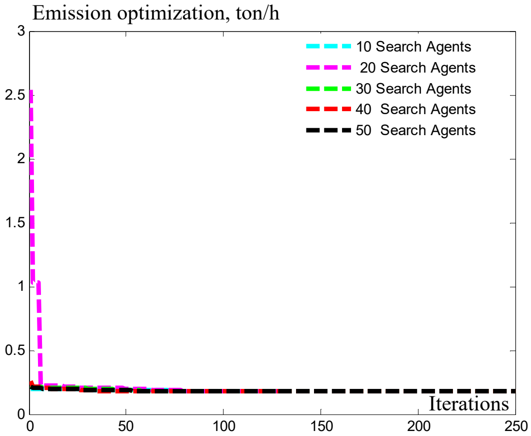

Fig. 4. Convergence algorithm for case 4

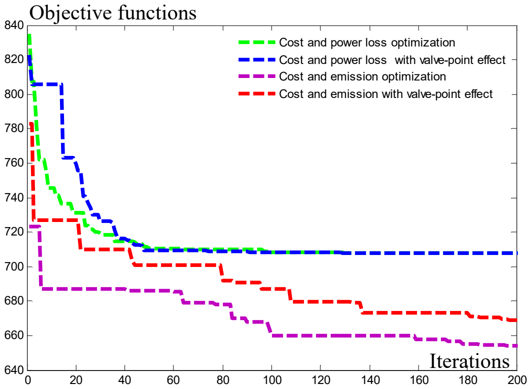

Fig. 5. Convergence algorithm for cases 5 and 6

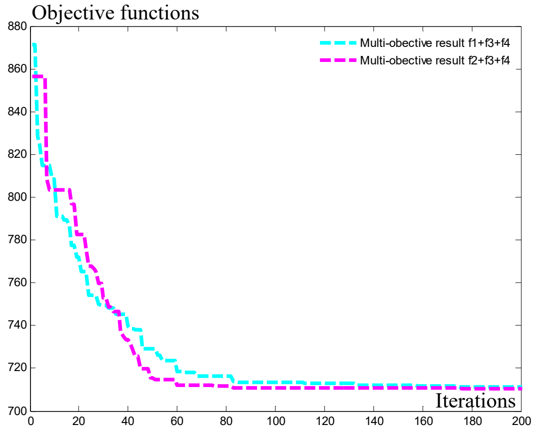

Fig. 6. Convergence algorithm for case 7

Table 2

Results of cases 4, 5, 6 and 7 for test system

Control variables	Optimal values			
	Case 4	Case 5	Case 6	Case 7
P_{G2}, MW	76.762	60.385	47.081	53.489
P_{G5}, MW	50	26.084	20.674	30.009
P_{G8}, MW	26.991	15.136	21.764	34.998
P_{G11}, MW	30	20.436	13.838	18.426
P_{G13}, MW	40	23.063	15.590	23.746
V_1, pu	1.042	1.078	1.083	1.073
V_2, pu	1.032	1.064	1.065	1.060
V_5, pu	1.003	1.034	1.033	1.032
V_8, pu	0.999	1.038	1.040	1.039
V_{11}, pu	1.004	1.098	1.069	1.082
V_{13}, pu	1.011	1.049	1.045	1.051
Q_{com10}, MVAr	2.887	3.674	2.488	2.286
Q_{com12}, MVAr	2.193	3.143	1.277	1.414
Q_{com15}, MVAr	1.092	2.047	2.774	1.749
Q_{com17}, MVAr	1.771	2.508	1.688	4.259
Q_{com20}, MVAr	3.213	2.539	2.294	2.561
Q_{com21}, MVAr	2.972	1.584	1.297	3.274
Q_{com23}, MVAr	3.749	1.330	3.604	1.828
Q_{com24}, MVAr	3.506	4.274	1.192	2.970
Q_{com29}, MVAr	3.247	0.313	2.277	2.971
$T_{6\text{-}9}$	1.078	1.036	1.041	1.010
$T_{6\text{-}10}$	0.939	0.940	0.922	0.995
$T_{4\text{-}12}$	1.006	0.971	0.974	0.994
$T_{27\text{-}28}$	0.924	0.980	0.973	0.982
Cost, $/h	–	**814.45**	**801.88**	**823.00**
Losses, MW	–	**7.40**	–	**6.038**
Emission, ton/h	**0.215**	–	**0.267**	**0.227**
Slack, MW	63.681	145.69	173.28	128.768
CPU time, s	74.987	81.601	86.01	99.374

For the IEEE-30 bus system, 24 control variables (5 generators excluding slack bus, 6 generators magnitude voltages, 4 transformers taps and 9 reactive powers compensators) were optimized. Tables 3 shows a comparison between the obtained results.

Table 3

Comparison of obtained results for cases 5, 6 and 7

Methods		Cost, $/h	Losses, MW	Emission, $/ton
Methods	Reference			
Case 5				
Proposed	–	**814.45**	**7.40**	**0.2524**
MSA	[25]	859.191	4.540	–
ABC	[9]	854.913	4.982	–
PSO	[20]	878.873	7.810	–
DE	[15]	820.880	5.594	–
Case 6				
Proposed	–	**801.88**	–	**0.267**
GA	[19]	820.166	–	0.271
MICA	[24]	865.066	–	0.222
Case 7				
Proposed	–	**823.00**	**6.038**	**0.227**
GA	[19]	793.605	8.450	0.187
IABC	[9]	851.611	4.873	0.223
ABC	[9]	854.916	4.982	0.228
DE	[15]	867.980	5.563	0.266

Conclusions. In this paper, the grey wolf optimization approach is implemented and applied successfully to solve the multi-objective optimal power flow. The obtained results with proposed method in all cases are much better. Therefore, in the multi-objective case, taking into account generation cost, the active power losses optimization and emission optimization all results were significantly decreased to 823 $/h, 6.038 MW and 0.227 ton/h, which are considered 5.85 %, 61.61 % and 44.63 %, respectively, lower than the initial case (load flow). With comparison, the obtained results validate the advantage of the proposed approach over many other methods used to solve the optimal power flow in terms of solution quality. It is concluded that the proposed method has the ability to obtain near global solution with stable convergence characteristics. Thus, the may be recommended the proposed approach as a promising algorithm for solving some more complex engineering problems. The versatility of optimization is illustrated by various tests by changing the parameters of proposed approach such as number of population size and control parameter α_0 coefficient. The simulation results demonstrated the effectiveness and robustness of the proposed methodology.

Conflict of interest. The authors declare that they have no conflicts of interest.

REFERENCES

1. Dommel H., Tinney W. Optimal Power Flow Solutions. *IEEE Transactions on Power Apparatus and Systems*, 1968, vol. PAS-87, no. 10, pp. 1866-1876. doi: https://doi.org/10.1109/TPAS.1968.292150.

2. Talaq J.H., El-Hawary F., El-Hawary M.E. A summary of environmental/economic dispatch algorithms. *IEEE Transactions on Power Systems*, 1994, vol. 9, no. 3, pp. 1508-1516. doi: https://doi.org/10.1109/59.336110.

3. Nicholson H., Sterling M.H. Optimum Dispatch of Active and Reactive Generation by Quadratic Programming. *IEEE Transactions on Power Apparatus and Systems*, 1973, vol. PAS-92, no. 2, pp. 644-654. doi: https://doi.org/10.1109/TPAS.1973.293768.

4. Santos A.Jr., da Costa G.R.M. Optimal-power-flow solution by Newton's method applied to an augmented Lagrangian function. *IEE Proceedings - Generation, Transmission and Distribution*, 1995, vol. 142, no. 1, pp. 33-36. doi: https://doi.org/10.1049/ip-gtd:19951586.

5. Giras T.C., Talukdar S.N. Quasi-Newton method for optimal power flows. *International Journal of Electrical Power & Energy Systems*, 1981, vol. 3, no. 2, pp. 59-64. doi: https://doi.org/10.1016/0142-0615(81)90010-7.

6. Stott B., Hobson E. Power System Security Control Calculations Using Linear Programming, Part I. *IEEE Transactions on Power Apparatus and Systems*, 1978, vol. PAS-97, no. 5, pp. 1713-1720. doi: https://doi.org/10.1109/TPAS.1978.354664.

7. Sasson A. Nonlinear Programming Solutions for Load-Flow, Minimum-Loss, and Economic Dispatching Problems. *IEEE Transactions on Power Apparatus and Systems*, 1969, vol. PAS-88, no. 4, pp. 399-409. doi: https://doi.org/10.1109/TPAS.1969.292460.

8. Capitanescu F., Glavic M., Ernst D., Wehenkel L. Interior-point based algorithms for the solution of optimal power flow problems.

Electric Power Systems Research, 2007, vol. 77, no. 5–6, pp. 508-517. doi: https://doi.org/10.1016/j.epsr.2006.05.003.

9. Mouassa S., Bouktir T. Artificial Bee Colony Algorithm for Solving OPF Problem Considering the Valve Point Effect. *International Journal of Computer Applications*, 2015, vol. 112, no. 1, pp. 45-53. Available at: https://www.ijcaonline.org/archives/volume112/number1/19634-1208 (accessed 23 May 2021).

10. Zakaria Z., Rahman T.K.A., Hassan E.E. Economic load dispatch via an improved Bacterial Foraging Optimization. *2014 IEEE 8th International Power Engineering and Optimization Conference (PEOCO2014)*, 2014, pp. 380-385. doi: https://doi.org/10.1109/PEOCO.2014.6814458.

11. Lai L.L. *Intelligent System Applications in Power Engineering: Evolutionary Programming and Neural Networks*. Wiley Publ., 1998. 286 p.

12. Khazali A.H., Kalantar M. Optimal reactive power dispatch based on harmony search algorithm. *International Journal of Electrical Power & Energy Systems*, 2011, vol. 33, no. 3, pp. 684-692. doi: https://doi.org/10.1016/j.ijepes.2010.11.018.

13. Abd Elazim S.M., Ali E.S. Optimal Power System Stabilizers design via Cuckoo Search algorithm. *International Journal of Electrical Power & Energy Systems*, 2016, vol. 75, pp. 99-107. doi: https://doi.org/10.1016/j.ijepes.2015.08.018.

14. Yuryevich J., Kit Po Wong. Evolutionary programming based optimal power flow algorithm. *IEEE Transactions on Power Systems*, 1999, vol. 14, no. 4, pp. 1245-1250. doi: https://doi.org/10.1109/59.801880.

15. Abou El Ela A.A., Abido M.A., Spea S.R. Optimal power flow using differential evolution algorithm. *Electric Power Systems Research*, 2010, vol. 80, no. 7, pp. 878-885. doi: https://doi.org/10.1016/j.epsr.2009.12.018.

16. Abido M.A. Optimal Power Flow Using Tabu Search Algorithm. *Electric Power Components and Systems*, 2002, vol. 30, no. 5, pp. 469-483. doi: https://doi.org/10.1080/15325000252888425.

17. Jeon Y.-J., Kim J.-C. Application of simulated annealing and tabu search for loss minimization in distribution systems. *International Journal of Electrical Power & Energy Systems*, 2004, vol. 26, no. 1, pp. 9-18. doi: https://doi.org/10.1016/S0142-0615(03)00066-8.

18. Bhowmik A.R., Chakraborty A.K. Solution of optimal power flow using nondominated sorting multi objective gravitational search algorithm. *International Journal of Electrical Power & Energy Systems*, 2014, vol. 62, pp. 323-334. doi: https://doi.org/10.1016/j.ijepes.2014.04.053.

19. Yaşar C., Özyön S. A new hybrid approach for nonconvex economic dispatch problem with valve-point effect. *Energy*, 2011, vol. 36, no. 10, pp. 5838-5845. doi: https://doi.org/10.1016/j.energy.2011.08.041.

20. Abido M.A. Optimal power flow using particle swarm optimization. *International Journal of Electrical Power & Energy Systems*, 2002, vol. 24, no. 7, pp. 563-571. doi: https://doi.org/10.1016/S0142-0615(01)00067-9.

21. Ketabi A., Alibabaee A., Feuillet R. Application of the ant colony search algorithm to reactive power pricing in an open electricity market. *International Journal of Electrical Power & Energy Systems*, 2010, vol. 32, no. 6, pp. 622-628. doi: https://doi.org/10.1016/j.ijepes.2009.11.019.

22. Padaiyatchi S.S. Hybrid DE/FFA algorithm applied for different optimal reactive power dispatch problems. *Australian Journal of Electrical and Electronics Engineering*, 2020, vol. 17, no. 3, pp. 203-210. doi: https://doi.org/10.1080/1448837X.2020.1817233.

23. Attia A.-F., El Sehiemy R.A., Hasanien H.M. Optimal power flow solution in power systems using a novel Sine-Cosine algorithm. *International Journal of Electrical Power & Energy Systems*, 2018, vol. 99, pp. 331-343. doi: https://doi.org/10.1016/j.ijepes.2018.01.024.

24. Ghasemi M., Ghavidel S., Ghanbarian M.M., Gharibzadeh M., Azizi Vahed A. Multi-objective optimal power flow considering the cost, emission, voltage deviation and power losses using multi-objective modified imperialist competitive algorithm. *Energy*, 2014, vol. 78, pp. 276-289. doi: https://doi.org/10.1016/j.energy.2014.10.007.

25. Mohamed A.-A.A., Mohamed Y.S., El-Gaafary A.A.M., Hemeida A.M. Optimal power flow using moth swarm algorithm. *Electric Power Systems Research*, 2017, vol. 142, pp. 190-206. doi: https://doi.org/10.1016/j.epsr.2016.09.025.

26. El-Hana Bouchekara H.R., Abido M.A., Chaib A.E. Optimal Power Flow Using an Improved Electromagnetism-like Mechanism Method. *Electric Power Components and Systems*, 2016, vol. 44, no. 4, pp. 434-449. doi: https://doi.org/10.1080/15325008.2015.1115919.

27. Mezhoud N., Ayachi B., Bahri A. Wind Driven Optimization Approach based Multi-objective Optimal Power Flow and Emission Index Optimization. *International Research Journal of Multidisciplinary Technovation*, 2022, pp. 21-41. doi: https://doi.org/10.54392/irjmt2223.

28. Hasan F., Kargarian A., Mohammadi A. A Survey on Applications of Machine Learning for Optimal Power Flow. *2020 IEEE Texas Power and Energy Conference (TPEC)*, 2020, pp. 1-6. doi: https://doi.org/10.1109/TPEC48276.2020.9042547.

29. Akbari E., Ghasemi M., Gil M., Rahimnejad A., Andrew Gadsden S. Optimal Power Flow via Teaching-Learning-Studying-Based Optimization Algorithm. *Electric Power Components and Systems*, 2021, vol. 49, no. 6–7, pp. 584-601. doi: https://doi.org/10.1080/15325008.2021.1971331.

30. Mohamed A.-A.A., El-Gaafary A.A.M., Mohamed Y.S., Hemeida A.M. Multi-objective Modified Grey Wolf Optimizer for Optimal Power Flow. *2016 Eighteenth International Middle East Power Systems Conference (MEPCON)*, 2016, pp. 982-990. doi: https://doi.org/10.1109/MEPCON.2016.7837016.

31. Dilip L., Bhesdadiya R., Trivedi I., Jangir P. Optimal Power Flow Problem Solution Using Multi-objective Grey Wolf Optimizer Algorithm. In: Hu Y.C., Tiwari S., Mishra K., Trivedi M. (eds) *Intelligent Communication and Computational Technologies. Lecture Notes in Networks and Systems*, 2018, vol. 19. Springer, Singapore. doi: https://doi.org/10.1007/978-981-10-5523-2_18.

32. Ayachi B., Boukra T., Mezhoud N. Multi-objective optimal power flow considering the multi-terminal direct current. *Electrical Engineering & Electromechanics*, 2021, no. 1, pp. 60-66. doi: https://doi.org/10.20998/2074-272X.2021.1.09.

33. Pradhan M., Roy P.K., Pal T. Grey wolf optimization applied to economic load dispatch problems. *International Journal of Electrical Power & Energy Systems*, 2016, vol. 83, pp. 325-334. doi: https://doi.org/10.1016/j.ijepes.2016.04.034.

34. El-Fergany A.A., Hasanien H.M. Single and Multi-objective Optimal Power Flow Using Grey Wolf Optimizer and Differential Evolution Algorithms. *Electric Power Components and Systems*, 2015, vol. 43, no. 13, pp. 1548-1559. doi: https://doi.org/10.1080/15325008.2015.1041625.

35. Lee K.Y., El-Sharkawi M.A. (Eds.). *Modern Heuristic Optimization Techniques*. John Wiley & Sons, Inc., 2008. 586 p. doi: https://doi.org/10.1002/9780470225868.

Received 17.04.2022
Accepted 25.05.2022
Published 20.07.2022

Nabil Mezhoud[1]*, PhD of Power Engineering,*
Bilel Ayachi[1]*, PhD of Power Engineering,*
Mohamed Amarouayache[1]*, PhD of Power Engineering,*
[1] Electrotechnical Laboratory Skikda (LES),
Electrical Engineering Department, Faculty of Technology,
University 20 August 1955, Skikda, Algeria,
e-mail: mezhounab@yahoo.fr (Corresponding author);
b.ayachi@univ-skikda.dz; Amarouayachemohamed@yahoo.fr

How to cite this article:
Mezhoud N., Ayachi B., Amarouayache M. Multi-objective optimal power flow based gray wolf optimization method. *Electrical Engineering & Electromechanics*, 2022, no. 4, pp. 57-62. doi: https://doi.org/10.20998/2074-272X.2022.4.08

UDC 621.3 https://doi.org/10.20998/2074-272X.2022.4.09

A. Zeghoudi, H. Slimani, A. Bendaoud, B. Benazza, S. Bechekir, H. Miloudi

Measurement and analysis of common and differential modes conducted emissions generated by an AC/DC converter

Introduction. *Rectifiers are the most important converters in a very wide field: the transport of electrical energy in direct current and in the applications of direct current motors. In most electrical and electronic systems, rectifiers are non-linear loads made up of diodes, therefore they are a source of harmonic pollution at a base frequency with a distorting line current signal that generates electromagnetic interference. There are two disturbance modes: common mode and differential mode. These disturbances caused by the rapid variation of current and voltage as a function of time due to the switching of active components, passive components such as inductors, capacitors, coupling, etc.* ***The purpose*** *of this work is to study the conducted emissions generated by a rectifier connected to the Line Impedance Stabilizing Network in an electric circuit. The determination of these disturbances is done for firstly both common and differential modes at high frequency, and secondly harmonics current, line current at low frequency.* ***The novelty*** *of the proposed work consists in presenting a study of disturbance generated by rectifiers using simulation and also experimental measurements at low and high frequencies in order to compare the results.* ***Methods.*** *For the study of the disturbances conducted by the diode bridge converter (rectifier), the sources of conducted electromagnetic disturbances were presented in the first time. Then, the common and differential modes were defined. This converter was studied by LTspice Software for simulation and also experimental measurements at low frequency for harmonics current and high frequencies for disturbances in common and differential modes.* ***Results.*** *All the simulations were performed using the LTspice software and the results obtained are validated by experimental measurements performed in the APELEC laboratory at the University of Sidi Bel-Abbes in Algeria. The obtained results of conducted emissions at high frequency and total harmonics distortion of current at low frequency are compared between simulation and experiment.* References 22, figures 13.

Key words: **electromagnetic disturbances, rectifier, line impedance stabilizing network, common mode, differential mode, simulation, measurement.**

Вступ. *Випрямлячі є найважливішими перетворювачами у дуже широкій сфері застосування: передача електроенергії постійного струму та застосування двигунів постійного струму. У більшості електричних та електронних систем випрямлячі є нелінійними навантаженнями, що складаються з діодів, тому вони є джерелом гармонійних «забруднень» на базовій частоті зі спотворенням сигналу лінійного струму, що генерує електромагнітні завади. Існує два режими завад: загальний та диференціальний режим. Ці завади викликані швидкою зміною струму і напруги в залежності від часу через перемикання активних компонентів, пасивних компонентів, таких як котушки індуктивності, конденсатори, муфти та ін.* ***Метою*** *даної роботи є вивчення кондуктивних випромінювань, створюваних випрямлячем, під'єднаним до мережі стабілізатора повного опору лінії в електричному колі. Визначення цих завад проводиться, по-перше, як для загального, такі для диференціального режимів на високій частоті, а по-друге, для гармонічного струму, лінійного струму на низькій частоті.* ***Новизна*** *запропонованої роботи полягає у поданні дослідження завад, створюваних випрямлячами, з використанням моделювання, а також експериментальних вимірювань на низьких та високих частотах для порівняння результатів.* ***Методи***. *Для дослідження завад, створюваних діодним мостовим перетворювачем (випрямлячем), вперше були представлені джерела електромагнітних завад, що виникають. Потім було визначено загальний та диференціальний режими. Цей перетворювач був вивчений програмним забезпеченням LTspice для моделювання, а також експериментальними вимірюваннями на низьких частотах для гармонійного струму та високих частот для завад у загальному та диференціальному режимах.* ***Результати***. *Усі моделювання були виконані з використанням програмного забезпечення LTspice, а отримані результати підтверджені експериментальними вимірюваннями, проведеними в лабораторії APELEC в Університеті Сіді-Бель-Аббес в Алжирі. Отримані результати для кондуктивних завад на високій частоті та повних гармонічних спотворень струму на низькій частоті порівнюються стосовно моделювання та експерименту.* Бібл. 22, рис. 13.

Ключові слова: **електромагнітні завади, випрямляч, мережа стабілізатора повного опору лінії, загальний режим, диференціальний режим, моделювання, вимірювання.**

Introduction. With the development of electrical energy installations, more and more static converters are being connected to the electrical network. They inject the electric power supplied by the generators on the network, but unlike the classical electro-technical systems, they also introduce harmonics LF (low frequency) and HF (high frequency) in two different modes (common mode and differential mode). Electromagnetic compatibility (EMC) is one of the major constraints in the design of power electronics structures. In the case of static converters, the switching of semiconductors and their interactions with environmental interference are the main source of conducted disturbances.

Static converters are made up of electronic switches (diode, IGBT, MOSFET) and passive components (inductance, capacitance), and resistors allowing the conversion and/or the regulation of a voltage (or a current). However, electrical conversion systems are sources of electromagnetic pollution due to the frequency of switching of electronic devices, and the rapid variation of voltage and current as a function of time [1-3]. So the main sources of electromagnetic interference (EMI) in power electronics come from switching converters switches and produce essentially conducted and radiated emissions [4-6]. On the basis of their modes of propagation, disturbances can be distinguished into two types: conducted disturbances, which propagate by electrical conduction, and radiated disturbances, which circulate through an electromagnetic field in the air [6, 7].

The most common conducted disturbances are current and voltage harmonics at low frequencies and electromagnetic disturbances either in common mode or in differential mode at high frequencies, harmonic generators are non-linear loads. They don't absorb a sinusoidal current, although they are supplied with a sinusoidal voltage (diode and thyristor rectifiers, discharge lamps, etc) [8-11].

Rate of harmonic distortion at low frequencies. The total harmonic distortion (THD) rate represents the ratio of the effective value of the harmonics to the effective value of the fundamental. It can be concluded that there are no harmonics on the network if the THD is equal to zero. It is defined as:

$$THD = \sqrt{\sum_{n=2}^{\infty}\left(\frac{x_n}{x_2}\right)^2}, \qquad (1)$$

where x_n is the harmonic component of rank n; x_2 is the second harmonic.

The individual harmonic rate of the current (THD) is defined by the ratio of the amplitude of the n^{th} order harmonic component to the amplitude of the fundamental term component

$$THD_n = \frac{I_1}{I_n}, \qquad (2)$$

where I_n is the harmonic component of rank n; I_1 is the fundamental harmonic.

Figure 1 shows a distorted input current signal due to the non-linear load, due to the presence of the third order harmonic of frequency 150 Hz.

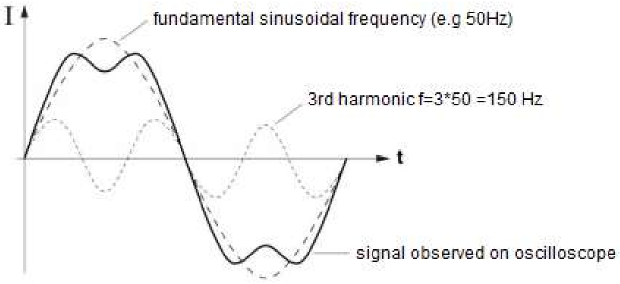

Fig. 1. Input current distortion due to non-linear load [12]

Conducted disturbances in power electronic devices. Various studies [12-16] on conducted electromagnetic pollution have presented measurement techniques in the different types of converters. In [12] the disturbances generated by the chopper are determined in common and differential mode with simulation and experimental. Thus, the interference generated in an inverter fed AC motor [13, 14], in our work we have determined the emissions conducted at LF (odd harmonics) and HF (common mode and differential mode) generated by a single-phase diode bridge in the time approach and frequency approach. The temporal approach uses LTspice circuit simulation software and the noise spectrum is obtained by a fast Fourier transform (FFT) [17, 18].

The emissions conducted at HF subdivides has two categories. The emissions in common mode are generated by the flow of current that propagates in all conductors in the same direction and the return is through the ground or ground plane. This tendency is mainly due to parasitic capacitances in the system that are sensitive to voltage variations and products dv/dt on the lines, and the second category is the differential mode. They are caused by the flow of current that propagates in one conductor in a direction and return in the other conductor in the opposite direction. This current is mainly due to parasitic inductances of the system, which are sensitive to variations in the current di/dt generated on the conductors [19-22].

Figure 2 illustrates the EMI measurement setup in a diode bridge rectifier AC/DC converter with LF. As shown in Fig. 2 in order to visualize the line current and the source voltage, and to determine the odd harmonics generated by the diode bridge rectifier.

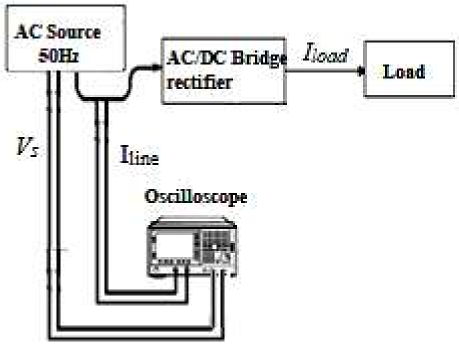

Fig. 2. Descriptive diagram of the single-phase rectifier experimental bench at LF

The second part of the measurement is devoted to the HF conducted emissions, as shown in Fig. 3. The line impedance stabilizing networks (LISN) was inserted between the source and the rectifier. An equivalent circuit for the LISN is shown in Fig. 2. The LISN was used to stabilize the input line impedance and to ensure that the measurement results are only related to the equipment under test without influence of the line impedance [13]. The LISN is connected to a 50 Ω termination or to a spectrum analyzer with an input impedance of 50 Ω. A voltage drop across either 50 Ω impedance constitutes the total conducted noise voltage.

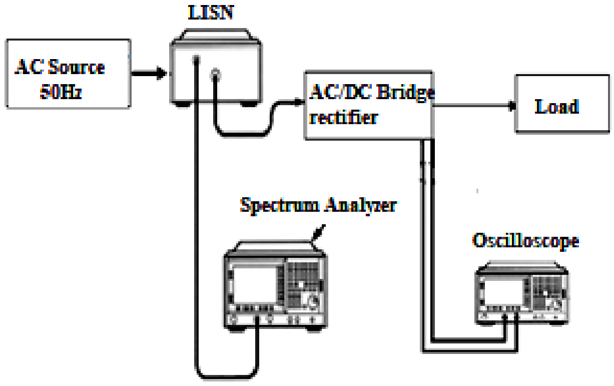

Fig. 3. Descriptive diagram of the single-phase rectifier experimental bench at HF

Study of the disturbances of the AC/DC converters. As long as the line current is positive, energy is supplied by the network, which allows the capacitor to charge. As soon as this current is cancelled, the diodes are blocked. The load and the network are then disconnected, which causes the capacitor to discharge into the resistor. The study of electromagnetic disturbances in static AC/DC converter is done in two steps: study of LF and HF disturbances.

Study of LF disturbances. Simulation of the single-phase diode bridge rectifier. The single-phase rectifier circuit simulated by LTspice Software (Fig. 4) has the following data: V_{res} = 25 V; L_{res} = 600 μH; R_{res} = 0.4 Ω; f = 50 Hz; C_{ch} = 940 μF; R_{ch} = 82 Ω.

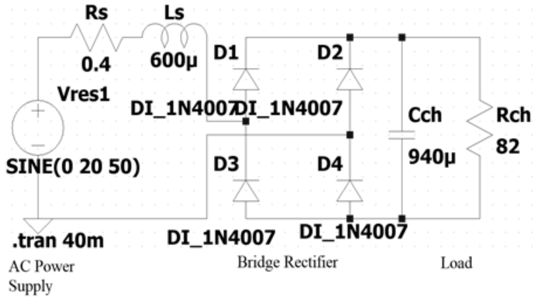

Fig. 4.Diode bridge delivering on a load (LF model)

Experimental measurements. Figures 4, 5 represent respectively the descriptive diagram and a photograph of the experimental bench that has been realized representing the single-phase rectifier of type PD2 based on the rectifier diodes 1N4007.

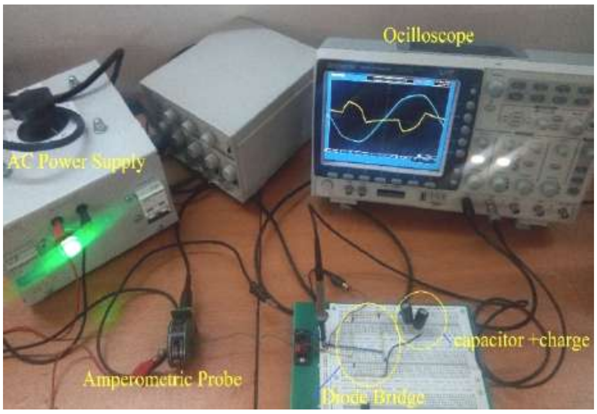

Fig. 5. Photo of the measurement bench of the electromagnetic disturbances generated by a single-phase rectifier in diode bridge

Figures 6, 7 illustrate respectively the voltage at the bridge terminals and the line current I_{lin} that we obtained by simulation and by experimental measurement.

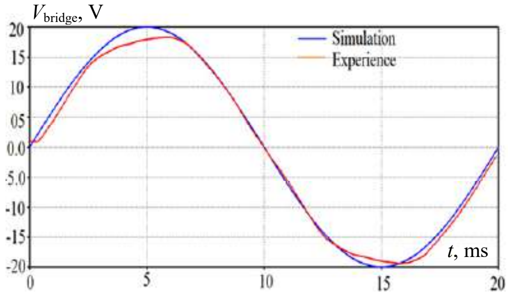

Fig. 6. Voltage at the terminals of the diode bridge V_{bridge}

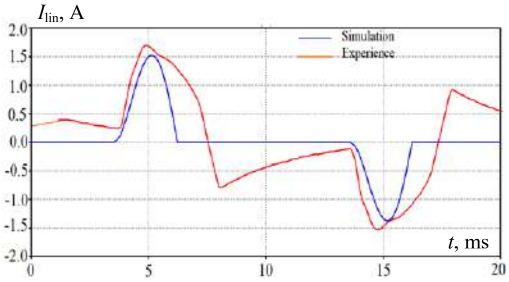

Fig. 7. Line current in the single-phase rectifier I_{lin}

From the voltage at the terminals of the bridge V_{bridge} represented in Fig. 6 and the current of the line I_{lin} represented in Fig. 7 we notice a concordance between the simulation and the measurements, the curves of simulation and measurements are not purely sinusoidal. They present deformations on the voltage at the input of the converter and the current requested by the converter is a periodic signal of period rigorously identical to the initial sinusoid but of very different form because of the non-linear load.

Figure 8 shows the frequency spectrum of the line current I_{lin} that we obtained by simulation and by experimental measurement.

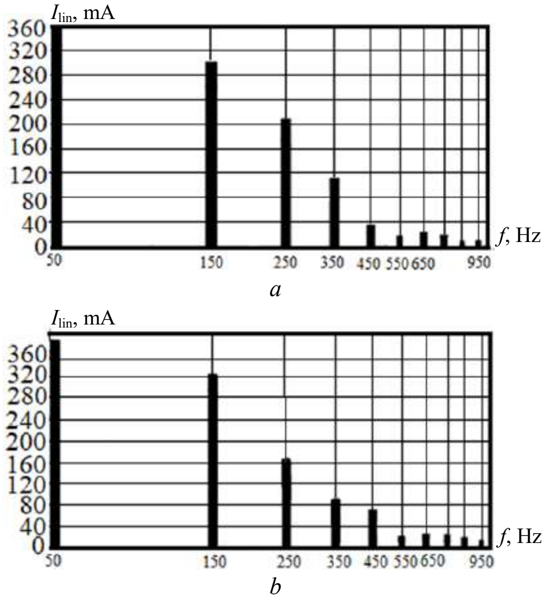

Fig. 8. Line current spectrum:
a) simulation results; *b*) experimental results

From the experimental results obtained, we find that it has a good agreement with those of the simulation. The analysis of the results shows that the amplitudes of the odd LF harmonics of the line current in the case of a single-phase rectifier are larger because the rectifiers (non-linear loads) are sources of harmonics.

Figure 9 shows the temporary variations of the rectified voltage across the load that we obtained by simulation and experimental measurement.

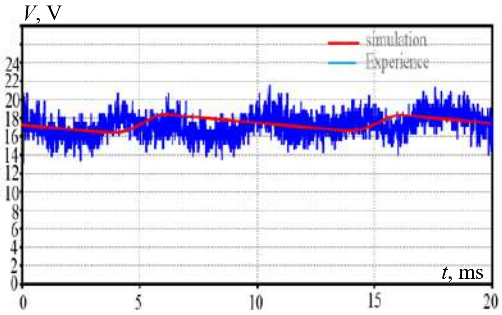

Fig. 9. Rectified voltage at the terminals of the load

Figure 10 shows the frequency variation of the rectified voltage across the load that we obtained by simulation and experimental measurement.

From Fig. 9 we notice a ripple in the rectified voltage, this ripple shows the charge and discharge of the capacitor. In Fig. 10, we notice the harmonics at LF because of the non-linear charge. Thus a resonance peak at 10 kHz, after this resonance frequency there is a slight disturbance.

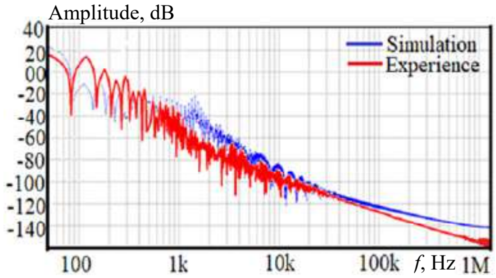

Fig. 10. Frequency variation of the rectified voltage across the load

Study of HF disturbances. All equipment with switching power components produces and emits HF noise. This noise can interfere with the reception of useful signals and can cause system and equipment malfunctions.

In this section, we will present the two main modes of propagation for EMI: the differential mode and the common mode. The disturbances are measured by using the LISN. Two quantities have all the information concerning the diode bridge and the load: the line current and the voltage across the bridge.

Simulation of a single-phase bridge rectifier with LISN. We consider a single-phase rectifier with a LISN and a resistance R_C for load. The circuit of Fig. 11 has the following data: $V_{res} = 20$ V; $f = 50$ Hz; $C_{ch} = 940$ µF; $R_{ch} = 82$ Ω.

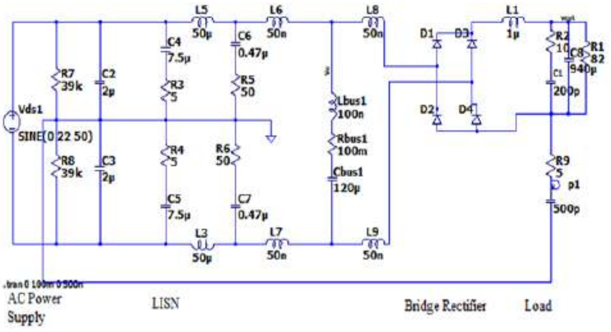

Fig. 11. Diagram of a single-phase diode rectifier with the LISN under LTspice software

Experimental measurements. After the realization of the single-phase diode bridge rectifier, we connected it in series with the LISN, in order to measure the electromagnetic disturbances, as it is presented in Fig. 3.

Study of the disturbances in differential mode. Figure 12 illustrates the frequency variations of the voltage across the LISN equivalent measurement resistor, which represents the current image of the differential mode disturbances generated by the diode bridge.

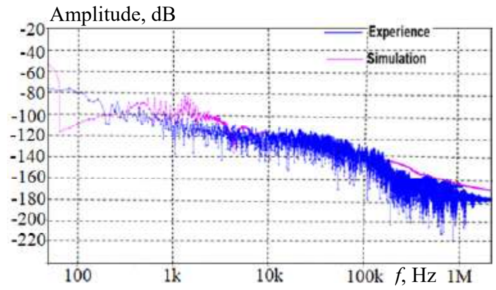

Fig. 12. Spectrum of localized differential disturbances on LISN

From the results of Fig. 12 we note that at the blocking of the diodes an oscillatory phenomenon of a frequency and important amplitude appears. This phenomenon is similar to the voltage jump at the end of the encroachment of the bridge diodes. A similar resonance and the same resonance frequency appear on the spectrum of the AC voltage of the bridge.

Study of the disturbances in common mode. The common mode disturbances were measured in order to compare them with the simulation. In Fig. 13, the results of the frequency variation (common mode current), obtained by simulation and by experimental measurement, are presented.

The results of Fig. 13 present the spectrum of the current in common mode, where we notice an oscillatory phenomenon of a frequency and important amplitude that appears and also a resonance.

By comparing the results of the current spectrum of the two modes, it can be seen that the common mode current spectrum is very high compared to the differential mode current.

In practice, in order to minimize the effect of the common mode current on the differential mode current, the semiconductor radiators and the load ground plane are isolated from the converter ground plane. In reality, the HF behavior of the load requires a more complex analysis of the EMI propagation paths [1].

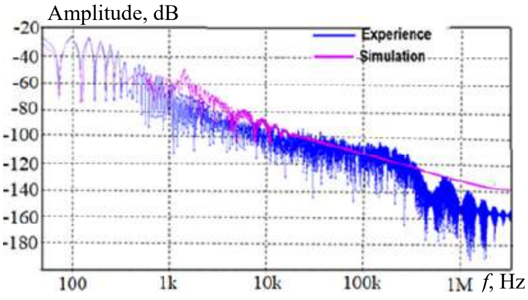

Fig. 13. I_{CM} common mode current spectrum

Conclusions.

1. Considering the importance of the determination of the conducted disturbances generated by the static converters AC/DC in the electric systems, it was decided to carry out this study which is based on the use of the simulation and also the realization of an experimental bench to quantify this emission in the two common and differential modes.
2. From the results obtained, it has been proved practically that the disturbances in common mode are very high compared to the disturbances in differential mode, which requires the use of reduction means in order to weaken or eliminate this type of disturbance, which will be addressed in other future works.
3. The AC/DC converter was studied by LTspice Software for simulation and also experimental measurements at low and high frequencies in order to compare the results. We notice the harmonics at low frequency because of the non-linear charge. Thus a resonance peak, after this resonance frequency there is a slight disturbance.

Conflict of interest. The authors declare that they have no conflicts of interest.

REFERENCES

1. Slimani H., Zeghoudi A., Bendaoud A., Reguig A., Benazza B., Benhadda N. Experimental Measurement of Conducted Emissions Generated by Static Converters in Common and Differential Modes. *European Journal of Electrical Engineering*, 2021, vol. 23, no. 3, pp. 273-279. doi: https://doi.org/10.18280/ejee.230312.

2. Zeghoudi A., Bendaoud A., Canale L., Tilmatine A., Slimani H. Common Mode and Differential Mode noise of AC/DC LED Driver. *2021 IEEE International Conference on Environment and Electrical Engineering and 2021 IEEE Industrial and Commercial Power Systems Europe (EEEIC / I&CPS Europe)*, 2021, pp. 1-6. doi: https://doi.org/10.1109/EEEIC/ICPSEurope51590.2021.9584616.

3. Miloudi M., Bendaoud A., Miloudi H. Common and differential modes of conducted electromagnetic interference switching power converters. *Revue Roumaine des Sciences Techniques Serie Electrotechnique et Energetique*, 2017, vol. 62, no. 3, pp. 246-251.

4. Miloudi M., Bendaoud A., Miloudi H., Nemmich S. Etude et Réduction des Emissions Conduites Générées par l’Alimentation à Découpage (SMPS). *Conférence national sur l’inductique. CI'03*, Tizi–Ouzou, Algérie, April 2013. (Fra).

5. Fakhfakh L., Ammous A. New simplified model for predicting conducted EMI in DC/DC converters. *Electrical Engineering*, 2017, vol. 99, no. 3, pp. 1087-1097. doi: https://doi.org/10.1007/s00202-016-0474-2.

6. Miloudi M., Bendaoud A., Miloudi H. Characterization of Conducted Electromagnetic Interference (EMI) Generated by Switch Mode Power Supply (SMPS). *International Electrical Engineering Conference*, Nov. 2012, Batna, Algeria.

7. Song Zhenfei, Su Donglin, Dai Fei, Duval F., Louis A. A novel electromagnetic radiated emission source identification methodology. *2010 Asia-Pacific International Symposium on Electromagnetic Compatibility*, 2010, pp. 645-648. doi: https://doi.org/10.1109/APEMC.2010.5475803.

8. Costa F., Rojat G. CEM en Electronique de Puissance, Sources de Perturbations, Couplage, SEM. *Techniques de l’ingénieur, Traité Génie Electrique*, D 3290, 15 Août, 2008. (Fra).

9. Hanzelka Z., Bien A. *Guide Power Quality, Section 3: Harmoniques*. Leonardo Energy, Edition Août 2007, AGH University of Science and Technology.

10. Zeghoudi A., Bendaoud A., Canale L., Tilmatine A., Slimani H. Determination of Power Factor and Harmonic Distortion of AC/DC LED Driver. *2021 IEEE International Conference on Environment and Electrical Engineering and 2021 IEEE Industrial and Commercial Power Systems Europe (EEEIC / I&CPS Europe)*, 2021, pp. 1-6. doi: https://doi.org/10.1109/EEEIC/ICPSEurope51590.2021.9584665.

11. Roger C. Dugan, Surya Santoso, Mark F. McGranaghan, H. Wayne Beaty. *Electrical Power System Quality*. McGraw Hill Professional, 2002. 528 p.

12. Zeghoudi A., Bendaoud A., Slimani H., Benazza B., Bennouna D. Determination of electromagnetic disturbances in a buck chopper. *Australian Journal of Electrical and Electronics Engineering*, 2022, vol. 19, no. 2, pp. 149-157. doi: https://doi.org/10.1080/1448837X.2021.2023073.

13. Miloudi H., Bendaoud A., Miloudi M. Réduction des perturbation électromagnétique conduites dans la machine asynchrone. *Mediterranean Journal of Modeling and Simulation*, 2014, vol. 2, no. 1, pp. 8-15.

14. Miloudi H., Bendaoud A., Miloudi M., Gourbi A., Slimani H. Common Mode conducted electromagnetic interference in inverter fed-AC motor. *Przeglad Elektrotechniczny*, 2010, vol. 86, no. 12, pp. 272-275.

15. Miloudi M., Miloudi H., Bendaoud A., Salhi M.A., Al-Omari A.N. Experimental characterization of the high-frequency isolating power transformer. *Elektrotehniski Vestnik/Electrotechnical Review*, 2019, vol. 86, no. 4, pp. 211-218.

16. Chikhi N., Bendaoud A. Evaluation of Conducted Disturbances Generated by the Chopper-rectifier Association Propagating to the Electrical Network. *European Journal of Electrical Engineering*, 2019, vol. 21, no. 1, pp. 1-6. doi: https://doi.org/10.18280/ejee.210101.

17. Tarateeraseth V., Maio I.A., Canavero F.G. Assessment of Equivalent Noise Source Approach for EMI Simulations of Boost Converter. *2009 20th International Zurich Symposium on Electromagnetic Compatibility*, 2009, pp. 353-356. doi: https://doi.org/10.1109/EMCZUR.2009.4783463.

18. Fakhfakh L., Ammous A. New simplified model for predicting conducted EMI in DC/DC converters. *Electrical Engineering*, 2017, vol. 99, no. 3, pp. 1087-1097. doi: https://doi.org/10.1007/s00202-016-0474-2.

19. Leitungstheorie B., Moschytz G.S., Brugger U., Rosenblatt J. *Transmission on Lines*. 1998. 61 p. Available at: http://ivanlef0u.fr/repo/madchat/coding/electro/Transmission%2520sur%2520lignes.pdf (accessed 10 May 2021).

20. Angénieux G. *Transmission Lines in Harmonic and Transient Regime*. University of Savoy, France, 2009.

21. Montrose M.I. *Printed circuit Board Design Techniques For EMC Compliance. A Handbook for Designers, 2nd Edition*. Wiley-IEEE Press, 2000, 336 p.

22. Wang S. *Characterization and Cancellation of High-Frequency Parasitics for EMI Filters and Noise Separators in Power Electronics Applications*. Thèse de Doctorat, Faculté de l'Institut polytechnique de Virginie, May 2002. Available at: http://hdl.handle.net/10919/27885 (accessed 15 July 2021).

Received 12.02.2022
Accepted 18.04.2022
Published 20.07.2022

Abdelhakim Zeghoudi[1], *PhD,*
Helima Slimani [1,2], *Lecturer,*
Abdelber Bendaoud [1], *Professor,*
Baghdadi Benazza[3], *Lecturer,*
Seyfeddine Bechekir[4], *PhD,*
Houcine Miloudi[1], *Lecturer,*
[1] Laboratory of Applications of Plasma, Electrostatics and Electromagnetic Compatibility (APELEC),
Djillali Liabes University of Sidi Bel-Abbes, Algeria,
e-mail: hakooumzeghoudi@gmail.com,
babdelber@gmail.com (Corresponding author);
el.houcine@yahoo.fr
[2] University of Tiaret, Algeria,
e-mail: Slimani.Halima@yahoo.fr
[3] University of Ain Temouchent, Algeria,
e-mail: benazza13@yahoo.fr
[4] Intelligent Control and Electrical Power Systems (ICEPS) Laboratory, Department of Electrical Engineering,
Djillali Liabes University, Sidi Bel-Abbes, Algeria,
e-mail: seyfeddine.electrotechnique@gmail.com

How to cite this article:
Zeghoudi A., Slimani H., Bendaoud A., Benazza B., Bechekir S., Miloudi H. Measurement and analysis of common and differential modes conducted emissions generated by an AC/DC converter. *Electrical Engineering & Electromechanics*, 2022, no. 4, pp. 63-67. doi: https://doi.org/10.20998/2074-272X.2022.4.09

UDC 621.316 https://doi.org/10.20998/2074-272X.2022.4.10

S. Boumous, Z. Boumous, Z. Anane, H. Nouri

Comparative study of 220 kV overhead transmission lines models subjected to lightning strike simulation by using electromagnetic and alternative transients program

Introduction. *In high voltage networks intended for the transport of electrical energy, lightning can strike an electric line striking either a phase conductor, a pylon or a ground wire, causing significant overvoltage on the transmission lines classified as stresse**s the** most dangerous for transformer stations and electro-energy systems in general. Modeling transmission lines becomes more complicated, if the frequency dependence of resistance and serial inductance due to the effect of lightning strike in the conductors and in the earth is considered. The difficulty increases the fact that the parameters of the line can be defined and calculated only in the frequency domain, while the simulation of transients is wanted to be in the time domain.* ***Problem.*** *Several models (J.R. Marti, Bergeron, nominal PI, Semlyen and Noda) exist for the modeling of transmission lines, the Electromagnetic Transients Program/Alternative Transient Program software (EMTP/ATPDraw) gives the possibility to choose between these models which is delicate due to the fact that we do not have experimental results to validate and justify the choice among the models available in the software. In this context,* ***practical value: the*** *overhead transport line OAT-El Hassi (220 kV) of the city of Sétif located in the north east of Algeria* ***is*** *used for the modeling of lightning strike by using the EMTP/ATPDraw software.* ***Originality.*** *A comparative study of the* ***investigation*** *of a lightning* ***strike*** *on an existing high voltage transmission line by different models of existing lines in the EMTP/ATPDraw software library of this software.* ***Results.*** *It was concluded that the choice of the model of the line is very important given the accuracy and quality of the curves of the voltage presented at the different calculation points.* References 29, tables 1, figures 9.

Key words: **high voltage, lightning strike, electromagnetic and alternative transients program, line models.**

Вступ. *У високовольтних мережах, призначених для передачі електроенергії, блискавка може вдарити по лінії електропередач, уразивши або фазний провід, опору, або заземлюючий провід, викликаючи значні перенапруги на лініях електропередач, визначені як загрози, найбільш небезпечні для трансформаторних підстанцій та електроенергетичних систем загалом. Моделювання ліній електропередач ускладнюється, якщо враховувати частотну залежність опору та послідовної індуктивності внаслідок дії удару блискавки у провідниках та землі. Складність підвищується тим, що параметри лінії можуть бути визначені і розраховані тільки в частотній області, в той час як моделювання перехідних процесів бажано проводити в часовій області.* ***Проблема.*** *Існує кілька моделей (J.R. Marti, Bergeron, номінальна П-подібна схема заміщення, Semlyen і Noda) для моделювання ліній електропередач, комп'ютерна програма електромагнітних перехідних процесів/альтернативна програма перехідних процесів EMTP/ATPDraw дає можливість вибирати між цими моделями, що є «тонким питанням» через те, що ми не маємо експериментальних результатів для перевірки та обґрунтування вибору серед моделей, доступних у програмному забезпеченні. У цьому контексті,* ***практична цінність****: для моделювання удару блискавки за допомогою програмного забезпечення EMTP/ATPDraw використана повітряна лінія електропередачі OAT-Ель-Хассі (220 кВ) міста Сетіф, розташованого на північному сході Алжиру.* ***Оригінальність.*** *Порівняльне дослідження вивчення удару блискавки на існуючій високовольтній лінії електропередач за різними моделями існуючих ліній у бібліотеці програм EMTP/ATPDraw цього програмного забезпечення.* ***Результати.*** *Зроблено висновок, що вибір моделі лінії дуже важливий з урахуванням точності та якості кривих напруг, представлених у різних розрахункових точках.* Бібл. 29, табл. 1, рис. 9.

Ключові слова: **висока напруга, удар блискавки, програма електромагнітних та альтернативних перехідних процесів, моделі ліній.**

Introduction. The direct and indirect impact of lightning on one of the conductors is illustrated by the bidirectional propagation of a surge wave of several hundred kV and can reach 200 kA. In the field of insulation coordination as well as electromagnetic compatibility, the stresses produced by lightning always remain of major interest and should be taken into account as a priority in the implementation of any protection system [1]. The influence of a lightning current model that employs simulations of the geometry and maximum values of overvoltages generated in high voltage transmission networks during a direct lightning strike to overhead lines [2-4].

Several models exist for the simulation of transmission lines. The Electromagnetic Transients Program/Alternative Transient Program software (EMTP/ATPDraw) gives the possibility to choose between these models which are delicate due to the fact that we do not have experimental results to validate and justify. In simulations with the EMTP/ATP, the Heidler and CIGRE (Conseil International des Grands Réseaux Électriques) models of lightning current were used [5].

When the frequency dependence of resistance and series inductance owing to skin effect in conductors and in the earth is taken into account, transmission line modeling gets more sophisticated. The challenge is compounded by the fact that line parameters can only be defined and calculated in the frequency domain, but transient simulation should be done in the time domain. The input/output relationships in the frequency domain i.e. multiplications with transfer functions become convolutions in the time domain.

Modeling of transmission lines as a function of frequency can be summarized as follows:

1. Line functions in the frequency domain are calculated (frequency response). The modal decomposition is used in the case of polyphase lines to derive the wave deformation function or the characteristic impedance / admittance, for example.
2. To approximate these functions, direct approximation in the frequency domain or in the time domain following a digital transformation from the frequency domain is used (inverse Fourier transform, or the Laplace transform).
3. Time-domain transients are calculated numerically or analytically by evaluating the convolutional integral.

In the case of an analytical solution the model of the line can be reduced to the equivalent Norton circuit, which is desirable for implementation in EMTP [6, 7].

EMTP/ATP is better for both real and idealized transmission line simulations. The LCC module (LCC module of the ATP-EMTP uses Carson's equations to estimate the transmission line parameters from the data entered by the user) is the most useful because it simply requires the geometry and material characteristics of the line/cable. Skin effect, bundling, and transposition can all be taken into account automatically. Most transmission line models use modal components for simulation in the time domain [8].

The following transmission line models for the calculation of transients are given in order of model complexity:

1. Mutually coupled RLC elements (PI circuits);
2. Constant distributed parameter line model (LPDC).
3. Line model based on the 2nd order recursive convolution (Semlyen);
4. Frequency dependent line model (J. Marti);
5. Frequency dependent ARMA line model (auto-regressive moving average line model that is implemented in the ATP version of EMTP) (Taku Noda).

The PI model only suitable for short cables and known frequency, Bergeron – only suitable for known frequency, but Bergeron, J. Marti and Semlyen – work in the modal domain and assume a constant transformation matrix. The most recent model, NODA, however, works directly in the phase domain [9].

The aim of the work is to compare the impact of a direct lightning strike on an existing high voltage power line according to various models in the EMTP/ATP draw software library.

Transmission line models.

1) Linear PI model (short lines). This is the model which represents the simplest approach to model a transmission line. In Fig. 1 we give the typical scheme of the model multi-conductor PI model circuit. In the case of symmetrical single-phase or three-phase lines, the PI model is represented by matrixes with multi-conductor overhead line parameters. These matrixes are size of 3×3. The elements of the impedance matrix [*Z*] (resistance and inductance) are a function of the arrangement and geometry of the conductors, while the parameters of the admittance matrix [*Y*] (susceptance and conductance) represent overhead line losses. Figure 1 shows a section of a line with a multiconductor arrangement [10]. The total number of PI circuits used for the simulation depends on the particular simulated system.

The PI model is characterized by the absence of dependencies of the calculation time step on the simulation results. The PI model is mainly recommended for short distance modeling overhead lines (<80 km) [11].

In positive sequence as well as for zero sequence, the linear parameters of the overhead line PI model can be obtained from a support program (LINE CONSTANS) implemented in the EMTP/ATP software. The calculations are based on geometric data from the overhead line [12].

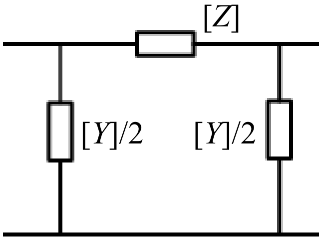

Fig. 1. Typical scheme of multi-conductor nominal PI line model [12]

2) J. Marti: frequency-dependent model with constant transformation matrix. For numerical simulation of electromagnetic transients on overhead wires, the Marti transmission line model is the most commonly employed. It's a distributed parameter model in which the simulator automatically translates the line's parameter frequency fluctuation into a frequency range. The transmission line equations are solved in the modal domain, where a system of n linked conductors is represented by n single-phase lines that, owing to a similarity transformation, are independent of each other. A constant and real transformation matrix computed at a frequency set by the user is taken into account when calculating voltages and currents in the time domain [12].

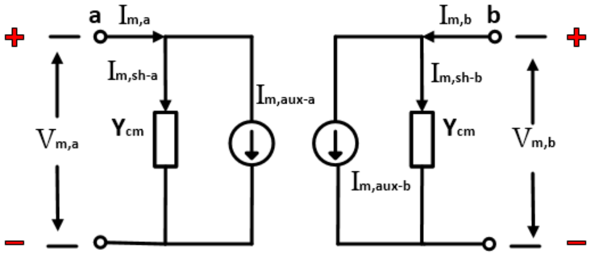

Fig. 2. Principle scheme of J.R. Marti model

3) Bergeron: constant-parameter K.C. Lee or Clark models. The Bergeron model is a very simple model. It is based on a distributed LC-parameter traveling wave line model with overall resistance. This Bergeron model in the time domain is commonly used in the analysis of transient faults of the electrical network [13]. It represents in a distributed way, the elements L and C of a section PI.

Bergeron's model, like the PI section model, only depicts the fundamental frequency (50 Hz) with precision; thus, the surge impedance is constant. As long as the losses do not vary, it can also represent impedances at different frequencies. The mathematical equations of this model have been detailed in [14, 15], the equivalent circuit of the Bergeron model impedances is given in the Fig. 3.

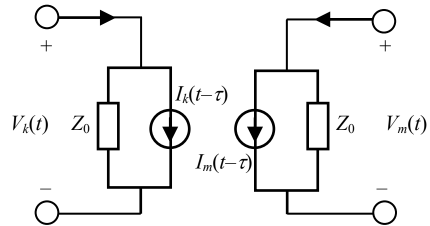

Fig. 3 . Equivalent circuit of Bergeron model

4) Semlyen: frequency-dependent simple fitted model. The frequency-dependent model of Semlyen is a method for iteratively performing a real-time convolution in the [15-18]. The proposed line model accounts for the characteristic admittance's frequency dependence. The method produces a simple line equivalent circuit based on a Norton- type circuit, consisting of a constant admittance and a current source. Therefore, this line model is easy to integrate into programs based on the representation of the nodal system.

Semlyen's model reduced computational time and storage requirements to limits close to those of transient calculations with lossless (frequency independent) line representations. The precision of the frequency-dependent modeling is however preserved since the proposed method is based on rigorously valid simplifications, rather than simply empirical ones [18].

Lightning source. Lightning is a very strong electrical stress that can reach 200 kA in a few microseconds and has extremely high frequencies [19]. The lightning-strike concept is represented by a current source with parallel resistance in the EMTP/ATP software. Lightning-path impedance is the parallel resistance. The Heidler current model was utilized in this study, and it takes into account four features of lightning current amounts at the striking point.

The EMTP/ATP software gives the possibility to introduce the characteristic values of lightning such as the rise time, the peak of the lightning current, fall time and the pulse duration [20, 21]. It can be represented by a current source of exponential shape in parallel with a resistor representing the lightning channel (about 400 Ω) or even a voltage source always having an exponential shape. In the present investigation, thunderbolt is represented by a voltage source of exponential form based on the second Heidler (Fig. 4) [20, 21].

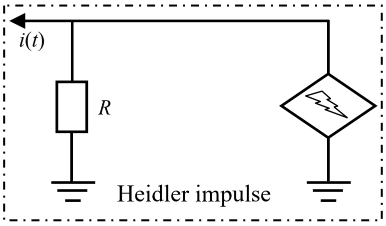

Fig. 4. Heidler type model

Power system description. The OAT-El Hassi line (220 kV) located in the north east of Algeria in the wilaya of Setif. The line is divided into a number of identical sections as shown in Fig. 5 for the 220 kV line. Authors chose a length of portion equal to 2.4 km divided into 8 spans (Fig. 5).

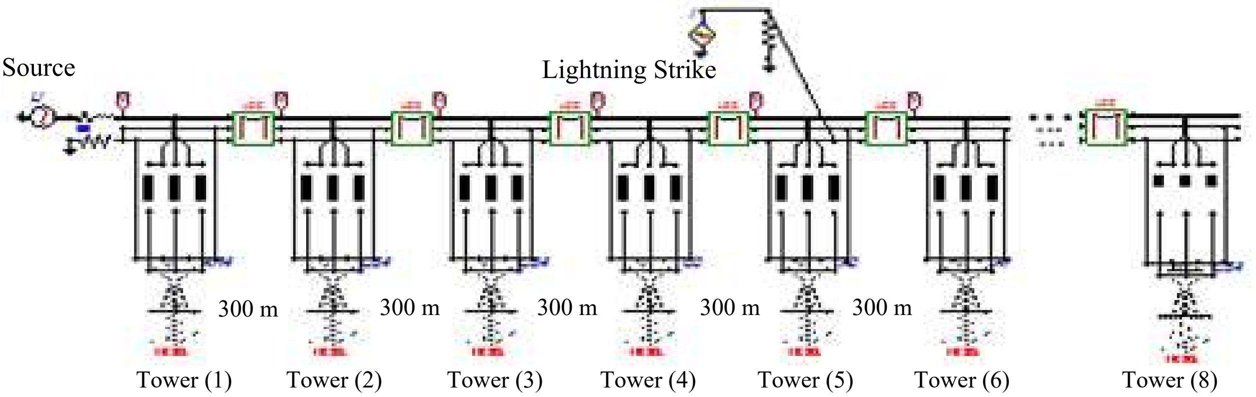

Fig. 5. The OAT-El Hassi line (220 kV) subjected to a 1200 kV overvoltage

Each span has a length of 300 m which is close to the average value of the spans of this line of OAT-El Hassi in Setif, supplied with 220 kV, shown in [22].

This line comprises the following elements: towers, earthing resistance, insulators, sections of the overhead line, ground wire and the lightning current channel [23].

The characteristic tower overvoltage impedance is:

$$Z_T = 60\cdot\left[\ln\left(\sqrt{2}\cdot\frac{2\cdot h}{r_x}\right)-1\right], \qquad (1)$$

where r_x is the tower base radius, m; h is the tower height, m [24, 25].

The tower earthing system can be modeled as a non-linear resistance, the CIGRE [26] model is used, which is modeled as a non-linear resistance of Type-91 in EMTP/ATP:

$$R_T(I)=\frac{R_0}{\sqrt{1+I/I_g}}, \qquad (2)$$

where R_0 is the tower footing resistance at low frequency and low current; R_T is the tower footing resistance, Ω; I_g is the limiting current to initiate sufficient soil ionization, A; I is the lightning current through the footing impedance, A.

The limiting current is a function of soil ionization is given by:

$$I_g=\frac{1}{2\pi}\cdot\frac{E_0\cdot\rho}{R_0^2}, \qquad (3)$$

where ρ is the soil resistivity, Ω·m; E_0 is the soil critical electric field intensity (approximately 300 kV/m).

For the insulator the CIGRE [26] model was used and modeled by a capacitance connected in parallel with a model which represents the overflow mechanism of the insulator. The latter is represented by a switch controlled through models, by the implementation of the equations:

$$\mathrm{d}l/\mathrm{d}t = k_3\cdot V\cdot[V/(D-L)-E_0], \qquad (4)$$

where $\mathrm{d}l/\mathrm{d}t$ is the speed of the arc, m/s; k_3 is the constant, $\mathrm{m}^2\cdot\mathrm{kV}^2\cdot\mathrm{s}^{-1}$; V is the instantaneous voltage across the insulator or the gap, kV; D is the length of the insulator or the length of the gap, m; l is the length of the arc, m, $l \geq D$; E_0 is the strength of the critical electric field, kV/m.

Simulation results. In order to compare influence of various overhead line models on simulation results, simulation of a lightning strike located in the middle of high voltage transmission line have been performed for power system presented in Fig. 5. The modelled 220 kV overhead transmission line with 8 towers was used for lightning-surge simulation. The towers were modelled in simple distributed line model.

In this study, two amplitudes of lightning current (positive polarity) were used to perform shielding failure pattern analysis on the modelled circuit. Simulations are thus conducted with 2 levels of lightning-strike current – 50 kA and 100 kA [27] (Table 1).

Table 1

Lightning amplitudes, front times, and tail times

Lightning current amplitude, kA	Tail time, µs	Front time, µs
50	50	1.2
100	77.5	2

For the simulation, lightning-surge current was injected into ground wire of the fourth tower (middle tower). The voltage patterns due to the direct lightning strike on the ground wire are recorded throughout the distance from the network at each section of 300 m.

Lightning strike on ground wire: When lightning strikes the overhead ground wire, a voltage builds up in the cable, causing a traveling wave to flow down to the bottom of the concrete pole, through the external ground wire, and in both directions along the overhead ground wire. The result voltage is determined by the striking current and total impedance of the overhead ground wire and the external ground wire.

Case 1: 100 kA, 2 µs, 77.5 µs. Figure 6 illustrates the amplitudes of induced voltage across the ground wire when a lightning strike current of 100 kA occurs with a tail time of 77.5 µs and a front time of 2 µs, as simulated by the 4 types of line models – J.R. Marti, PI, Bergeron, and Semlyen.

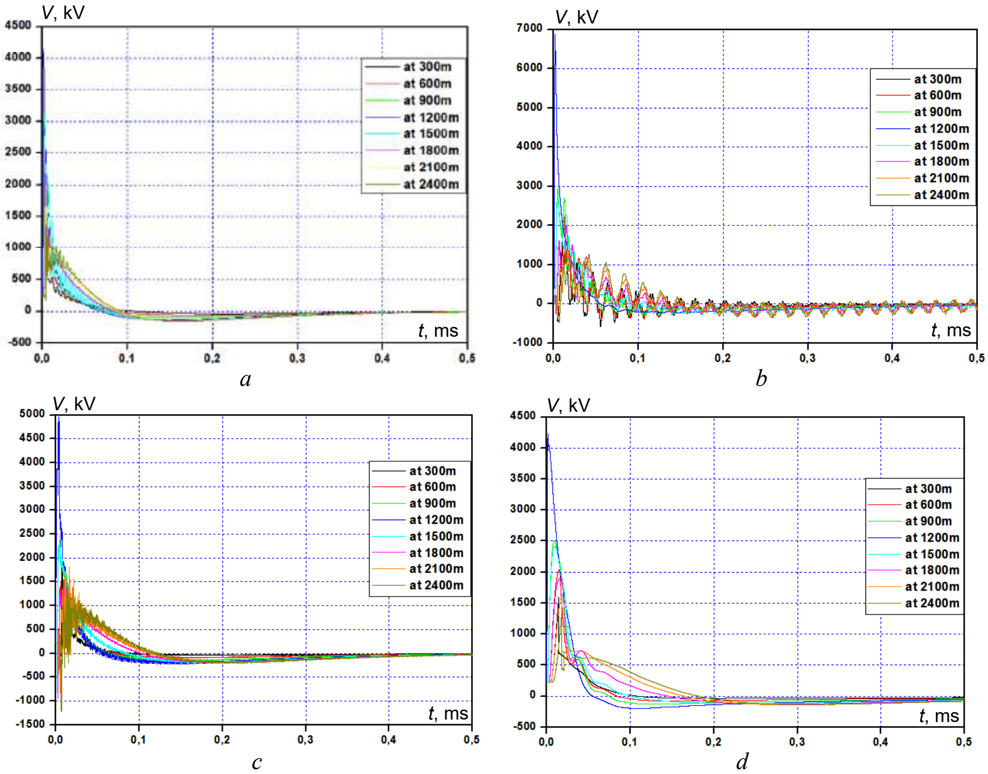

a *b* *c* *d*

Fig. 6. Induced voltage across the ground wire by different model:
a – J.R. Marti model; *b* – PI model; *c* – Bergeron model; *d* – Semlyen model

Case 2: 50 kA, 1.2 µs, 50 µs. Figure 7 shows amplitudes of induced voltage across the ground wire when lightning-strike current of 50 kA, with tail time 50 µs and 1.2 µs front time, simulated by the 4 types of the line model J.R. Marti, PI, Bergeron and Semlyen respectively.

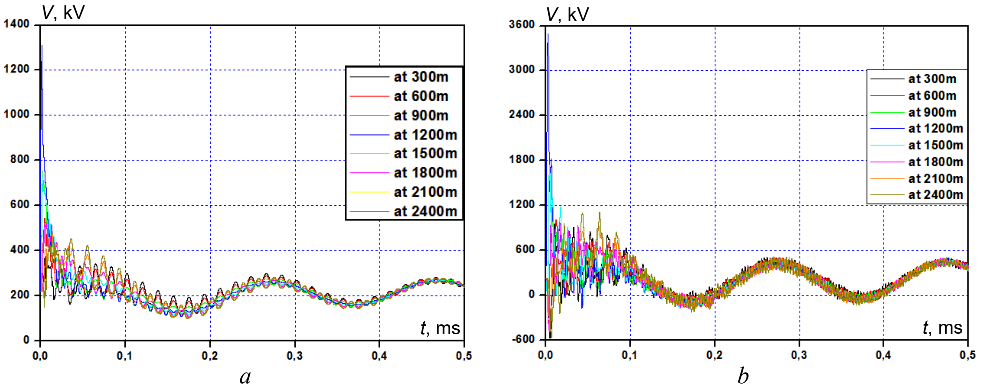

a *b*

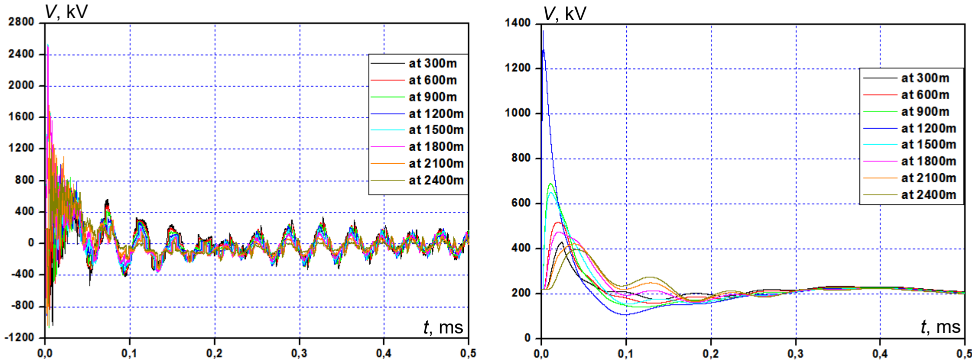

c *d*

Fig. 7. Induced voltage across the ground wire by different model:
a – J.R. Marti model; *b* – PI model; *c* – Bergeron model; *d* – Semlyen model

Lightning strike on phase A. Case 1: 100 kA, 2 μs, 77.5 μs. Figure 8 shows amplitudes of induced voltage across the phase A when lightning-strike current of 100 kA with tail time 77.5 μs and 2 μs front time, simulated by the 4 types of the line model J.R. Marti, PI, Bergeron and Semlyen respectively.

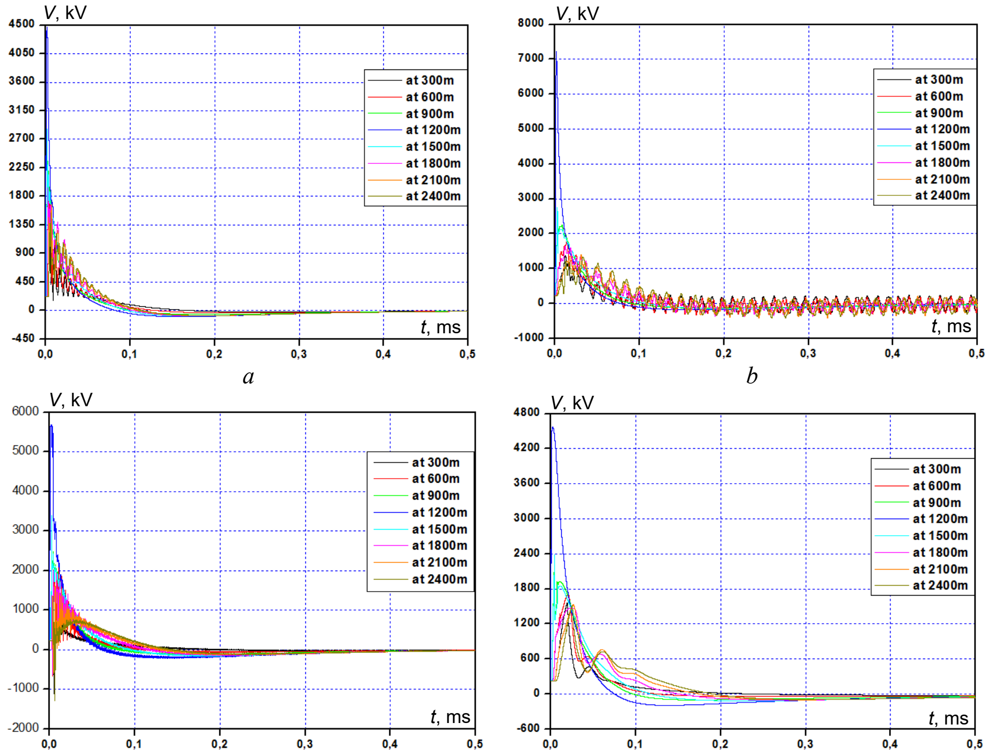

a *b* *c* *d*

Fig. 8. Induced voltage across the phase conductor by different model:
a – J.R. Marti model; *b* – PI model; *c* – Bergeron model; *d* – Semlyen model

Case 2: 50 kA, 1.2 μs, 50 μs. Figure 9 shows amplitudes of induced voltage across the phase A when lightning-strike current of 50 kA, with tail time 50 μs and 1.2 μs front time, simulated by the 4 types of the line model J.R. Marti, PI, Bergeron and Semlyen respectively.

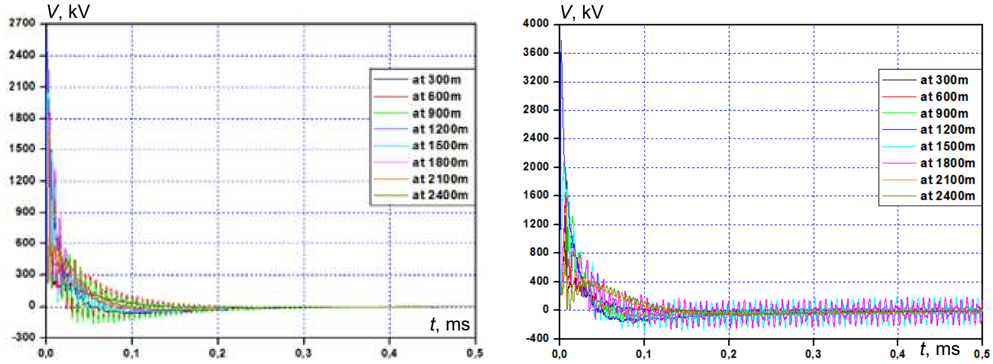

a *b*

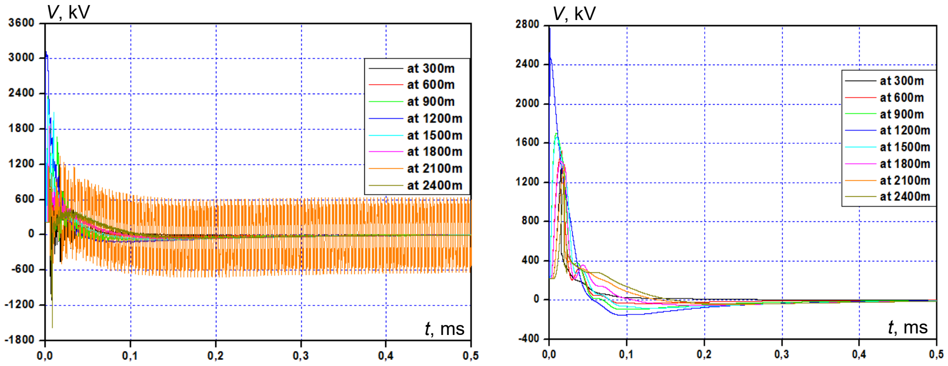

c *d*

Fig. 9. Induced voltage across the phase conductor by different model:
a – J.R. Marti model; *b* – PI model; *c* – Bergeron model; *d* – Semlyen model

In the study cases the phase A voltage attenuates completely and becomes zero after less than 0.1 s and that for the 4 models J.R. Marti, PI, Bergeron and Semlyen, which is in good agreement with the results obtained in [28].

According to the simulation results obtained in Fig. 8, 9 the increase in the complexity of the model has an impact on the peak voltages and the waveform. The calculated voltage waveforms are indeed similarly different, but the oscillations of the PI model dominate, same remarks were observed in the search results exposed in reference [29].

The direct lightning strike on one of the phases conductors of the overhead transmission line causes serious faults, exclusively the deactivation of this phase which results in an imbalance and instability in the line which requires the intervention of maintenance personnel emergency. Surge arresters on all phases of the conductors have been suggested as potential solutions; however, while surge arresters are the best solution, they are quite expensive, which is important for transmission lines where corona attenuation is insufficient to reduce the lightning surge to security levels.

Conclusions. Lightning has always been a source of disruption for electricity users, however, the demand for electrical systems is relatively increasing and the quality (reliability, availability, continuity of service, etc.) must be taken into account, as well as the permanent need to minimize the cost of production and improve the level of insulation of electrical equipment.

The simulation of lightning strike by existing models in Electromagnetic Transients Program / Alternative Transient Program software was studied in this paper; each model of overhead transmission line has these advantages and disadvantages, from our study results:

- the J. Marti model that traditionally is suitable for overhead line modelling show significant weaknesses both in the fitting process and in the calculation of induced voltages;
- the PI model and Bergeron model resulted in unstable responses and also required fine-tuning of the fitting parameters and large time steps;
- the Semlyen model actually gave the overall best and most reliable results; however, such model is only suitable for cases where the fundamental frequency is known.

Conflict of interest. The authors declare that they have no conflicts of interest.

REFERENCES

1. Baranov M.I., Buriakovskyi S.G., Kniaziev V.V., Rudenko S.S. Analysis of characteristics and possibilities of high-voltage electrical engineering complex Scientific-&-Research Planning-&-Design Institute «Molniya» of NTU «KhPI» for the tests of objects of energy, armament, aviation and space-rocket technique on electric safety and electromagnetic compatibility. *Electrical Engineering & Electromechanics*, 2020, no. 4, pp. 37-53. doi: https://doi.org/10.20998/2074-272X.2020.4.06.

2. Carneiro S., Marti J.R. Evaluation of Corona and Line Models in Electromagnetic Transients Simulations. *IEEE Power Engineering Review*, 1991, vol. 11, no. 1, p. 60. doi: https://doi.org/10.1109/MPER.1991.88674.

3. Pereira T.M., Tavares M.C. Development of a Voltage-Dependent Line Model to Represent the Corona Effect in Electromagnetic Transient Program. *IEEE Transactions on Power Delivery*, 2021, vol. 36, no. 2, pp. 731-739. doi: https://doi.org/10.1109/TPWRD.2020.2990968.

4. Hongtao R. Simulation Analysis of Counterattack Lightning Overvoltage of 500 kV Transmission Line Considering Impulse Corona. *2021 6th International Conference on Power and Renewable Energy (ICPRE)*, 2021, pp. 168-173. doi: https://doi.org/10.1109/ICPRE52634.2021.9635350.

5. Furgał J. Influence of Lightning Current Model on Simulations of Overvoltages in High Voltage Overhead Transmission Systems. *Energies*, 2020, vol. 13, no. 2, p. 296. doi: https://doi.org/10.3390/en13020296.

6. Anane Z., Bayadi A., Harid N. A dynamic corona model for EMTP computation of multiple and non-standard impulses on transmission lines using a type-94 circuit component. *Electric Power Systems Research*, 2018, vol. 163, pp. 133-139. doi: https://doi.org/10.1016/j.epsr.2018.06.006.

7. Anane Z., Bayadi A., Bernadić A. Analysis of lightning strike with corona on OHTL near the substation by EMTP. *Advances in Engineering: an International Journal*, 2016, vol. 1, no. 1, pp. 55-71. Available at: https://www.airccse.com/adeij/papers/1116adeij06.pdf (accessed 26 May 2021).

8. Kanwar M., Arora K., Sharma S.K. Comparison of Simulation Tools ATP-EMTP and MATLAB-Simulink for Time Domain Power System Transient Studies. *International Journal of Research Studies in Computer Science and Engineering*, 2014, vol. 1, no. 3, pp. 50-56.

9. Høidalen H.K., Soloot A.H. Cable Modelling in ATP – from NODA to TYPE 94. *THE EEUG Meeting, European EMTP-ATP Conference,* 2010, pp. 115-126. Available at: https://www.researchgate.net/publication/236620920_Cable_Modelling_in_ATP_-_from_NODA_to_TYPE94 (accessed 26 May 2021).

10. Wedepohl L.M. Application of matrix methods to the solution of travelling-wave phenomena in polyphase systems. *Proceedings of the Institution of Electrical Engineers*, 1963, vol. 110, no. 12, pp. 2200-2212. doi: https://doi.org/10.1049/piee.1963.0314.

11. Colqui J.S.L., Eraso L.C.T., Caballero P.T., Filho J.P., Kurokawa S. Implementation of Modal Domain Transmission Line Models in the ATP Software. *IEEE Access*, 2022, vol. 10, pp. 15924-15934. doi: https://doi.org/10.1109/ACCESS.2022.3146880.

12. Marti J.R. Accurate Modeling of Frequency-Dependent Transmission Lines in Electromagnetic Transient Simulations. *IEEE Power Engineering Review*, 1982, vol. PER-2, no. 1, pp. 29-30. doi: https://doi.org/10.1109/MPER.1982.5519686.

13. Zawani N., Junainah, Imran, Faizuhar M. Modelling of 132 kV Overhead Transmission Lines by using ATP/EMTP for Shielding Failure Pattern Recognition. *Procedia Engineering*, 2013, vol. 53, pp. 278-287. doi: https://doi.org/10.1016/j.proeng.2013.02.037.

14. Torrez Caballero P., Marques Costa E.C., Kurokawa S. Frequency-dependent line model in the time domain for simulation of fast and impulsive transients. *International Journal of Electrical Power & Energy Systems*, 2016, vol. 80, pp. 179-189. doi: https://doi.org/10.1016/j.ijepes.2016.01.051.

15. Yu Ting-Chung. *Full Frequency-Dependent Modelling of Underground Cables for Electromagnetic Transient Analysis*. Theses and Dissertations, University of British Columbia, 2001. Available at: https://open.library.ubc.ca/collections/ubctheses/831/items/1.0065367 (accessed 26 May 2021).

16. Ikeda Y., Nagaoka N., Baba Y., Ametani A. A circuit model of vertical conductor using Semlyen's line model based on transient response calculated by FDTD. *Electric Power Systems Research*, 2014, vol. 113, pp. 151-156. doi: https://doi.org/10.1016/j.epsr.2014.02.039.

17. Shendge A., Nagaoka N. A modeling method and EMTP simulations of an inverter surge. *IEEJ Transactions on Electrical and Electronic Engineering*, 2014, vol. 9, no. 1, pp. 1-6. doi: https://doi.org/10.1002/tee.21929.

18. Semlyen A., Dabuleanu A. Fast and accurate switching transient calculations on transmission lines with ground return using recursive convolutions. *IEEE Transactions on Power Apparatus and Systems*, 1975, vol. 94, no. 2, pp. 561-571. doi: https://doi.org/10.1109/T-PAS.1975.31884.

19. Islam M.Z., Rashed M.R., Yusuf M.S.U. ATP-EMTP modeling and performance test of different type lightning arrester on 132 kV overhead transmission tower. *2017 3rd International Conference on Electrical Information and Communication Technology (EICT)*, 2017, pp. 1-6. doi: https://doi.org/10.1109/EICT.2017.8275172.

20. Gary C., Le Roy G., Hutzler B., Lalot J., Dubanton C. *Les propriétés diélectriques de l'air et des très hautes tensions*. Ed. EDF, Eyrolles, Paris, 1984, 628 p. (Fra).

21. Heidler F., Cvetic J.M., Stanic B.V. Calculation of lightning current parameters. *IEEE Transactions on Power Delivery*, 1999, vol. 14, no. 2, pp. 399-404. doi: https://doi.org/10.1109/61.754080.

22. Anane Z. *Modèle dynamique de l'effet couronne pour l'étude de la propagation de la surtension le long des lignes de transmission HT en utilisant l'EMTP*. Thesis doctorate, University of Sétif, Algeria, 2018. (Fra).

23. Ishii M., Kawamura T., Kouno T., Ohsaki E., Shiokawa K., Murotani K., Higuchi T. Multistory transmission tower model for lightning surge analysis. *IEEE Transactions on Power Delivery*, 1991, vol. 6, no. 3, pp. 1327-1335. doi: https://doi.org/10.1109/61.85882.

24. Sliskis O., Dvornikovs I., Ketners K., Sobolevsky D. Specification of transmission tower structure for following surge protection simulation. *2015 16th International Scientific Conference on Electric Power Engineering (EPE)*, 2015, pp. 137-140. doi: https://doi.org/10.1109/EPE.2015.7161151.

25. Anane Z., Bayadi A., Huang K. Distortion phenomena on transmission lines using corona modeling ATP/EMTP. *IEEE Transactions on Dielectrics and Electrical Insulation*, 2018, vol. 25, no. 2, pp. 383-389. doi: https://doi.org/10.1109/TDEI.2017.006484.

26. Eriksson A., Dellera L., Elovaara J., Hileman A., Houlgate R., Huse J., Weck K.W. *Guide to procedures for estimating the lightning performance of transmission lines*. 1991, CIGRE Report 63.

27. Martínez-Velasco J.A., Castro-Aranda F. Modeling of overhead transmission lines for lightning overvoltage calculations. *Ingeniare. Revista Chilena de Ingeniería*, 2010, vol. 18, no. 1, pp. 120-131. doi: https://doi.org/10.4067/S0718-33052010000100013.

28. Sestasombut P., Ngaopitakkul A. Evaluation of a Direct Lightning Strike to the 24 kV Distribution Lines in Thailand. *Energies*, 2019, vol. 12, no. 16, p. 3193. doi: https://doi.org/10.3390/en12163193.

29. Oramus P., Florkowski M. Influence of various transmission line models on lightning overvoltages in insulation coordination studies. *Zeszyty Naukowe Wydziału Elektrotechniki i Automatyki*, 2014, no. 40, pp. 81-84. Available at: https://files.pg.edu.pl/api/v1/file/preview?path=eia%2F04-nauka%2F01-zeszyty-naukowe%2F02-numery-do-pobrania%2F2014+-+nr+40.pdf&response-content-disposition=attachment (accessed 23 May 2021).

Received 08.03.2022
Accepted 07.05.2022
Published 20.07.2022

Samira Boumous[1], *Doctor of Science*,
Zouhir Boumous[1], *Doctor of Science*,
Zahira Anane[2], *Doctor of Science*,
Hamou Nouri[2], *Professor*,
[1] Laboratory of Electrical Engineering and Renewable Energies,
Mohamed Cherif Messaidia University,
Souk Ahras, Algeria,
e-mail: boumous@yahoo.fr (Corresponding author);
zsid3@yahoo.fr
[2] Automatic Laboratory of Setif, Faculty of Technology,
The University Ferhat Abbas of Setif,
Setif, Algeria,
e-mail: zahiraelect@yahoo.fr; Hnouri19@univ-setif.dz

How to cite this article:

Boumous S., Boumous Z., Anane Z., Nouri H. Comparative study of 220 kV overhead transmission lines models subjected to lightning strike simulation by using electromagnetic and alternative transients program. *Electrical Engineering & Electromechanics*, 2022, no. 4, pp. 68-74. doi: https://doi.org/10.20998/2074-272X.2022.4.10

UDC 621.316.9 https://doi.org/10.20998/2074-272X.2022.4.11

D.G. Koliushko, S.S. Rudenko, O.Ye. Istomin, A.N. Saliba

Simulation of electromagnetic processes in the grounding system with a short circuit in the operating high-voltage substation

The aim *of the work is a test of the developed mathematical model of electromagnetic processes of short circuit and approbation of the created software complex «LiGro» on its basis for the existing grounding system located in three-layer soil.* ***Methodology****. To improve the accuracy of calculating the normalized parameters of operating power stations and substations, the authors developed the «LiGro» software package based on the expressions obtained in for calculating the potential of the electric field of a non-equipotential grounding system (GS). To monitor the state and assess the efficiency of the GS of operating power facilities, the electromagnetic diagnostics is used. The topology of the GS was determined with the induction method by complex KNTR-1, the geoelectric structure of the soil was determined by the method of vertical electrical sounding using the Wenner installation, the interpretation of the sounding results was made by the «VEZ-4A» program.* ***The calculation results*** *show that for the selected substation, the model developed in the «LiGro» complex has a deviation δ_2 from the experimental values U_t by an average of 8,2 %, and the model implemented in Grounding 1.0 (IEEE model) δ_1 is 17,2 %.* ***Originality****. The results of the study confirm the adequacy of the developed GS model in the «LiGro» complex based on a three-layer soil model, with the experimental values of the touch voltage obtained by simulating a single-phase ground fault on a real GS in operation. The first time was made approbation of the «LiGro» software package when performing the EMD of the GS of an operating substation with a voltage class of 150 kV.* ***Practical significance.*** *The program software can be used by special measuring's laboratory to determining electrical safety parameters: touch voltage, GS voltage, and GS resistance.* References 17, tables 2, figures 9.

Key words: **grounding system, modeling of the electromagnetic processes, touch voltage, grounding system resistance, grounding system voltage, electromagnetic diagnostics.**

Метою роботи є перевірка розробленої математичної моделі електромагнітних процесів короткого замикання та апробація створеного програмного комплексу «LiGro на її основі для існуючого заземлювального пристрою (ЗП), який розташовано в тришаровому ґрунті. Перевірка практичного застосування була виконана на діючий підстанції класом напруги 150 кВ з використанням вдосконаленої методики електромагнітної діагностики. Топологія ЗП була визначена індукційним методом за допомогою приладу KNTR-1, параметри ґрунту визначені чотириелектродною симетричною установкою за схемою Веннера методом вертикального електричного зондування, інтерпретація результатів зондування виконана спеціалізованою програмою VEZ-4A. Результати порівняння розрахунку показують, що для обраної підстанції модель розроблена в комплексі LiGro має відхилення від експериментальних значень в середньому на 8,2 %, а модель реалізована в Grounding 1.0 (IEEE model) – 17,2 %. Виконано розрахунок нормованих параметрів ЗП в режимі короткого замикання: напругу дотику, опір ЗП та напругу на ЗП. Встановлено, що вони не перевищують допустимого значення. Проаналізовано переваги розрахункового комплексу у порівнянні з аналогами. Отримані результати дозволяють виконати повномасштабне впровадження програмного комплексу в діагностику стану ЗП. Бібл. 17, табл. 2, рис. 9.

Ключові слова: **заземлювальний пристрій, моделювання електромагнітних процесів, напруга дотику, опір заземлювального пристрою, напруга на заземлювальному пристрої, електромагнітна діагностика.**

Problem formulation. To monitor the state and assess the efficiency of the grounding system (GS) of operating power facilities, the electromagnetic diagnostics (EMD) [1, 2] is used, which involves three stages: experimental, calculated, and the stage of issuing recommendations [3]. In the process of research, the topology of the GS is determined, as well as the normalized parameters (NP) of the GS, such as the GS resistance, the voltage across the GS, and the touch and step voltages.

The impossibility of controlling these parameters by direct or even indirect measurements leads to an increase in the urgency of the problem in the field of calculating the GS NP of operating power stations and substations using software [4, 5].

Literature analysis. Several works [4–12] are devoted to the issues of modeling electromagnetic processes that occur in the GS during the flow of emergency currents. In most cases, a mathematical model of the GS located in two-layer soil is used (in particular, with the help of [7], more than 1000 power facilities of Ukraine with voltage classes of 35-750 kV were calculated, and the software package [9, 10] based on it is one of the most commercial versions popular in the world).

The calculation of the GS is usually carried out in two modes: a single-phase ground fault on the territory of the power facility and outside it. The following calculation methods are used to determine the touch voltage:

- finite element method in the time domain (so-called FDTD method);
- method of integro-differential equations;
- method of optical analogy.

Each of these methods has a similar algorithm [13]: geometric and electrical data are entered into the initial data block (GS dimensions, location, depth, and cross-section of groundings, short-circuit current, electrophysical characteristics of the soil, electrical resistivity of the grounding material, etc.). This is followed by the calculation of longitudinal active and inductive resistances of connections, and the coefficients of the system of linear algebraic equations are determined for calculating the density of currents flowing from the ground electrode. Because of the complex dependence of the resistance of the electrode material on the magnitude of the current flowing through them, the solution of the problem is found by the method of successive approximations.

The method of integro-differential equations is based on the analytical solution of the problem of the electric field potential of a point current source [6, 7, 9–13]. Programs based on this method with a two-layer electric soil structure are used to carry out calculations by the world's leading scientific research institutions and following the international standards IEEE Std. 80 and 81 [13, 14].

In Ukraine, for power facilities, the number of GS located in two-layer soil is only 10 % [6]. In other cases, it is necessary to apply equivalence techniques with the reduction of a multilayer structure to a two-layer calculation model, which can give a significant methodological error (from 20 % to 100 %).

The use of a mathematical model of GS [6], located in a three-layer soil, allows to directly (without equivalentization) perform a calculation for 80 % of the existing energy facilities in Ukraine and determine the resistance of GS with an error of up to 10 % (confirmed according to the calculation data of more than 50 substations with a voltage class 35 kV). Comparison with the experimental value of the contact voltage showed more than 90 % falling into the calculated range for the GS of three test substations [3].

To improve the accuracy of calculating the NP of operating power stations and substations, the authors developed the «LiGro» software package based on the expressions obtained in [6] for calculating the potential of the electric field of a non-equipotential GS.

From the existing world analogues [7–12] for determining the NP of GS of operating power stations and substations when the GS is located in three-layer soil, this software package is distinguished by:

- the calculation of the electric field is based on the analytical solution of the problem of the electric field potential of a point current source in a three-layer half-space;
- the possibility of the arbitrary orientation of the grounding in space;
- the consideration of non-equipotentiality of the groundings;
- saving the duration of the calculation at the level of two-layer models.

The assessment of the adequacy of the developed mathematical model and the created software package was carried out by comparing the results of experimental studies for operating high-voltage power facilities in Ukraine with the calculation results, and is given in [3].

The calculation of the GS NP can be divided into three stages:

- the preparation of initial data for modeling;
- the calculation of the experiment to assess the adequacy of the constructed GS model to the real GS according to the method given in [15];
- the calculation of the GS NP in the short circuit mode.

The aim of the work is a test of the developed mathematical model of electromagnetic processes of short circuit and approbation of the created software complex «LiGro on its basis for the existing grounding system located in three-layer soil.

Research materials.

1. Initial data. To carry out the research, the substation with a voltage class of 150 kV, located in the central part of Ukraine, was taken as operating.

The initial data for the simulation are the characteristics of the substation (short circuit current, outflow current in the neutral, protection response time), the topology of the GS, and the geoelectric structure of the soil.

Using the induction method, within the first stage of EMD of GS (see Fig. 1), using complex KNTR-1 [15], the topology of the GS was determined, it is shown in Fig. 2.

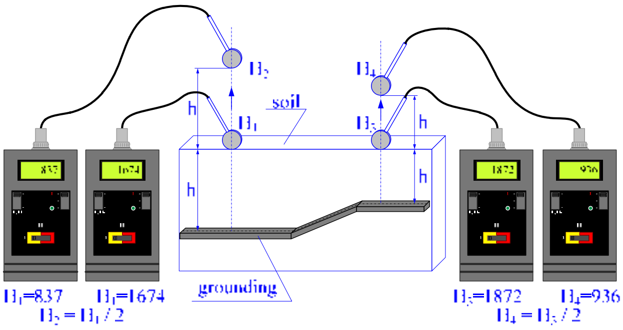

Fig. 1. Determination of GS topology

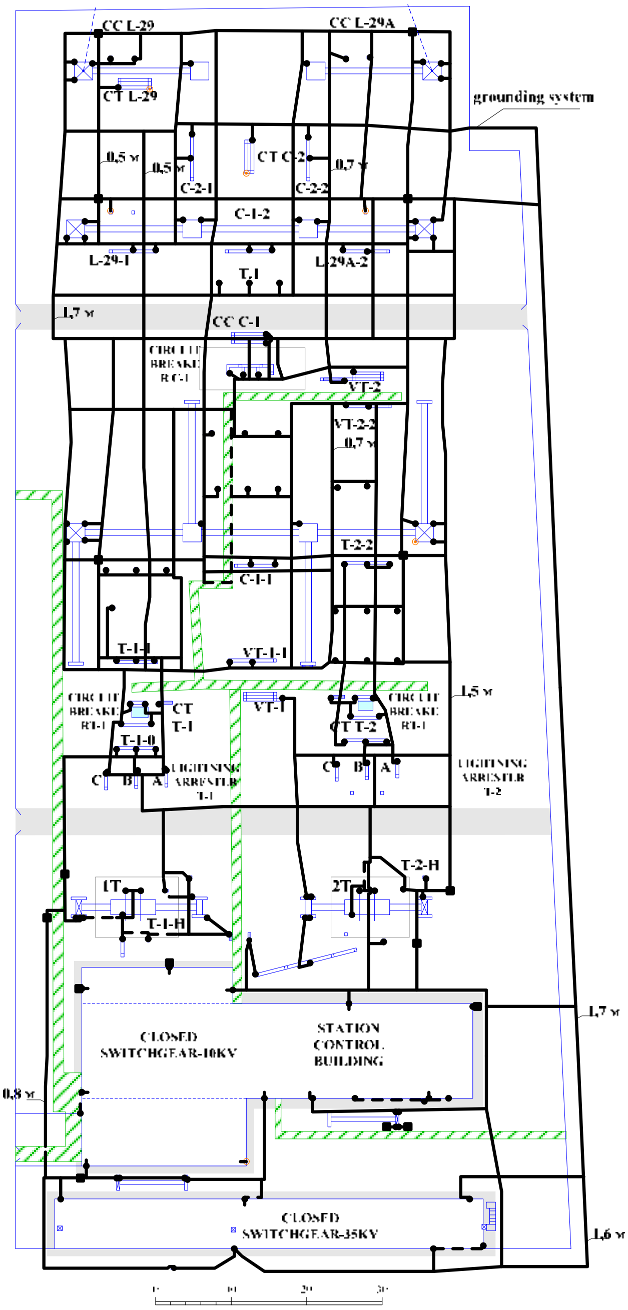

Fig. 2. GS topology of investigated substation 150 kV

It was found that the GS of the substation is a branched grid of horizontal groundings and vertical electrodes, with dimensions of 65 m × 164 m. Horizontal groundings are made of a steel staff of 4 mm × 40 mm and hot-rolled steel with a diameter of ∅14 mm, vertical electrodes are made of rolled steel of 16 mm and 3 m long.

The horizontal groundings are marked with a thick black line, the grounding conductors connecting the equipment with grounding are marked by points, and the name of the equipment on which the measurements have been carried out as well as the power transformers 1T and 2T are shown (see Fig. 2).

The geoelectric structure of the soil was determined by the method of vertical electrical sounding using the Wenner installation (see Fig. 3) [16].

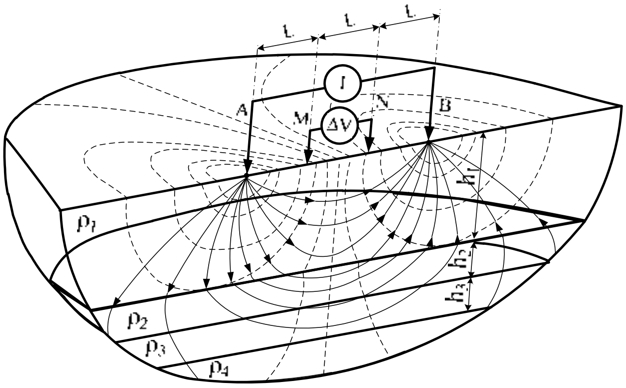

Fig. 3. Soil sounding by using the Wenner installation

Using the «VEZ-4A» program (see Fig. 4), which is created by authors and built into the «LiGro» complex, it was found that the soil is a three-layer geoelectric structure, and the interpretation of the sounding results showed that the resistivity is equal to:

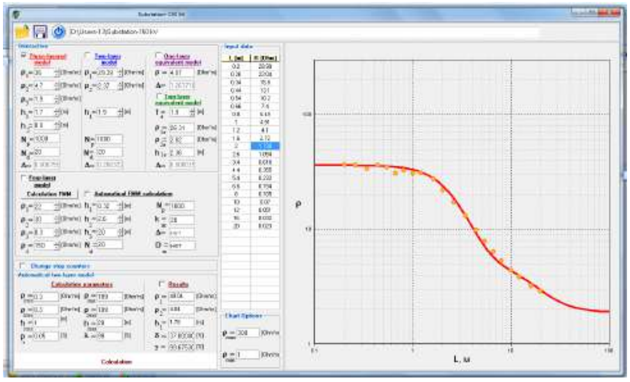

Fig. 4. A working window of the software for multi-layer soils interpretation «VEZ-4A»

- for the first layer at a depth of up to 1,6 m – 34,5 Ω×m;
- for the second layer at a depth from 1,6 m to 8,1 m – 5,5 Ω×m;
- for the third layer at a depth from 8,1 m – 1,85 Ω×m.

To compare the calculation results with two-layer models, in particular, the IEEE model, the three-layer soil structure was reduced to an equivalent two-layer model:

- for the first layer at a depth of up to 1,9 m – 29,39 Ω×m;
- for the second layer at a depth from 1,9 m – 2,37 Ω×m.

The given initial data were entered into the «LiGro» software package, and a model of the GS of the studied substation was created. Fig. 5 shows the GS scheme, where the blue color indicates groundings located underground at the same depth, the green color – groundings at varying depths, the purple/red color – buildings and structures, and the metal construction of the substation equipment.

To create a calculation model the «LiGro» complex, in contrast to [7–12], has ample opportunities and allows to:

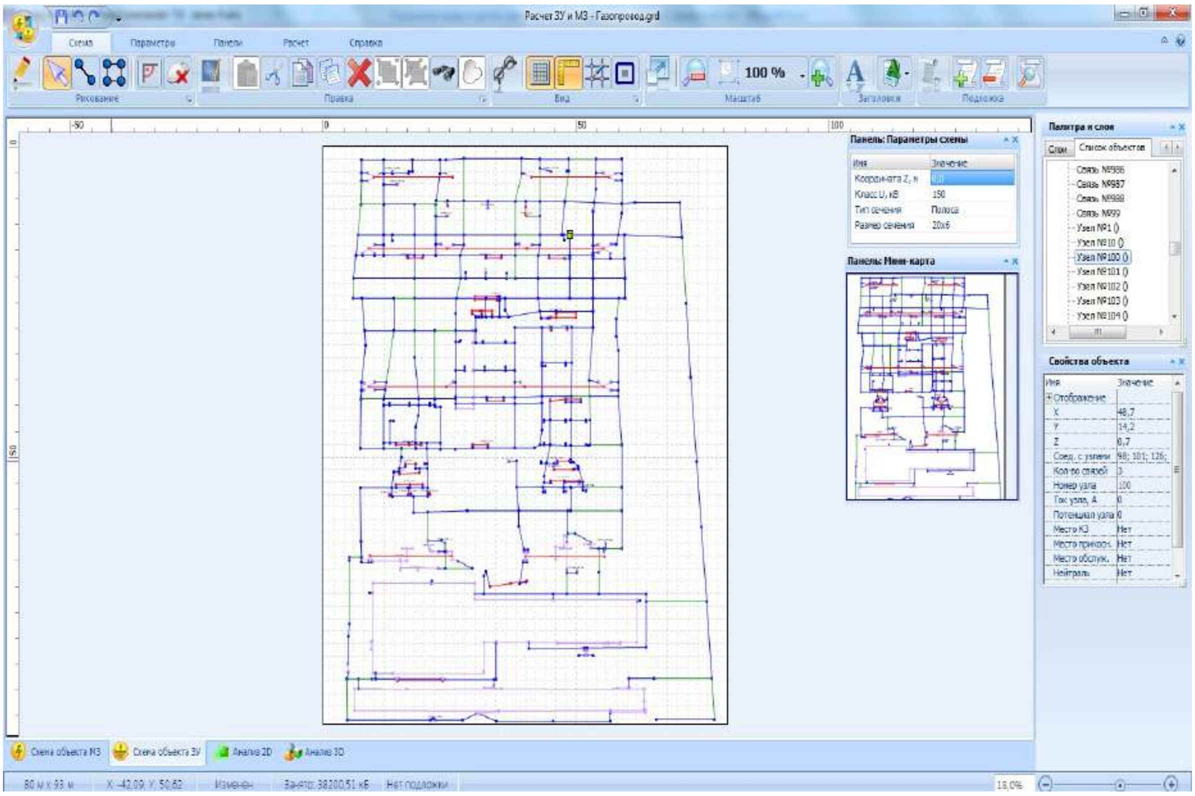

Fig. 5. Model of the GS of investigated substation 150 kV by software «LiGro»

- set in any node (see Fig. 6) its individual properties (voltage class, short circuit location, touch point, service point, experiment measurement point, neutral with setting the current in the neutral for each voltage class, base resistance, initial current in the node);
- build a grounding system on a scale with an arbitrary configuration (directions of groundings location and their cross-section);
- carry out both group and individual editing of properties (coordinates, parameters, etc.) of objects (nodes and links);
- copy individual elements of GS, create palettes of standard elements, automatically build grounding grids with specified parameters, perform quick navigation through the scheme.

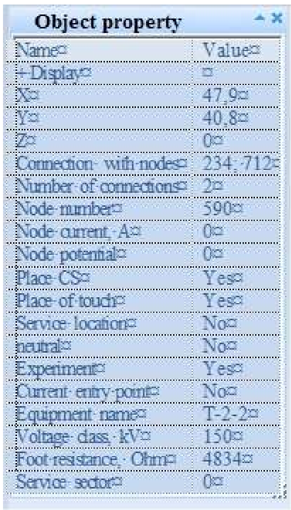

Object property

Name	Value
+Display	
X	47,9
Y	40,8
Z	0
Connection with nodes	234; 712
Number of connections	2
Node number	590
Node current, A	0
Node potential	0
Place CS	Yes
Place of touch	Yes
Service location	No
neutral	No
Experiment	Yes
Current entry point	No
Equipment name	T-2-2
Voltage class, kV	150
Foot resistance, Ohm	4834
Service sector	0

Fig. 6 Property of the node-object GS of investigated substation 150 kV by software «LiGro»

2. Calculation of the experiment to assess the adequacy of the constructed model. The test was based on a comparison of the touch voltage on several selected substation equipment units when simulating a single-phase ground fault. The analysis was carried out on six equipment of substations with voltage class 150 kV. In this case, the traditional method of the set of experimental data was used to assess the adequacy of the mathematical model of the GS which is presented in [3] (see Fig. 7) with measuring current – 5,13 A. Figures 2 and 5 show the layouts of the GS locations for the specified substation.

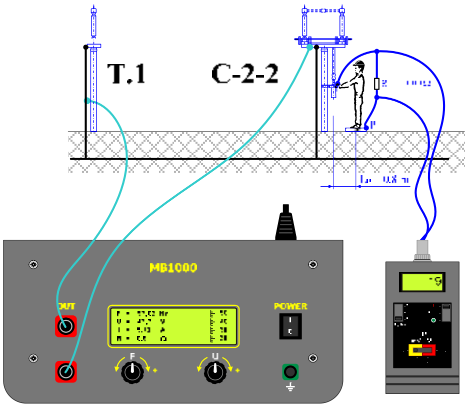

Fig. 7. Method of the set of experimental data to assess the adequacy of the mathematical model of the GS

The result of the calculation is the maximum and minimum value of the touch voltage within a radius of 0.8 m around the point of study. The evaluation of the results of the calculation was as follows: the experimentally measured value of the touch voltage U_t should be in the interval between the minimum and maximum calculated values for the corresponding point. Table 1 shows the results of the comparison of U_t for disconnectors of substations. Table 1 shows the calculated (U_{t1} and U_{t2}) and experimental values of the voltage U_t obtained, respectively, by mathematical modeling and simulating a single-phase short circuit on the territory of the substation with the return of the entire short circuit current to the grounding conductor of the supporting insulator (point T.1, see Fig. 2). When comparing, the calculated current was taken equal to the measuring one, foot resistance (R_O) was determined experimentally at each measuring point.

Table 1

Results of the comparison of touch voltage

Name of the equipment	Experimental results		Calculated results			
			IEEE model		LiGro	
	U_t, mV	R_O, Ω	U_{t1}, mV	δ_1, %	U_{t2}, mV	δ_2, %
C-2-2	19	1146	19,87	4,6	18,8	1,1
C-2-1	38	565	32,22	15,2	34,4	9,5
L-29-1	16	425	16,95	5,9	15,9	0,6
C-1-1	20	399	23,39	17,0	22,0	10,0
VT-2-2	37	472	22,09	33,4	30,9	16,5
T-2-2	6	4834	3,58	27,3	5,3	11,7

The calculation results show that for the selected substation, the model developed in the «LiGro» complex has a deviation δ_2 from the experimental values U_t by an average of 8,2 %, and the model implemented in Grounding 1.0 (IEEE model) δ_1 is 17,2 %. Thus, the results of the study confirm the adequacy of the developed GS model in the «LiGro» complex based on a three-layer soil model, with the experimental values of the touch voltage obtained by simulating a single-phase ground fault on a real GS in operation. In addition, the three-layer model showed higher accuracy than the one reduced to the two-layer model.

3. Calculation of GS NP in short circuit mode. Following the requirements of regulatory documents, when determining the allowable value of the touch voltage, the sum of the protection time at the substation and the total time of the circuit breaker off should be taken as the estimated duration of the operation.

According to the data of the operating organization: the voltage class is 150 kV, short-circuit current value is 14,156 kA, operating mode of transformer neutrals – grounded. When carrying out the calculations, allowable contact voltage was assumed to be equal to 213,3 V for all equipment, based on the protection duration of 0,48 s [17].

With the help of the «LiGro» complex, it was determined:

- touch voltage (see Fig. 8) on each unit of equipment in all modes of a single-phase short circuit to earth, taking into account the current in the grounded neutrals of transformers and additional galvanic connections (pipelines, cables, portals);

- GS voltage;
- GS resistance;
- the value of the electric field potential in each node and the current in each grounding (see Fig. 9).

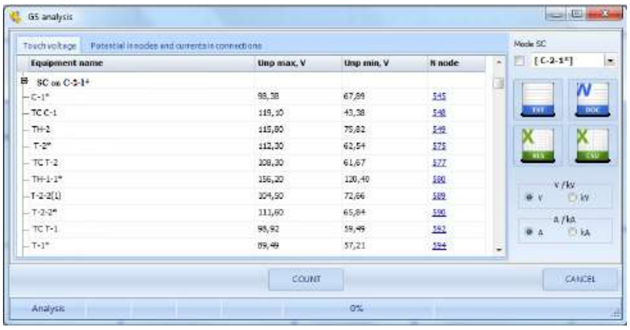

GS analysis

Touch voltage | Potential in nodes and currents in connections

Equipment name	Unp max, V	Unp min, V	N node
SC on C-2-1*			
C-1*	98,38	67,89	545
TC C-1	119,10	43,38	548
TH-2	115,80	75,82	549
T-2*	112,30	62,54	575
TC T-2	108,30	61,67	577
TH-1-1*	156,20	120,40	580
T-2-2(1)	104,50	72,66	589
T-2-2*	111,60	65,84	590
TC T-1	98,92	59,49	592
T-1*	89,49	57,21	594

Mode SC ☐ [C-2-1*]

V /kV ● V ○ kV

A /kA ● A ○ kA

Analysis 0%

Fig. 8. Calculation results of touch voltage of the investigated substation 150 kV by software «LiGro»

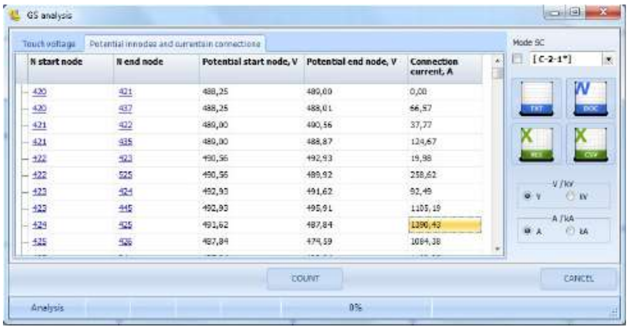

GS analysis

Touch voltage | Potential in nodes and currents in connections

N start node	N end node	Potential start node, V	Potential end node, V	Connection current, A
420	421	488,25	489,00	0,00
420	437	488,25	488,01	66,57
421	422	489,00	490,56	37,77
421	435	489,00	488,87	124,67
422	423	490,56	492,93	19,98
422	525	490,56	489,92	258,62
423	424	492,93	491,62	92,49
423	445	492,93	495,91	1105,19
424	425	491,62	487,84	1390,43
425	526	487,84	474,59	1084,38

Mode SC ☐ [C-2-1*]

V /kV ● V ○ kV

A /kA ● A ○ kA

Analysis 0%

Fig. 9. Calculation results of potential and current in the GS of the investigated substation 150 kV by software «LiGro»

It should be noted that the derivation of the voltage value in the nodes helps to determine the places for laying additional groundings to equalize the potential on the soil surface and to reduce the touch voltage.

As the calculation results showed, during a short circuit on the territory of the 150 kV substation, the touch voltage on all equipment does not exceed the allowable value (see Table 2).

The maximum value of the voltage on the substation GS in the case of a short circuit is 616 V.

The calculated value of the substation GS resistance, taking into account only artificial groundings, was 0,0454 Ω, which does not exceed the allowable value of 0,5 Ω.

Conclusions.

1. The adequacy of the developed mathematical model of the existing substation was confirmed by comparing the calculated and experimental measurements of the touch voltage by the simulation of the short - circuit current. It is shown that the average error in determining the touch voltage of the specified substation is 8,2 %.

2. Approbation of the created «LiGro» software package was carried out when performing the electromagnetic diagnostics of the grounding system of an existing substation with a voltage class of 150 kV in terms of determining electrical safety indicators: touch voltage, grounding voltage, and grounding system resistance. The authors was to the developed LiGro software package, as well as the VEZ-4A, received the copyright certificate.

Table 2

Calculation results of the touch voltage on equipment

Name of the equipment	$U_{t\max}$, V	$U_{t\min}$,V
CIRCUIT BREAKER C-1	130,9	94,21
CT T-1	139,6	50,46
VT-2	120,7	78,66
CIRCUIT BREAKER T-2	164,4	98,01
CT T-2	141,3	78,01
TH-1-1	222,1	173,6
T-2-2	133,4	93,91
CT T-1	125,8	74,19
CIRCUIT BREAKER T-1	135,9	93,87
T-1-0	159,2	81,57
T-2-0	154,1	86,14
T-2-H	208,7	90,99
C-1-1	158,4	130,3
VT-2-2	163,9	105,9
L-29-1	181,7	121,3
C-1-2	193,7	152,1
L-29A-2	177,7	116,3
C-2-1	237,6	124,9
C-2-2	217,2	141,1
T-1-1	115,7	79,61
CC-L-29	154,5	97,95
CC-L-29A	196,6	97,85
TC L-29	189,1	82,42
TC C-2	194,5	127,2
TN-1	184,4	99,82
2T	266,1	247,6
1T	368,4	362,8

3. It was confirmed that the advantages of the complex in its practical application are:

- the presence of a module for interpreting the results of soil sounding;
- calculation of the GS located in three-layer soil, which allows covering 90 % of energy facilities in Ukraine;
- taking into account all the design parameters of the GS;
- the presence of the analysis module with the display of currents in the connections, potentials in the nodes, the output of the maximum values of the touch voltage for the corresponding short circuit mode or for all points in all modes.

Conflict of interest. The authors declare no conflict of interest.

Acknowledgment. The work was carried out with the financial support of LLC «Industrial and commercial company CASKAD GROUP» within the scope under contracts (no. 16544 and no. 16553).

REFERENCES

1. *Natsional'nyy standart Ukrayiny. SOU 31.2-21677681-19:2009. Viprobuvannya ta kontrol' prystroyiv zazemlennya elektroustanovok. Tipova instruktsiya* [National Standard of Ukraine SOU 31.2-21677681-19:2009. Test and control devices, electrical grounding. Standard instruction]. Kyiv, Minenergovugillya Ukrayiny Publ., 2010. 54 p. (Ukr).

2. Koliushko D.G., Rudenko S.S., Plichko A.V., Shcherbinin V.I. Modernization of the complex type IK-1U for measuring the impedance of the grounding device of a lightning arrester and supports of transmission lines. *Electrical Engineering & Electromechanics*, 2019, no. 3, pp. 55-58. doi: https://doi.org/10.20998/2074-272X.2019.3.09.

3. Koliushko D.G., Rudenko S.S. Experimental substantiation of the calculation procedure of normalized parameters of grounding device based on the three-layer soil model. *Electrical Engineering & Electromechanics*, 2018, no. 1, pp. 66-70. doi: https://doi.org/10.20998/2074-272X.2018.1.11.

4. O. Rezinkin, M. Rezinkina, A. Danyluk, R. Tomashevskyi, Formation of high-voltage pulses with nanosecond fronts in low-impedance loads. *IEEE 2nd Ukraine Conference on Electrical and Computer Engineering (UKRCON)*, 2019, pp. 464-467. doi: https://doi.org/10.1109/UKRCON.2019.8880015.

5. Rezinkina M., Rezinkin O., D'Alessandro F., Danyliuk A., Lisachuk G., Sosina E., Svetlichnaya E. Influence of corona on strike probability of grounded electrodes by high voltage discharges. *Journal of Electrostatics*, 2016, vol. 83, pp. 42-51. doi: https://doi.org/10.1016/j.elstat.2016.07.005.

6. Koliushko D.G., Rudenko S.S. Determination the electrical potential of a created grounding device in a three-layer ground. *Technical Electrodynamics*, 2018, no. 4, pp. 19-24. doi: https://doi.org/10.15407/techned2018.04.019.

7. Koliushko D.G. *Sovershenstvovanie diagnostiki zazemliaiushchikh ustroistv elektroenergoob'ektov. Diss. cand. techn. nauk* [Improving the diagnosis of grounding devices for electric power objects. Cand. tech. sci. diss.]. Kharkiv, 2003. 172 p. (Rus).

8. Turri R., Andolfato R., Cuccarollo D. A numerical simulation tool for cathodic protection and electromagnetic interference analysis. *NACE Milano Italia Section – Conference & Expo 2016 «A European event for the Corrosion Prevention of Oil&Gas industry»*. 17 p. Available at: https://www.researchgate.net/publication/303685228_A_NUME (accessed 10 April 2022).

9. Hossain M.S., Ahmed R., Hossain S. Design and Optimization of Substation Grounding Grid for Ensuring the Safety of Personnel and Equipment. *Journal of Electrical Power & Energy Systems*, 2021, vol. 5, no. 1, pp. 71-80. doi: https://doi.org/10.26855/jepes.2021.08.001.

10. Tabatabaei N.M., Mortezaeei S.R. Design of grounding systems in substations by ETAP intelligent software. *International Journal on «Technical and Physical Problems of Engineering» (IJTPE)*, 2010, iss. 2, vol. 2, no. 1, pp. 45-49. Available at: http://www.iotpe.com/IJTPE/IJTPE-2010/IJTPE-Issue2-Vol2-No1-Mar2010/9-IJTPE-Issue2-Vol2-No1-Mar2010-pp45-49.pdf (accessed 05 April 2022).

11. Cardoso C., Rocha L., Leiria A., Teixeira P. Validation of an integrated methodology for design of grounding systems through field measurements. *CIRED - Open Access Proceedings Journal*, 2017, vol. 2017, no. 1, pp. 897-901. doi: https://doi.org/10.1049/oap-cired.2017.0452.

12. Uma U., Uzoechi L., Robert B. Optimization design of ground grid mesh of 132/33 kV substation using Etap. *Nigerian Journal of Technology*, 2016, vol. 35, no. 4, pp. 926-934. doi: https://doi.org/10.4314/njt.v35i4.30.

13. *IEEE Std 80-2013. Guide for Safety in AC Substation Grounding.* New York, IEEE, 2013. 206 p. doi: https://doi.org/10.1109/IEEESTD.2015.7109078.

14. *IEEE Std 81-2012. Guide for Measuring Earth Resistivity, Ground Impedance, and Earth Surface Potentials of a Grounding System.* New York, IEEE, 2012. 86 p. doi: https://doi.org/10.1109/IEEESTD.2012.6392181.

15. Koliushko D.G., Rudenko S.S., Koliushko G.M., Plichko A.V. Testers for Measuring the Electrical Characteristics of Grounding Systems by IEEE Standards. *2020 IEEE KhPI Week on Advanced Technology (KhPIWeek)*, 2020, pp. 216-220. doi: https://doi.org/10.1109/KhPIWeek51551.2020.9250116.

16. Koliushko D.G., Rudenko S.S., Saliba A.N. Method of integro-differential equations for interpreting the results of vertical electrical sounding of the soil. *Electrical Engineering & Electromechanics*, 2021, no. 5, pp. 67-70. doi: https://doi.org/10.20998/2074-272X.2021.5.09.

17. Electrical installation regulations. Kharkiv, Fort Publ., 2017. 760 p. (Ukr).

Received 11.04.2022
Accepted 13.05.2022
Published 20.07.2022

D.G. Koliushko[1], *PhD, Senior Research Scientist,*
S.S. Rudenko[1], *PhD, Senior Research Scientist,*
O.Ye. Istomin[1], *PhD, Senior Research Scientist,*
Abdel Nour Saliba[2], *General Manager, Postgraduate Student,*
[1] National Technical University «Kharkiv Polytechnic Institute»,
2, Kyrpychova Str., Kharkiv, Ukraine, 61002,
e-mail: nio5_molniya@ukr.net (Corresponding author)
[2] TMC Group,Beirut, Horsh Tabet, Sin el Fil, Lebanon,
e-mail: abdel.nour.saliba@gmail.com

How to cite this article:
Koliushko D.G., Rudenko S.S., Istomin O.Ye., Saliba A.N. Simulation of electromagnetic processes in the grounding system with a short circuit in the operating high-voltage substation. *Electrical Engineering & Electromechanics*, 2022, no. 4, pp. 75-80. doi: https://doi.org/10.20998/2074-272X.2022.4.11

Матеріали приймаються за адресою:
Кафедра "Електричні апарати", НТУ "ХПІ", вул. Кирпичева, 2, м. Харків, 61002, Україна
Електронні варіанти матеріалів по e-mail: a.m.grechko@gmail.com

Довідки за телефонами: +38 067 359 46 96 Гречко Олександр Михайлович

Передплатний індекс: 01216